PFC/RR-86-8

DOE/ET-51013-177
UC20a,20f

Study of Electron Temperature Evolution During Sawtoothing and Pellet Injection Using Thermal Electron Cyclotron Emission in the Alcator C Tokamak

Gomez, Camilo Ciro

May 1986

Plasma Fusion Center
Massachusetts Institute of Technology
Cambridge, MA 02139

This work was supported by the U.S. Department of Energy Contract No. DE-AC02-78ET51013. Reproduction, translation, publication, use and disposal, in whole or in part by or for the United States government is permitted.

STUDY OF ELECTRON TEMPERATURE EVOLUTION DURING SAWTOOTHING AND PELLET INJECTION USING THERMAL ELECTRON CYCLOTRON EMISSION IN THE ALCATOR C TOKAMAK

by

CAMILO CIRO GOMEZ

S.B. Massachusetts Institute of Technology, 1981

Submitted to the

Department of Physics

in Partial Fulfillment of the Requirements

for the Degree of

DOCTOR OF PHILOSOPHY

at the

MASSACHUSETTS INSTITUTE OF TECHNOLOGY

April 1986

Signature of Author_____

Department of Physics

April, 1986

Certified by _____

Doctor Stephen M. Wolfe

Thesis Supervisor

Accepted by _____

Professor George F. Koster

Chairman, Graduate Committee

To Kim

STUDY OF ELECTRON TEMPERATURE EVOLUTION DURING SAWTOOTHING AND PELLET INJECTION USING THERMAL ELECTRON CYCLOTRON EMISSION IN THE ALCATOR C TOKAMAK

by

CAMILO CIRO GOMEZ

Submitted to the Department of Physics

in April 1986 in Partial Fulfillment of the Requirements

for the Degree of Doctor of Philosophy in

Physics

ABSTRACT

A study of the electron temperature evolution has been performed using **thermal electron cyclotron emission.** A six channel far-infrared polychromator was used to monitor the radiation eminating from six radial locations. The time resolution was $< 3\mu s$. Three events were studied, the **sawtooth disruption**, propagation of the sawtooth generated **heatpulse** and the electron temperature response to **pellet injection.**

The sawtooth disruption in Alcator takes place in $20-50\ \mu s$, the energy mixing radius is $\sim 8\ cm$ or $a/2$. It is shown that this is inconsistent with single resonant surface Kadomtsev reconnection. Various forms of scalings for the sawtooth period and amplitude were compared. A study of **exotic** sawteeth has also been done. These differ from the normal sequence in that they exhibit very large $m = 1$ succerssor oscillations and involve a double disruption. The exotic sawtooth event is found to be strongly correlated with the presence of impurities. We suggest a model which may unify normal and exotic sawteeth.

The electron heatpulse propagation has been used to estimate χ_e(the electron thermal diffusivity). The importance of non-diffusive effects on the evolution of the heatpulse has been considered and it is found that at moderate to high densities ($n > 2\times 10^{14} cm^{-3}$) coupling between the electron and ion heatpulse may be important. A method of analysis has been developed which accounts for a non-quiescent background and near-field effects. We show that near-field effects are important in estimating χ_e. The χ_e estimate in this model reflets a local value rather than an average value. Comparisons have been done of the heatpulse estimated χ_e with that estimated by power balance. The agreement is found to be within a factor of two. Using the heatpulse technique a scaling has been done of χ_e as a function of the density. We consider the possible implications this has in interpreting the global confinement saturation observed in Alcator.

The fast temperature relaxation observed during pellet injection has also been studied. Electron temperature profile reconstructions have shown that the profile shape can recover to its pre-injection form in a time scale of $200\ \mu s - 3\ ms$ depending on pellet size. The transition between the slow and fast decay is rather adrupt. How this transition correlates with various plasma parameters will be discussed. The pellet generates transport coefficients which are roughly two orders of magnitude larger than the bulk. It is shown that the region of anomalous electron thermal

transport propagates with the pellet. The improved impurity confinement observed after pellet injection is strongly correlated with the form of the electron temperature relaxation that takes place early during injection. Pellet injection has also been used to study profile consistency. For $q_l < 8$, the post pellet electron temperature profile recovers its pre-injection profile width. For $q_l > 8$ a noticeable deviation from the self-consistent profile width takes place, with post-injection profile being different from the pre-injection profile.

Thesis Supervisor: Dr. Stephen M. Wolfe

ACKNOWLEDGEMENTS

This work was performed at the MIT Plasma Fusion Center and was supported by the United States Department of Energy under contract number DE-AC02-78 ET51013.

This thesis represents the culmination of several years of work. I wish to thank the Alcator Group for its contribution in making this work possible. As always there are a few individuals deserving of special mention.

Special thanks go to Dr. Stephen M. Wolfe, my thesis advisor for his work, guidance and support on this project. To Professor Ian H. Hutchinson who has provided me with many hours of useful discussion. Steve and Ian with their knowledge and physical insight have considerably increased my level of understanding of the subject matter. To Professor Benjamin Lax, my Bachelor's thesis advisor and graduate advisor, for providing me with intellectual challange and support over the years. He is a man whose intelligence and humanity are worthy of emulation. I thank Drs. Rex Gandy and Martin Greenwald for teaching me much about ECE and pellets respectively. To Professor Ronald R. Parker, leader of the Alcator Group, for nurturing the Alcator atmosphere, necessary for this kind of work to take place. To Professor Derek Boyd from the University of Maryland for providing the grating polychromator used in this study.

On a more personal note I would like to thank Camilo Sr. and Aida, my parents, for a lifetime of unwavering support and encouragement of my intellectual persuits. Odessa, my daughter, who over the last year has provided me with much enjoyment and through her playfullnes constantly reminds me not to take events too seriously. Finally I would like to thank Kim, my wife and partner, to whom this thesis is dedicated, for providing me with moral support and the privileges necessary for me to finish this work, our personal long march.

TABLE OF CONTENTS

III HEATPULSE PROPAGATION

0) Introduction to thesis

0.1) Fusion in a very small nutshell

Let us begin by giving a very rough picture of the fusion process, which is of course at the heart of our efforts to harness fusion energy.

Fusion involves the collision of two or more nucleii, in the process changing their nature as well as converting some of their mass into energy. This is to be compared to the fission reaction in which a single unstable nucleus decays into two lighter stable ones, in this process energy is also liberated by the loss of some of the original nuclear mass. The fusion reaction of most interest to the civilian fusion effort is that of deuterium and tritium, both isotopes of hydrogen (fig. 0.1). The reason for this is that it is the one with the largest fusion cross section at the lowest temperatures, making it the easiest to achieve. The envisioned cycle is as shown in (fig. 0.1). The two nucleii (D, T) are heated to a temperature of $0.02 Mev$ $(1 Mev \sim 10^{10}\ ^{o}K)$, this is necessary so that the nucleii can overcome their electrostatic repulsion and fuse. The by-products of the fusion reaction are an alpha particle (He^4) with an energy of $3.5 Mev$ and a neutron with an energy of $14 Mev$. The way a stable cycle is expected to be produced is by 'igniting' the fusing medium. This can be done by confining the alpha particles so that they will dissipate their energy in heating the fuel (D and T) to the required temperatures. The neutron can not be confined as easily and will usually escape the reaction region. It is the energy of the neutron that is expected to be harnessed. In the picture in (fig. 0.1) the neutron is absorbed by a surrounding wall (blanket), heating the blanket in the process. This can then be used to produce steam to drive a turbine to produce electricity. This of course is only one of many schemes for harnessing fusion energy. Because of the abundance of hydrogen in the universe, the harnessing of the controlled fusion process promises a nearly unlimited energy source.

At these temperatures the natural state for the reacting fuel will be that of a plasma. This is were plasma physicists come in. A plasma is an electrically neutral gas of ions and electrons (fig. 0.2). The goal of a sucessful fusion reactor is to be

able to confine the reacting plasma at sufficiently high density and temperatures for a sufficiently long time in order to produce enough fusion reactions to give a net energy gain.

As can be appreciated from the high temperatures involved, no ordinary confinement vessel will do to contain a burning plasma. In nature these conditions may exist in stars which by their sheer size can gravitationally contain the plasma. One approach for confinement on earth is to build a magnetic 'bottle' to contain the plasma. If a magnetic field is imbeded in a plasma the motion of the ions and electrons will be to gyrate about the field lines (fig. 0.2). By properly tailoring the magnetic field, the plasma can be trapped in it. In practice this is an extremely difficult problem, for the physics that governs the behaviour of a plasma is not well understood. The great promise of fusion and the complexity of the plasma physics problem has motivated an intense international effort to try to understand basic plasma physics and harness fussion.

0.2) The Alcator tokamak

The most most succesful scheme to date for confining a plasma magnetically is that of the **tokamak**. The original tokamak concept was proposed by the Soviets[1.1](tokamak is the Russian acronym for toroidal magnetic chamber). The concept involves forming the magnetic field into a closed toroidal geometry(like a doughnut). Early successes on the T-3 tokamak[1.2] stimulated growth in pursuing this concept.

The tokamak used for study in this thesis is the MIT ALCATOR C device(Alcator is an acronym for **AL**to **CA**mpo **TOR**us), a schematic of which is shown in (fig. 0.3). The plasma is created and confined in the toridal vacuum chamber. The toroidal magnetic field used to provide plasma stability is produced by a stack of Bitter magnets surrounding the vacuum chamber. The plasma is generated through electrical breakdown of the gas. The closed loop created by the plasma acts as the secondary of a transformer; current can be driven through it by inducing an electric field generated by a primary winding located at the center of the machine. The

current performs a dual function in the plasma. First it provides an effective way of heating the plasma and second the magnetic field generated by it confines the plasma. Alcator like most other present day tokamaks is designed to study the plasma physics involved in a fusion reactor not the fusion reaction itself. As such the working gases that form the plasma are H_2, D_2, and He. Tritium is not used because its radioactive properites would make handling very expensive.

The Alcator parameters are:

Major radius	$R_0 = 64cm$
Minor radius	$a = 16.5cm$
Toroidal magnetic field	$B_T < 12T$
Plasma current	$I_p < 800kA$
Plasma density	$n < 2 \times 10^{15} cm^{-3}$
Electron temperature	$T_e < 3keV$
Ion temperature	$T_i < 1.5keV$

What makes Alcator unique among tokamaks is its rather high magnetic fields and small size. Internal disruptions in tokamaks(sawteeth, to be discussed in great detail in chapter II) limit the current density that can be achieved. This is a serious limitation in terms of heating a plasma Ohmically and in plasma confinement. The central sawtooth limited current density scales as

$$J_0 \sim \frac{B_T}{R}$$

thus the higher the magnetic field and the smaller the major radius, the larger the current density that can be achieved.

0.3) Motivation of thesis

The hostile conditions in a high temperature plasma prohibit any direct sampling of the plasma properties. These must be inferred by use of some benign technique. This can take the form of measuring the electro-magnetic radiation or particles emanating from the plasma or by injecting laser or particle beams and observing their interaction with the plasma.

In this thesis we shall focus on the use of electron cyclotron emission (ECE) to measure the electron temperature of the plasma. As the electrons in the plasma gyrate about the magnetic field lines, the continual acceleration causes them to radiate. The radiation tends to have peaks at the cyclotron harmonics of the local magnetic field at the radiator. For the case in which the emission is black-body(i.e. it reflects the local temperature at the radiator) and the magnetic field profile is known, we can then associate a given frequency with a given spatial location in the plasma. The toroidal field in Alcator is such that the useful radiation is in the far infrared(FIR) range of frequencies. A six channel FIR grating polychromator was used, allowing continuous measurement of the electron temperature at six radial locations in the plasma.

Sawtooth disruptions (fig. 0.4) as was mentioned earlier represent a limitation on the current density that can be achieved in a tokamak. The periodic disruptions will dominate the transport and profiles in the central region of the plasma. Our dealings with sawteeth will involve two phases. The first is the direct study of the sawtooth disruption and the second concerns the plasma response to the sawtooth disruption. The most common diagnostic used to measure the dynamics of the sawteeth has been the soft-Xray emission[0.3,0.4]. While this technique has good signal to noise and good spatial resolution, the signal is a complicated function of electron temperature, density and impurities. This leads to great ambiguities in trying to unfold the electron temperature evolution. The ECE techniques as described above provide a unique opportunity to measure the electron temperature evolution in sawtoothing plasmas.

Several models have been proposed to explain the mechanism of a disruption[0.5,0.6,0.7]. The most detailed of these have been that of Kadomtsev[0.5] and Jahns[0.6]. We shall use these models to predict how the electron temperature should behave in Alcator during a sawtooth disruption. We can then make comparisons to gauge which of these models or part thereof agrees or disagrees with the observed behaviour. In the end we suggest a model which we feel fits the Alcator results.

The sawtooth disruption leads to a rapid redistribution of the energy in the central region of the plasma. This generates a heatpulse which propagates out of the plasma. Callen and Jahns [0.4] first proposed to study the evolution of this pulse to infer what the transport coefficients are in the outer regions of the plasma where the sawtooth disruption does not have a direct effect. They used the soft-Xray emission to try to follow the evolution of the electron heat pulse. Because of the ambiguities involved in the soft-Xray signal, they were limited in how much information could be used to infer the electron thermal diffusivity. By using the ECE we actually measure the electron temperature; thus fuller use of the electron temperature evolution can be made.

We shall develop a general formalism to describe the heatpulse evolution based on a Fourier decomposition of the sawtooth signal. This differs from previous treatments in that it explicitly accounts for the fact that the plasma is not in a quiescent equilibrium. A study will be done of the effect non-diffusive terms have on the estimate of the electron thermal diffusivity. Previous workers have assumed these to be negligible, however we shall find that at high densities some of these effects can be important. We shall use the techniques developed in this thesis to study the scaling of the electron thermal diffusivity.

Pellet injection promises to be an efficient way of fuelling a thermonuclear reactor. It has been found that pellet fuelled discharges exhibit improved confinement over gas fuelled discharges[0.8]. Most workers have focused on the long time scale effects of pellet fuelling, leaving the actual physics involved in pellet penetration into the plasma largely unexamined. We shall use the ECE techniques to measure the evolution of the electron temperature during the injection process (fig. 0.4). We find that the transport rather than being dominated by the transprot coefficients active before injection are enhanced by as much as two orders of magnitude. As we shall see, this self generated transport can have important implications when considering the fuelling process.

A common observation in several machines, including Alcator, has been that under certain conditions the electron temperature profile seems to have a canonical

shape. During pellet injection we have found that this mechanism is active under certain conditions. Pellet injection has provided us with a way to perturb the plasma by generating electron temperature profiles which can differ from the canonical shape. The general observation has been that the electron temperature profile, for high current discharges, recovers its canonical shape on extremely fast time scales which are consitent with the large pellet generated transport.

0.4) Organization of thesis

This thesis is divided into five chapters beyond this one. Each chapter is fairly self contained and may be read independent of the others.

Chapter I deals with a discussion of electron cyclotron emission. We discuss under what conditions the radiation can be used to make a temperature measurement. A discussion of the instrumentation is also given.

Chapter II discusses the nature of sawteeth. A review of the various models proposed is given as well as their implications for Alcator. A summary of results is given.

Chapter III develops the formalism used in studying the heatpulse propagation. We also discuss a single sawtooth model used to asses the importance of non-diffusive terms. A summary is given.

Chapter IV gives a treatment of the electron temperature evolution during pellet injection and a discussion of profile consistency. A summary of results is given.

Chapter V gives a summary of the main conclusions found.

References for chapter 0

[0.1] Tam I.E. and Sakharov A.D. in Plasma Physics and the Problem of Cotrolled Thermonuclear Reactions,vol. 1 edited by M.A. Leontovich (Pergamon Press N.Y. 1961)

[0.2] Artsimovich L.A., Nucl. Fus. 2(1972)215

[0.3] von Goeler S., et. al. Phys. Rev. Lett. 33(1974)1201

[0.4] Callen J.D., Jahns G.L., Phys. Rev. Lett. 39(1977)491

[0.5] Kadomtsev B.B., Sov. J. Plasma Phys. v1 n5(1975)389

[0.6] Jahns G.L., et. al., Nucl. Fus. 18 5(1978)609

[0.7] Equipe TFR IAEA-CN-35/A8

[0.8] Greenwald M., et. al. Phys. Rev. Lett. v53 n4(1984)352

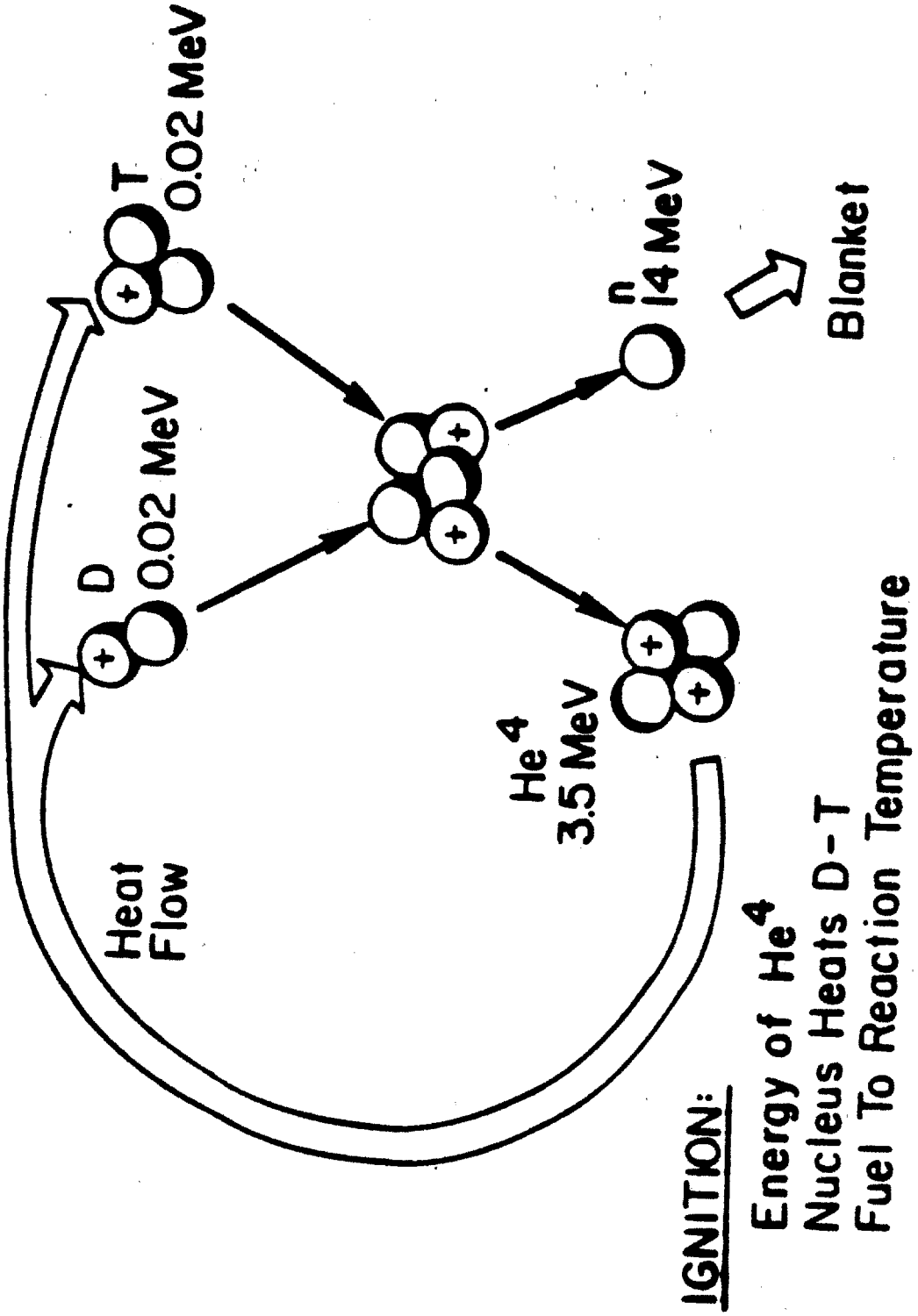

Figure 0.1 — D-T reaction

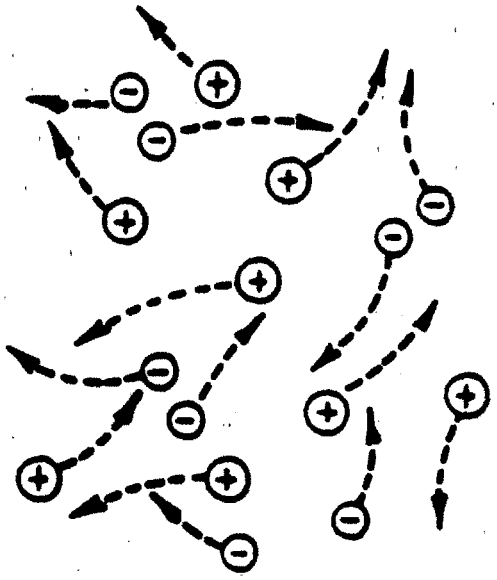

Plasma: A Hot Gas
of Ions and Electrons

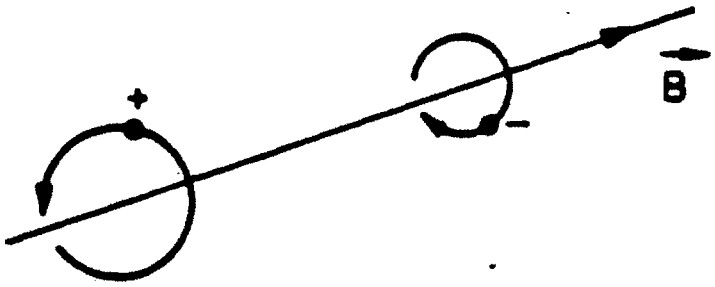

Magnetic Confinement
of Charged Particles

Figure 0.2 — The top figure depicts the motion of ions(+) and electrons (−) in an unmagnetized plasma. The bottom figure shows the motion of an ion and an electron in a magnetic field.

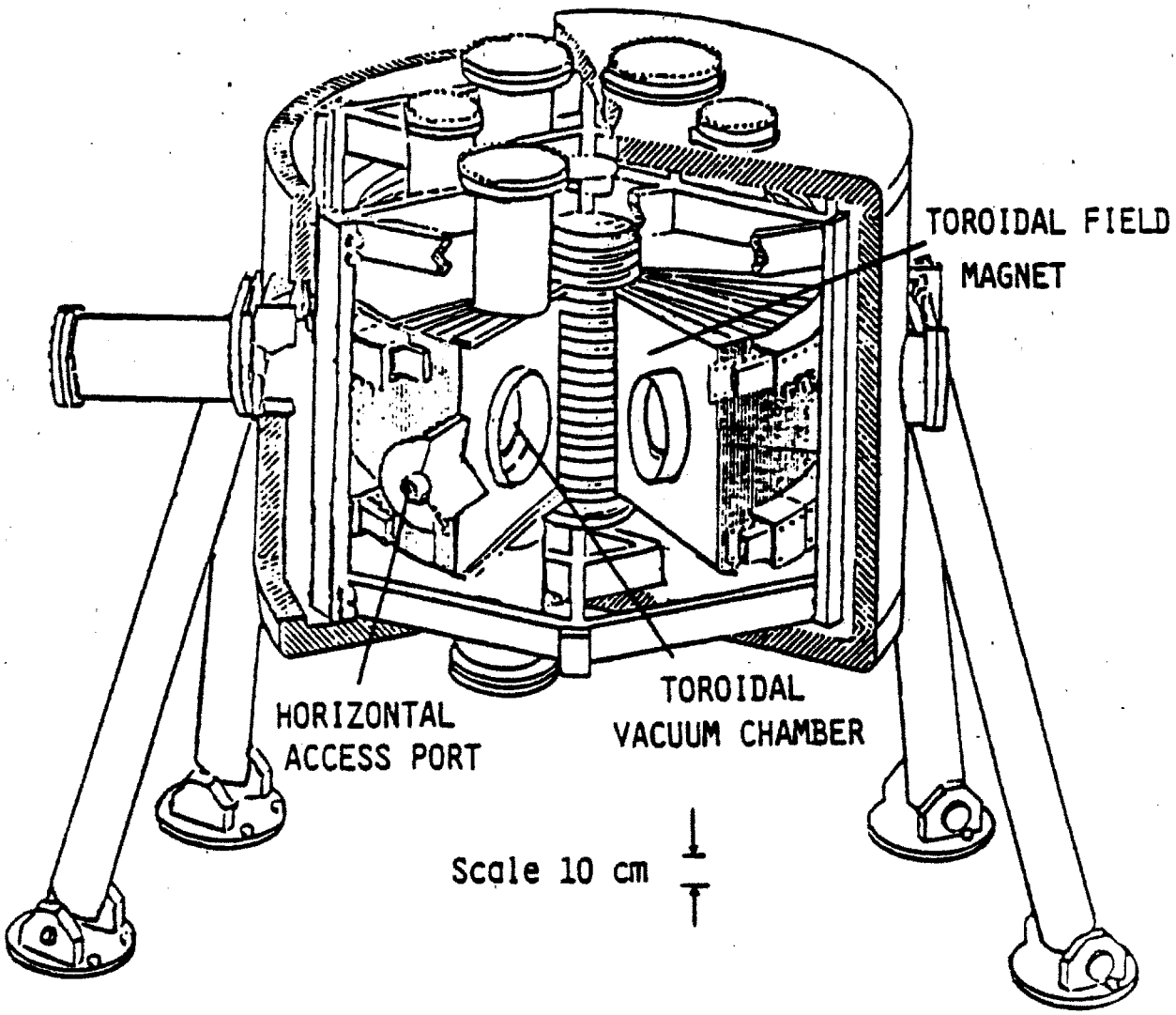

Figure 0.3 — Geometry of Alcator

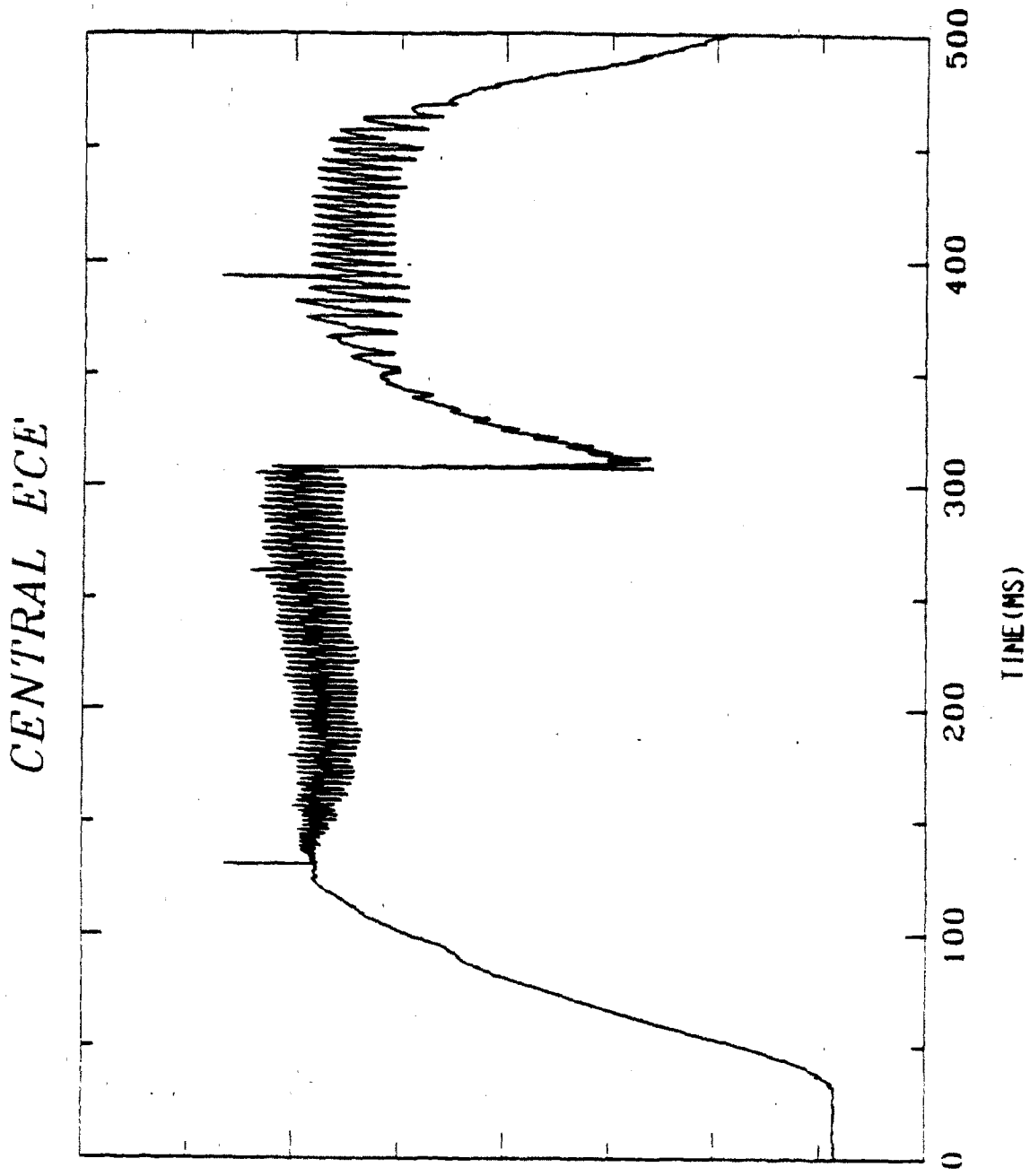

Figure 0.4 — This is a trace of the evolution of the central temperature showing the characteristic sawtooth like disruption. The large drop in temperature at $t \sim 300ms$ is due to the injection of a pellet.

I) Electron Cyclotron Emission and Instrumentation

1.1) Introduction

Electron cyclotron emission (ECE) is common to all magnetically confined plasmas. Because of the continual acceleration of the electrons in their helical orbits about the magnetic field, they radiate with peaks at harmonics of the local cyclotron frequency. Under certain conditions the electrons can be treated as free radiators. The ions also undergo radiation, but because of their large mass and shielding by the plasma, the frequency and intensity of their radiation is much lower than that for the electrons.

Interest in ECE was first motivated in considering the power loss in a thermonuclear plasma [1.1]. In this work it was found that ECE would contribute a substantial loss of energy from the plasma. Engelman and Curatolo [1.2] wrote an influential paper suggesting the use of ECE as an electron temperature diagnostic. In the case of a monotonically varying magnetic field such as in a tokamak, the highly localized radiation peaks and the use of optically thick lines (that is lines with very high absorption), could give a local measurement of the electron temperature. Technical problems have tended to limit the development of this diagnostic. The magnetic field values in current and future tokamaks put the useful ECE harmonics in the far-infrared range of frequencies $60 - 600GHz$. The technology has advanced to the point were ECE has become a routine diagnostic in all major tokamaks [1.3,1.4,1.5,1.6].

The most common forms of instrumention have been the scanning Michelson interferometer [1.7] and more recently the scanning Fabry-Perot [1.8]. The Michelson allows measurement of a wide frequency range of the ECE spectrum. A more specialized instrument is the scanning Fabry-Perot which measures a much narrower range of the spectrum, but has higher time resolution ($3ms$ vs. $15ms$ for the Michelson). This instrument is usually used to monitor the electron temperature profile. Another instrument in common use is the FIR grating polychromator[1.5,1.7]. This instrument allows measurement of a finite number of frequencies with very high

time resolution ($1 - 5\mu s$), the limitation in this case is the detector response, rather than the scan frequency as in the Michelson or Fabry-Perot.

In this thesis we have used a modified version of the grating used in [1,5]. Because of its fast time response, the grating is well suited for the study of transient temperature phenomena, which is the subject of this thesis. In the following sections of this chapter we discuss the principles involved in electron cyclotron radiation as well as how to use it to arrive at the electron temperature profile. A description of the grating instrument is also given.

1.2) Radiation transport

Let us begin our discussion by considering how radiation in general is transported through an active medium. The radiation transfer equation is:[1.9,1.10]

1.2.1)

$$\frac{d}{ds}\left(\frac{I}{n_r^2}\right) = \frac{j}{n_r^2} - \alpha\left(\frac{I}{n_r^2}\right)$$

I:intensity of radiation per unit solid angle along ray path

j:volume emissivity

α:absorptivity

The ray refractive index n_r is defined in [1.10] as

$$n_r^2 = n^2\left|\frac{sin\theta}{cos\beta\frac{\partial}{\partial\theta}(cos(\theta-\beta))}\right|$$

where θ: is the angle of propagation relative to B (fig. 1.2)

n:real index of refraction

$$tan\beta = \frac{1}{k'}\frac{\partial k'}{\partial\theta}$$

$$k' = Re(k)$$

For the case of an isotropic plasma or when $\theta = \pi/2$ in a toroidally and poloidally symmetric plasma then $\partial k'/\partial\theta \to 0$ and $n_r^2 \to n^2$. Eq.1.2.1 is valid for a particular frequency and mode of the medium. Eq. 1.2.1 can be integrated to give

1.2.2)

$$\frac{I(0)}{n^2(0)} = \frac{I(2)}{n^2(2)}e^{-\tau_2} + \int_0^{\tau_2} S(\tau)e^{-\tau}d\tau$$

where $d\tau = \alpha ds$. Refer to fig. 1.1 for an explanation of coordinates

τ_2 is the integrated optical depth from $\tau = 0$ to point (2).

$S(\tau) \equiv j/n^2\alpha$ is the source function.

If we make the assumption that at points 0 and 2 , $n \sim 1$ and the medium is passive (non absorbing, non emitting) between point 1 and the detector then $\tau_1 = 0$, $\tau_2 = \tau_0$ then we can write eq. 1.2.2 as

1.2.3)

$$I(0) = I(2)e^{-\tau_0} + \int_0^{\tau_0} S(\tau)e^{-\tau}d\tau$$

If we assume that at the frequency of interest, the medium is passive except for a well localized resonance, then the contribution to τ comes from the resonance layer. The source function can be taken as constant over the range of τ . Eq. 1.2.3 then becomes

1.2.4)

$$I(0) = I(2)e^{-\tau_0} + \frac{j}{n^2\alpha}(1 - e^{-\tau_0})$$

$j/n^2\alpha$ is evaluated at the resonance.

For the case in which the medium is in local thermal equilibrium (LTE), that is the local temperature of the plasma and that of the radiation are the same then,

$$I_{bb} = \frac{j}{n^2\alpha} = \frac{\omega^2 T}{8\pi^3 c^2} \qquad \text{if} \qquad \hbar\omega \gg T$$

For the remainder of this work I will concentrate on frequencies and modes for which $\tau_0 \gg 1$ and LTE is satisfied. Then eq 1.2.4 becomes

1.2.5)

$$I(0) = \frac{j}{n^2\alpha} = \frac{\omega^2 T}{8\pi^3 c^2}$$

The intensity at I(0) reflects the 'blackbody-body' temperature at the resonant surface.

Up to now our discussion of radiation has been general; it can be applied to electron cyclotron emission as well as any other emitting and absorbing process. If we want a temperature diagnostic we need a mechanism for which the black

surface for a particular frequency and mode is well resolved in space. We must now become more specialized in our treatment and discuss electron cyclotron emission, which is a mechanism that satisfies the above conditions to give a spatially resolved measurement of the electron temperature.

1.3) Discrete particle treatment of electron cyclotron emission.

In this work I will not try to give anything close to a comprehensive review of electron cyclotron emission(ECE). There are numerous works in the literature that do an outstanding job[1.9,1.10,1.11]. I will present the salient results as they relate to temperature measurements.

A single electron placed in a homogeneous magnetic field will undergo gyrating motion (fig 1.2). Because of continual acceleration it radiates with the following intensity distribution at the particle:[1.9]

1.3.1)

$$\frac{d^2P}{d\omega d\Omega} = \frac{e^2\omega^2}{2\pi c}\sum_{l=1}^{\infty}\delta\left[(1-\beta_{\parallel}cos\theta)\omega - l\omega_c\right]\times$$

$$\left|\hat{x}\frac{cos\theta}{sin\theta}(cos\theta-\beta_{\parallel})J_l(\xi)+\hat{y}(-i\beta_{\perp})J_l'(\xi)+\hat{z}(cos\theta-\beta_{\parallel})J_l(\xi)\right|^2$$

where

$$\beta_{\parallel,\perp} = \frac{v_{\parallel,\perp}}{c}$$

$$\xi = \frac{\omega}{\omega_c}sin\theta$$

One observation that can be made is that emission takes place at a discrete set of frequencies.

1.3.2)

$$\omega_l = l\omega_c = \frac{l\omega_{c0}\sqrt{1-\beta^2}}{(1-\beta_{\parallel}cos\theta)}$$

ω_{c0} is the rest fundamental cyclotron frequency. The discreteness of the spectrum can be understood from the periodic motion of the electrons. The radiation can be decomposed into two modes, the extraordinary mode(X mode) with $E\perp B_z$ and the ordinary mode (O mode) with $E\|B_z$.

The radiation emanating from the plasma is not due to a single electron but rather an ensemble. If eq .1.3.1 is to have any relevance, the plasma must be sufficiently tenuous so that collective effects can be neglected. We integrate eq 1.3.1 over the particle distribution function to get the emissivity. From eq 1.3.2 we can see two mechanisms that will introduce a shift in the radiation frequency due to motion of the electrons;

1)Doppler broadening

$$1 - \beta_{\parallel} cos\theta$$

2)Relativistic broadening

$$\sqrt{1 - \beta^2}$$

The angle of propagation determines which of these two effects is important. In general if

$$cos\theta < \beta$$

relativistic broadening will be dominant. For a plasma of $T_e \sim 1keV$, this corresponds to an angle $\pm 3^o$ from the perpendicular of the magnetic field. In Alcator C because of limited port access, we are confined to viewing in a region where relativistic broadening is the dominant mechanism.

The lines for which $\tau_0 \gg 1$ in Alcator like plasmas turn out to be 2^{nd} harmonic X-mode and fundamental O-mode eq. 1.3.3. Because of the spatial variation in the magnetic field, absorption takes place over a region of the plasma of length:

$$L \sim \Delta\omega \left| \frac{d(l\Omega)}{ds} \right|^{-1}$$

If relativistic broadening is dominant

$$\Delta\omega \sim \frac{T}{m_e c^2} l\Omega$$

and

$$l\Omega = l\Omega_0 \frac{R_0}{R}$$

so

$$L \sim \frac{T}{m_e c^2} R$$

for Alcator

$$R = 64 \text{ cm}$$

$$T \sim 1 \text{ kev}$$

$$L \sim .13 \text{ cm}$$

Because of the small size of the absorption region, the optical depth for a fixed frequency can be treated as a local quantity.

The optical depth can be calculated in several ways. The imaginary part of the index of refraction can be considered, or, since we are looking at lines which radiate from a population in LTE we can relate α to j by using Kirchoff's relation (eq. 1.2.5).

Useful approximate expressions for the optical depths have been given by [1.6] for $\omega_p < \omega$ and perpendicular propagation

$$\tau^X_{n=2} = 4\pi \frac{R}{c} \frac{\omega_p^2}{\omega} \frac{kT_e}{m_e c^2}$$

1.3.3

$$\tau^O_{n=1} = \frac{\pi}{2} \frac{R}{c} \frac{\omega_p^2}{\omega} \frac{kT_e}{m_e c^2}$$

A more accurate formalism is discussed by Tamor [1.11].

1.4) Toroidal plasma effects.

The toroidal geometry modifies the ECE spectrum in some very important ways. The most salient of these is the inhomogeneity of the magnetic field.

1.4.1)

$$B = B_0 \frac{R_0}{R}$$

This has two effects; it broadens the line width of the harmonics (fig1.3a) and because it is monotonically varying, it establishes a 1:1 correspondence between frequency and spatial position (fig 1.3b). We see that over certain regions of space there is harmonic overlap, however these take place at the edge which contains little energy. By considering fig. 1.4 we can arrive at the overlap condition for a harmonic

$$l \geq \frac{1}{2}\left(\frac{R_0}{a} - 1\right)$$

R_0:major radius

a: limiter radius

The plasma also modifies the spectrum through its dielectric properties. These affect the ray path and can thus add uncertainty to the measurement of the temperature profile. Another important effect is that of resonance and cutoff.

The plasma dispersion relation for the X and O modes are, for perpendicular propagation

$$n_X^2 = \frac{(\omega^2 - \omega_R^2)(\omega^2 - \omega_L^2)}{\omega^2(\omega^2 - \omega_U^2)} \qquad \text{(X-mode)}$$

1.4.2)

$$n_O^2 = 1 - \frac{\omega_p^2}{\omega^2} \qquad \text{(O-mode)}$$

where

$$\omega \begin{pmatrix} R \\ L \end{pmatrix} = \frac{1}{2}\left[(\omega_c^2 + 4\omega_p^2)^{\frac{1}{2}} \pm \omega_c\right]$$

$$\omega_U^2 = \omega_{pe}^2 + \omega_{ce}^2$$

ω_{pe} is the electron plasma frequency

The condition for cutoff is $n^2 \Rightarrow 0$, that for resonance is $n^2 \Rightarrow \infty$

For the X-mode this implies a non-propagation region of

$$\omega_U < \omega < \omega_R$$

$$\omega < \omega_L$$

for the O-mode

$$\omega < \omega_{pe}$$

see fig 1.4

Because we are restricted to view from the low field side, the fundamental X-mode will always encounter the upper hybrid resonance layer, thus it does not propagate out of the plasma. The O-mode is limited by the ω_{pe} cutoff. The right hand cutoff is usually well below the 2^{nd} harmonic X-mode thus leaving this line relatively unaffected by dielectric effects.

Because the plasma in the laboratory is usually inside some sort of container, the radiation can be modified by interaction with the container. Reflections from

the walls tend to enhance the observed radiation and thus 'thicken' the line. Because tokamak walls are not usually smooth, a fraction of the reflected radiation tends to be scattered into the other mode of polarization. This effect will tend to isotropise the radiation inside a tokamak. This isotropization has been used to explain the large ratio of the ordinary to extra-ordinary emission of the harmonic [1.4,1.12]. The spectra of the horizontal and vertical emission were compared and found to be similar [1.3,1.13]. Since the field in the vertical direction is uniform, we would expect the spectrum to consist of a series of lines at the cyclotron harmonics of the field along the viewing chord with the broadening determined by the beam spot size. The observed lines have a width consistent with the horizontal spectrum. The interpretation is that reflections from the back wall scatter radiation from other regions of the plasma.

A simple model has been proposed in [1.4] to explain the enhanced polarization ratio. Consider the plasma to be between two parallel walls and consider only perpendicular propagation with only X and O modes. Define r as being the coefficient for reflection into the same polarization and p the coefficient for reflection into the other polarization. The ratio of polarization for a harmonic becomes ($\tau_0 \ll 1$)

$$\frac{I_O}{I_X} = \frac{p}{1-r}$$

the intensity for the X mode is then

$$I_X = I_{bb}\frac{1-e^{-\tau x}}{1-\rho e^{-\tau x}}$$

$$\rho = r + \frac{p^2}{1-r}$$

We see that as $\rho \to 1$ the intensity approaches the black body level.

1.5) Measurement of the electron temperature profile.

We have shown that for an optically thick harmonic eq. 1.2.5 gives

$$I \sim \omega^2 T_e$$

For a tokamak like Alcator, the optically thick lines are the O mode fundamental and the X mode second harmonic. Because of the ω^2 dependence, the radiation intensity for the second harmonic is a factor of four higher than that for the fundamental. Because of the higher frequencies plasma effects are less on the second harmonic than on the fundamental. For these reasons we have used the second harmonic in making our electron temperature measurements. The requirement that $\tau > 1$ is satisfied for the second harmonic if

$$B_z \beta_e > 8.3 \times 10^{-4}$$

where $\beta_e = nT_e/(\frac{B_z^2}{2\mu_0})$ and B_z is the local magnetic field in Tesla. Fig 1.5 shows τ as a function of plasma position for typical Alcator parameters.

Central to the profile measurement is the assumption that we know the magnetic field in the plasma. For a given cyclotron harmonic, an uncertainty in the magnetic field leads to an uncertainty in the location of the point of emission. This will affect the apparent temperature profile. We can make a lowest order estimate of the spatial uncertainty by using the vacuum profile:

$$|\delta R| = -\frac{R}{B}|\delta B|$$

δB is the difference between the real field and the assumed vacuum field, δR is the difference between the location of the real field and that corresponding to the vacuum profile. In order to find estimates for δB we need to consider the plasma effects that lead to deviation from the vacuum field. Two effects will be considered

1) β_θ effects, 2)uncertainty in field calibration. The proper scale length with which to compare δR, is the effective spatial resolution of the instrument used in making the measurement.

Plasma effects will change the value of B_z from that of its vacuum value. From simple MHD equilibrium considerations we can show that the change in B at the center is

$$\delta B = \left(\frac{\hat{\beta}_\theta}{2} - 1\right)\frac{B_\theta^2(a)}{B_z}$$

correct to order $(a/R)^2$. Here for simplicity we have assumed a uniform current profile and

$$\hat{\beta}_\theta \equiv \frac{p_e(0) + p_i(0)}{B_\theta(a)^2/2\mu_0}$$

This introduces a shift in the apparent position of the emitting surface of order

$$\delta R = R\left(\frac{\hat{\beta}_\theta}{2} - 1\right)\frac{B_\theta^2(a)}{B_z^2}$$

For a plasma of $\overline{n} = 2 \times 10^{14} cm^{-3}$ $T_e \sim 2keV$ $B_t = 8T$ $R = 64cm$

$$\hat{\beta}_\theta = 0.65$$

$$\delta R = 0.16cm$$

The instrumental resolution for the far-infrared grating used here is of order 2 cm, thus β_θ effects should not be important.

Although field calibration does not affect the profile shape, it is important in relating the measured temperature profile in frequency to absolute spatial location in the plasma. A 3% uncertainty in the magnetic field yields a spatial uncertainty of $\sim 2cm$. Field calibration for the ECE was accomplished in the following way. By measuring the center of sawtooth activity using the ECE which is frequency resolved (equivalently B resolved) and comparing it to the center found from some other diagnostic which is spatially resolved, we can arrive at a self-consistent field calibration. It should be pointed out that for the case of measuring the profile shape the situation is better.

Let

$$R_1 = \frac{C}{B_1}$$

R_1 is the major radius location associated with the ECE measured field B_1. C is a coefficient which contains the field calibration. The distance between two points in the plasma along the toroidal plane is

$$d = R_1 - R_2 = C(\frac{1}{B_1} - \frac{1}{B_2})$$

the uncertainty in d is

$$\delta d = \delta C(\frac{1}{B_1} - \frac{1}{B_2})$$

$$\frac{\delta d}{d} = \frac{\delta C}{C} = \frac{\delta R}{R}$$

so

$$\delta d = d\frac{\delta R}{R}$$

For Alcator plasmas $d \sim 10cm$ $R = 64cm$ using $\delta R \sim 2cm$ then

$$\delta d \sim .3cm$$

which is much less than the instrumental resolution of $2cm$.

Another issue that must be considered is the effects of finite instrumental resolution. This washes out features of high spatial frequency. We can relate the measured temperature profile to the actual profile by the equation

1.5.1)

$$T_m(x) = \int dx' g(x - x') T_r(x')$$

Here we have made the conversion to spatial coordinates

T_m is the measured temperature profile

T_r is the 'real' temperature profile

g is the normalized instrumental function

$$\int dx g(x) \equiv 1$$

If the spatial extent of $g(x)$ is much less than that of $T(x)$ we can expand $T_r(x')$ about $x' = x$.

$$T_r(x') = T_r(x) + \left.\frac{\partial T_r}{\partial x'}\right|_{x'=x} (x' - x) + \frac{1}{2} \left.\frac{\partial^2 T_r}{\partial x'^2}\right|_{x'=x} (x' - x)^2$$

then

$$T_m(x) = T_r(x) + \left.\frac{\partial T_r}{\partial x'}\right|_{x'=x} \int dx' g(x-x')(x'-x) + \frac{1}{2} \left.\frac{\partial^2 T_r}{\partial x'^2}\right|_{x'=x} \int dx' g(x-x')(x'-x)^2$$

If we take the instrumental function to be symmetric about x then

$$\int dx' g(x - x')(x' - x) = 0$$

defining

$$\sigma^2(x) \equiv \frac{1}{2} \int dx' g(x - x')(x' - x)^2$$

then

$$T_m(x) = T_r(x) + \frac{\partial^2 T_r}{\partial x'^2} \sigma^2(x)$$

if

$$\sigma^2 \ll \frac{T_m(x)}{\left(\frac{\partial^2 T_m}{\partial x^2}\right)}$$

we can neglect the contribution from the second term. This condition is well satisfied in the measurement of the background temperature profile. However in studying the heatpulse propagation, we need to study the evolution of the incremental temperature profile which may have a large second derivative term. The measured incremental profile can be related to the real profile by replacing the total temperature with the incremental piece. It is convenient to express the incremental temperature normalized to the backgound temperature. This eliminates the effects of calibration from affecting the deconvolution

1.5.2)

$$\frac{\tilde{T}_m(x)}{T_m(x)} = \int dx' g(x-x') \frac{\tilde{T}_r(x)}{T_r(x)}$$

For computational ease I will assume a gaussian line shape, with a resolution of $2.5cm$, which is consistent with the grating resolution. Fig. 1.6 shows examples of the convolution of two possible incremental profiles. Case no 1 represents an experimental profile, case no 2 is a profile consistent with a flattening of the electron temperature out to a radius of $\sim \sqrt{2}r_i$(inversion radius of sawtooth oscillation). We see that for the case of the experimental profile, the effect is small, at least it is within the mesurement error. The difference between the convoluted profiles of case no. 1 and 2 is sufficiently large, such that we can differentiate between the two profiles for the given grating resolution.

1.6)Instrumentation

The instrument used to make the ECE mesurements in this thesis has been a six channel far-infrared(FIR) grating of the Czerny-Turner type[1.5,1.7,1.14]fig. 1.8. This instrument is ideally suited for this kind of measurement, for it allows many spatial points with good time resolution ($\leq 3\mu s$). The number of spatial locations is limited by the number of detectors and grating geometry and the time resolution by the detector response.

The grating achieves frequency selection by scattering radiation from a periodic structure. The direction of the reflected radiation will depend on the wavelength. In the following I will give a scalar treatment of grating performance. In the strict sense this is not valid since d(grating constant) $\approx 1.5\lambda$, however it is the simplest theory that allows understanding of grating efficiency at different orders and does give qualitative agreement with actual performance.

Fig 1.7 shows the kind of grating geometry used to describe the grating dispersion. By considering a plane wave incident on the grating, the intensity of the diffracted wave is of the form:

1.6.1)

$$I(\vec{k}',\vec{k}) = I(\vec{k})\left|f_0(\vec{k}',\vec{k})\right|^2 \frac{sin^2\left(\frac{1}{2}N\eta\right)}{sin^2\left(\frac{1}{2}\eta\right)}$$

$$\eta = \frac{2\pi d}{\lambda}\left(sin\alpha + sin\beta\right) = \left(\vec{k}-\vec{k}'\right)\cdot\vec{d}$$

$\left|f_0\right|^2$:grating efficiency for a given mode.

N:number of lines illuminated

In eq.1.6.1 the quantities $I(k)$, $|f_0|^2$ vary slowly as a function of $\vec{k}$, $\vec{k}'$. It is found that the line shape is determined by the function

$$\frac{sin^2\left(\frac{1}{2}N\eta\right)}{sin^2\left(\frac{1}{2}\eta\right)}$$

It has primary peaks at

$$\eta = \pm 2\pi m \qquad\qquad m = 0, 1, 2, \ldots$$

secondary peaks at

$$\eta = \pm\frac{\pi}{N}\left(1 + 2p\right) \qquad\qquad p = 0, 1, \ldots$$

and zeroes at

$$\eta = \pm\frac{2\pi}{N}n \qquad\qquad n = 1, 2, \ldots$$

The ratio of the primary to secondary peak intensity is found to be over an order of magnitude, so energy is contained mostly in the primary peaks. The grating equation is given by the resonance condition

1.6.2)

$$m\lambda = d\left(sin\alpha + sin\beta\right)$$

For most grating arrangements as well as the one used here the angle between the incident and diffracted beams is held fixed. We can then rewrite eq 1.6.2 in terms of two new angles θ, ϕ defined in fig 1.7 as

1.6.3)

$$m\lambda = 2dsin\theta cos\phi$$

ϕ is the $\frac{1}{2}$ angle between the incident and diffracted beams

θ is the angle between the grating normal and the ray bisector

The first zeroes about the resonance define the minimum line width. We can show the resolving power to be

1.5.4)

$$\frac{\lambda}{\Delta\lambda} = Nm$$

Typically we operate with $m = 1$ $N \approx 200$ so $\lambda/\delta\lambda = 200$; in practice this value is very hard to achieve, but as we shall see this is generally not important since the limiting resolution will be defined by the slit size. What we require is that the grating resolving power be much greater than that defined by the slit.

As mentioned above the slits determine the resolving power of the grating; the reason for this is that the resolution is detector limited, that is if we could build an instrument with a resolving power approaching that of the grating, the power reaching the detector would give an unacceptably low signal to noise ratio.

The size of the entrance slit is chosen so that for the given etendue of the system the input radiation illuminates all of mirror M1 fig 1.8. The system etendue is defined at the machine side of the optical path to insure optimum power coupling.

To estimate the bandwidth of the grating we can use eq. 1.6.3 to arrive at an expression for the rate of change of wavelength with exit plane position, f_l is the focal length of the mirrors, s is a displacement in the exit plane.

1.6.5)

$$\frac{\delta\lambda}{\delta s} = \frac{\lambda}{2f_l}\sqrt{\left(\frac{2dcos\phi}{m\lambda}\right)^2 - 1}$$

The bandwidth of the instrument is defined as

$$\Delta\lambda = \frac{\delta\lambda}{\delta s}\Delta s_{eff}$$

where Δs_{eff} is the effective slit width of the instrument , accounting for diffraction and mode effects. Measurements have been done using a grating of d=1.733mm with $\lambda \sim 2.3mm$ $\phi \sim 17.8°$; the measured bandwidth for this case is $\Delta\lambda = 0.038mm$. This gives an effective slit width of $\sim 1.4cm$ and the actual slit width is $1.5cm$. For operation at $B_t = 8T$, this implies a radial resolution of $\delta R \sim 2.5cm$.

For operation, it is more convenient to define $\theta = \theta_g - \phi$, where θ_g, is the angle between the incident ray and the grating normal. Eq. 1.6.3 can now be written as

1.6.6)

$$m\lambda = 2dsin(\theta_g - \phi)cos\phi$$

The grating constant d and θ_g determines the dispersion of the grating. Since the slit locations are fixed, they determine which frequencies are seen by each detector. We pick d so that each channel sees a frequency which corresponds to a location in the plasma. Fig 1.9 shows the corresponding plasma positions for a toroidal field $B_t = 8T$ as a function of grating angle (θ_g) for $d = 0.867mm$.

We improve considerably on the grating efficiency by tailoring our choice of blaze angle θ_B see fig. 1.7 to match the spectral range of frequencies used. We see from fig 1.7 that if the diffracted angle for wavelength λ is equal to the angle of specular reflection from face (a) of the grating, this wavelength will be diffracted very efficiently. We define the blaze wavelength as

1.6.7)

$$\lambda_B = 2dsin(\theta_B)$$

This is the wavelength of maximum efficiency for the grating.

The theoretical efficiency has been calculated using scalar theory as described in [1.14]. Since we want maximum efficiency at $\lambda_B \approx 0.6mm$ and $d = 0.867mm$ gives a blaze angle of $\theta_B = 23^o$. The efficiency calculated for this grating is shown on fig 1.10. We see that at the blaze wavelength all orders are equally efficient but higher orders fall off much faster than first order when one goes off the blaze angle.

Generally one would operate at $\theta > \theta_B$ to reduce the transmission of higher orders. However at the frequencies we operate ($\approx 500GHz$) the detector response for the higher harmonics is negligible. Also these higher orders correspond to fourth or higher harmonic emission from the plasma which is down by a factor of $\left(\frac{T}{m_e c^2}\right)^2$ or more from the second harmonic, also whatever overlap there is between the fourth and third harmonic takes place at the edge of the plasma. So we can operate at close to the blaze angle in first order without much contribution from the higher

harmonics thus optimizing the grating efficiency. The above argument does not hold for plasmas with a significant non-thermal electron population.

To get the radiation to the grating we use an optical system like the one shown in fig 1.11. Imaging is done with a TPX lens of $f_l = 57cm$. The iris is focused at the plasma center with a magnification of 1.2, defining vertical and azimuthal resolution. It is the iris that determines the vertical and horizontal resolution. This is normally set to match the radial resolution as fixed by the grating. A 1000 l/in polarizer is used as a mode selector to pick between the X and O modes. The etendue of the system is defined by the lens diameter and the chosen iris diameter. For maximum efficiency the remainder of the system is designed to have the same etendue. From the iris the radiation goes into a $\sim 10ft$ straight light pipe for low loss transmission. A beam splitter is then placed in the beam path to allow operation of a scanning Fabry-Perot from the same beam line. A matching cone is then used to couple the radiation from the larger diameter light pipe to the entrance slit. The system from the machine window to the matching cone is designed to operate in low vacuum to eliminate any water vapor absorption.

Detection is done by using six He cooled InSb detectors [1.15]. By cooling to liquid He($\sim 4^oK$) the thermal noise of the device is reduced to $\leq 1nV/\sqrt{Hz}$. Radiation is absorbed by the electrons in the conduction band. For very pure crystals at low temperature the coupling to the lattice is low and because of the low electron density large changes in the effective electron temperature (and thus the resistance of the crystal) can be effected with low signal levels. The noise in the system is limited by that of the first amplifying element. This was reduced by using a large gate FET (no. 2N6550). The pre-amplifier used is based on one suggested by Hutchinson [1.16], the circuit is shown in fig. 1.12. The overall gain of the circuit shown is ~ 100 set by R_3/R_2 with an effective input noise of $1 - 1.5nV/\sqrt{Hz}$. The bandwidth is $\sim 100kHz$ set by R_3, C_1. The signals were then amplified by a second stage to an overall gain of 1000. The signals were then recorded on two Le Croy 8210 digitizers at a rate of $200kHz$ allowing a $40ms$ slice of the plasma shot to be recorded.

References for chapter 1

[1.1] Trubnikov B.A.,Bazhanova A.E., Plasma Physics and the problem of controlled thermonuclear reactions,vol. III,141,Pergamon Press,Oxford, UK(1959).

[1.2] Engelman F.,Curatolo M., Nuclear Fusion, 13 (1973)497

[1.3] Costley A.E. and the TFR group, Phys. Rev. Lett., v38 n25(1977)1477

[1.4] Hutchinson I.H.,Komm D.S., Nuclear Fusion,vol. 17,no. 5 (1977)1077

[1.5] Tait G.D.,et. al.,Physics of Fluids,vol. 24,no. 4 (1981)719

[1.6] Costley A.E.,et.al.,EC-4 Fourth Int'l Workshop on ECE and ECRH,Frascati,March 1984.

[1.7] Kimmitt M.F.,Far-infrared techniques,Pion Limited,London(1972)

[1.8] Walker B.,et. al., Development of a Fabry-Perot interferometer for measurement of tokamak electron cyclotron emission,NPL special investigation no. 89/0457.

[1.9] Bekefi G.,Radiation processes in plasmas,Wiley and sons Inc.,NY (1966).

[1.10] Bortanici M.,et.al.,Nucl. Fus., vol. 23 no. 9 (1983)1153.

[1.11] Tamor S.,Report no. LAPS-26 SAI 77-593-LJ, Science Applications Inc. (1977)

[1.12] Kissel S.,Plasma Fus. Center report no. PFC/RR-82-15

[1.13] Kato K.,Hutchinson I.H.,PFC report no. PFC/JA-86-3.

[1.14] Maden R.P.,Strong J., Concepts of classical optics, Freeman,San Francisco (1958)

[1.15] Putley E.H., Applied Optics, vol. 4 no. 6 (1965)649

[1.16] Hutchinson I.H.,private communication

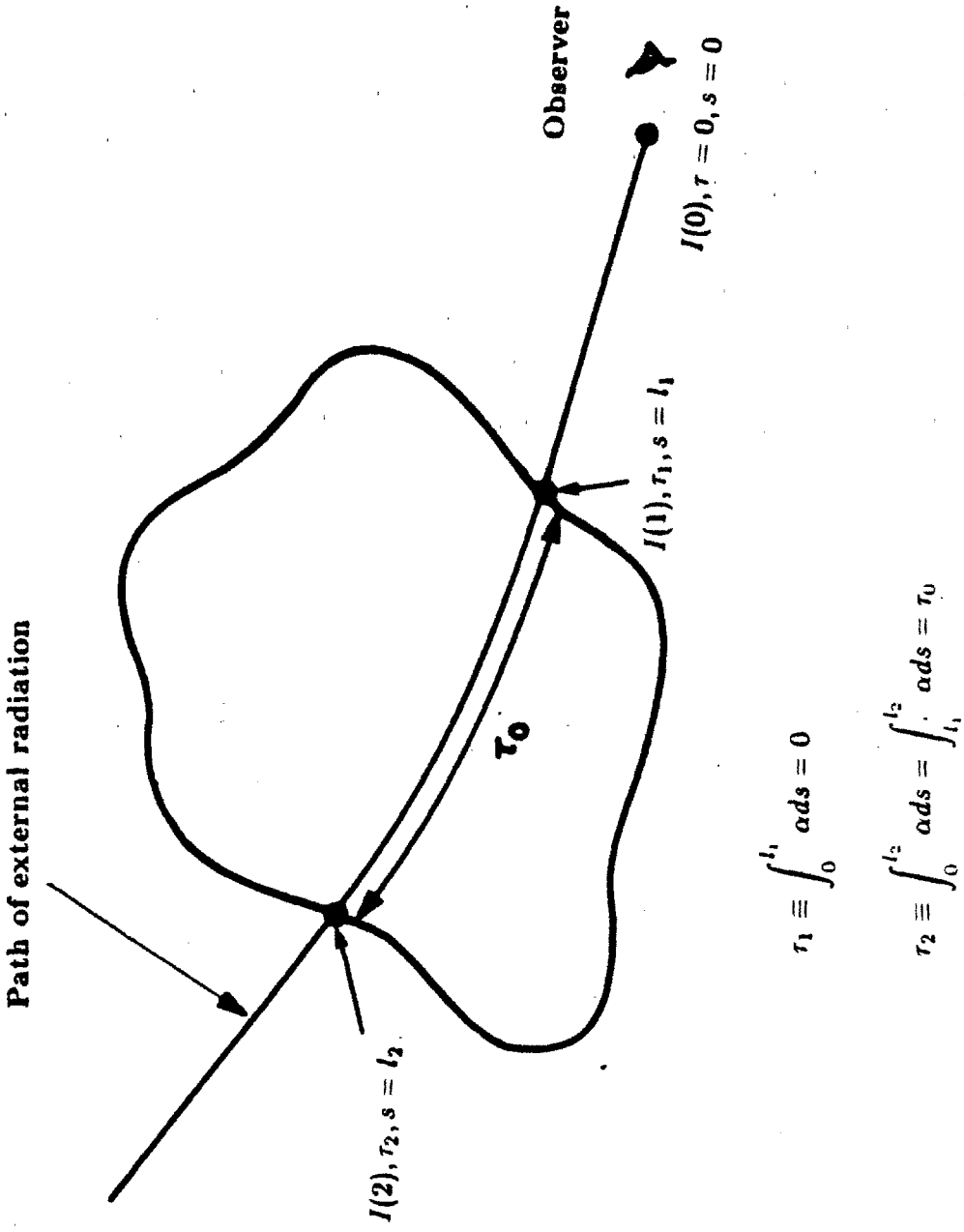

Figure 1.1 — Geometry of ray path with explanation of optical depth. α is the local absorption coefficient of the mode under consideration.

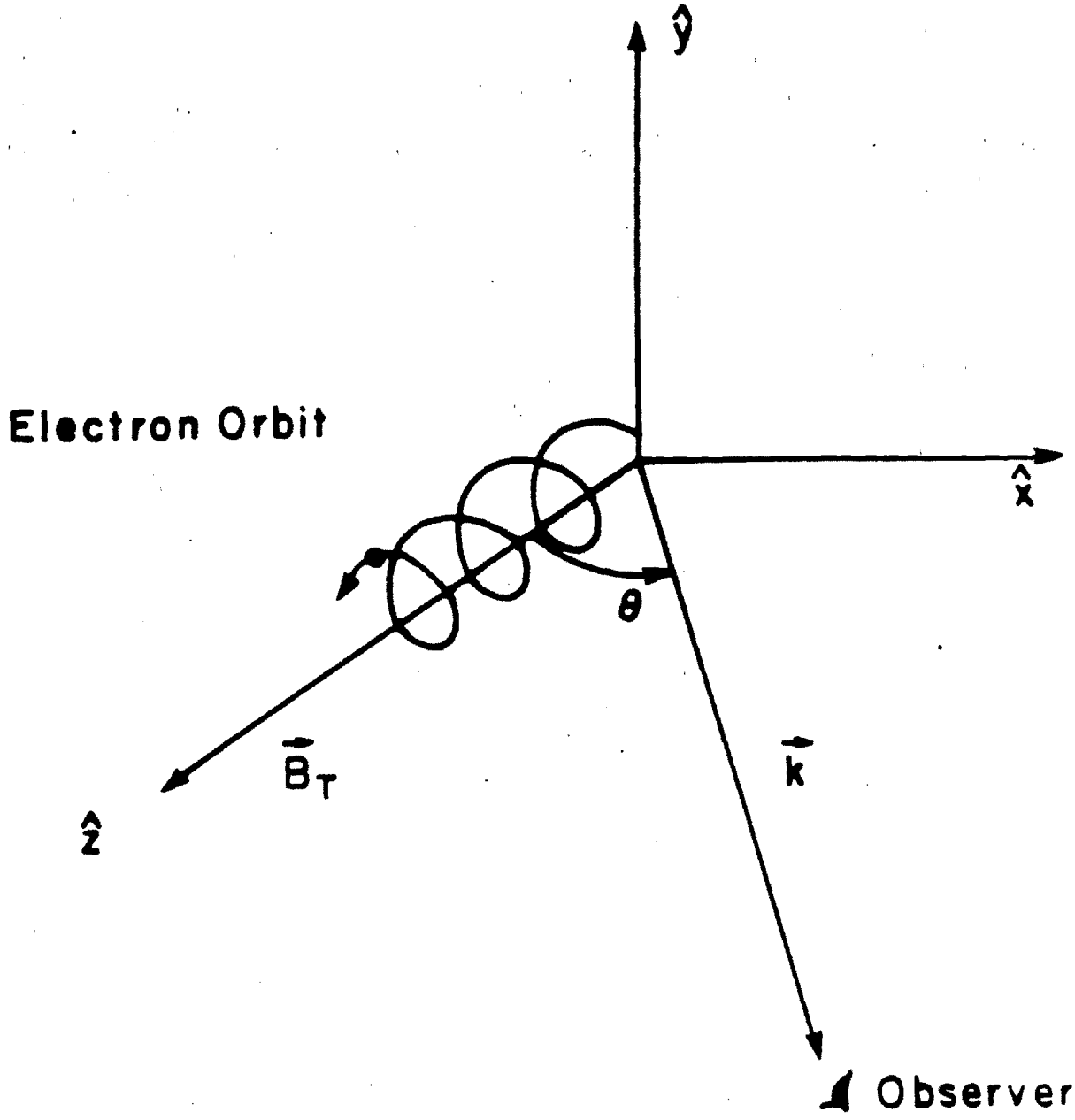

Figure 1.2 — Electron orbit in homogeneous magnetic field.

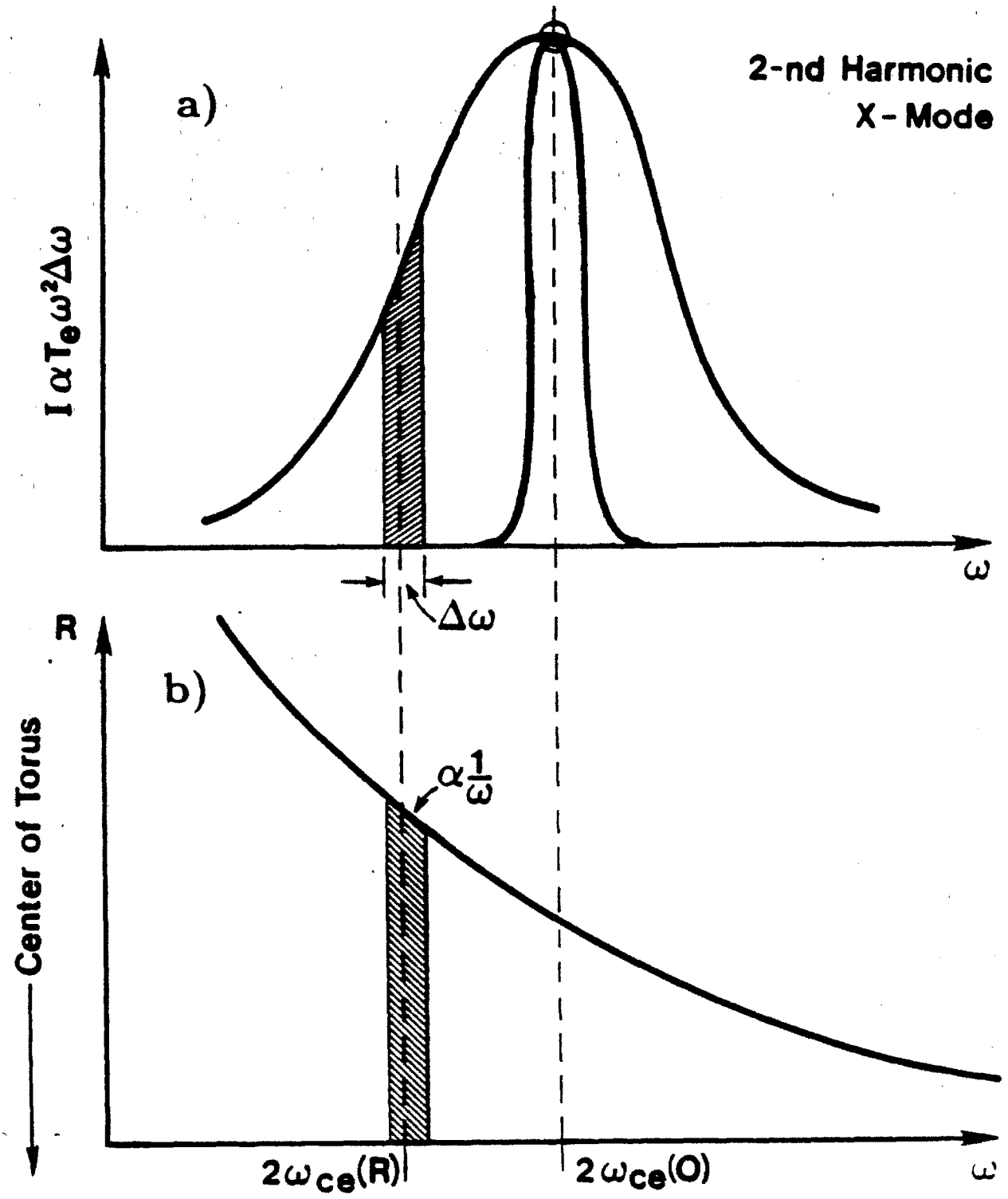

Figure 1.3 — a) This figure shows the broadening of the emission line due to the inhomogenity of the magnetic field. b) If the field varies monotonically with radius and we exclude regions of harmonic overlap, there is a 1:1 correspondence between the major radius position and frequency.

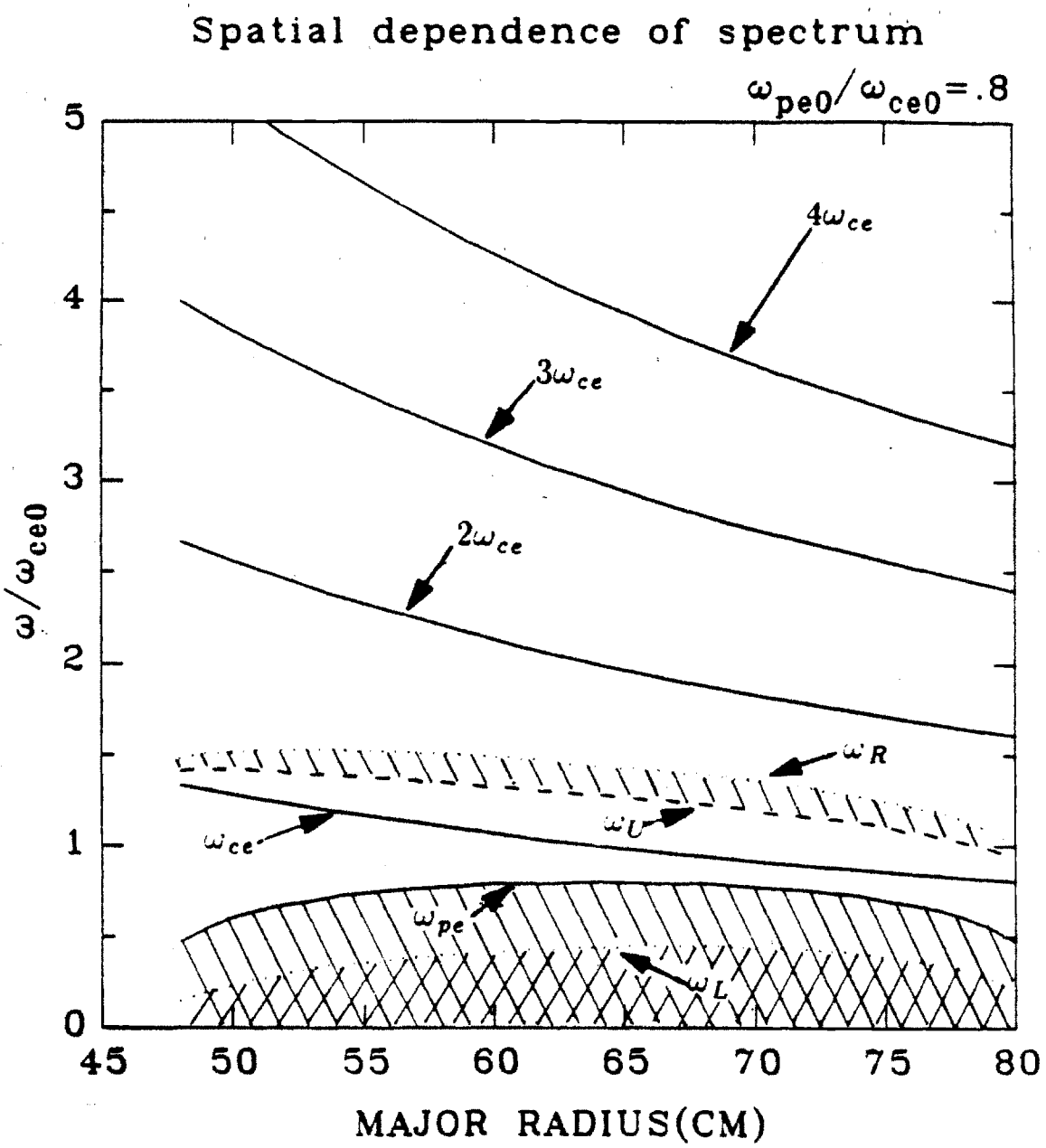

Figure 1.4 — Spatial dependence of cyclotron frequency for the first four harmonics. The magnetic field is assumed to vary as $1/R$, the density profile is taken to be a parabola going to zero at $R = 48, 80cm$.

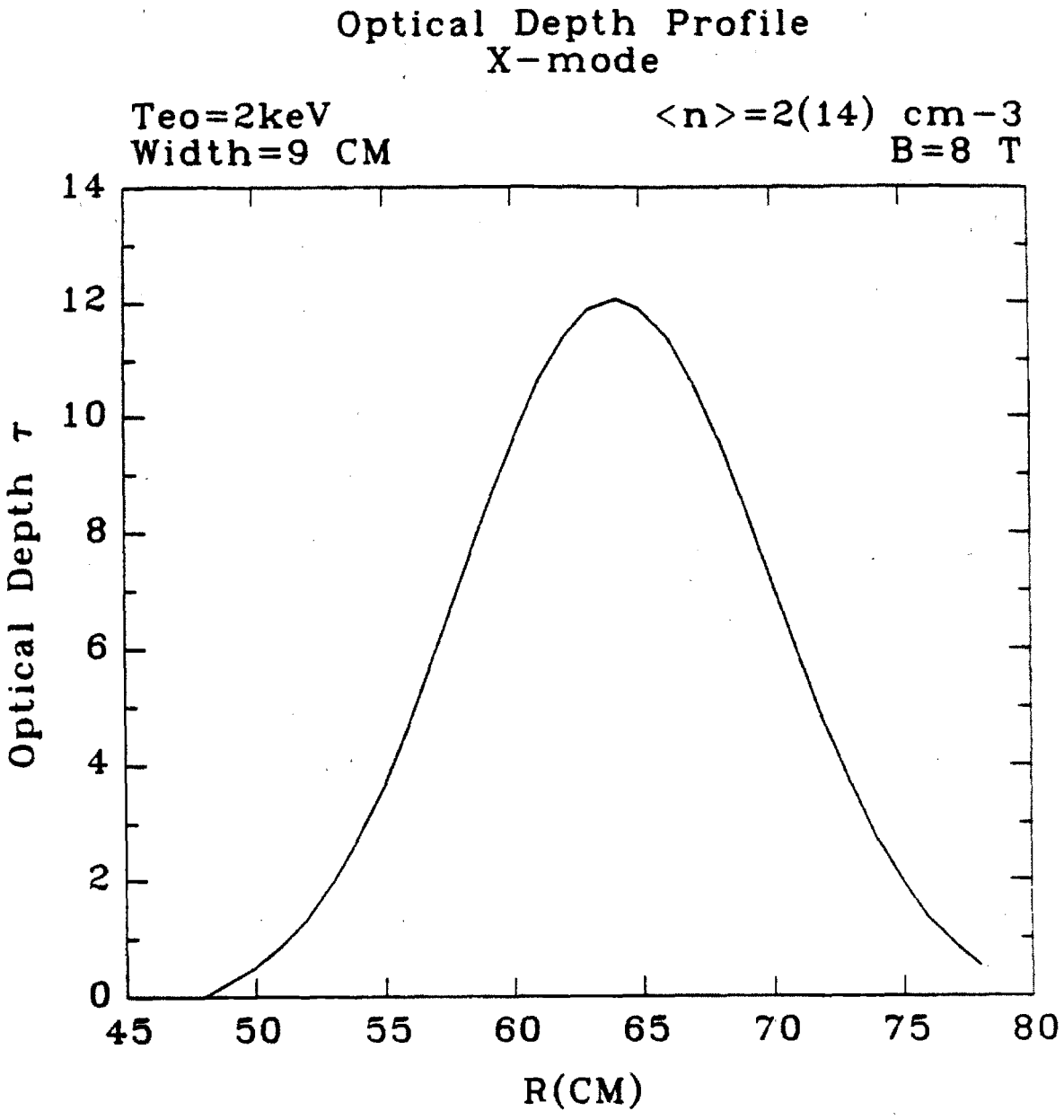

Figure 1.5 — Optical depth of the X mode second harmonic using eq. 1.3.3. The density profile is a parabola and the temperature Gaussian.

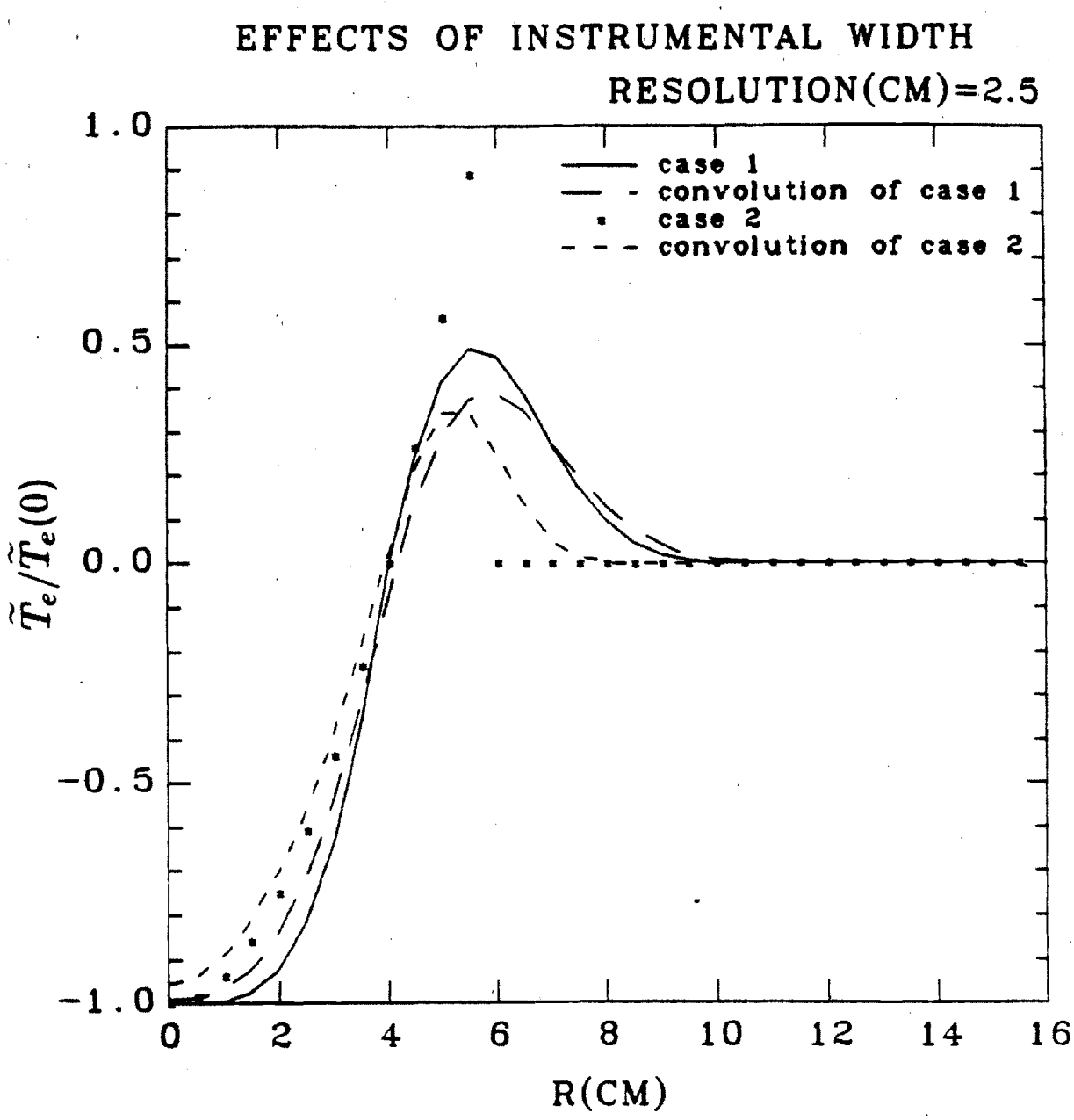

Figure 1.6 — Results of convolution using a Gaussian instrumental line shape with a $1/e$ width of $2.5cm$. Case 1 assumes a parabolic temperature perturbation, while case 2 is consistent with a measured profile.

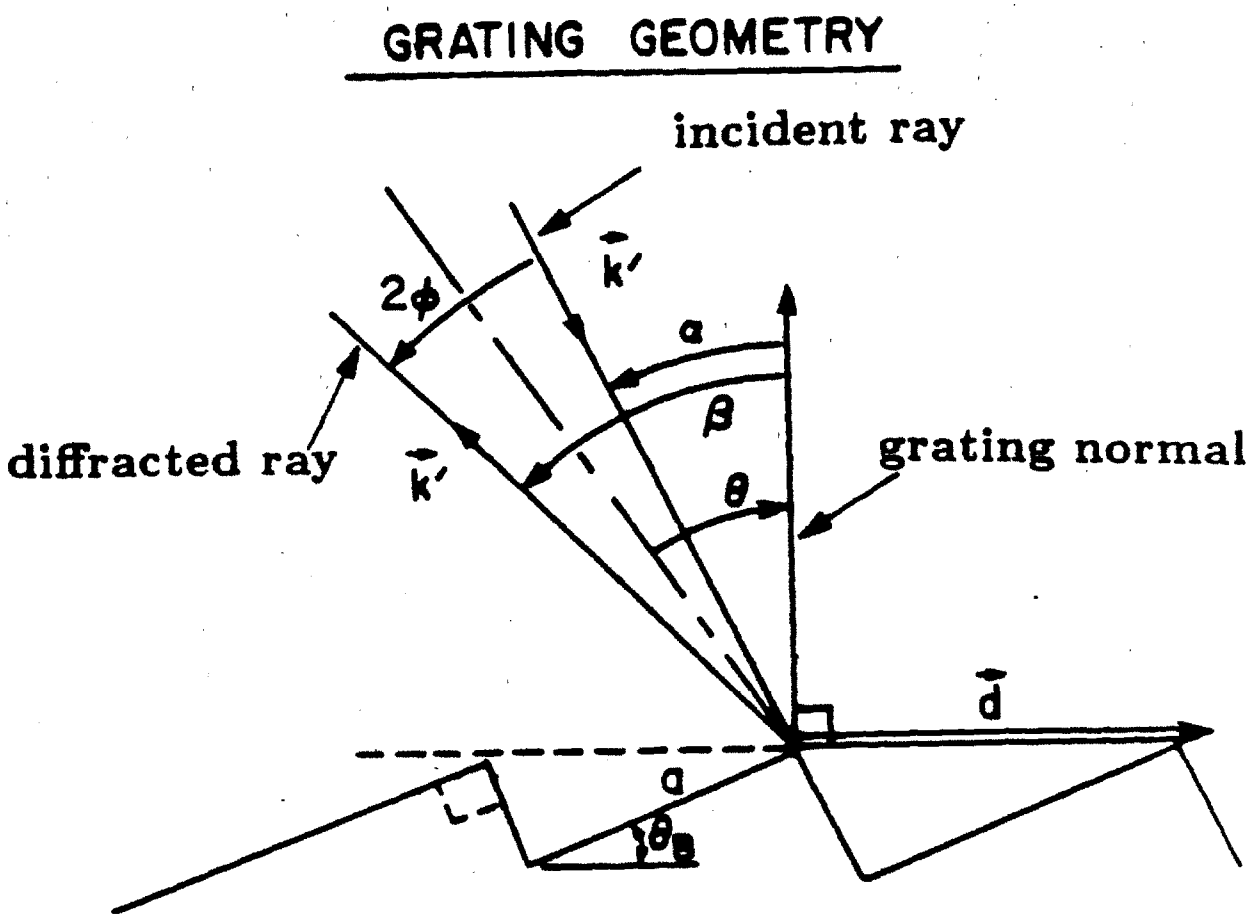

Figure 1.7 — Grating geometry and coordinate system used to describe the incident and scattered rays.

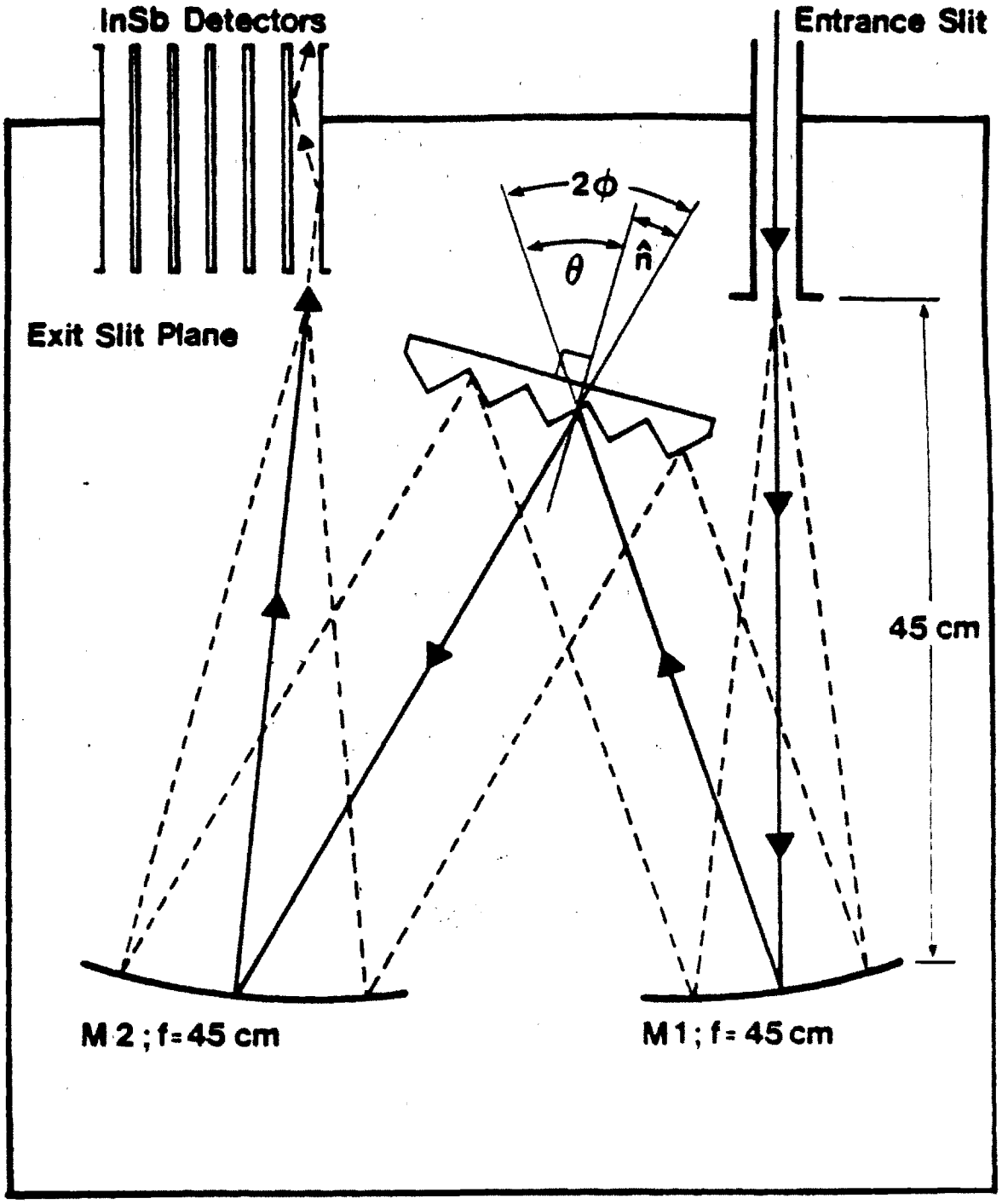

Figure 1.8 — Instrument geometry. The grating configuration is of the Czerny-Turner form. Frequency selection is achieved by rotating the graitng.

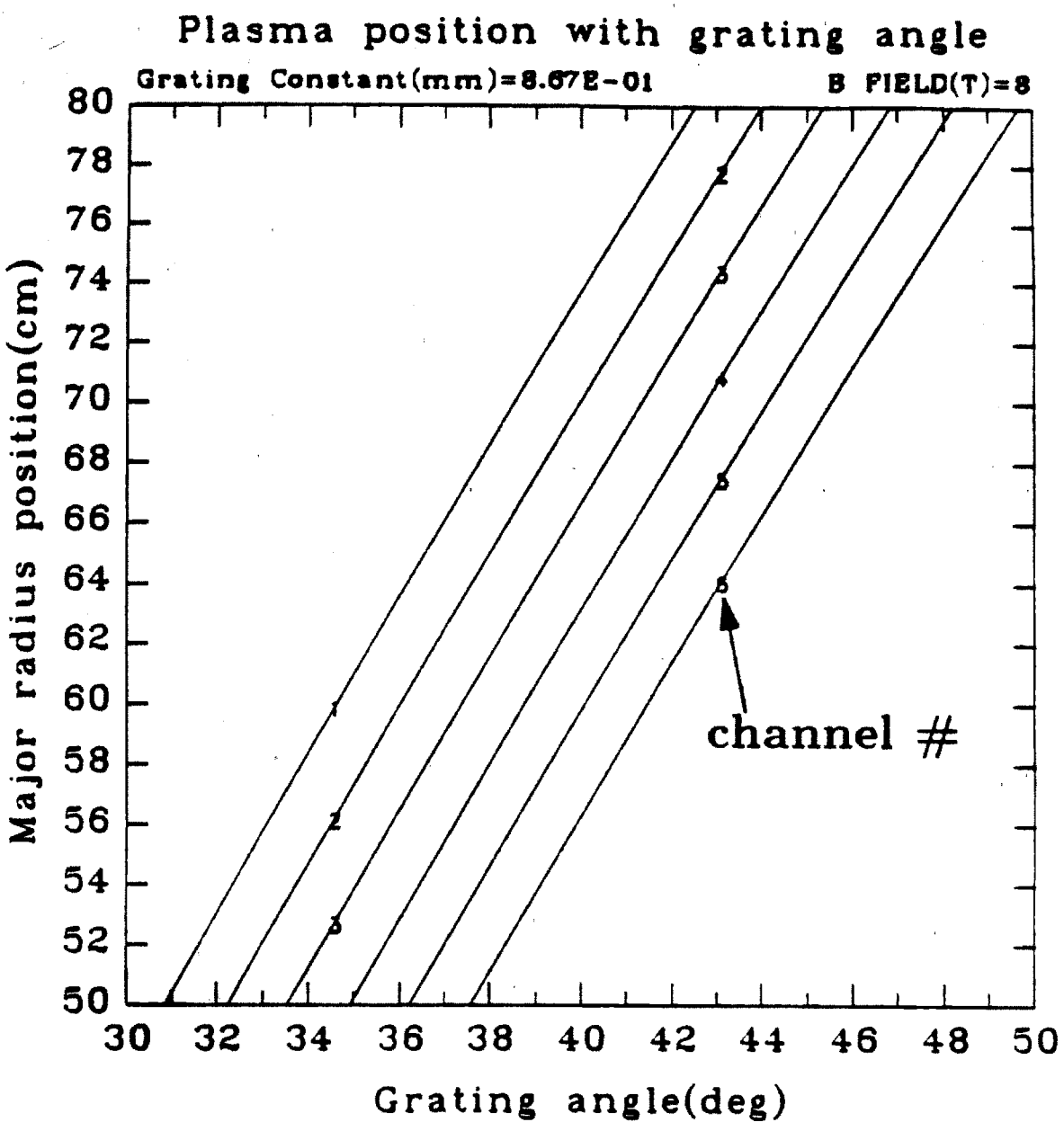

Figure 1.9 — Plot of the effective major radius position seen by the six channels as a function of grating angle θ_g.

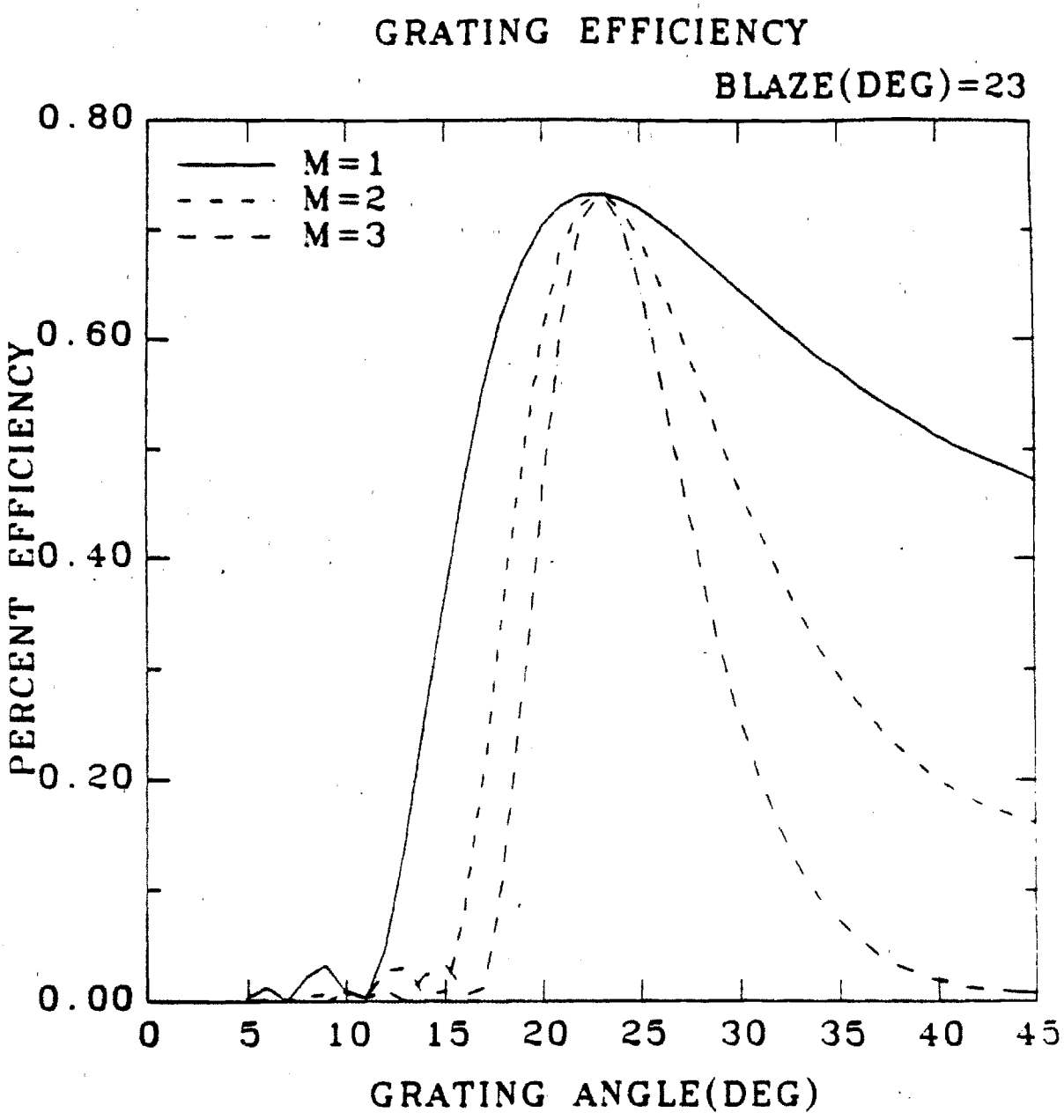

Figure 1.10 — Grating efficiency using scalar theory for a grating of $d = 0.867$ and $\theta_B = 23°$. the blaze wavelength is $\lambda_B = 0.6mm$. The efficiencies shown are for the first three orders.

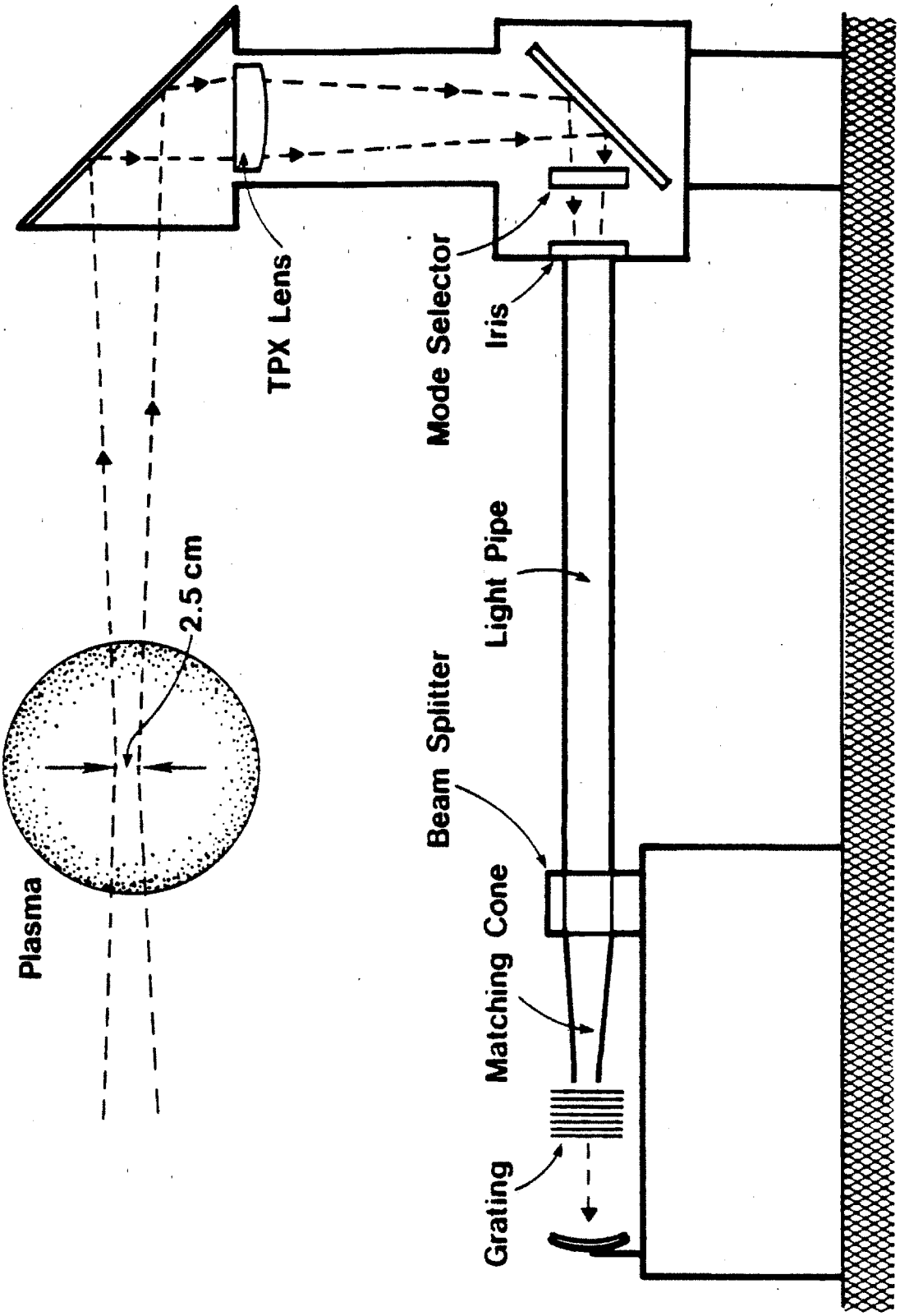

Figure 1.11 — Diagram of optical system.

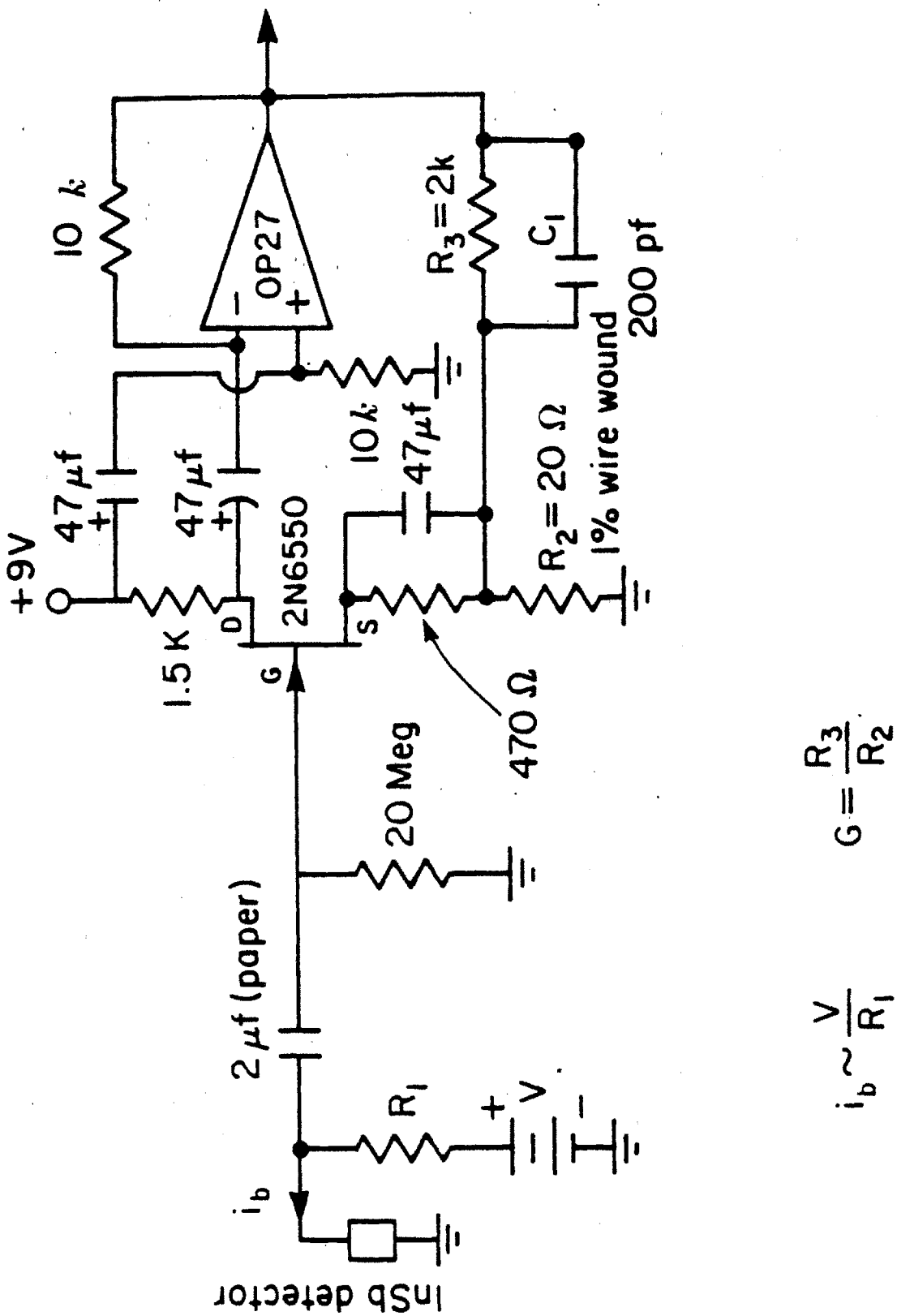

Figure 1.12 — Pre-amplifier circuit and detector bias arrangement.

II Sawteeth

2.1)Introduction

The sawtoothing phenomenon in plasmas was first observed in the central soft Xray emission. It is characterized by a periodic 'sawtooth' like structure (fig. 2.1). Subsequently the same behaviour has been observed in other plasma parameters such as electron and ion temperatures, density, etc. Sawtooth oscillations were first observed on the T-4 device[2.1] and later on the ATC tokamak[2.2]. The first attempt at a description for sawteeth was given by von Goeler et. al. using results from the ST tokamak[2.3]. It was found that the sawteeth led to a redistribution of energy and particles, near the center of the plasma. Using a diode array, they were able to characterize the evolution of the soft Xray emission. For illustration fig. 2.1 shows a set of Xray traces for the case of Alcator C. Near the center of the plasma the sawteeth exhibit a slow almost linear rise and then a sudden decay. Farther out in the plasma the sawteeth undergo inversion, with a rapid rise followed by a slow decay. The rapid spatial phase reversal suggests a fast redistribution of energy from the plasma center to the region outside the inversion radius. This rapid mixing leads to no immediate loss of plasma energy. By examining the behaviour of the outer traces we see that they all exhibit the inverted shape, however the time of arrival of the peak increases with radius. This suggests the existence of an outwardly propagating energy pulse. The evolution of this pulse is found to be diffusive as will be discussed in great detail in the next chapter.

The radius of inversion of the soft Xrays was found to be near the q=1 surface[2.3]. The safety factor q describes the magnetic field topology in a tokamak, in the cylindrical limit it is defined as

$$q = \frac{rB_T}{RB_\theta}$$

where r: minor radius

R:major radius

B_θ:poloidal field

B_T: toroidal field

see fig. 2.2. The magnetic field lines can be shown to follow a trajectory of the form

$$e^{i(m\theta+n\phi)}$$

where θ :poloidal angle

ϕ : toroidal angle

m :poloidal number

n :toroidal number

The angular numbers are related to the safety factor

$$q = \frac{m}{n}$$

Thus the inversion surface takes place at radii in which $m/n = 1$. The angular numbers m, n are in general non-integral values; for the special case in which they have integral values they represent modes of the toroidal cavity. It was also found that the disruption would be preceded by oscillations with an $m = 1$ character. They tend to have a maximum at the inversion radius, suggesting that the magnetic topology of the perturbation at $q = 1$ is $m = 1$,$n = 1$, generally exhibiting an exponential growth, reaching a maximum just before the disruption. Von Goeler et. al. [2.3] suggested that these precursors were the trigger for the sawtooth disruption.

Kadomtsev[2.4,2.5] proposed a heuristic model to explain the observed behaviour of sawteeth. In it he assumed the existence of a time growing perturbation which has the same topology as the magnetic field at the resonant surface. The effect this has on the plasma is to shift the center, introducing an $m = 1$ asymmetry. In the ideal MHD limit this shifting causes a pinching of current over a small region of the plasma around the resonant radius. The large current generated causes the

low resistivity of the plasma to have an important effect over this small region. Current diffusion leads to a reconnection of the field lines, with lines inside of the resonant surface connecting to those outside. It is this reconnection that leads to the rapid mixing of energy and particles along field lines. To describe the process, he introduced an auxiliary field (which for the resonant surface at $q = 1$) is

$$\vec{B}_* = \vec{B}_p - \hat{\theta}\frac{r}{R}B_T$$

In [2.6] it is shown that the MHD equations can be recast in terms of this field. Physically what we are doing is moving our reference frame to be parallel to the field lines at the $q = 1$ surface, so that at this surface $\vec{B}_* = 0$, and has opposite sign to either side (fig. 2.3). As the plasma is pushed towards the outside, the current in the pinched layer begins to diffuse causing the field lines to reconnect and reducing the energy of the system. The reconnection increases the magnetic pressure in the region opposite the reconnection layer, thus driving the center of the plasma into the reconnection layer at an ever faster rate. The process will not stop until the whole central section of the plasma has been reconnected, and the field lines $\vec{B}_*$ have the same sense and $q > 1$ everywhere. This has is to flatten the current profile near the center, as the current begins to peak up again due to diffusion, a small reversed field layer is generated in the center of the plasma and grows outward with the peaking current. This will continue until a sufficiently large pinched current is reached and the reconnection begins again. This kind of a process is what leads to the cyclic nature of the sawteeth. During this process most of the perturbed magnetic energy is dissipated in Joule heating at the reconnection layer. Although this model does not specify the instability that drives the reconnection, it does give a specific mapping of the field lines between the initial to final state. In [2.4,2.5] reconnection was considered for the case of a single resonant surface. Parail and Pereversev [2.7] later gave a more detailed description of the reconnection process with more than one resonant surface. Although these models leave many questions unanswered, they do form the basis for one of the most succesful descriptions for

the sawtooth phenomenon. As such we shall devote the next section of the chapter to a more detailed discussion of magnetic reconnection.

One of the requirements of a succesful model is that it give a self consistent description of the problem. Experimental verification of the Kadomtsev model has been very difficult, however extensive numerical simulations have been done which show the model to be at least self consistent. One weakness of the model is its inability to give the proper trigger mechanism for the onset of the instability causing the sawtooth disruption. The simulations discussed below all have imposed an artificial trigger to the problem.

Early numerical simulations were done by Waddel et. al. [2.8] and Sykes and Wesson [2.9]. In ref. [2.8] the reconnection started when the width of the $m = 1$ island was approximately twice the resonant radius. The model was applied to ST data and the predicted disruption time showed good agreement. Sykes and Wesson[2.9] gave a description which tried to simulate the periodic behaviour of sawtoothing. The qualitative behaviour of the sawteeth was able to be generated for a few periods, however after several periods a saturated $m = 1$ island developed with $q > 1$ everywhere preventing any further reconnection. Dnestrovskii et. al. [2.10] overcame this problem by including a self consistent solution to the transport equations. The onset of the reconnection was taken when $q < 1$ at the observed inversion radius. During reconnection the profiles were governed by the Kadomtsev model. Afterwards the profiles evolved according to the transport equations. With this, they were able to simulate T-4 discharges with good agreement, giving rise to stable sawtooth oscillations. Parail and Pereversev [2.7] gave simulations which agreed well with T-10 results. In them, they required the current profile to be hollow giving rise to two $q = 1$ surfaces. With this model they were able to predict the inversion radius as well as the sawtooth period and amplitude. The particulars for this model will be discussed in a later section after the idea of flux functions have been introduced.

Jahns et. al. [2.11] proposed a model which attempts to arrive at a self consistent description for the sawteeth, while assuming an explicit mechanism for the

instability. They assume that the instability is driven by the $m = 1$ tearing mode. Von Goeler [2.3] found that the simple $m = 1$ tearing mode growth rate was too large to explain the growth of the $m = 1$ precursors. By including the effects of diamagnetic drifts Janhs et.al. were able to reduce the growth rate of the tearing instability. Rather than follow the strict Kadomtsev prescription for profile rearrangement, they assumed that all profiles were flattened about the inversion radius, the extent of the flattened region was determined by conservation of the plasma parameter being rearranged. They pointed out that the slow almost linear recovery of the center was due to the domination of Ohmic heating over diffusive loss. Farther out in the discharge because of the large gradients set up by the mixing, diffusion dominated the evolution. They tried to develop experimentally measured scalings. The reduced growth rate is taken to be of the form

$$\gamma = \frac{\gamma_T^3}{\omega_{*i}\omega_{*e}}$$

for

$$\gamma < \frac{\omega_{*i}}{2}, \frac{\omega_{*e}}{2}$$

where

$$\gamma_T = \frac{\alpha^{2/3}}{S^{1/3}\tau_A}$$

is the tearing mode growth rate

$$\alpha = r_l \frac{dq}{dr}|_{r_s}$$

is the shear,r_s is the resonant radius,r_l limiter radius.

$$S = \frac{\tau_r}{\tau_A}$$

is the magnetic Reynolds number

$$\tau_r \equiv \frac{\mu_0 r_l^2}{\eta}$$

resistive skin time

$$\tau_A \equiv \frac{R(\mu_0\rho)^{1/2}}{B_z}$$

poloidal Alfven transit time.

The drift frequencies are defined as

$$\omega_{*i} = \frac{1}{eB_z}\frac{m}{nr_s}\frac{dP_{0i}}{dr}\Big|_{r_s}$$

$$\omega_{*e} = \frac{1}{eB_z}\frac{m}{r_s}\Big[\frac{1}{n}\frac{\partial}{\partial r}P_{0e} + 0.71\frac{\partial}{\partial r}T_e\Big]_{r_s}$$

To estimate the shear α the current profile was assumed not to change appreciably due to diffusion during reconnection. The change in J is dominated by the change in η the resistivity, due to the temperature fluctuations. The temperature perturbation near the center is assumed to evolve as

$$\tilde{T}_e(r,t) = \tilde{T}_e(0,t)(1 + ar^2 + br^3)$$

with $\tilde{T}_e(0,t)$ linearly increasing with time and a, b are time independent.

Using this form for the temperature they arrive at the shear rate

$$\alpha = \alpha_0 + \bar{\alpha}t^2$$

where α_0 is the initial shear and

$$\bar{\alpha} = 9\frac{q_0}{B_{\theta_0}}\frac{r_l}{r_s^2}\frac{\eta_0 J_{z0}}{\tau_h}$$

$$\tau_h = \frac{3nT_e0}{2\eta J^2}$$

reheat time. The growth rate is then given by

$$\gamma = \frac{(\alpha_0 + \bar{\alpha}t^2)^2}{\omega_{*i}\omega_{*e}\tau_A^2\tau_r}$$

The amplitude of the $m = 1$ oscillations are related to the growth rate by

$$\frac{\partial}{\partial t}\widetilde{A} = \gamma \widetilde{A}$$

with the solution

$$ln\frac{\widetilde{A}}{\widetilde{A}(0)} = \int_0^t \gamma(t')dt'$$

They take the solution in two limits

$\alpha_0 \gg \overline{\alpha}$

$$ln\frac{\widetilde{A}}{\widetilde{A}(0)} = \gamma_0 t$$

$$\gamma_0 = \frac{\alpha_0^2}{\omega_{*i}\omega_{*e}\tau_A^2\tau_r}$$

$\overline{\alpha} \gg \alpha_0$

$$ln\frac{\widetilde{A}}{\widetilde{A}(0)} = Ct^5$$

$$C = \frac{\overline{\alpha}\alpha^2}{5f\tau_A^2\tau_r\overline{\omega}_*^2}$$

$$f = 1.71\frac{T_i}{T_e}$$

$$\overline{\omega}_* = \frac{m}{eB_z r_s}\frac{\partial}{\partial r}T_{e0}|_{r_s}$$

They apply these results to ORMAK discharges and show that both limits can be seen depending on discharge conditions.

An expression for the sawtooth repetition time was developed using the more common limit of $\overline{\alpha} \gg \alpha_0$. The disruption condition was taken when the width of the $m = 1$ island is equal to the inversion radius. The island width is given by

$$ln\frac{W_f}{W_i} = \frac{1}{2}\int_0^{t_0} \gamma(t')dt'$$

Solving explicitly for t_0 we arrive at the scaling

$$t_0 \sim d(nB_z T_i T_e r_s^2 R^2/v^3)^{1/3} \qquad ms$$

$$d = 13\Big[ln(W_f/W_i)\Big]^{1/3}$$

While this model had success in explaining ORMAK data, it's general validity is unclear. The t^5 dependence of the $m = 1$ growth is sensitively dependent on the form we take for the temperature profile evolution near the inversion radius. This region in general has a complicated time history, not necessarily linear as assumed in this model.

Several researchers have developed empirical scaling laws to describe the sawtooth behaviour. There is some question as to whether the reduction of the $m = 1$ tearing mode growth rate due to diamagnetic drifts is required in accounting for the precursor evolution. By taking a sufficiently small shear the growth rate can be reduced to match that observed. McGuire and Robinson [2.12] developed a scaling of the sawtooth period based on both forms of the tearing mode growth rate. The general form for the scaling is

$$t_0 = K t_1^a t_2^b t_3^c ....$$

where $t_1, t_2, t_3 ...$ are the characteristic time scales of the problem and K is a dimensionless constant. One general requirement is that $1 = a + b + c + ...$ In considering the $m = 1$ tearing mode and the diamagnetic drift corrected tearing mode, the time scales of interest are:

resistive skin time

$$\tau_r = \frac{\mu_0 r_s^2}{\eta}$$

Alfven time

$$\tau_A = \frac{R}{v_A} = \frac{R(\mu_0 \rho)^{1/2}}{B_T}$$

reheat time

$$\tau_h = \frac{3nT_e}{2\eta J^2}$$

diamagnetic drift frequency

$$\omega_* = (\frac{\partial}{\partial r} P)/eB_T r_s n$$

If γ is the uncorrected growth rate they found the appropriate scaling to be

$$t_0 \sim \tau_r^{3/7} \tau_A^{2/7} \tau_h^{2/7}$$

If γ is reduced by diamagnetic drifts

$$t_0 \sim \tau_r^{3/5}\tau_A^{2/5}\tau_h^{2/5}\omega_*^{2/5}$$

An empirical fit was done to data from a variety of machines. Using the uncorrected form

$$t_0 \sim \tau_r^{0.42}\tau_A^{0.14}\tau_h^{0.44}$$

with a linear correlation of 0.985 For the reduced form

$$t_0 \sim \tau_r^{0.35}\tau_A^{0.04}\tau_h^{0.44}\omega_*^{-0.16}$$

with a linear correlation of 0.986 For practical purposes the data is well fit by both scalings, however the coefficients for the unshifted scaling are in better agreement with the theoretical values.

An extensive amount of work has been done by the TFR group in studying the sawtooth phenomenon[2.13,2.14,2.15,2.16]. A series of empirical scalings were found for the sawtooth period, amplitude and inversion radius. They are

$$r_s \sim \frac{a}{q(a)^{1/2}}$$

$$t_0 \sim n r_s^2 R$$

$$\frac{\delta A}{A} \sim \frac{1.5}{(q(a))^{3/2}}$$

They also found that the $m = 1$ oscillations previously seen only before the crash, could persist at a lower frequency after the crash. At high density operation the $m = 1$ oscillations were hardly visible. Measurements implied that the $m = 1$ island width was only $r_s/3$, much smaller than that which most models required for reconnection to the center. In conjunction with the sawtooth crash large high

frequency spikes were observed near the inversion radius which are unaccountable with a reconnection model.

For the above reasons the TFR group came to the conclusion that the reconnection mechanism and the $m = 1$ instability could not be the cause of the sawtooth disruption. To do so it would require an abnormally large growth rate which is not predicted by theory. An alternative model was proposed, in which the sawtooth disruption was caused by the rapid propagation of a turbulent region originating at the inversion surface. The turbulence could be driven by the large current gradients set up by the $m = 1$ mode.

To compare both models, simulations were done in which (1) the Kadomtsev reconnection is followed but the growth rate of the $m = 1$ is enhanced to match observations and (2) a small scale turbulent region is created when the island is small. By enhancing the growth rate in the first case by as much as a factor of 100, they could not duplicate the large transient spikes near the inversion radius. The agreement found using the turbulence model was much better. One of the problems that this model has is that it does not specify how the turbulent region comes about, or how it propagates through the plasma.

The purpose of this chapter is to study in some detail the evolution of sawteeth in Alcator C. Previous studies have used the soft Xray signals which measure the line integral of a complicated function of temperature, density and impurities. This has led to some question as to which plasma parameter is responsible for the sawteeth and how the actual profiles change. By using the six channel FIR grating discussed in the previous chapter, we can essentially make a point measurement of the electron temperature, thus removing many uncertainties inherent in the Xray measurements.

In the next section we give a detailed discussion of magnetic reconnection, focusing on the single resonant surface (i.e. single $q = 1$ surface) reconnection. We shall arrive at some basic measureable properties of single resonant surface reconnection. In the subsequent sections we will study the properties of 'normal' and 'exotic' sawteeth. In the process we shall try to develop a unified picture of sawteeth which includes both the 'normal' as well as the 'exotic' cases.

2.2)Magnetic reconnection

In this section we shall give a fairly detailed discussion of magnetic reconnection in tokamaks, establishing measureable properties for the various reconnecting models. Those who wish to skip the details can read the last paragraph of this section where the main results are summarized.

We begin our discussion by developing as auxiliary field $\vec{B}_*$ following the development of Kadomtsev[2.5]. We assume the existance of a helical perturbation of the form

$$f(r, \theta - \alpha z)$$

If there are field lines in the plasma which have this topology, we can expect strong coupling of the perturbation. An auxiliary field is defined to be of the form

2.2.1)

$$\vec{B}_* = \vec{B}_p - \hat{\theta}\alpha r B_z$$

The coefficient α is set by requiring $\vec{B}_{*\theta} = 0$ at the radial location r_s(resonant radius) where the helicity of the perturbation and the magnetic field match. In this frame, the fields to either side of r_s have opposite sense. This allows us to see how the field lines reconnect in a very intuitive way. Then at r_s we relate B_θ, B_z and α

$$B_\theta = \alpha r_s B_z$$

Using the safety factor at r_s

$$q_s = \frac{r_s B_z}{R B_\theta} \Rightarrow \alpha = \frac{1}{R q_s}$$

giving

2.2.2)

$$\vec{B}_* = B_p - \hat{\theta}\frac{r}{R}\frac{B_z}{q_s}$$

For the case of sawteeth $q_s = 1$

2.2.3)

$$\vec{B}_* = \vec{B}_p - \hat{\theta}\frac{r}{R}B_z$$

We can express the auxiliary magnetic field in terms of a flux function

2.2.4)

$$\vec{B}_* = \hat{\theta} \times \nabla\psi$$

to find ψ, we solve the equation

$$\frac{\partial\psi}{\partial r} = B_{*\theta} = B_\theta - \frac{r}{R}B_z$$

At the resonant radius

$$\frac{\partial\psi}{\partial r} = 0$$

Whether this is a maximum or a minimum depends on the unperturbed safety factor profile. The second derivative of ψ is

$$\frac{\partial^2}{\partial r^2}\psi = -\frac{B_z}{Rq^2}\frac{\partial}{\partial r}q + (\frac{1}{q} - 1)\frac{B_z}{R}$$

if $q = 1$ at a resonant surface then

2.2.5)

$$\frac{\partial^2}{\partial r^2}\psi = -\frac{B_z}{R}\frac{\partial}{\partial r}q\Big|_{r_s}$$

If q is a monotonically increasing function of r as is the case for a peaked current profile then $\psi(r_s)$ will allways be a maximum. If q is not monotonic as in the case of a hollow current profile, then $\partial q/\partial r$ may be < 0 in which case $\psi(r_s)$ is a minimum.

To develop the general principles involved we shall consider the case of only one resonant surface with a monotonically increasing q profile fig. 2.4 . The flux function is

$$\psi - \psi_c = \int_0^r dr'(B_\theta - \frac{r'}{R_0}B_z)$$

Since ψ_c is arbitrary we shall set it to zero.

By considering figs. 2.3,2.4 we see that the volumes that reconnect are those with the same ψ. If the plasma is taken to be incompressible then the area of the reconnecting region is conserved. This leads to the expression

2.2.6)

$$\psi_\infty r dr = \psi_0(r_1) r_1 dr_1 + \psi_0(r_2) r_2 dr_2$$

which is a specific example of flux conservation

$$\int \psi r dr = const.$$

In the above ψ_0 is the initial profile while ψ_∞ is the profile after reconnection.

We can easily see that after reconnection the maximum value of $\psi(r_s)$ ends up at the center. Since it is the ψ values that are conserved, we shall use it as the free parameter to express r. For a given ψ_0 there are two possible values for r (r_1, r_2) about the resonant surface. Eq. 2.2.6 can be written as

2.2.7)

$$r dr = r_1 dr_1 + r_2 dr_2$$

and

$$dr_1 = \frac{1}{f_1(\psi)} d\psi$$

$$dr_2 = \frac{-1}{f_2(\psi)} d\psi$$

where

$$f_1 = \frac{\partial}{\partial r}\psi\Big|_{r_1}$$

$$f_2 = \frac{\partial}{\partial r}\psi\Big|_{r_2}$$

The eq. 2.2.7 can then be written as

$$r' dr' = \Big[\frac{-r_1(\psi_0)}{f_1(\psi_0)} + \frac{r_2(\psi_0)}{f_2(\psi_0)}\Big] d\psi_0$$

Integrating the LHS from $0 \rightarrow r$ and the RHS from $\psi_{max} \rightarrow \psi$ we have

2.2.8)

$$r^2 = 2\int_{\psi_{max}}^{\psi} \left[\frac{-r_1(\psi_0)}{f_1(\psi_0)} + \frac{r_2(\psi_0)}{f_2(\psi_0)}\right] d\psi_0$$

This integral gives the general mapping for the final ψ_∞ profile given the initial profile. The radius of extent of the reconnection is determined by flux conservation or

2.2.9)

$$\psi_0(0) = \psi_0(r_M)$$

The final profile will have $\psi_\infty(0) = \psi_0(r_s)$ and $\psi_\infty(r_M) = \psi_0(r_M)$. To better understand reconnection, consider the following problem. Assuming that the current profile near the center of the plasma is peaked and can be modeled by a function of the form

2.2.10)

$$j = j_0(1 - (r/a_j)^\beta)$$

where (a_j) is the scale length of the current near the center of the plasma. The poloidal field is then

2.2.11)

$$B_\theta = \alpha r\left(\frac{2+\beta}{2}a_j^\beta - r^\beta\right)$$

where

$$\alpha = \frac{B_z}{Rq_s}\frac{1}{\left(\frac{2+\beta}{2}a_j^\beta - r_s^\beta\right)}$$

Using eq. 2.2.11 we can find the initial ψ profile to be

2.2.12)

$$\psi(r) = \alpha\frac{r^2}{2}\left(r_s^\beta - \frac{2}{2+\beta}r^\beta\right)$$

The simplest thing that can be done is to find the magnetic mixing radius r_M using eq. 2.2.9. This gives the relation

2.2.13)

$$\frac{r_M}{r_s} = \left(1 + \frac{\beta}{2}\right)^{\frac{1}{\beta}}$$

This is a monotonically varying function of β with

$$\frac{r_M}{r_s}(\beta = 0) = e^{1/2}$$

$$\frac{r_M}{r_s}(\beta \to \infty) = 1$$

Since eq. 2.2.10 can be adjusted to approximate all single resonance surface cases, the maximum possible ratio of r_M/r_s consistent with a single resonant surface is $e^{1/2}$.

To find the final ψ profile, the inverse of eq. 2.2.12 has to be found, which in general is not trivial. In order to proceed with our discussion we shall consider the special case of $\beta = 2$. This gives

$$\frac{r_M}{r_s} = \sqrt{2}$$

and

2.2.14)

$$\psi_0 = \alpha \frac{r^2}{2}\left(r_s^2 - \frac{r^2}{2}\right)$$

The above can be inverted to give

$$r^2 = r_s^2 \pm \sqrt{r_s^4 - \frac{4\psi_0}{\alpha}}$$

The integral of eq. 2.2.8 can be evaluated and inverted to give

2.2.15)

$$\psi_\infty = \frac{\alpha}{4}\left(r_s^4 - \frac{r^4}{4}\right)$$

Since we require ψ to be continuous at $r = r_M$ and not $\partial\psi/\partial r$, we will usually end up with a return skin current at the mixing radius. It is Kadomtsev's contention that this skin current dissipates in a very short time scale.

To examine this question we solved the magnetic diffusion equation for a skin current at $r = r_M$

$$j \sim \delta(r - r_M)$$

The equation solved is

$$\frac{\partial}{\partial t} j = \frac{1}{r}\frac{\partial}{\partial r} r \frac{\partial}{\partial r}\left(\frac{\eta}{\mu_0} j\right)$$

we assume η/μ_0 is constant over the central region and set

$$x = \frac{r}{r_s}$$

$$\tau = \frac{\eta t}{\mu_0 r_s^2}$$

then the solution to the equation can be written as

$$j(x,\tau) = \frac{1}{2\tau} e^{-x^2/4\tau} \int_0^{x_M^+} dx' x' e^{-x'^2/4\tau} I_0\left(\frac{xx'}{2\tau}\right) j(x',0)$$

$$j(x,\tau) = \frac{x_M}{2\tau} e^{-x^2/4\tau} e^{-x'^2/4\tau} I_0\left(\frac{xx'}{2\tau}\right)$$

if $x_M = \sqrt{2}$ then

$$j(x,\tau) = \frac{1}{\sqrt{2}\tau} e^{(-x^2/4+1/2)/\tau} I_0\left(\frac{x}{\sqrt{2}\tau}\right)$$

Fig. 2.5 shows the evolution of the current assuming Spitzer resistivity and T_e - $1500ev$. The evolution was followed for $3ms$ which is the typical sawtooth period. Within $300us$ the current peak has essentially washed out and thus the current profile should be continuous. If this were not the case, the reconnection model

would lead to the permanent existance of a return skin current near the center of a sawtoothing plasma.

The sawtooth disruption takes place on a much faster time scale than that for cross field diffusion. According to the reconnection model the rapid rearrangement of the plasma profiles comes about by the rapid transport along the field lines as they open up and reconnect. By neglecting any perpendicular transport we can arrive at a prescription for how plasma parameters should mix.

Any quantity that must be conserved can be mapped in a similar way as eq. 2.2.6

2.2.16)

$$Z_\infty(r)rdr = Z_0(r_1)r_1dr_1 + Z_0(r_2)r_2dr_2$$

using eq. 2.2.7 for the incompressible plasma case we have

$$Z_\infty(r) = \frac{Z_0(r_1)r_1dr_1 + Z_0(r_2)r_2dr_2}{r_1dr_1 + r_2dr_2}$$

expressing the problem in terms of $d\psi$ we have

$$Z_\infty(r) = \frac{Z_0(r_2)r_2/f_2 - Z_0(r_1)r_1/f_1}{r_2/f_2 - r_1/f_1}$$

The density becomes

$$n_\infty(r) = \frac{n_0(r_2)r_2/f_2 - n_0(r_1)r_1/f_1}{r_2/f_2 - r_1/f_1}$$

using energy conservation

$$(nT)_\infty(r) = \frac{(nT)_0(r_2)r_2/f_2 - (nT)_0(r_1)r_1/f_1}{r_2/f_2 - r_1/f_1}$$

A point should be made that this is only an approximation, for during reconnection a large fraction of the perturbed magnetic energy is converted into heat by Joule heating in the reconnection layer. However this is typically $< 2\%$ of the total redistributed thermal energy.

The temperature can be expressed by taking the ratio of the pressure and the density

2.2.20)

$$T_\infty(r) = \frac{(nT)_0(r_2)r_2/f_2 - (nT)_0(r_1)r_1/f_1}{n_0(r_2)r_2/f_2 - n_0(r_1)r_1/f_1}$$

To proceed we shall look at the example of 2.2.14. If we assume a constant density and the initial temperature profile of the form

2.2.21)

$$T_0(r) = T_p(1 - r^2/a_T^2)^\gamma$$

where a_T is the temperature scale length near the center. Using eq. 2.2.20 then the final temperature profile is

2.2.22)

$$T_\infty(r) = \frac{T_p}{2}\left\{(1 - r_s^2/a_T^2 + r^2/2a_T^2)^\gamma + (1 - r_s^2/a_T^2 - r^2/2a_T^2)^\gamma\right\}$$

For the case of $\gamma = 1$, we have

2.2.23)

$$T_\infty(r) = T_p(1 - r_s^2/a_T^2)$$

the profile is flat and has the value of the temperature at the resonant radius. This is the kind of profile that is assumed by Jahns et.al. [2.11] as discussed earlier.

In general however this is not the case, the final profile can remain peaked or become hollow depending on the initial profile. To address this question we consider the second derivative of T_∞ with respect to r^2/a_T^2 at $r = 0$

2.2.24)

$$\frac{\partial^2 T_\infty}{\partial(r^2/a_T^2)^2} = \gamma(\gamma - 1)\frac{1}{2}\{1 - \frac{r_s^2}{a_T^2}\}^{\gamma-2}$$

Then if $r_s < a_T$ we have

2.2.25)

$\gamma < 1$ peaked final profile

$\gamma > 1$ hollow final profile

$\gamma = 1$ flat final profile

Thus depending on the details of the initial current and temperature profile the final temperature profile can be either flat, hollow or peaked.

Another question that should be considered is how the temperature inversion radius (r_i) relates to the resonant radius r_s. By equating the initial and final profiles of eq. 2.2.21 and 2.2.22 we get

2.2.26)

$$(1-r_i^2/a_T^2)^\gamma = \frac{1}{2}\Big\{(1-r_s^2/a_T^2+r_i^2/2a_T^2)^\gamma + (1-r_s^2/a_T^2-r_i^2/2a_T^2)^\gamma\Big\}$$

this in general can not be solved in closed form, but if we assume that $r_i \sim r_s$, we can expand in $|(r_i - r_s)/a_T|$. Defining $x_s^2 = r_s^2/a_T^2$ and $x_s^2 + \delta = r_i^2/a_T^2$ we get

2.2.27)

$$\delta = \frac{\frac{1}{2}\Big\{(1-\frac{1}{2}x_s^2)^\gamma + (1-\frac{3}{2}x_s^2)^\gamma\Big\} - (1-x_s^2)^\gamma}{\gamma\Big\{(1-x_s^2)^{\gamma-1} - \frac{1}{4}(1-\frac{1}{2}x_s^2)^{\gamma-1} + \frac{1}{4}(1-\frac{3}{2}x_s^2)^{\gamma-1}\Big\}}$$

In most cases the temperature profile will be bounded by the following cases, consider $\gamma = 0.5$, $x_s = 0.3$, then $\delta = -.0005$, for $\gamma = 2$, $x_s = 0.3$, then $\delta = 0.0008$. Thus the maximum discrepancy between the profile inversion radius and resonant radius is 0.4%. This means that for the case of a single resonant surface, the inversion radius is very close to the resonant radius.

Kadomtsev's reconnection model allows prediction of the disruption time. We will briefly outline the argument given by Kadomtsev[2.4]. Plasma is pushed out of the reconnection layer as the central plasma column is pushed into it. The velocity with which mass moves out of the region is fixed by the Alfven velocity (in the transformed magnetic field) v_A^*; as the plasma is tied to the magnetic field. Fig. 2.6 shows the geometry used here. The velocity at which the central plasma column should move towards the reconnection layer is

$$v_c \sim \frac{V_{recon}}{V_c} v_A^*$$

where $V_{recon} \sim \delta l$ volume of reconnection layer

$V_c \sim r_s^2$ volume of central plasma

The width of the reconnection layer is determined by the width of the diffusing current layer

$$\delta^2 \sim \chi_{mag} t_0$$

$$\chi_{mag} \equiv \frac{\eta}{\mu_0}$$

t_0 is the average time scale that a field line remains in the reconnection layer. Since it is tied to the plasma, it is given by

$$t_0 \sim \frac{l}{v_A^*}$$

The width is then

$$\delta \sim \sqrt{\chi_{mag} \frac{l}{v_A^*}}$$

The reconnection time is roughly the time it takes for the center of the plasma to reach the reconnection layer

$$t_{rc} \sim \frac{r_s}{v_c}$$

which gives

$$t_{rc} \sim \frac{r_s^3}{l^{3/2}\sqrt{\chi_{mag} v_A^*}}$$

we can expect the length l of the reconnection to scale with r_s , so that the reconnection time t_{rc} becomes

2.2.28)

$$t_{rc} = \left(\frac{r_s^3}{\chi_{mag} v_A^*}\right)^{1/2} = (\tau_{r_s} \tau_A^*)^{1/2}$$

where

$$\tau_{r_s} = \frac{r_s^2}{\chi_{mag}}$$

$$\tau_A^* = \frac{r_s}{v_A^*}$$

For the typical Alcator parameters

$$t_{rc} \sim 200 - 300 \qquad \mu s$$

which can be an order of magnitude larger than the disruption times measured in Alcator, which are typically $20 - 50 \mu s$.

Parail and Pereversev [2.7] discussed reconnection with multiple resonant surfaces. Their original motivation was the observation that the mixing radius of sawteeth could be as large as half the minor radius. The kinds of flux functions considered are shown in fig. 2.7. The non-monotonic q profile is generated by a hollow current profile. The mechanism which generates the hollow profile may be attributable to the internal disruption themselves. As in previous cases the instability leading to the sawtooth crash was taken to go unstable when $q < 1$. They invoke the presence of a magnetic barrier which prevents the growth of the instability when

$$\psi(r_{s2}) < \psi(0)$$

They assume the barrier can be overcome and the instability develop when

2.2.29)

$$\psi(r_{s2}) \sim \psi(0)$$

The picture as described by this model is the following. Immediately after the disruption a flat ψ profile is generated as shown in fig. 2.7. As the current diffuses back in, the value of ψ at r_{s2} increases, when condition 2.2.29 is met then reconnection can proceed all the way to the center. Fig. 2.8 shows plots of the $\vec{B}_*$ field for this case. We see the formation of two opposing islands during the growth of the $m = 1$ instability. This may contribute to the suppression of the observed $m = 1$ precursors in the temperature. We shall discuss this more later with regards to exotic sawteeth. The mapping function for this kind of reconnection can easily be generalized from eq. 2.2.8. The plasma parameters profiles generated do not differ in shape from that of single reconnection. The reconnection in this case is the time it takes for the center to reconnect with r_{s2}. Thus we expect the same scaling as found in eq. 2.2.28 however this time using r_{s2} rather than r_{s1}.

At this time we should pause and recapitulate the main results arrived at in this section, so that they can be kept in mind while examining the sawteeth in Alcator C. From the reconnection of a single resonant surface, we found that the maximum value the ratio r_M/r_i could have is $e^{1/2}$. This is important because it gives us an experimentally measured number, which we can use to see if the

sawteeth are consistent with a single reconnecting surface. After developing the mapping function for the reconnection process, we saw that an initially peaked temperature profile could either become peaked or hollow depending on the degree of initial peakness and the current profile shape. The required degree of detail is more than the available diagnostics can give. Thus comparing the initial and final temperature profiles can not tell us whether Kadomtsev reconnection is consistent with the process or not. By considering the simple parabolic current profile and the more generalized temperature we showed that the observed inversion radius corresponds to the resonant radius. A scaling law for the reconnection time was developed similar to that in [2.4]. We found the predicted values for the disruption time to be as much as an order of magnitude higher than the measured values. This discrepancy may arise from the crudeness of the estimation rather than a discrepancy in the physics. Finally we considered reconnection of two resonant surfaces. The profiles arrived at by this method may allow larger values of r_M/r_i than the single resonant surface. The generation of two opposing $m = 1$ islands, as we shall argue later, may account for the reduction of $m = 1$ precursor oscillations in normal sawteeth. In discussing exotic sawteeth we shall see that the multiple resonant model may be applicable, thus allowing a unified explanation of all these seemingly disparate forms of sawteeth.

2.3)General observations

We have reviewed in some detail the results arrived at by other workers in the area of sawtooth activity, and have discussed with particular emphasis the magnetic reconnection picture. The reason for this as we shall show in this and the following sections is that this picture seems to provide a succesful explanation of the wide variety of sawteeth seen on Alcator C. In this section we shall give a general overview of the sawteeth seen on Alcator C, leaving the more detailed discussion of their various aspects to later sections.

Sawteeth are generally seen during normal Alcator operation, when the q_l (safety factor at limiter)< 7. This condition is associated with $q_0 < 1$ which as we saw in the previous sections is required for the sawtooth instability to take place. Several diagnostics show the signature of sawteeth, the rapid decay followed by a slow rise near the center with an inversion outside a given radius. Fig.2.9 shows some traces for the case of Alcator C. We see the sawtooth signature clearly on the central temperature and soft-Xray signals. Although the density is also expected to be rearranged during the disruption, because of its much flatter profile it will have a smaller sawtooth amplitude. Also the density interferometer measures the line integrated density, this will also tend to reduce the apparent amplitude of the density. The lack of current fluctutation implies that the total current is conserved, although the internal current profile is expected to be rearranged. The oscillations seen on the loop voltage are not due to the sawtooth oscillations, but are ripple from the OH power supplies. The signal due to the sawteeth is very small, reflecting the plasma's tendency to shield its interior from the outside. This is supported by simulations which show that for large internal voltage fluctuations, the external response is strongly suppressed.

In this thesis we shall concentrate on the sawtooth behaviour from the point of view of the electron temperature as measured by the ECE. This has the advantage that it is a local measurement of a single parameter. The disadvantage is that it has fewer spatial channels than the soft Xrays. To overcome this limitation,

profile parametrization was used. The form was determined from spatial scans of plasma shots with constant conditions. The initial incremental temperature profile, is defined as the difference between the final temperature profile and the initial. The initial and final times of the disruption are determined by fitting the channel closest to the center with a three step linear function around the time of the sawtooth crash. Fig.2.10 shows the data set used in the fitting. The pressure rather than the temperature is used in the fitting for later we shall impose energy conservation on the profile. The incremental pressure is here defined as the product of the incremental temperature times the unperturbed density profile, with the assumption that the density fluctuations do not make a large contribution. The functional form used in the fitting is:

2.3.1)

$$\delta(nT) = \begin{cases} A cos(\frac{\pi}{2}x^2) & x \leq 1 \\ B(x-1)e^{\sigma(x-1)^2} & x > 1 \end{cases}$$

where $x \equiv r/r_i$, r_i is the profile inversion radius. The fit was done by adjusting the parameters r_i, A, B, σ. Energy is conserved to better than 90%, which is consistent with total energy given the error bars. In doing the fit to only six channels, we shall remove one free parameter by imposing energy conservation giving the relation

2.3.2)

$$B = \frac{-A}{\frac{\pi}{\sigma}\left(1 + \frac{1}{2}\sqrt{\frac{\pi}{\sigma}}\right)}$$

Using this parametrized profile, a comparison of the initial and final total profiles are shown in fig. 2.11.

Fig. 2.12 shows the time trace for the six ECE channels for a plasma shot exhibiting the most common('normal') sawteeth found in Alcator. We note the absence of large precursor oscillations. This has long been taken as a problem for the reconnection model as proposed by Kadomtsev [2.4]. In it the generation of a large $m = 1$ island is required before reconnection can occur. The island is expected to rotate with the electron diamagnetic drift frequency. Fig. 2.12 shows some evidence of small $m = 1$ precursors, the measured frequeny for these is $\sim 8.2kHz$. If we use the diamagnetic drift frequency arrived at by Jahns[2.11] the estimated frequency

is $11kHz$ in good agreement with the observed value. The amplitude seen however indicate an island width at the time of disruption that is much smaller than the observed inversion radius. Similar observations have been made on TFR[2.14]. At lower densities they found evidence for $m = 1$ activity, but at high densities the $m = 1$ was strongly suppressed. However in all cases they found the expected island width to be $< r_i/3$. They also found that after the disruption there would be $m = 1$ successor oscillations, indicating that the island did not completely reconnect. This led them to propose that the $m = 1$ precursors are not directly responsible for the disruption. They attribute the sawtooth disruption to the formation of a turbulent region, emanating from the resonant layer. This turbulence could possibly be driven by large current gradients set up by the $m = 1$ instability. As the turbulent region propagates the disruption takes place, with the $m = 1$ island surviving. The successor oscillations rotate with a slower frequency, reflecting of the new smaller gradients. In the case of exotic sawteeth we see successor oscillations with amplitudes larger than the precursors. We shall discuss them later in more detail when considering exotic sawteeth.

At this point we would like to suggest an alternative explanation which will be developed throughout this chapter. In the previous section we considered the magnetic topology of two resonant surfaces (fig. 2.8). As the current penetrates two islands develop concurrently and opposite each other (fig. 2.13) about each resosnant surface in such a way as to reduce the net $m = 1$ signature as seen on the ECE. This process continues until the disruption begins which would normally involve the complete reconnection of both islands. This picture of multiple $m = 1$ islands will be used in later sections to explain the wide variety of sawtooth behaviour found in Alcator.

In the following sections we shall discuss in detail how various properties of the sawteeth scale and compare them to those of other machines as well as those predicted by models. The most common sawteeth are those which exhibit little if any $m = 1$ activity; these will be characterised by the inversion radius, energy mixing radius, sawtooth period, disruption time and central sawtooth amplitude.

We shall find that the data is not generally consistent with a single resonant surface model, but may be accounted for if we allow multiple resonant surfaces. In another section we shall discuss a number of exotic sawteeth which differ significantly from the normal case. These are generally seen in plasmas with a large impurity content. We shall see that the multiple resonance model may be capable of explaining much of this behaviour.

2.4)Scaling of sawtooth parameters

A study of the scaling of the temperature inversion radius and energy mixing radius has been done for the case of 'normal' sawteeth over a wide range of plasma parameters. The fill gases used were H_2,D_2,He, spanning a density range of $1 \leq \overline{n} \leq 5 \times 10^{14} cm^{-3}$, plasma current of $320 < I_p < 500kA$, a range of Z_{eff} from $1.1 < Z_{eff} < 1.3$ and $Z_{eff} \sim 2.2$ for H_e. In each case the initial perturbation profile was fitted by a function of the form of eq. 2.3.1 and from this the temperature inversion radius was determined.

At the time of the disruption, energy is displaced from the center of the plasma to the outer regions. The extent of this displacement will be known as the energy mixing radius. Any displacement that takes place on the disruption time scale must be associated with the magnetic disruption, since any bulk diffusive effects take place on a much longer time scale. From this argument we can expect the energy mixing radius to be a good measurement of the magnetic mixing radius. Since the parametrized profile is infinite in extent, we shall define the energy mixing radius as that which contains 95% of the redistributed energy. We shall denote it here as r_M and it is found from

2.4.1)

$$F(r_M) = \alpha U_i - \int_0^{r_m} dx 2\pi x n(x) T(x) = 0$$

where

$$U_i = \int_0^{r_i} 2\pi x n(x) T(x)$$

is the total displaced energy,for the 95% energy mixing radius we have $\alpha = 0.05$.

To see if q is consistent with $q \sim 1$ in the region of the inversion radius we can estimate the value of q at r_i by assuming that $j \sim T_e^{3/2}$ and $T_e \sim e^{-r^2/a_T^2}$ then the safety factor profile has the form

$$q(r) = q_l (\frac{r}{a_l})^2 \frac{1 - e^{-3a_l^2/2a_{T_e}^2}}{1 - e^{-3r^2/2a_{T_e}^2}}$$

since $a_l^2 \gg a_{T_e}^2$ we can write

2.4.2)

$$q(r) \sim q_l(\frac{r}{a_l})^2 \frac{1}{1-e^{-3r^2/2a_{Te}^2}}$$

Previously it has been shown that a_{Te}, scales with the safety factor for sawtoothing discharges[2.17]. Fig. 2.14 shows q_i to be independent of q_l and within the accuracy of this model to be $q_i \sim 0.96$. Some qualifications need to be added to the results as given by this model. Since the plasma is not in steady state, the electric field profile is not constant across the plasma thus our assumption of $j \sim T_e^{3/2}$ is strictly not valid. As we shall see in the next chapter the current profile just before the disruption may be somewhat flatter than the temperature profile.

A scaling for the inversion radius can be developed assuming q_i is a constant. Eq. 2.4.2 can be recast in terms of the central safety factor to give

2.4.3)

$$q(r) \sim q_l(\frac{r}{a})^2 \frac{1}{1-e^{-q_l r^2/q_0 a^2}}$$

since $r_i \ll a$ we can expand the exponent to get

2.4.3)

$$r_i^2 = \frac{a^2}{q_l}\frac{2q_0^2}{q_i}(\frac{q_i}{q_0} - 1)$$

If we use the value of $q_i = 0.96$ and $q_0 = 0.87$ (shown in ref.[2.17]) then we arrive at a scaling

2.4.4)

$$r_i = 0.44\frac{a}{\sqrt{q_l}}$$

This value is close to that arrived at by the TFR group[2.13]

$$r_i = 0.5\frac{a}{\sqrt{q_l}}$$

Fig. 2.15 shows a plot of the inversion radius and energy mixing radius with $a/\sqrt{q_l}$. The data set is not sufficiently wide to verify the scaling as shown in eq. 2.4.4, but we can see whether the scaling is at least consistent with the data over the narrow region. The average value of r_i in fig. 2.15 is $< r_i >= 3.63cm$, using the scaling of eq. 2.4.4 gives $r_i = 3.7$ and the TFR scaling gives $r_i \sim 4.24$. Thus we see there is

good agreement at least within this narrow data set between the TFR results and ours.

The average ratio of r_M/r_i for the cases shown in fig. 2.15 is $< r_M/r_i >= 2.2$. This is a number which can be compared to theoretical predictions. The first is the model proposed by Jahns[2.11] in which the pressure profile is flattened about the inversion radius and the mixing radius is determined by energy conservation. If we assume that the central pressure profile before the disruption can be represented by a parabola then this model predicts an $r_M/r_i = \sqrt{2}$. This is the same result we would arrive at had we used the Kadomtsev model with a parabolic current profile. If we use the current profile of eq. 2.2.10, the maximum value of r_M/r_i is

2.4.5)

$$\frac{r_M}{r_i} = e^{1/2}$$

Fig. 2.15 shows both of these cases to be below the measured value of r_M. For the Jahns case it implies that the data is inconsistent with a flat temperature profile outside r_i, but we knew this from actual measurements of the profiles. A more subtle implication is that we can not account for the measured ratio of r_M/r_i with any reconnection model that assumes a single resonant surface. The form of the current of eq. 2.2.10 can account for all single resonance cases. What this implies is that the mechanism active in these sawteeth is probably not single resonant surface reconnection.

Although the trigger mechanism for a sawtooth is not well known, all theories proposed depend on the form of the current profile. In estimating the scaling of the sawtooth period we only need to consider how long it takes for the background plasma profiles to reach the critical condition for disruption. The actual time of the disruption contributes a negligible amount to the sawtooth period.

TFR performed a series of scaling studies in varying plasma conditions and arrived at a simple scaling for the sawtooth period of the form

$$\tau_0 \sim \bar{n} r_i^2 R$$

The scaling can be understood in terms of the time scale for the current to reach the critical profile. The change in the current due to diffusion happens in a time scale which varies as r_i^2. The time scale for the temperature to recover varies with the energy confinement time $\tau_E \sim \overline{n} a_l^2 R$. Since for the case of Alcator R, a_l are constant we arrive at the scaling.

2.4.6)

$$\tau_0 \sim \overline{n} r_i^2$$

Fig. 2.16 shows the scaling for this case. Although the data has the general trend the agreement is not very good. The squared linear correlation coefficient is $C^2 \sim 0.86$ for this case.

Using the Jahns [2.11] scaling as discussed in sec.2.1 we have

$$t_0 \sim (\overline{n} B_z T_i T_e r_i^2 R^2 / V^3)^{1/3}$$

In our case we can neglect the R^2 scaling since it is a constant. Fig. 2.17 shows the result for the same data set considered in fig. 2.16 showing the TFR scaling. In this case the quality of the fit is much better, giving a correlation coefficient of $C^2 = 0.97$.

McGuire and Robinson[2.12] developed a scaling relation based on the tearing mode growth rate. The empirical scaling found by fitting a number of machines is of the form

$$t_0 \sim \tau_r^{0.42} \tau_A^{0.14} \tau_h^{0.44}$$

where as discussed in sec. 2.1, τ_r is the skin time, τ_A Alfven transit time, τ_h the Ohmic reheat time. Assuming Spitzer resistivity the sawtooth repetition time scales as

$$t_0 \sim \frac{r_i^{0.84} \overline{n}^{0.51} T_e^{1.73}}{B_T}$$

where r_i:cm

$\overline{n}$:$10^{14} cm^{-3}$

T_e:eV

B_T:Tesla

Fig.2.18 shows the scaling for this case. The linear correlation coefficient for this case is $C^2 = 0.99$.

Of the three scaling relations the McGuire and Jahns forms give the best agreement with the data. Although the McGuire scaling gives a slightly better correlation, the scatter in the data is such that we can not differentiate between the two. Thus sawtooth period scaling can not tell us which of the two forms of the growth rate is responsible for the disruption, if any of these are.

TFR used a turbulent model to explain the disruption. Fitting the decay to a diffusive model they found effective diffusivities of $\sim 10^2 cm^2/ms$ while the bulk diffusivity was $\sim 1 cm^2/ms$ or a two order of magnitude enhancement. Making a similar estimate for the Alcator data, the effective anomalous diffusivity is $\sim 400 cm^2/ms$ while the bulk $\sim 2 cm^2/ms$. This is of importance in the next chapter when we consider estimating the bulk thermal diffusivity by following the evolution of the sawtooth generated heat pulse. We must make sure not to include any section of the temperature trace which includes effects from this larger diffusivity.

The last parameter we look at in the case of normal sawteeth is that of the sawtooth amplitude. Here we shall refer to that found at the center of the plasma. The purpose here is to compare the empirical scaling found for the TFR case with that of Alcator. We can also develop a sawtooth scaling based on the sawtooth period and assuming that the central temperature evolution between disruption is dominated by Ohmic heating. It can be argued that the relative peak sawtooth amplitude must scale as

$$\frac{\delta A}{A} \sim \frac{\tau_0}{\tau_h}$$

where τ_0 is the sawtooth period and τ_h is the central reheat time.

By using the McGuire-Robinson scaling as discussed in the previous section

$$\tau_0 \sim \frac{r_i^{0.84}\overline{n}^{0.51}T_e^{0.41}}{B_T}$$

and a reheat time of the form

$$\tau_h \sim \frac{\overline{n}T_e^{5/2}}{B_T^2}$$

gives a relative sawtooth amplitude of the form

$$\frac{\delta A}{A} \sim \frac{r_i^{0.84}B_T}{(\overline{n}^{0.49}T_e^{0.77})}$$

Fig. 2.19 shows the results of using this scaling on Alcator data.

TFR developed an empirical scaling of the form

$$\frac{\delta A}{A} \sim \frac{1.5}{q_l^{3/2}}$$

Fig. 2.20 shows the scaling of Alcator data with a function of $1/q_l^{3/2}$. The data shows reasonable agreement with this kind of scaling, however rather than having the 1.5 factor as found for TFR, we find a constant closer to unity.

The fact that the simpler TFR scalings seem to work as well as those based on more complicated models, has been taken at times to indicate that simpler physical processes are active in the sawtooth disruption than the models proposed. A more likely explanation may be that because of other constraints in the system many of the assumed free parameters in the complicated sawtooth scaling may not be free at all, and may be represented by fewer plasma parameters.

2.5)Exotic sawteeth and impurities

Up to now we have been discussing the most common(normal) form of sawteeth seen in Alcator C. In this section we shall discuss the qualitative features of sawteeth that deviate from this category. These exotic sawteeth (examples of which can be found in figs. 2.21, 2.22,2.24) are seen in plasmas with large impurity concentrations. Unlike normal sawteeth, exotic sawteeth do not exhibit periodic behaviour, that is an exotic sawtooth event is usually preceeded and followed by either a normal sawtooth event or some other form of exotic sawtooth event. Exotic sawteeth in Alcator can be divided into three classes, although as we shall see later the normal as well as the exotic sawteeth may be explained as different manifestations of the same mechanism.

The first category of sawteeth we shall describe we shall call 'partial' sawteeth shown in fig. 2.21. These are characterized by two separate disruptions that are close to each other. The first disruption takes place at the same time as if it was a normal sawtooth. However in this case the disruption is arrested before completion, leaving the plasma inside of the profile inversion radius with a strong $m = 1$ oscillation. These oscillations can continue for several periods at which time a second disruption takes place. The overall amplitude of this complicated behaviour is consistent with the normal sawtooth amplitude. Outside the inversion radius, the electron temperature rises in response to the first disruption, in a manner similar to a normal sawtooth. However instead of breaking into $m = 1$ osillations like inside the inversion radius, these outside channels decay monotonially as in a normal sawtooth. At the time of the second disruption, there is again a rapid rise followed by a monotonic decay. The $m = 1$ oscillations are largest in the region nearest the inversion radius. After the first disruption they appear, but their amplitude changes little if any until the second disruption. The oscillation frequency for the case shown here is $4.2 - 4.6kHz$. If we consider the electron diamagnetic drift frequency using a flattened temperature profile which corresponds to that measured after a normal sawtooth disruption, we calculate a rotation frequency of $4.5kHz$ for the above shot.

The second type of sawteeth we shall denote as 'giants', an example of which is shown in fig. 2.22. Their main characteristic is the large amplitude disruption, which can be up to twice that of a normal sawtooth. At the center of the plasma the temperature rises linearly at the same rate as for normal sawteeth, however the time of the disruption is delayed thus generating the large amplitude. Many times on the channels near the inversion radius there is evidence of a minor disruption at the time which would correspond to a normal sawtooth crash. Inside of the inversion radius are seen small $m = 1$ oscillations as in the partial sawtooth case. Except for these small oscillations the giant sawtooth looks like a normal sawtooth. Sometimes they take place several at a time with similar properties, but most frequently only one giant disruption takes place with the subsequent one being a normal sawtooth. Fig. 2.23 shows a reconstruction of the incremental profiles after a giant sawtooth crash and that of a normal sawtooth crash. The inversion and mixing radius are the same, the only difference is the overall amplitude.

The third form of sawtooth is a 'compound giant' shown in fig. 2.24. This type of sawtooth generally starts off like a partial sawtooth, but rather than have the second disruption the $m = 1$ oscillation decay away as the central part of the plasma reheats, then after approximately twice the normal sawtooth period a large disruption takes place. Again the $m = 1$ oscillation exhibit the same behaviour as in the previous two cases. The incremental profile of the giant crash has the same form as that for the giant sawteeth shown in fig. 2.23.

The shots discussed in this section are all taken from a set of runs with similar plasma conditions. Fill gas was H_2,$\overline{n} = 1.7 \times 10^{14} cm^{-3}$,$I_p = 470kA$ with a baseline global $Z_{eff} \sim 1.2$. Varying amounts of Ar were injected into the plasma changing global $Z_{eff} \sim 1.4 - 2.4$. The central Z_{eff} rather than the global Z_{eff} may be the important parameter affecting the sawtooth mechanism. A better indicator of the central impurities is the central soft Xray emission as enhanced by line radiation ECE data was recorded over a $40ms$ window during the flat top of the discharge From this trace a frequency of incidence of exotic sawteeth can be established. Fig. 2.25 shows the scaling of this frequency with soft Xray signal. There is a clearly

marked threshold with impurity density. A similar plot with global Z_{eff} does not exhibit a clear threshold as above.

Pfeiffer[2.20,2.21] has reported giant sawteeth and what they call double sawteeth on Doublet-III during beam heating. These resemble the giant and partial sawteeth as seen on Alcator C. TFTR[2.19] has reported what they call a compound sawtooth which is very similar to the compound gaint seen on Alcator C.

The explanation given in [2.19,2.20,2.21] is based on a two resonant surface model, similar to that proposed by Parail[2.7]. However instead of the trigger condition being $\psi(r_{s2}) \sim \psi(0)$, reconnection can take place when $\psi(r_{s2}) < \psi(0)$, the trigger condition for the disruption being in this case the overlap of the islands created at each resonant surface. In these cases reconnection does not take place all the way to the center (fig. 2.26), it is referred to as partial reconnection. For the case of Alcator this interpretation at first has many appealing features. The presence of the impurities increases the local resistivity possibly allowing reconnection to take place at a much lower threshold. However this would imply that the time delay between the last disruption and the start of the next exotic sawtooth disruption should vary in a fashion according to the specifics of the impurities. In Alcator we have seen that exotic sawteeth do not take place in any extended sequence, they are usually bounded by normal sawteeth. We observe that the initial disruption which corresponds to an exotic sawtooth is delayed by the same amount from the previous as are normal sawteeth in the same sequence. For the case of partial sawteeth it is the first minor disruption that is delayed by this amount with the second disruption varying in delay. For the case of a giant sawtooth we have shown that there is evidence for a very small disruption which does not affect the center, however the delay of this disruption is the same as that for a normal sawtooth. The main crash can vary in delay after this, thus exhibiting a somewhat random period if taken as a single sawtooth. The compound giant is an even more special case. The first disruption takes place after one normal sawtooth period with the second large disruption after approximately another normal period, making the overall period twice that of a normal sawtooth.

What these observations imply is that the trigger mechanism active in the normal sawteeth must also be active in the exotic sawteeth. If we take the current as the trigger, then the current or ψ profile can not be very different for the case of an exotic sawtooth or a normal sawtooth. The difference between the normal and exotic sawtooth are their subsequent evolution. For the case of an exotic sawtooth the disruption is arrested before reconnection to the center can take place. The impurities probably play a role in modifying the evolution of the disruption. Further evidence for this view, lies with the observation that the profile inversion radius for the temperature and energy mixing radius do not differ significantly from that of a normal sawtooth. This implies that the initial and final current profiles must not differ significantly from those of a normal sawtooth. In [2.19,2.20,2.21] differences have been noted in the incremental profile of the soft Xrays, but (assuming these cases are also tied to the impurity content) these may stem from differences in the impurity profiles rather the temperature or density.

In all cases of exotic sawteeth we have discussed, we see evidence for $m = 1$ oscillations immediately after the first disruption and ending with the secondary disruption. If the reconnection process were as described in fig. 2.26 for the case of partial reconnection, the final state will have a single magnetic axis and probably be axi-symmetric. Evidence for $m = 1$ activity after reconnection tends to weigh against this picture for the case of Alcator. The $m = 1$ oscillations seem to start with maximum amplitude and either remain constant until the second disruption as in the case of the partial sawtooth, or decay away as in the giant and compound giant. In all of these cases there is little if any evidence for any $m = 1$ oscillations before the disruption. One possible explanation is that there are two $m = 1$ islands which exist before the disruption. As proposed in sec.2.3 they evolve in such a way as to reduce their net signature of on the ECE signal. In a normal disruption, reconnection would take place all the way to the center thus destroying both islands. In the case of partial reconnection, the symmetry with which the islands have evolved up to that point is destroyed and thus we are able to clearly see the signature of one or both islands. The second disruption finishes reconnection to the center.

The model for sawteeth we are suggesting is the following. For the case of Alcator both normal and exotic sawteeth involve at least a two resonant surface reconnection. For simplicity we shall discuss only two resonant surfaces, the model can be extended to more resonant surfaces easily. After a sawtooth disruption the current evolves so as to become hollow, as discussed by Parail and Pereversev[2.7] the sawteeth themselves may drive the current hollow. The evolution of the two resonant surfaces is such as to reduce the net $m = 1$ signature of any precursor oscillations. The trigger condition for the instability must be the same for the case of a normal sawtooth as well as for an exotic sawtooth. This is suggested by the observation that the delay for the main disruption in a normal sawtooth and the first disruption in an exotic sawtooth is the same.

Their is some question as to what form the trigger condition should have. Pfeiffer [2.20,2.21] has taken the trigger to be the overlap of the magnetic islands generated around each resonant surface during the linear rise of the sawtooth. The problem with this trigger is that the delay for a normal sawtooth disruption may be different than for a partial reconnection case. Also as pointed out before, the partial reconnection as proposed in [2.20,2.21] will lead to a state with a single magnetic axis and possibly be axisymmetric. This is not compatible with the large $m = 1$ oscillations observed in Alcator an exotic sawtooth crash. Parail and Pereversev [2.7] have taken the trigger to be of the form $\psi(0) \sim \psi(r_{s2})$. When $\psi(0) > \psi(r_{s2})$ they invoke the existance of a magnetic barrier, preventing the development of the sawtooth instability. Since $\psi(0)$ according to the reconnection model should not change before and after the disruption, this form of a trigger has the property that the delay to the next sawtooth disruption is constant whether the disruption ends as a normal sawtooth or as an exotic sawtooth.

If we use the Parail and Pereversev [2.7] trigger in our model, then the difference between a normal sawtooth and an exotic sawtooth depends on the subsequent evolution of the instability. Both cases have the potential for complete reconnection. For the case of a normal sawtooth the reconnection is complete and thus we see little if any evidence for $m = 1$ activity, before or after the disruption. For the case

of an exotic sawtooth the disruption begins as if it was a normal sawtooth, but its development is arrested, possibly by another magnetic barrier before reconnecting to the center. In this case the system is left with two magnetic axes and a highly asymmetric state(see 'reconnecting state' in fig. 2.8). This kind of a picture would naturally explain the large $m = 1$ oscillations seen after the first disruption. The plasma is left in this intermediate state until it can overcome the second magnetic barrier, at this time reconnection can proceed to the center. The difference between the partial, giant and compound giant, is the evolution of the intermidiate state.

As we have seen there is a clear correlation between the incidence of exotic sawteeth and impurity concentration. This suggests that the impurities may play a role in the generation of the second magnetic barrier. In order to create a magnetic barrier, we only need to change the topology of a few flux surfaces, so as to make it energetically unfavorable for reconnection.

This picture would also explain the apparent causal link between the first and second disruption in an exotic sawtooth. After the first disruption, the second disruption always proceeds to the center. This would suggest that the first disruption changed the plasma conditions so as to allow the second disruption to reconnect to the center. In our picture after the first disruption the plasma overcomes the magnetic barrier insuring that the second disruption proceeds to the center.

2.6) Conclusions

Previous workers studying sawteeth have done so using soft-Xray emission. This has led to a considerable source of uncertainty as to how each plasma parameter is behaving. The study done here, has focused on the evolution of the electron temperature using electron cyclotron emission, which may be quite different than that of the soft-Xrays.

The magnetic reconnection model as proposed by Kadomtsev[2.4], and later improved and modified by various authors, remains the most detailed description of the sawtooth disruption. It gives a specific prescription of how the profiles should change before and after the disruption. We considered the simplest case of magnetic reconnection; that involving a single resonant surface. Using a fairly general current profile near the center of the plasma, we showed that the maximum ratio of mixing radius to resonant radius (r_M/r_s) consistent with a single resonant surface is $e^{1/2}$. We showed that for this case the resonant radius should be very close to the observed profile inversion radius(r_i), this implies that r_M/r_i should also have a maximum of $e^{1/2}$. A multi-resonant surface model such as that discussed in [2.7] can be used to arrive at ratios of r_M/r_i larger than $e^{1/2}$. The r_M/r_i parameter is readily measured and thus provides a test to whether single resonant surface reconnection is consistent with the observed disruption.

The reconnection model specifies only that ψ be continuous at $r = r_M$. In general this will introduce a discontinuity in $\partial\psi/\partial r$ or equivalently in $\vec{B}_\bullet$. The discontinuity reflects itself in the generation of a return skin current at the mixing radius. If the reconnection model is to be consistent with the periodic behaviour of sawteeth, this return current must dissipate within one sawtooth period. To address this question, the magnetic diffusion equation was solved for the case of a current ring at $r = r_M$. It was found that the current distribution flattened on a time scale of $\sim 300\mu s$ as compared with a sawtooth period of $3ms$.

One question that is of importance is whether the measured change in the electron temperature profile is consistent with the Kadomtsev reconnection model.

We considered the simple case of a parabolic current profile and a more general initial temperature profile. It was found that the final temperature profile could be hollow, peaked or flat depending on what we chose for the initial profiles. This showed that the final profile is sensitively dependent on the initial temperature and current profile. We have measurements of the electron temperature profile, but we have no measurements of the current profile, thus making profile comparison an inconclusive test of the model.

A comparison of the total reconnection as predicted by Kadomtsev[2.4] and the measured disruption time was done. The results are that the predicted reconnection time is an order of magnitude larger than the measured disruption time. However this discrepancy may arise from the very rough nature of the modelling used in arriving at an estimate of the reconnection time and not necessarily a discrepancy in the physics.

We have identified the energy mixing radius with the magnetic mixing radius. Since the parametrized profile is infinite in extent we set the energy mixing radius to be that which contains 95% of the re-distributed energy. If we assume that the disruption involves a single resonant surface, then the profile inversion radius should be very close to the resonant radius. For the case of normal sawteeth we found an average value of $r_M/r_i = 2.2$. According to the single resonance model as developed in sec. 2.2 the maximum possible value that r_M/r_i could have is $e^{1/2} \sim 1.65$. The implication is that normal sawteeth, are incompatible with single resonance reconnection.

In Alcator as in TFR[2.13,2.14,2.15,2.16] precursor oscillation are usually very small with a frequency consistent with the electron diamagnetic frequency. By assuming a single resonance reconnection model the TFR group came to the conclusion that the width of the $m = 1$ island before the disruption was too small for any significant amount of reconnection to take place. This led them to suggest that magnetic reconnection could not be responsible for the sawtooth disruption. For the case of Alcator multiple resonant surface reconnection may explain the absence or reduction of the $m = 1$ precursors. The evolution of the magnetic islands in a

two resonant surface model may evolve in such a way as to reduce their net $m = 1$ signature. The size of the islands can be significant, but if they tend to evolve in a symmetric manner, their net signature will not be as evident as if there was only a single island.

A number of empirical studies have been done to determine scalings for the various sawtooth parameters. Since these are phenomenological in nature, it is necessary to have a sufficiently wide data base in order to gain confidence in them. Alcator's operating regime is rather unique among present day tokamaks. It will then be useful to compare Alcator sawtooth parameters with these various scalings. We will limit ourselves to study the case of normal sawteeth, since it is for these that scalings have been developed. The parameters studied are, sawtooth period, inversion radius and sawtooth amplitude.

The sawtooth period is the most widely studied sawtooth parameter, since it is the easiest to measure. Three scalings were compared, TFR[2.13], Jahns et. al. [2.11] and McGuire and Robinson [2.12]. Of the three the TFR scaling fit the data the worst although it showed the correct trend. The scalings developed in [2.11] and [2.12] are in good agreement with the data. The scaling in [2.12] was developed assuming a tearing mode growth rate that is uncorrected for diamagnetic drifts, while that developed in [2.11] is reduced by diamagnetic drift effects. The fact that the two agree fairly well implies that the sawtooth period can not be used to differentiate between the two forms for the instability which may be responsible for the disruption.

A scaling for the inversion radius could not be done because of the narrow parameter range in Alcator for which sawteeth are present. However we found the TFR scaling to be consistent with the values of r_i found for Alcator.

The last parameter studied was the central sawtooth amplitude. Here we compared two scalings, one was a TFR scaling and the second was one based on the McGuire-Robinson scaling for the sawtooth period. Both cases showed fair agreement with the data.

It is interesting to note that the simpler TFR scalings have faired well relative to the more complicated scalings driven by theoretical models, when compared to Alcator data. This has sometimes been interpreted to mean that the sawtooth mechanism may be of a simpler form than the present theories predict. A more likely explanation might be that the simple TFR scalings reflect the fact that some of the parameters which are assumed free in the more complicated scalings are actually constrained through mechanisms which may or may not be related to the sawtooth disruption.

We have also studied the special case of exotic sawteeth. These have been shown to be associated with larger than normal impurity concentrations near the center of the plasma. Sawteeth of a similar nature have been seen on TFTR[2.19] and Doublet III[2.20,2.21]. In Alcator exotic sawteeth seem to come in three varieties described in sec. 2.5, partial, giant and compound giant. All three cases are characterized by two consecutive disruptions separated in time by less than one sawtooth period. Large $m = 1$ oscillations near but inside the profile inversion radius, are seen between these two disruptions, the frequency of which seems to be consistent with the electron diamagnetic drift frequency, if we account for the flatter pressure gradients. Normally in these cases there is little if any $m = 1$ precursors. The delay between the previous sawtooth disruption and the first disruption of an exotic sawtooth has been found to be the same as for a normal sawtooth. This has led us to conclude that the trigger for the disruption must be the same in an exotic sawtooth as that in a normal sawtooth.

Based on the above observation of normal and exotic sawteeth a model was proposed which may explain both of these cases. We suggest that the trigger condition for the case of normal and exotic sawteeth is the same. What makes them different is their subsequent evolution. The normal sawteeth reconnect to the center, while the exotic sawteeth have their initial disruption arrested before complete reconnection can take place, leaving the plasma in an intermediate highly asymmetric state until the second disruption takes place. The role of the impurities may be to modify the evolution of the disruption. When considering sawtoothing

after pellet injection we will again find the impurities play an important role in the evolution of the sawteeth.

Each component of the model proposed was introduced to explain an observable. What needs to be done in the future is to show if the model is internally consistent. A better understanding of how magnetic barriers could arise in tokamaks is needed. The strong correlation between impurities and the incidence of exotic sawteeth suggests that if such a barrier exists, the impurities may play a role in generating it. Simulations have to be done to see by how much the $m = 1$ precursors are suppresed in a multiple resonance model. How the impurities can affect the reconnection process, needs to be understood. Direct evidence for the existance of two islands must be found. Tomographic reconstruction of the sawtooth disruption has failed to do so, however for the case of Alcator the spatial resolution of the soft Xray tomographs is $\sim 1cm$, thus if the islands do exist they may not be resolved.

References for chapter 2

[2.1] Vershkov V.A., et. al., Kurchatov Institute Report no. IAE-2291 (1973), PPPL report no. MATT-TRANS-112(1974)

[2.2] Smith R.R., PPPL report no. TM-273(1974)

[2.3] von Goeler S.,et. al. Phys. Rev. Lett. 33(1974)1201

[2.4] Kadomtsev B.B.,Sov. J. of Plas. Phys. v1#5(1975)389

[2.5] Kadomtsev B.B.,IAEA-CN-35/B1

[2.6] Kadomtsev B.B.,Pogutse O.P.,Sov. Phys.-JETP v38#2(1974)283

[2.7] Parail V.V.,Pereversev G.V.,Sov. J. Plas. Phy. 6,14(1980)

[2.8] Waddel B.V.,et. al. Nucl. Fus. 16(1976)528.

[2.9] Sykes A.,Wesson J.A.,Phys. Rev. Lett. v37n3(1976)140

[2.10] Denestrovskii Y.N., et. al.,Sov. J. Phys. 3,9(1977)

[2.11] Jahns G.L.,et. al.,Nucl. Fus. 18,5(1978)609

[2.12] McGuire K.,Robinson D.C.,Culham report #CLM-P 552 (1978)

[2.13] Equipe TFR, IAEA-CN-35/A8

[2.14] Equipe TFR, IAEA-CN-41/T2

[2.15] Dubois M.A.,et. al., Nucl. Fus. 23,2(1983)147

[2.16] Dubois M.A.,et. al.,Nucl. Fus. 20,9(1980)1101

[2.17] Kissel S.E., MIT PFC report PFC/RR-82-15(1982)

[2.18] Hirshman,et. al. Nucl. Fus. Lett. 17,3(1977)611

[2.19] McGuire K.,et. al.,Bull. Am. Phys. Soc. 6p9 v30,n9(1985)

[2.20] Pfeiffer W.,et. al.,Nucl. Fus. 25(1985)655

[2.21] Pfeiffer W.,Nucl. Fus. 25(1985)673

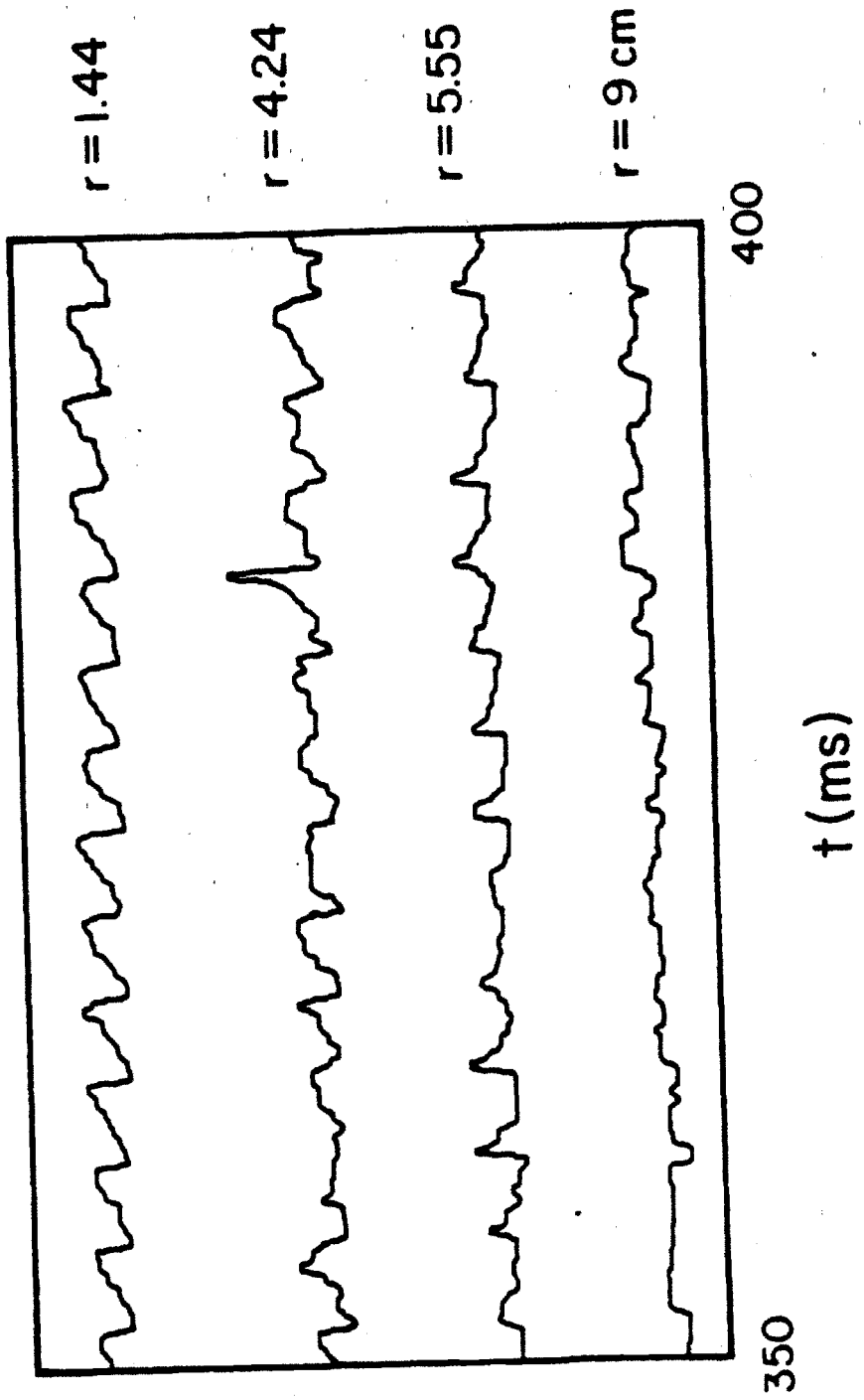

Figure 2.1 — Four Xray traces at different radial locations showing sawtooth structure

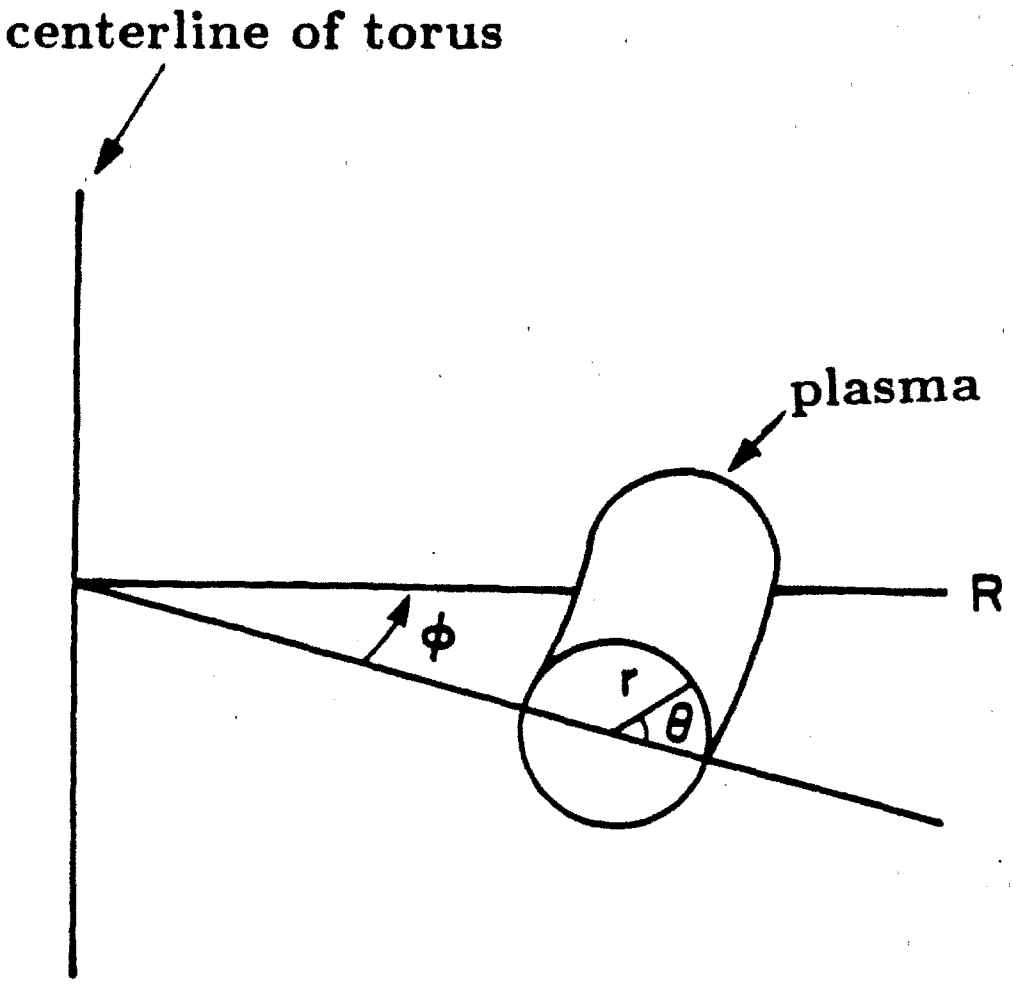

Figure 2.2 — Coordinate system used to describe plasma in a toroidal geometry.

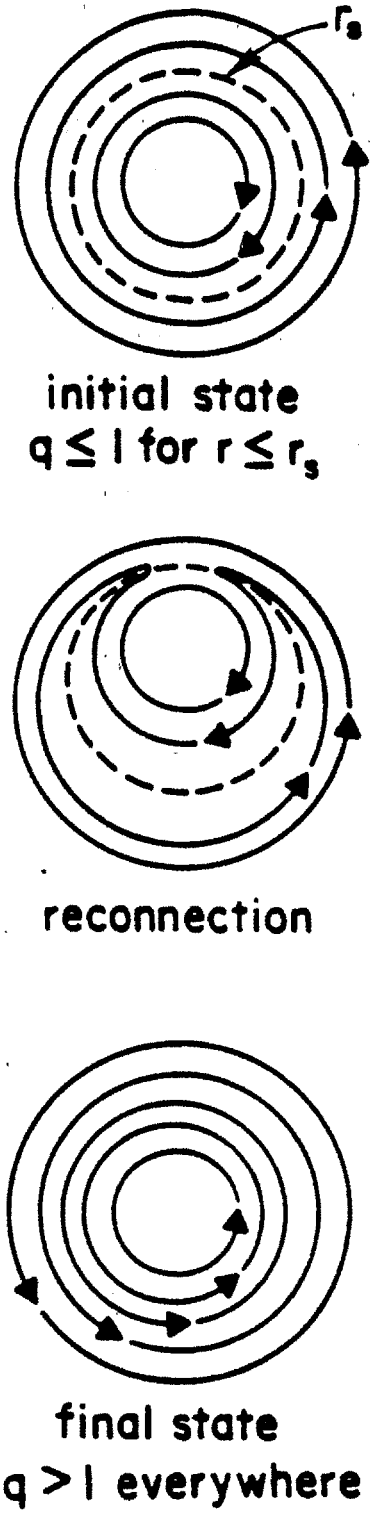

Figure 2.3 — Topology of auxiliary magnetic field $B_{*\theta}$ during Kadomtsev reconnection.

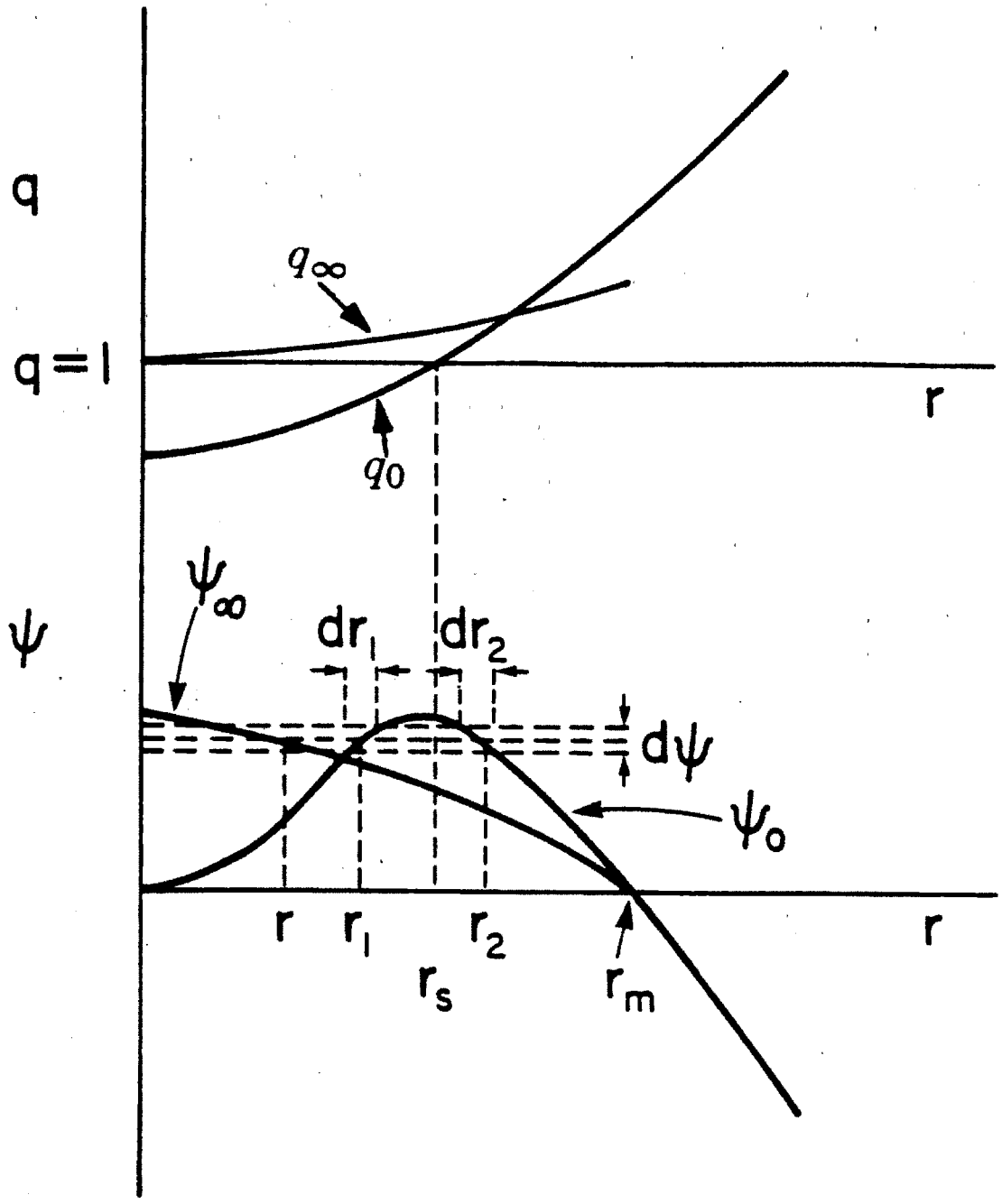

Figure 2.4 — The top figure shows the initial and final q profiles for the case of Kadomtsev reconnection. The bottom figure shows the initial and final ψ profile.

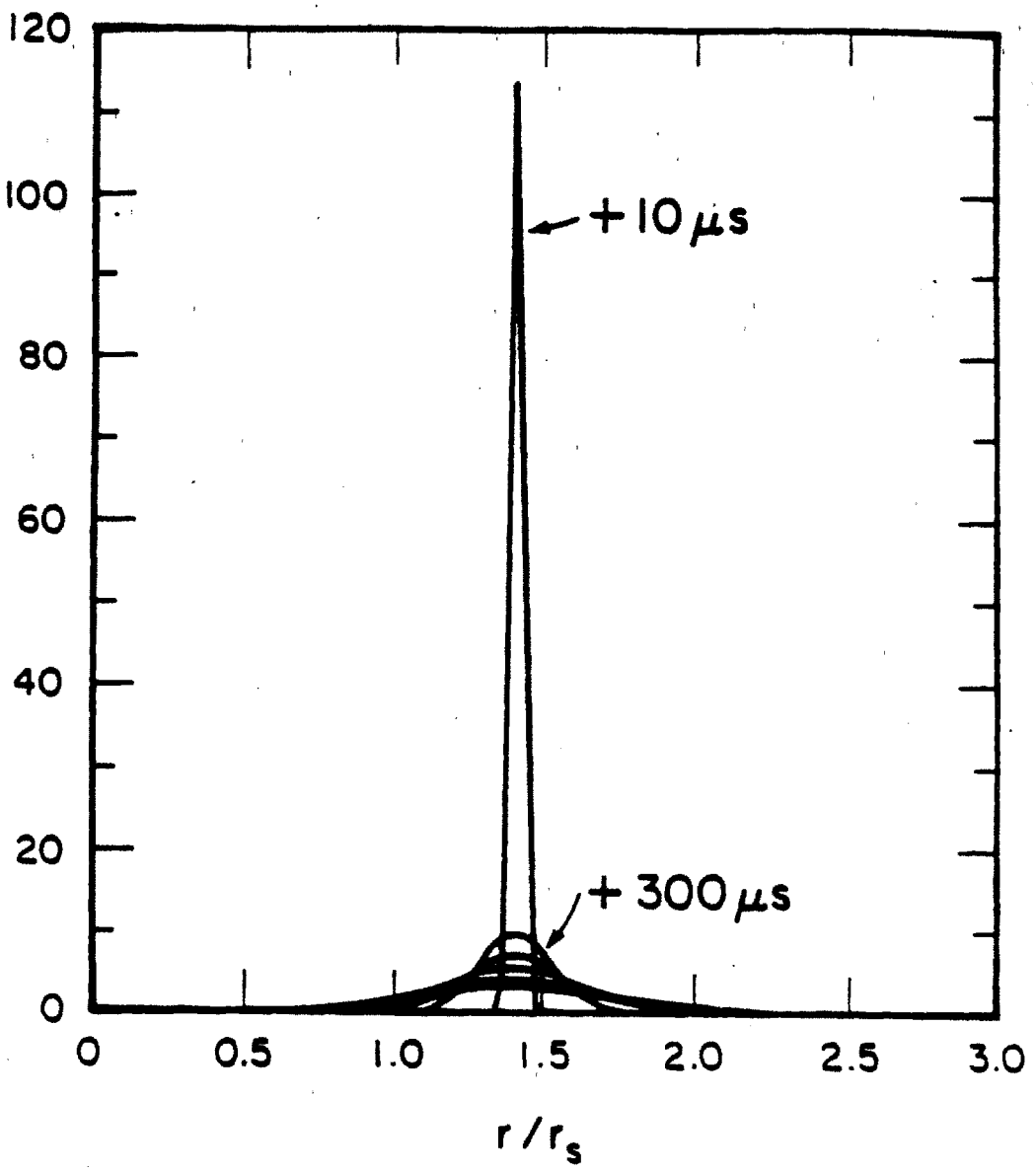

Figure 2.5 — Evolution of skin current generated during Kadomtsev reconnection.

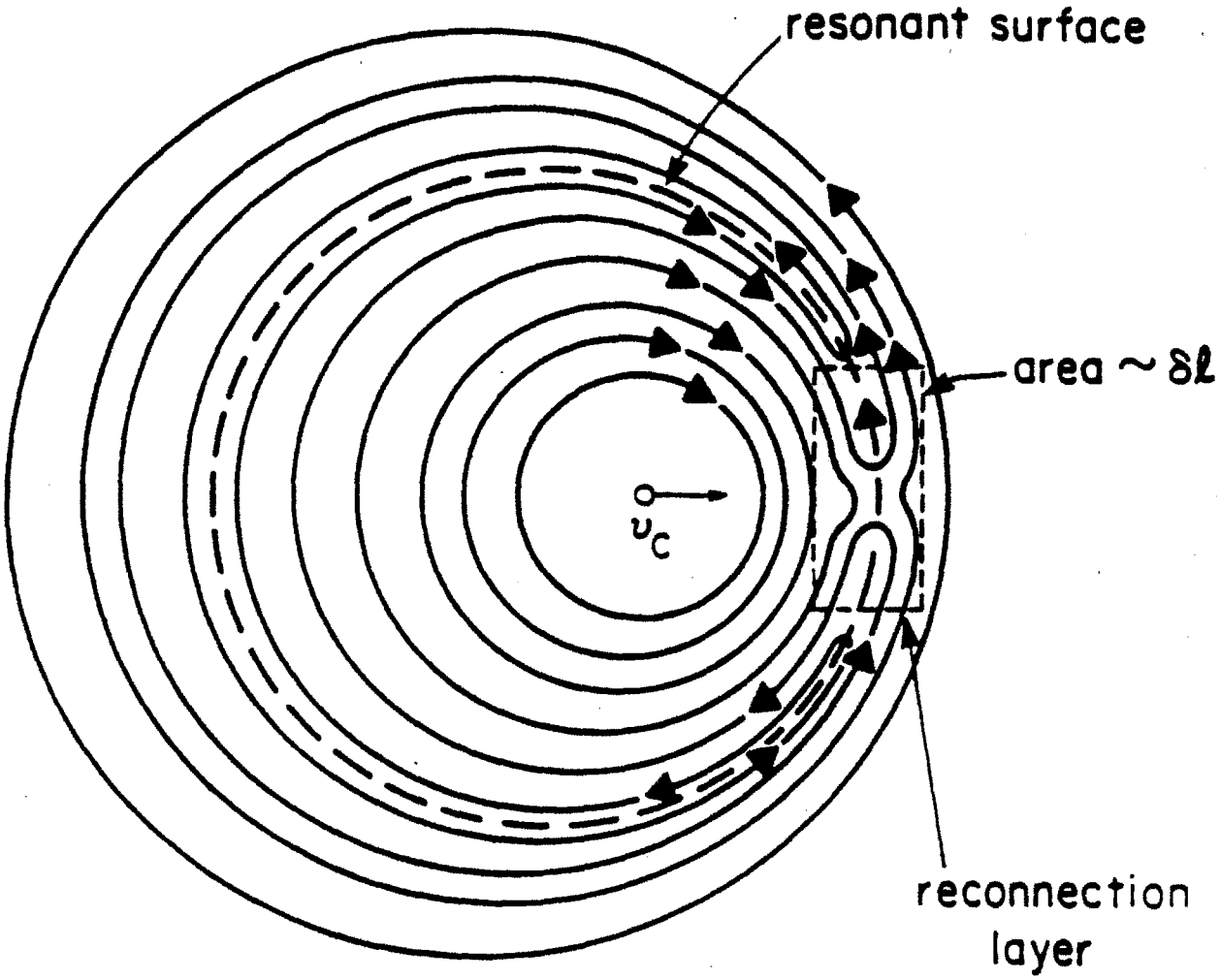

Figure 2.6 — Topology of B_* during reconnection.

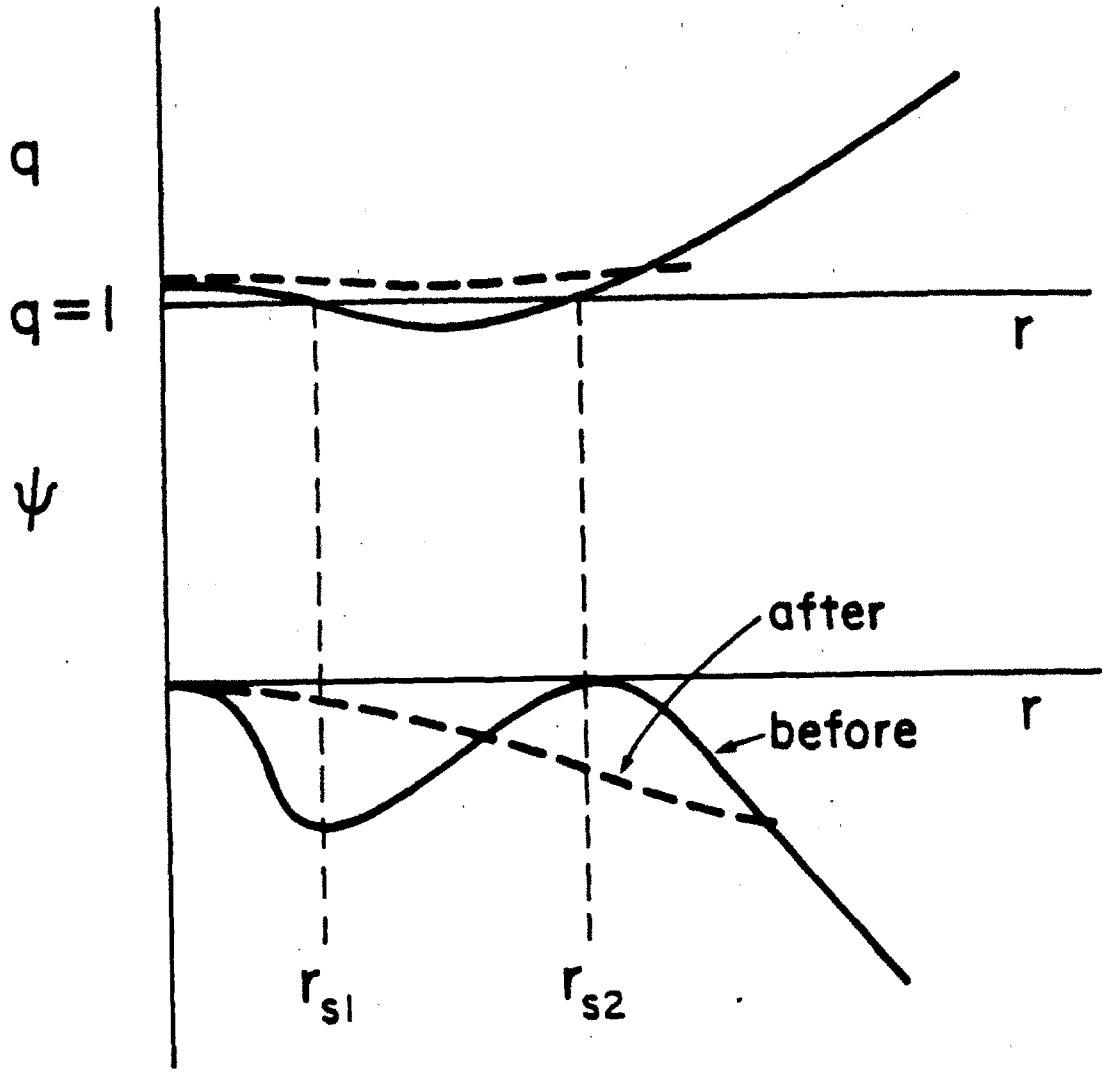

Figure 2.7 — Two resonant surface flux function.

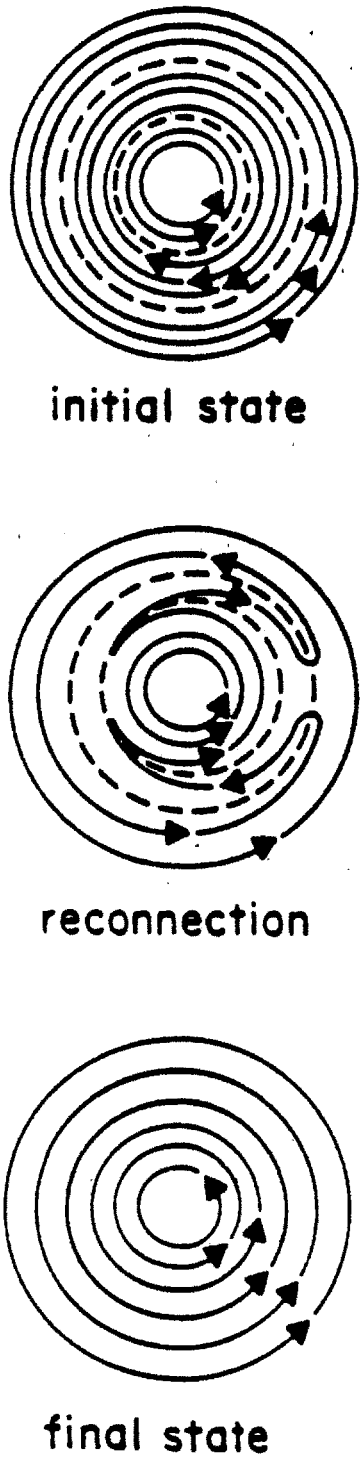

Figure 2.8 — Topology of B_s during two resonant surface reconnection.

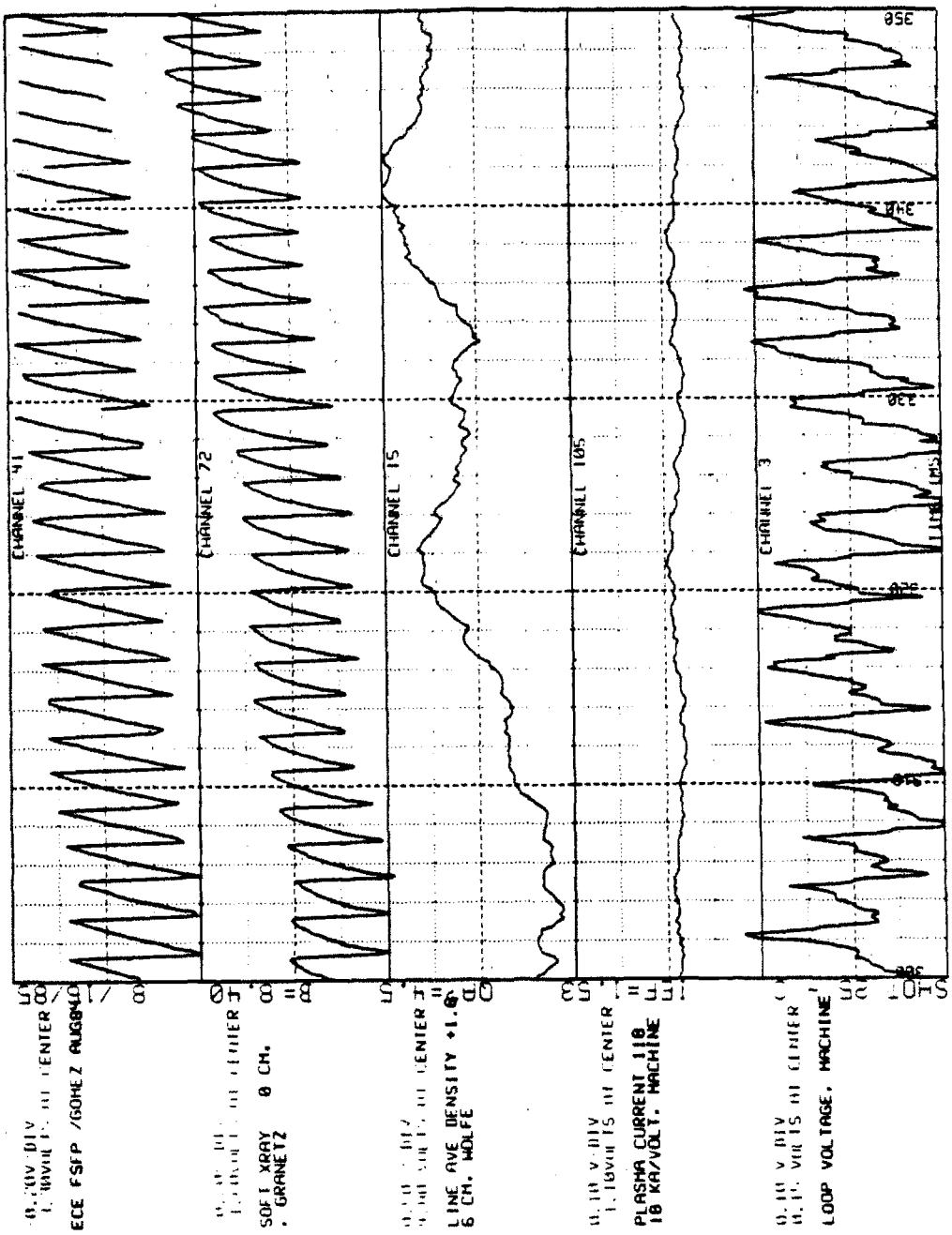

Figure 2.9 — Behaviour of some plasma parameters during sawtooth oscillations in Alcator C.

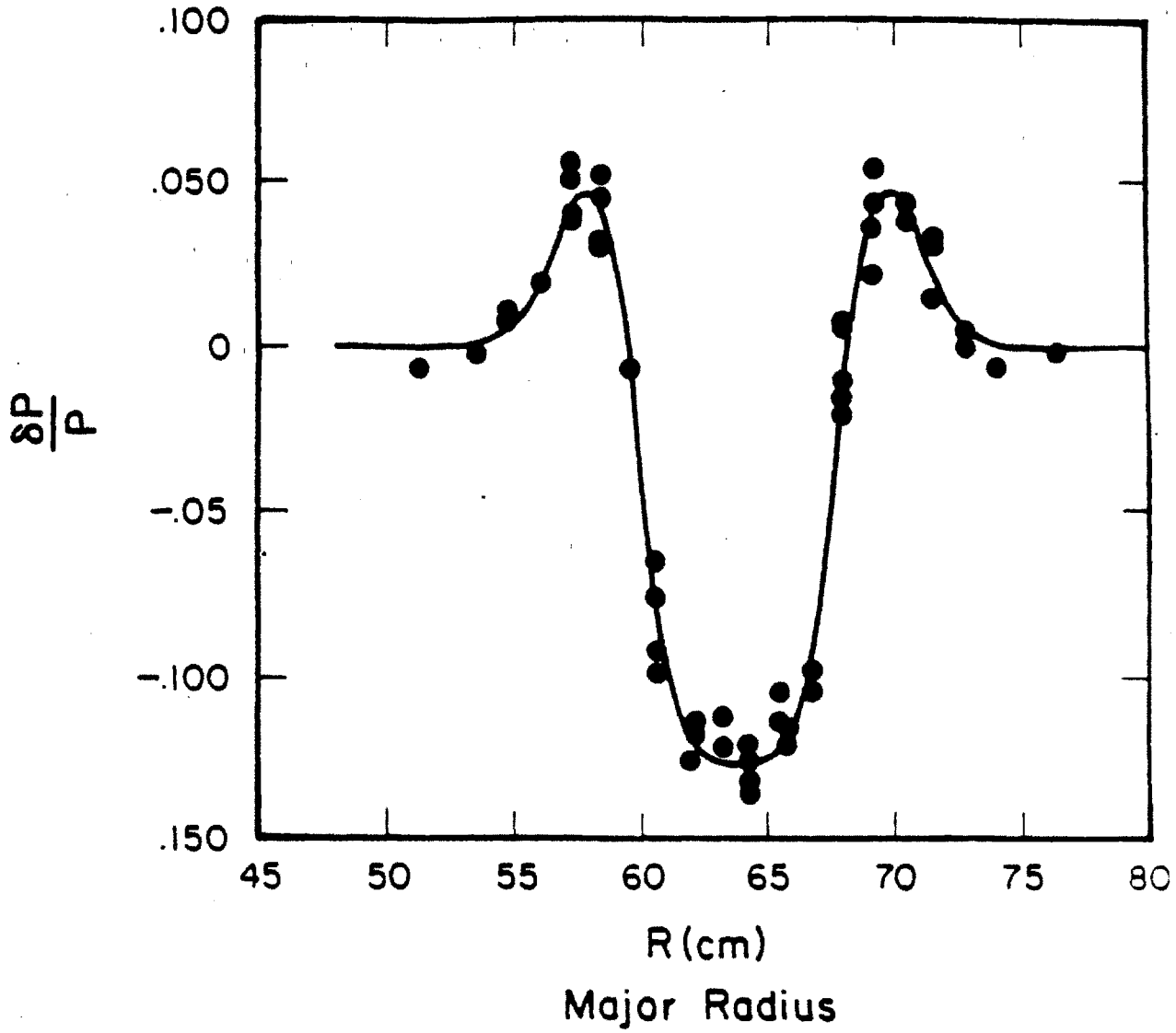

Figure 2.10 — Measured $\delta p/p$ data with fitted trace. The data represents a spatial scan of plasma shots with constant conditions.

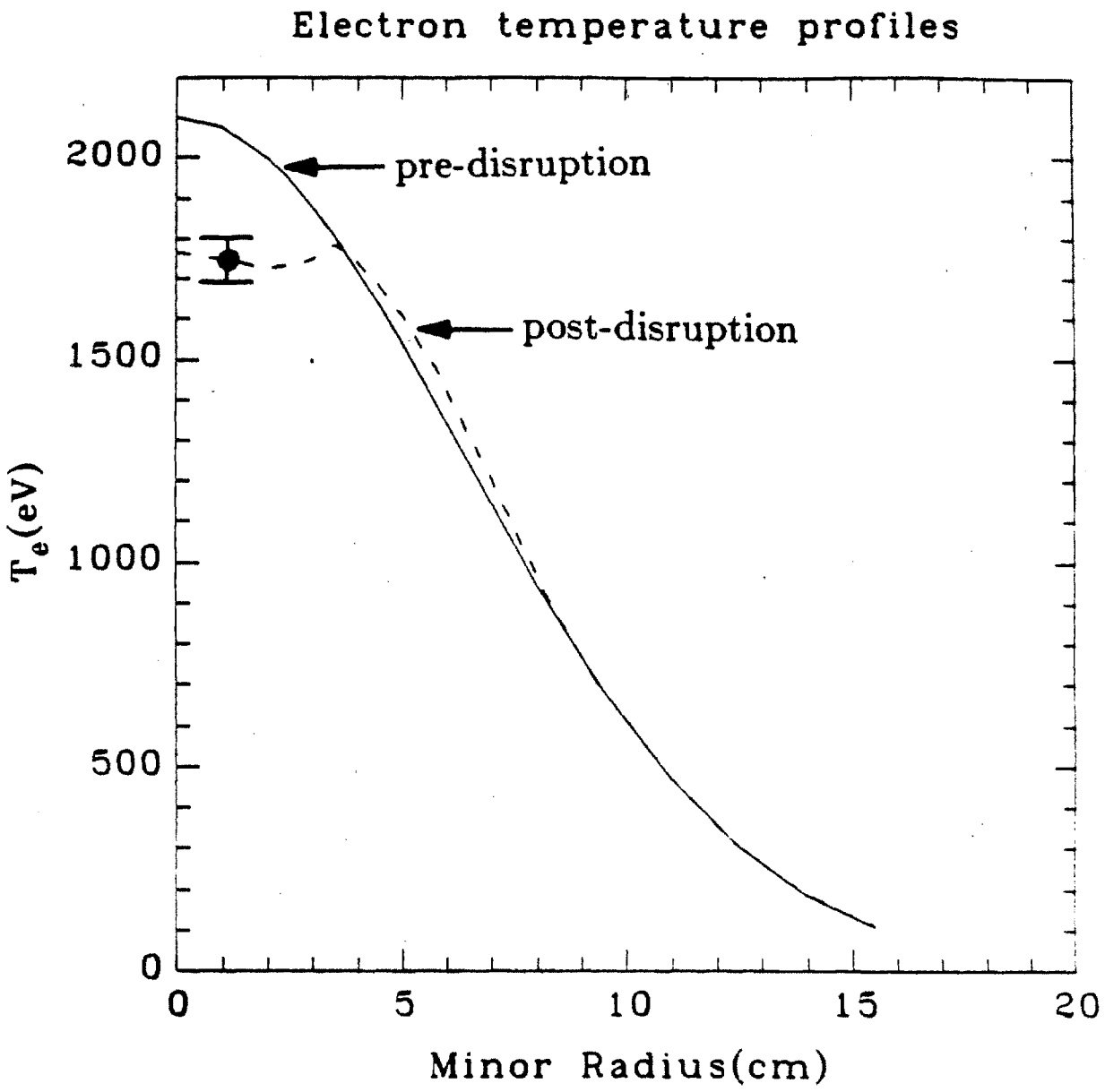

Figure 2.11 — Electron temperature profile as measured by ECE before and after a sawtooth disruption.

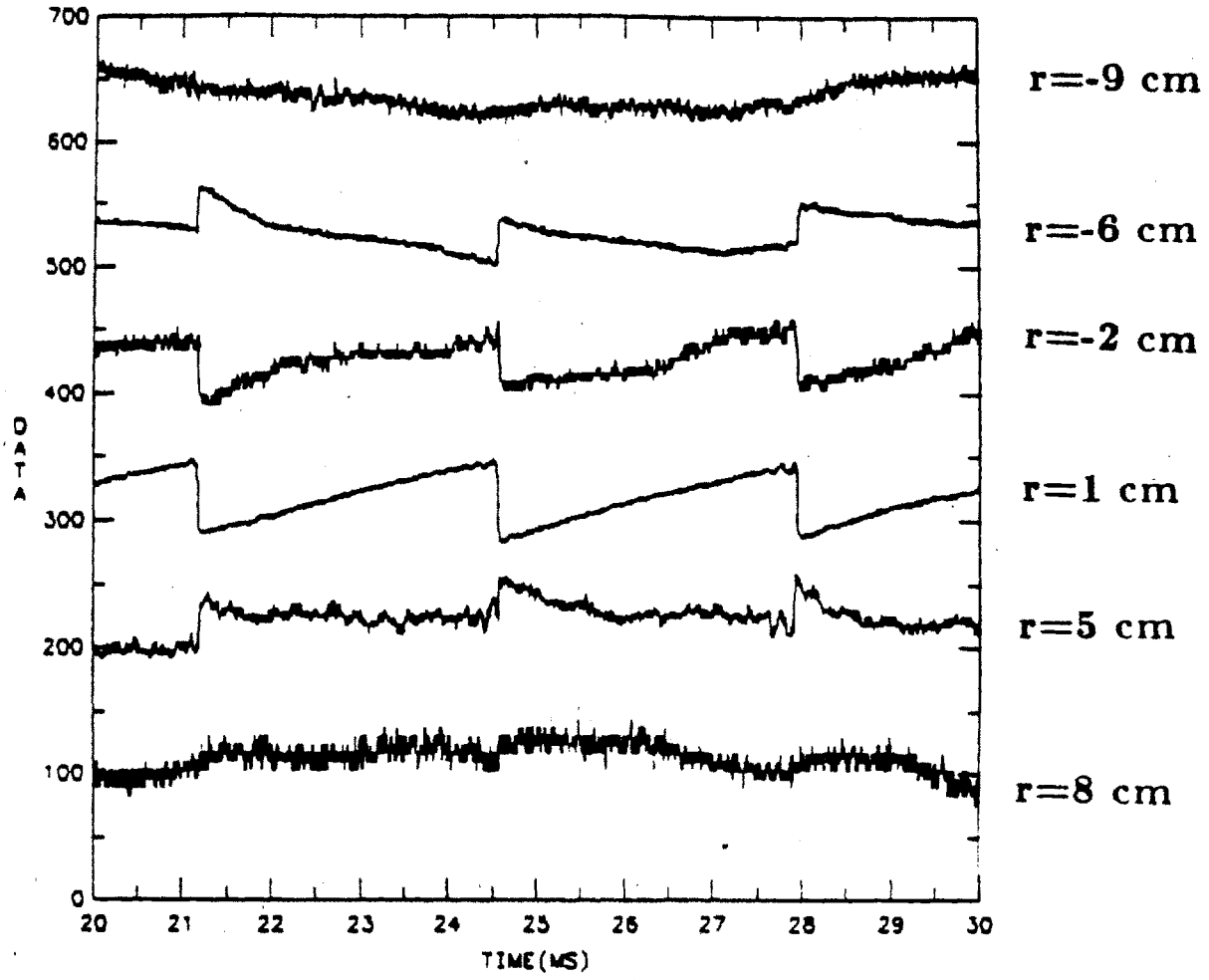

Figure 2.12 — Evolution of electron temperature as measured by ECE during sawtoothing.

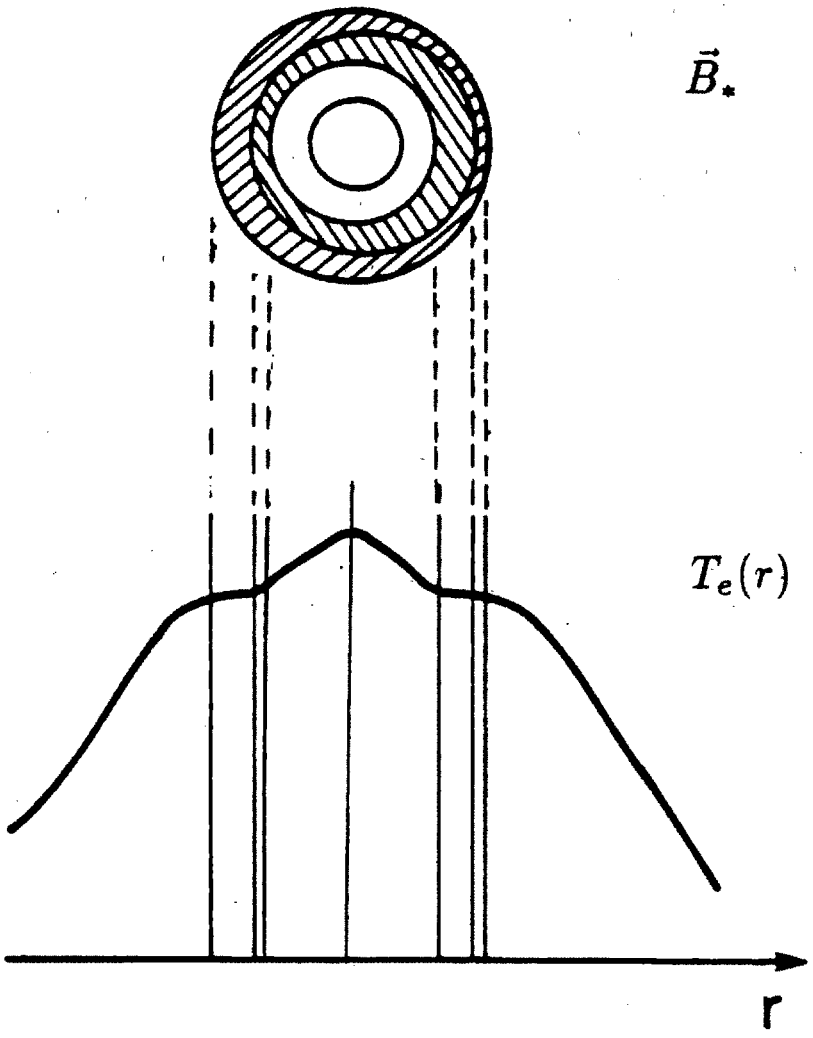

Figure 2.13 — Possible evolution of two $m = 1$ islands which will suppress their net $m = 1$ signature.

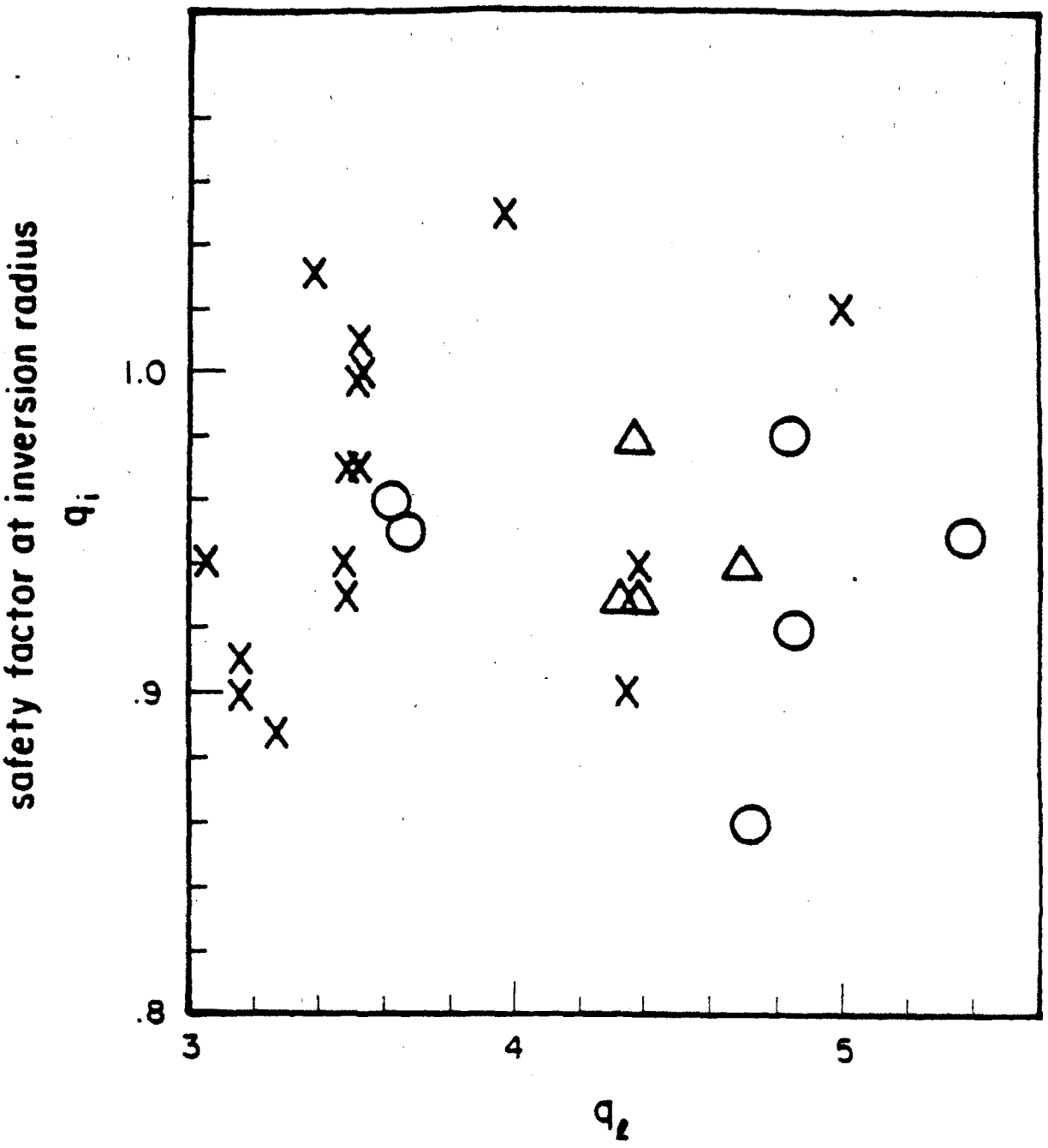

Figure 2.14 — Scaling of estimated value of q_i with q_l using eq. 2.4.2

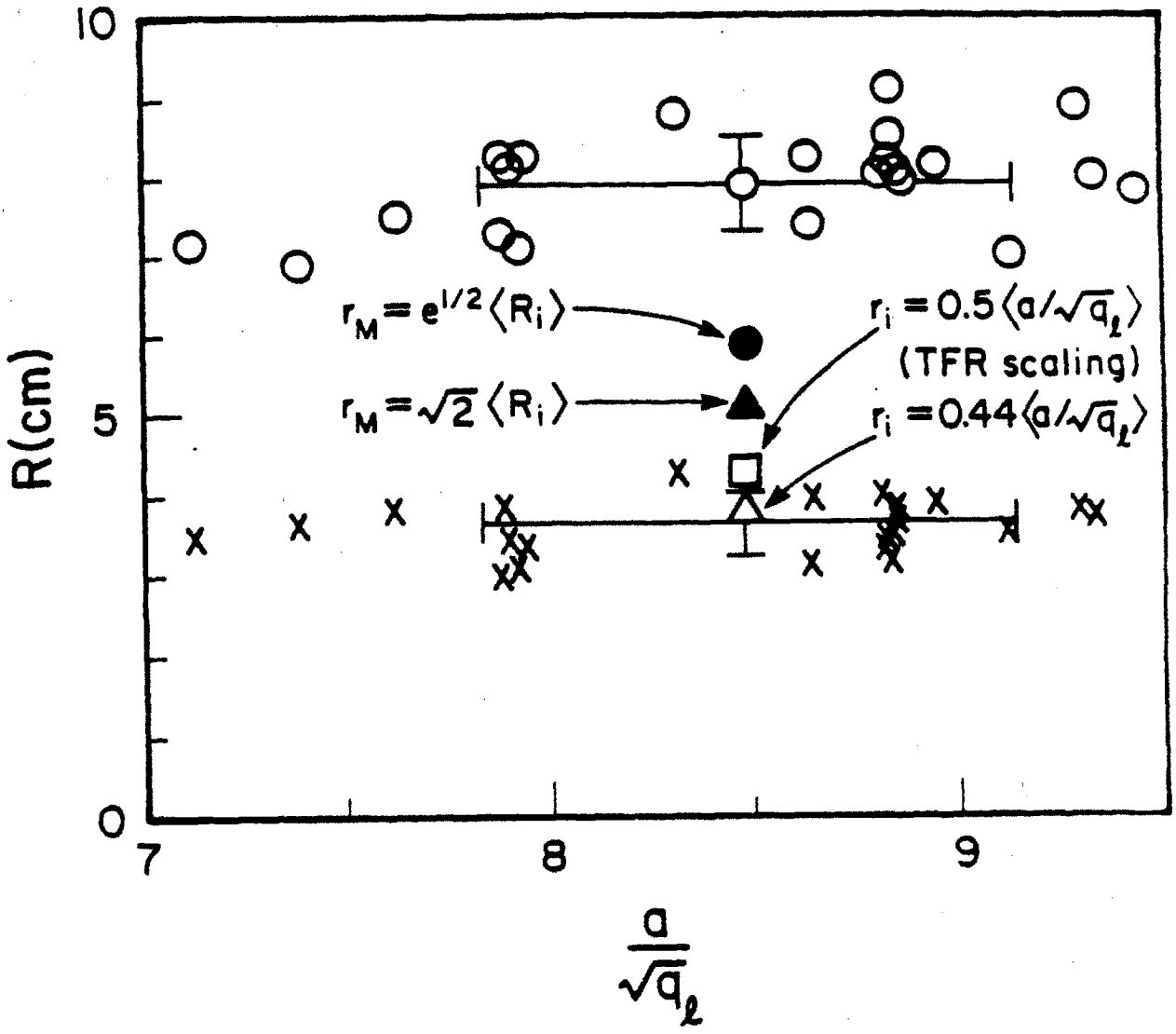

Figure 2.15 — Plot of measured inversion and energy mixing radii. Also shown are estimated values for both, using various scalings.

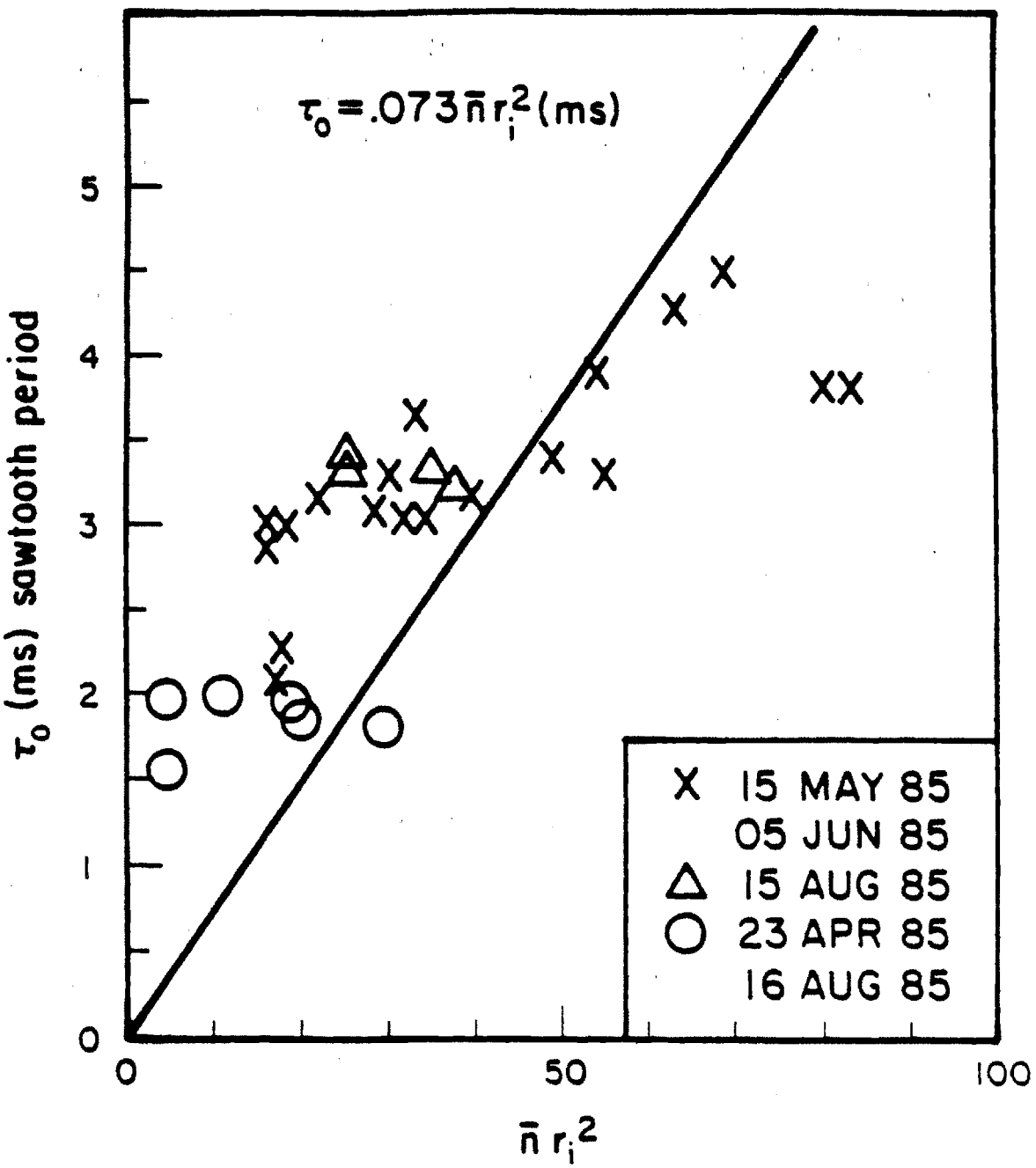

Figure 2.16 — Scaling of sawtooth period consistent with TFR form.

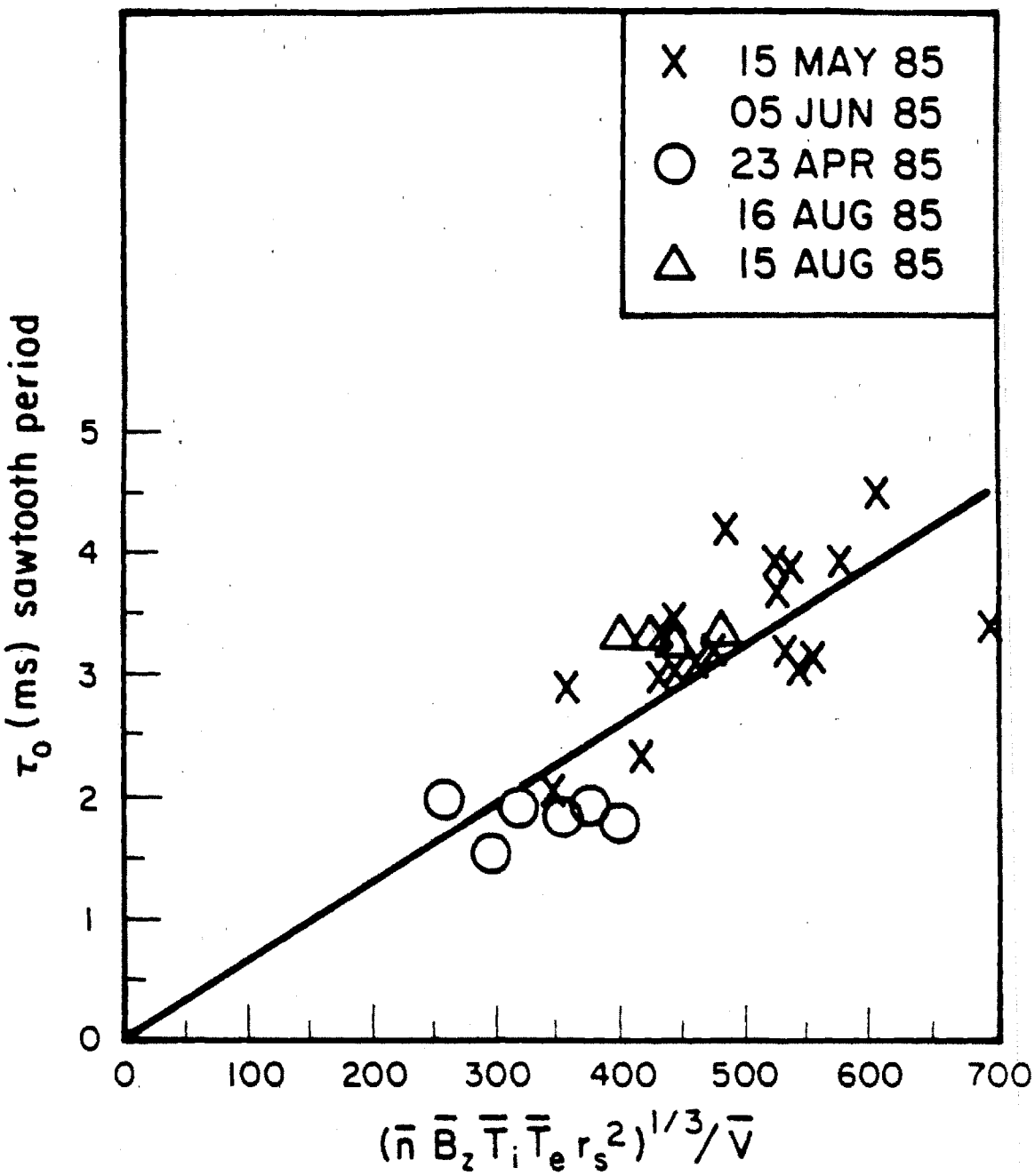

Figure 2.17 — Scaling of sawtooth period consistent with Jahns' form.

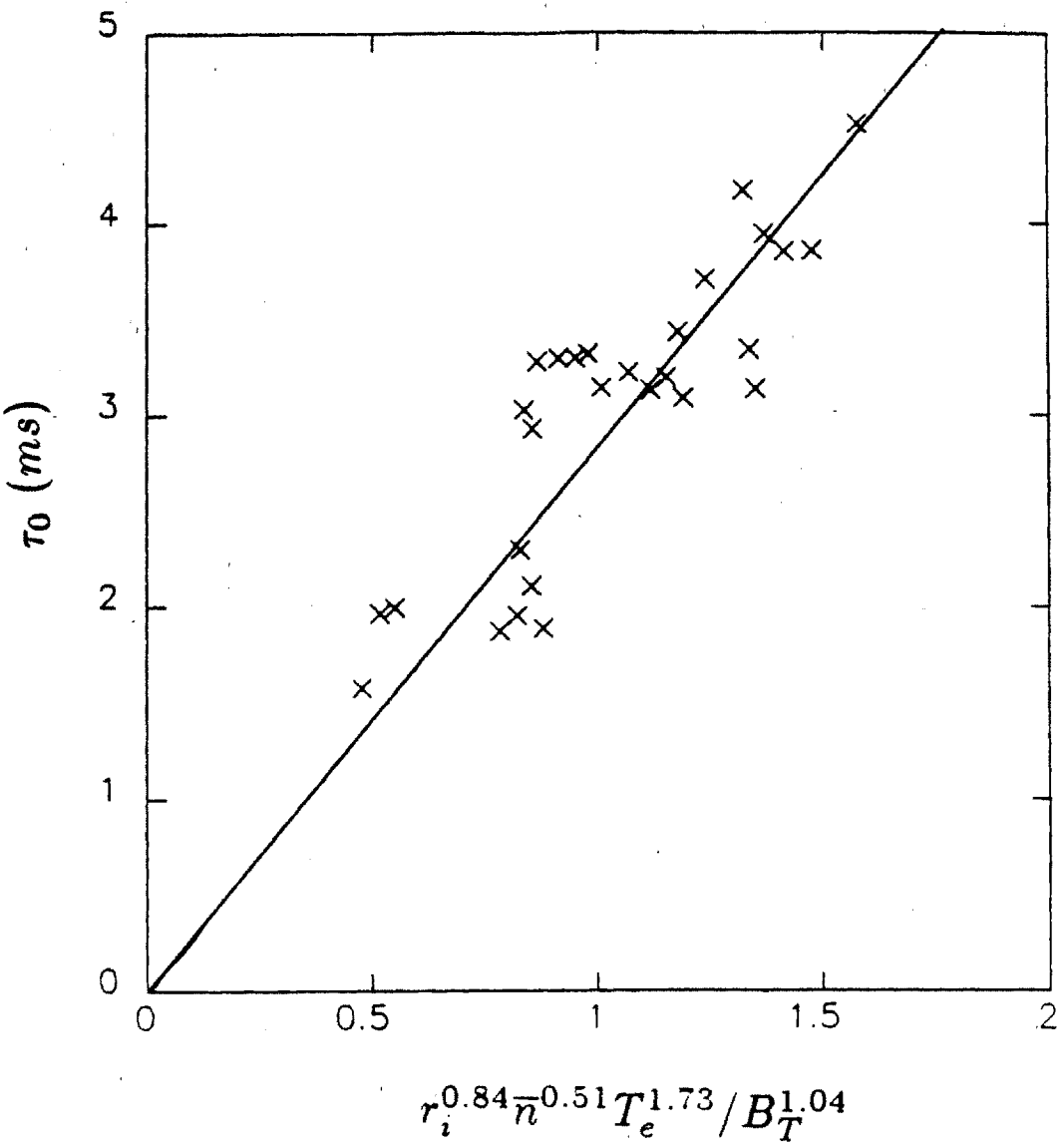

Figure 2.18 — Sawtooth period scaling consistent with McGuire-Robinson form.

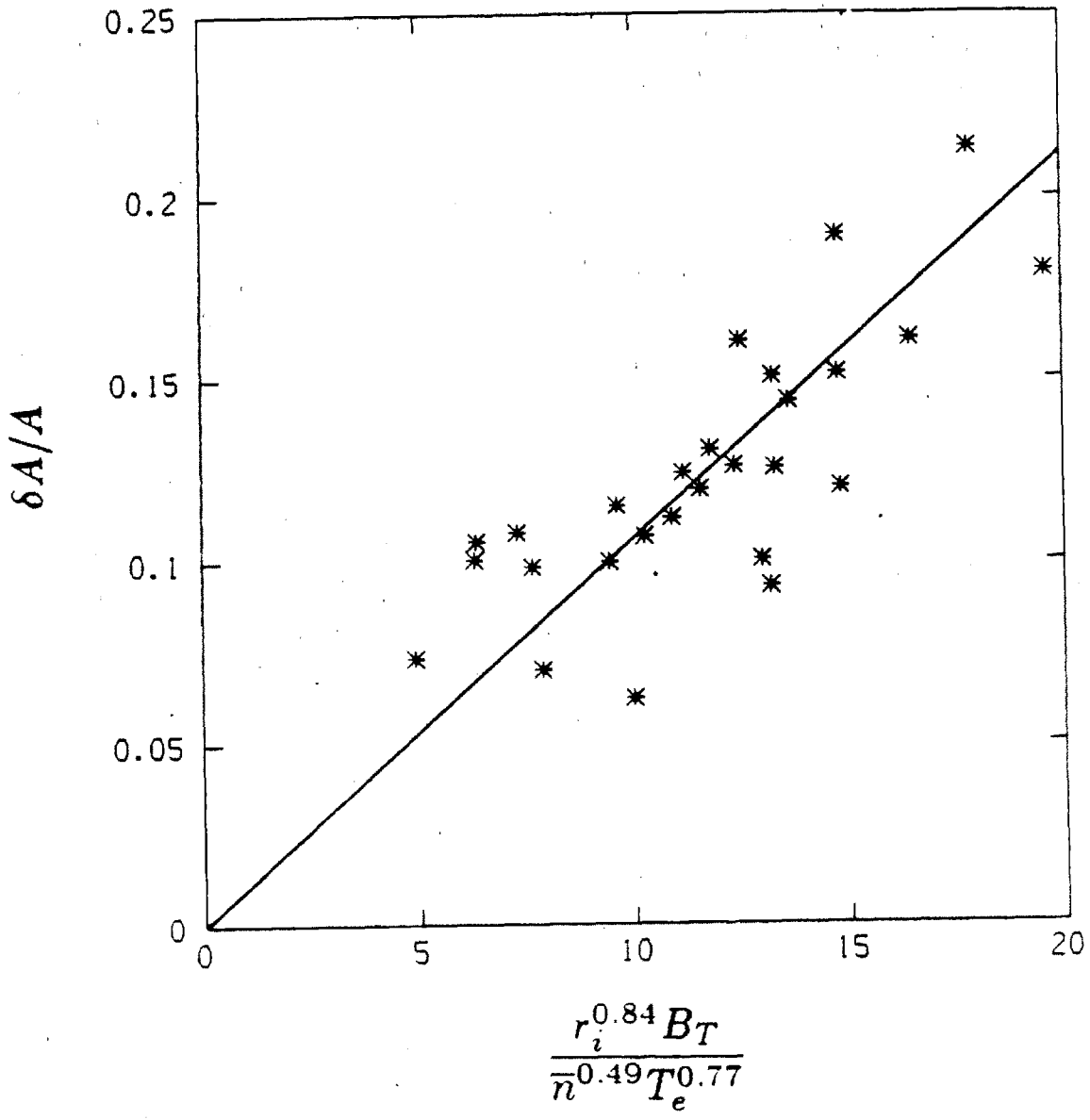

Figure 2.19 — Sawtooth amplitude scaling based on the McGuire-Robinson scaling for the sawtooth period.

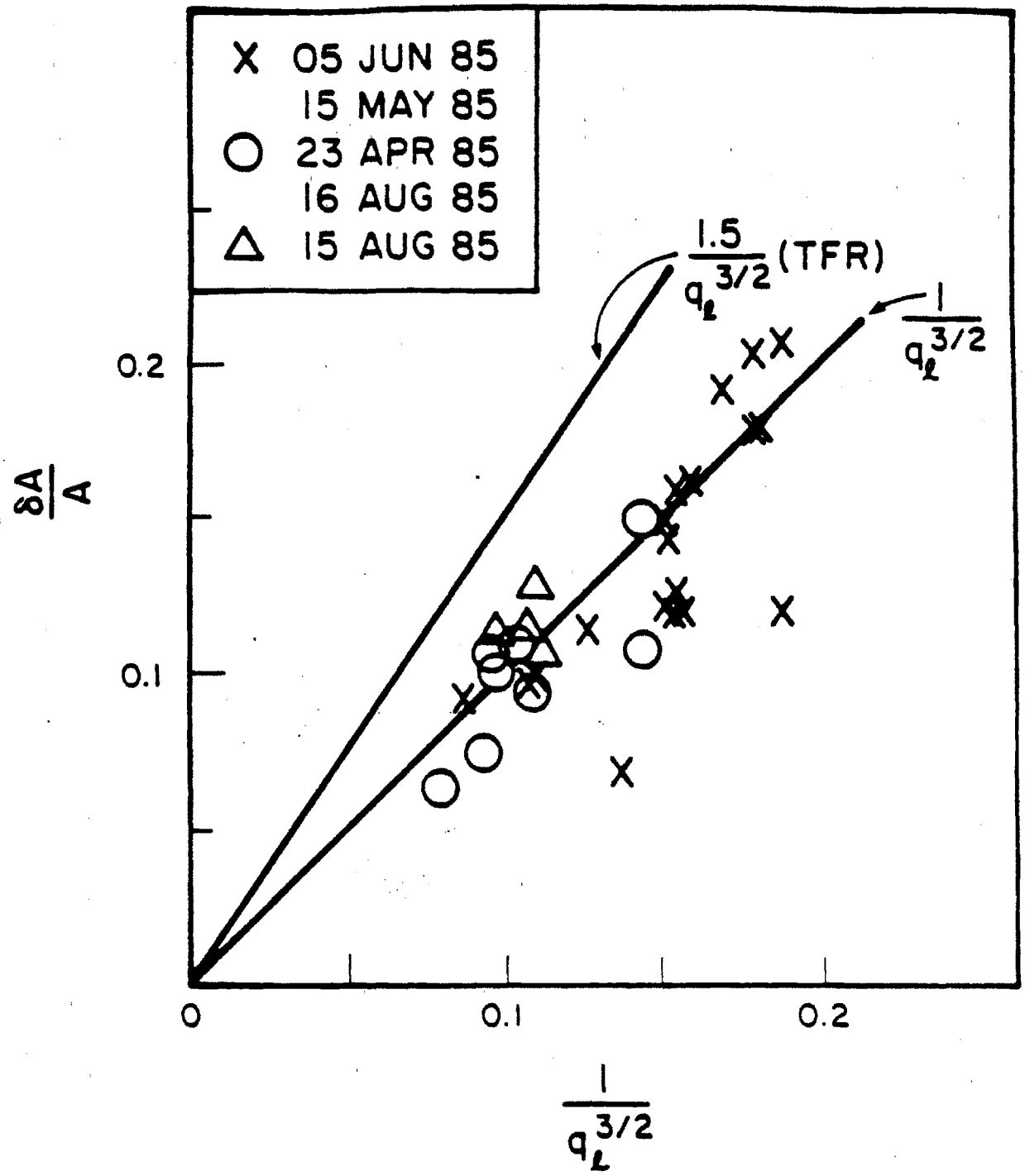

Figure 2.20 — Sawtooth amplitude scaling based on the TFR form.

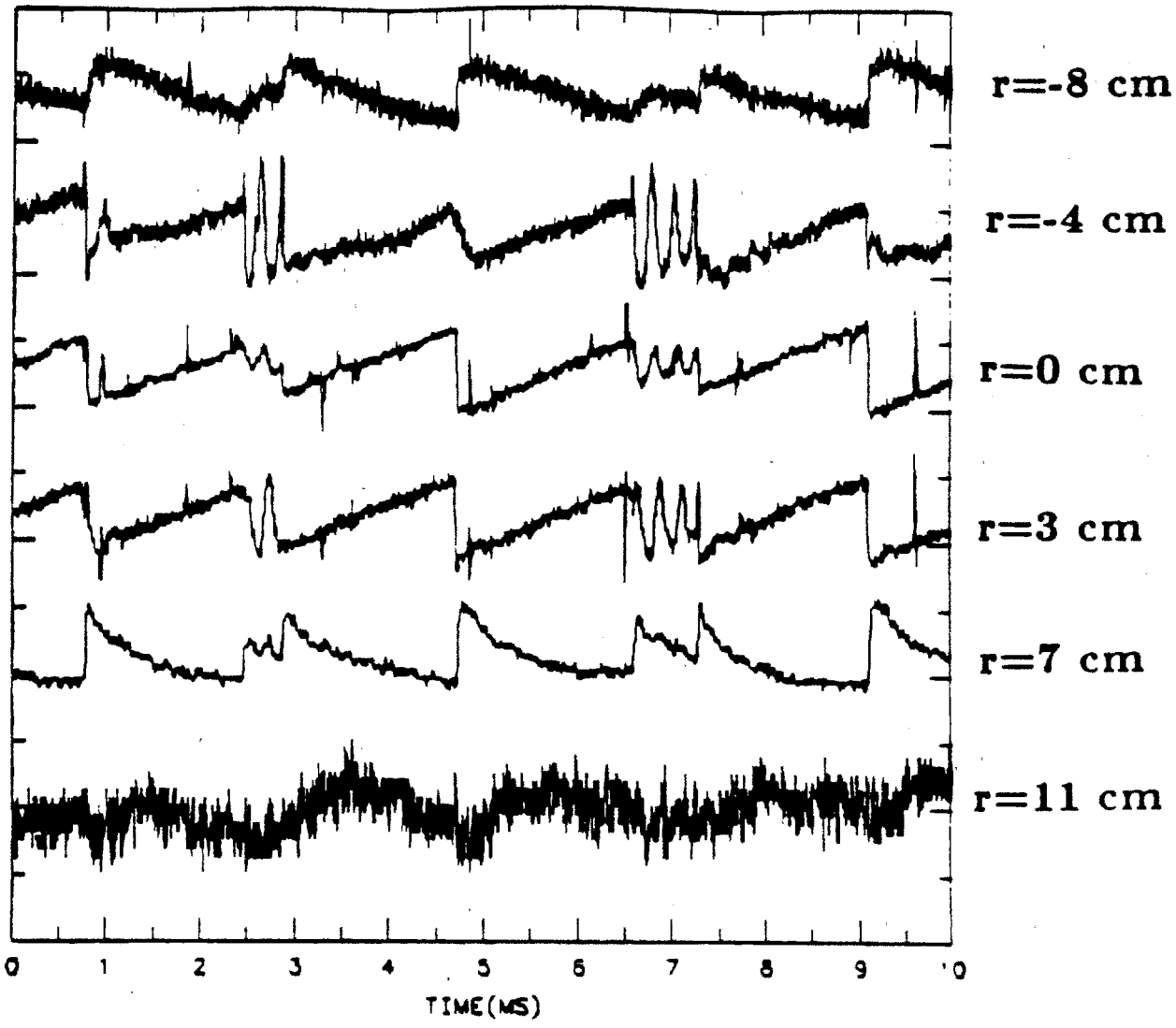

Figure 2.21 — Example of partial sawtooth as seen by the ECE.

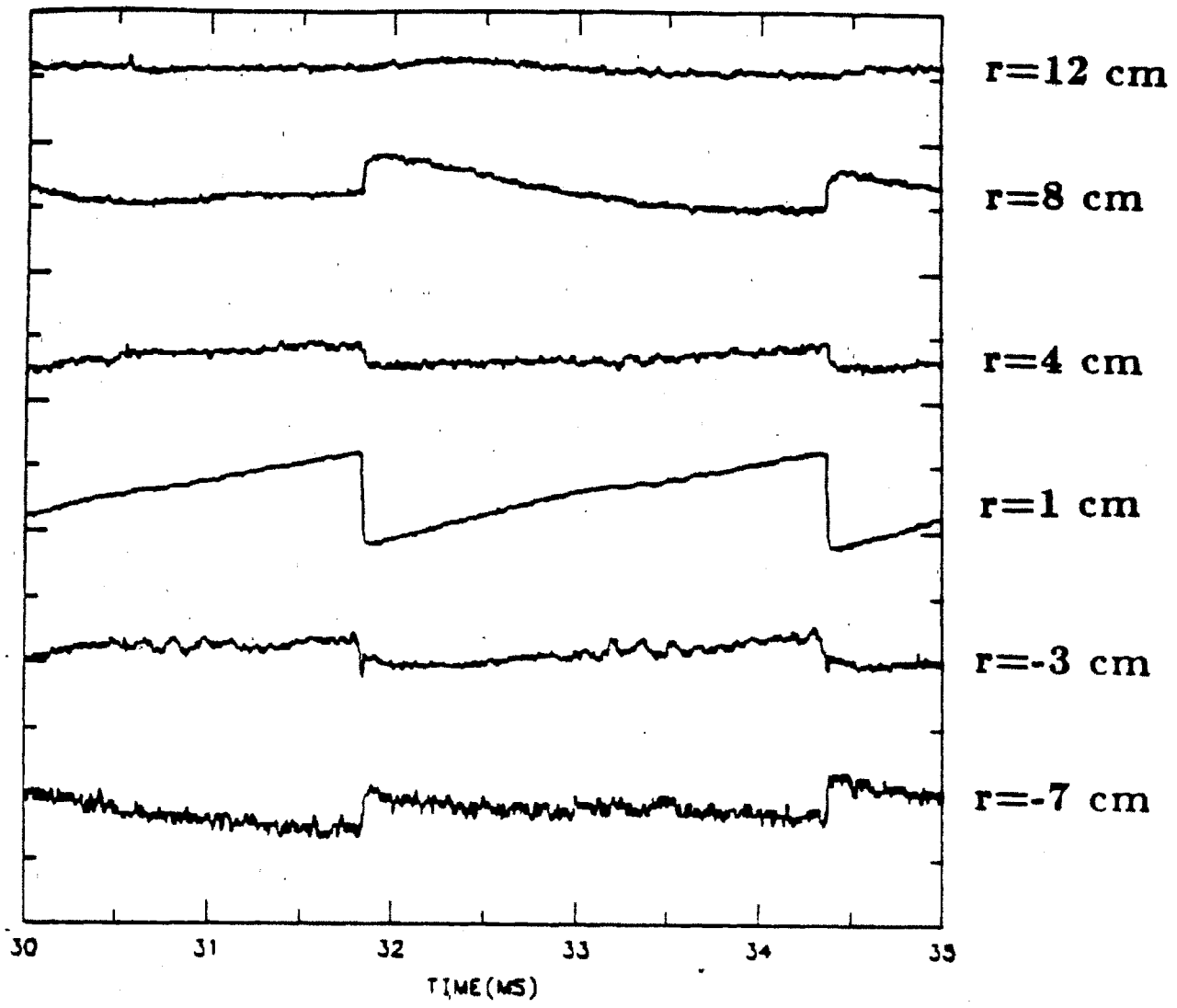

Figure 2.22 — Example of giant sawtooth as seen by the ECE.

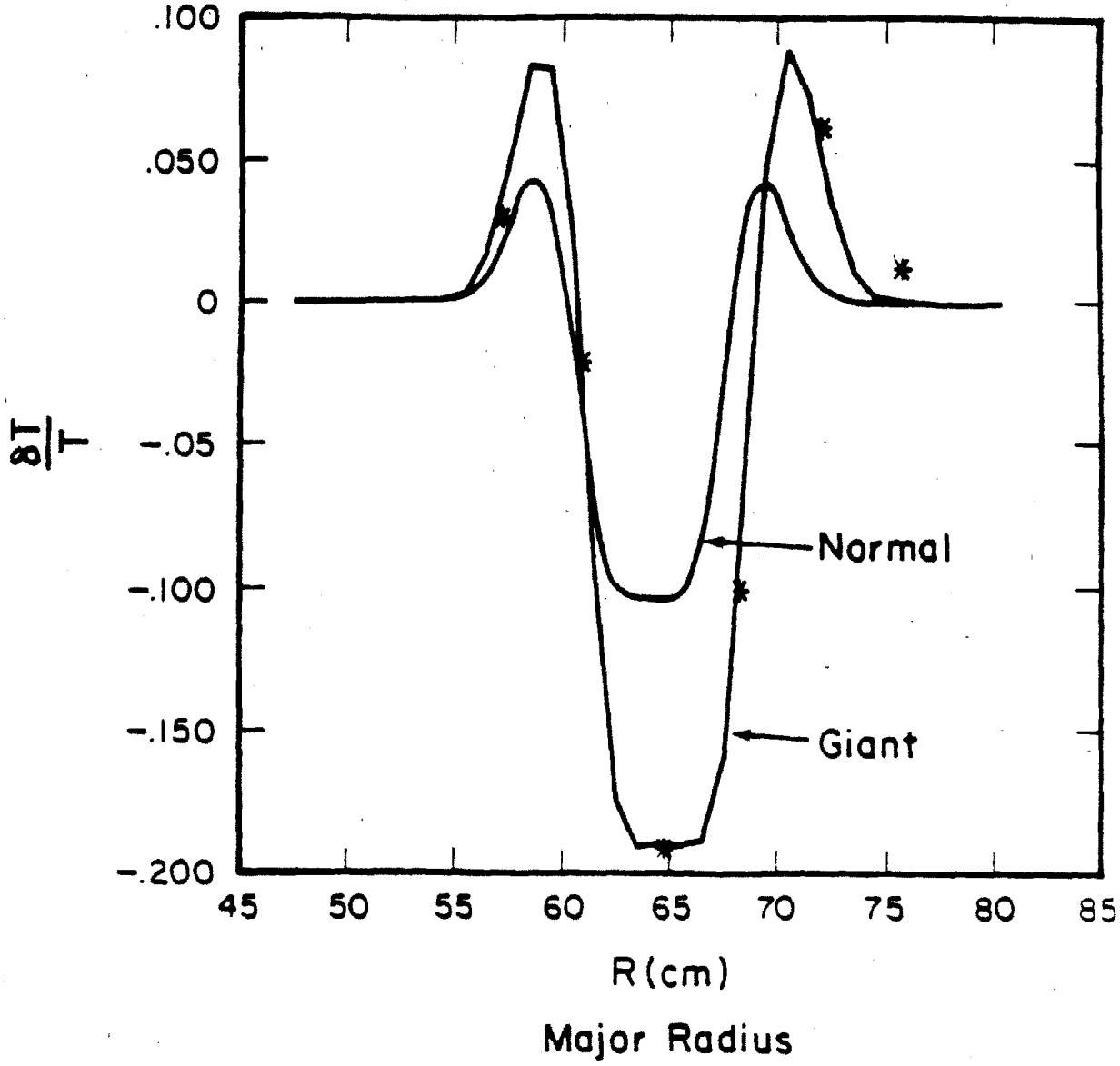

Figure 2.23 — Incremental temperature profile for the case of giant and normal sawteeth.

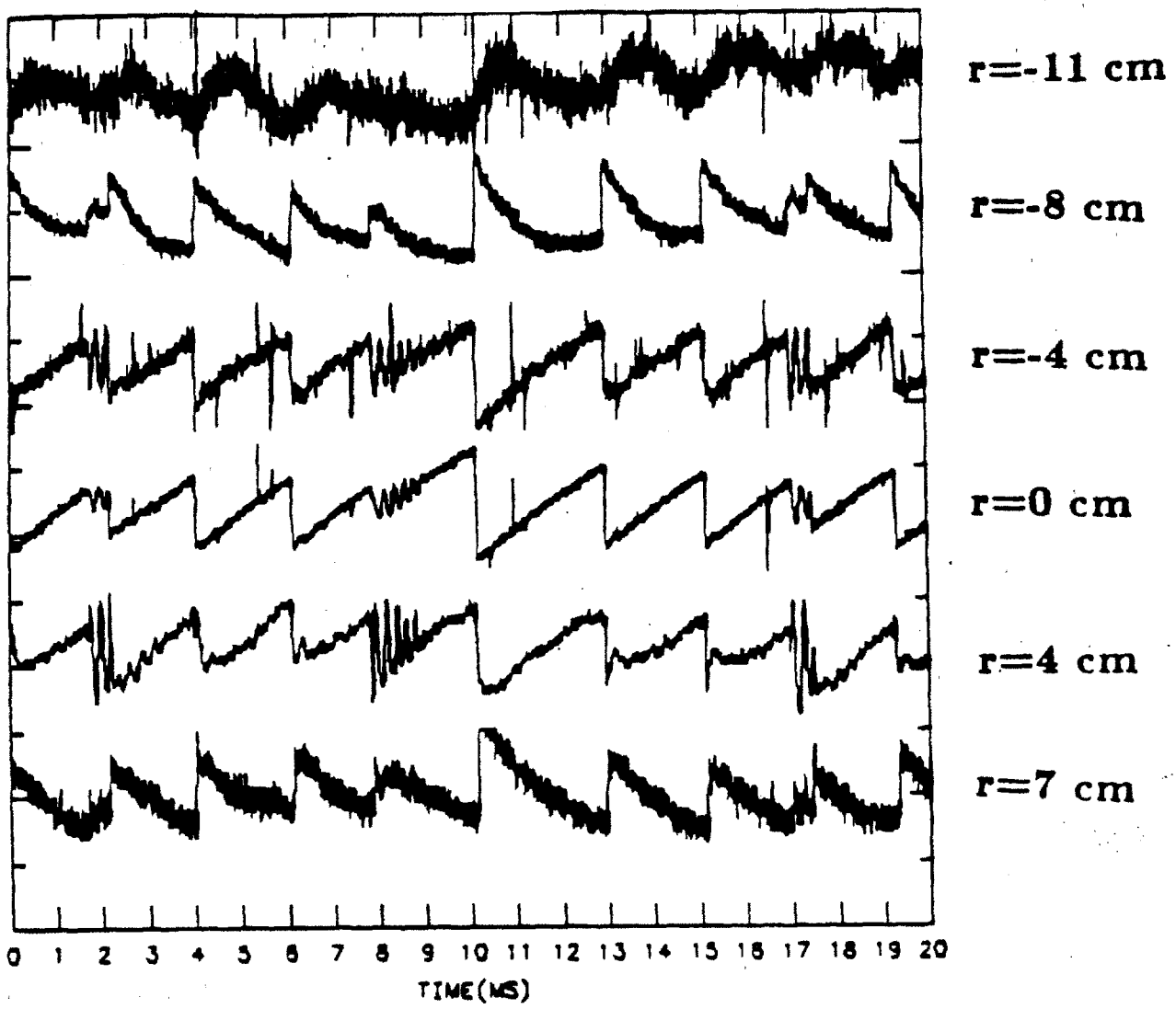

Figure 2.24 — Example of compound-giant sawtooth as seen by the ECE.

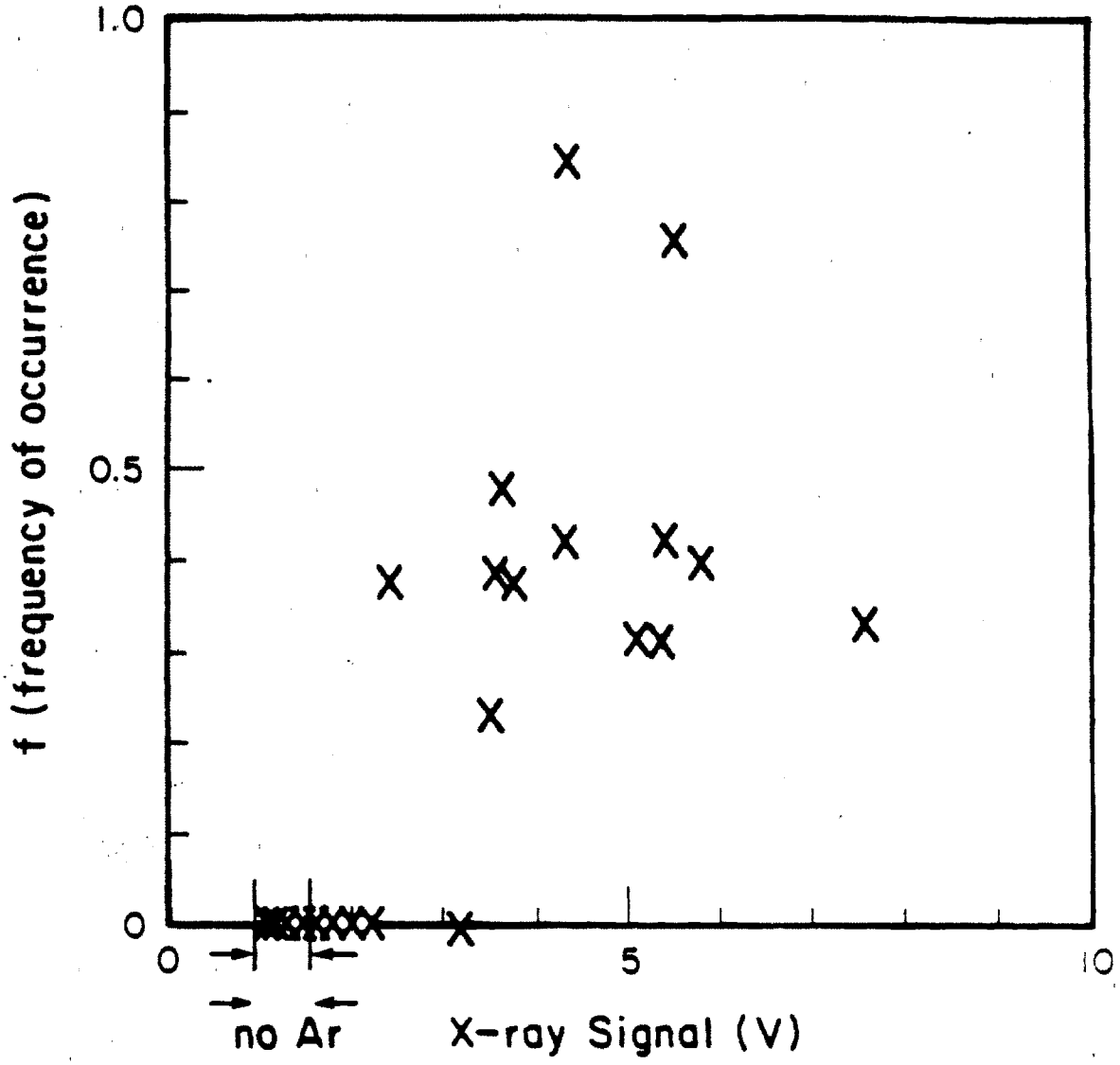

Figure 2.25 — Frequency on incidence of exotic sawteeth as a function of central soft Xray signal. For the case of constant shots, variations in the soft Xrays reflects changes in the impurities.

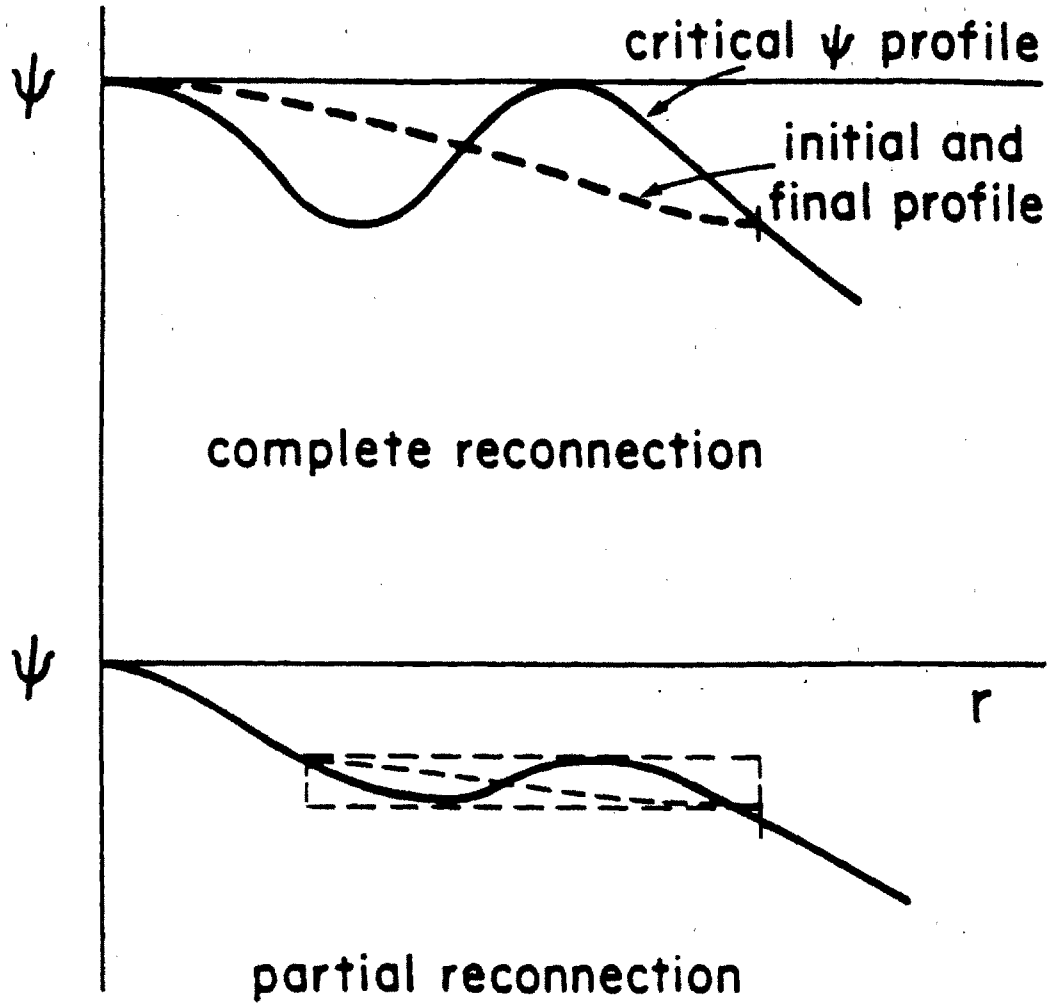

Figure 2.26 — Two resonant surface reconection. The top figure shows the case for complete reconnection and the bottom figure shows the case of partial reconnection.

III) Heat pulse propagation

3.1) Review of subject

The essence of heatpulse propagation studies, is to measure the thermal response of the medium (in this case the electrons in a plasma) to a known temperature perturbation. From this, in principle, we can infer the thermal conductivity of the electrons. In the case of a plasma, if the electron thermal response time is much shorter than any other energy transport time scale, the electron temperature will evolve in a decoupled manner dominated by the diffusive term in the transport equations; the evolution will then reflect the electron thermal conductivity. The sawtooth phenomenon in tokamaks provides a time resolved pulse, localized near the center of the plasma. By following the evolution of the electron temperature after each sawtooth crash, χ_e, the electron thermal diffusivity can be measured. Callen and Jahns [3.1] were the first to report results using this technique on the ORMAK tokamak. They pointed out that if one follows the perturbation in time and space, it evolves with the signature of a diffusive process. Fig 3.1 shows a set of traces from Alcator C using the FIR grating see sec. 1.6. If we follow the perturbation radially outward after each sawtooth crash, we find that the time of arrival of the peak increases with radius. This behaviour suggests the presence of a heatpulse that propagates out of the plasma. Callen and Jahns found that beyond the region immediately affected by the sawtooth, the delay (τ_p) increased as r^2.(Fig. 3.2 shows similar evolution for Alcator). Based on the radial scaling of the delay it was assumed that the evolution of the pulse was dominated by the diffusive component of the thermal transport equation. Ref[3.1] treated the sawtooth generated heatpulse as a perturbation on an otherwise quiescent background. Assuming a flat density and χ_e profile they arrived at a diffusion equation for the perturbation.

3.1.1)

$$\frac{3}{2}\frac{\partial \widetilde{T_e}}{\partial t} = \frac{\chi_e}{r}\frac{\partial}{\partial r} r \frac{\partial \widetilde{T_e}}{\partial r}$$

The diagnostic used in making the measurements was an array of soft X-ray detectors looking through various chords in the plasma. Since the signal generally

depends in a complicated way on the electron temperature and other plasma parameters, inversion to estimate the local electron temperature is not reliable. For this reason ref[3.1] and others have selected a parameter from the raw signal which is felt to be representative of the electron temperature evolution. Historically this has been the delay for the signal to peak at a given radial location after the sawtooth crash (τ_p).

In solving eq(3.1.1), it was assumed that 1)the disruptions were periodic in time(this is important to account in a simple way for the effects of multiple sawteeth.) 2)observations are made in the far field and 3) we can represent the perturbation as a monopole. They then arrived at a simple relation for τ_p .

3.1.2)

$$\tau_p = \frac{3}{8}\frac{r^2}{\chi_e}$$

By fitting the measured time delay they arrived at a self consistent χ_e. They found that the χ_e derived from this method (χ_e^{HP}) was about an order of magnitude higher than that calculated from power balance (χ_e^{Pb}) considerations. Jahns and Soler [3.2] later gave a more sophisticated description of the sawtooth crash (see the previous chapter for further details), which led to an improved estimate for the initial perturbation used in solving eq.(3.1.1). The sawtooth crash is assumed to flatten the temperature profile about the inversion radius out to a mixing radius (r_M) determined by energy conservation. Ref. [3.2] recognized that the initial perturbation can be so broad that a far field solution is not strictly valid anywhere in the plasma. For this reason they found a Green's function solution to eq. (3.1.1) assuming a flat n_e and χ_e. For the purpose of comparison with ref [3.1] they found a far field solution using a dipole perturbation as the lowest order profile, since the volume integrated energy of the perturbation is required to be zero. In this case the relation for τ_p is

$$\tau_p = \frac{r^2}{8\chi_e}$$

which gives a lower estimate for χ_e in the far field than [3.1]. For a given r_i(inversion radius) an initial perturbation of the form of fig. 3.3 was used in the Green's function

solution to eq. (3.1.1). The effective χ_e was adjusted so that the generated τ_p curve matched that measured. In this way much lower estimates of χ_e^{HP} were arrived at. A number of discharges were compared and the average $\chi_e^{HP}/\chi_e^{Pb} \sim 1.7$, however the error in the measurement was such that no clear correlation was found over the range of plasma parameters used.

Soler and Callen [3.3] later put the above formalism on a stronger mathematical foundation. They start with the general transport equation and assume that the electron temperature profile can be represented by two components

$$T_e(r,t) = T_0(r) + \tilde{T}(r,t)$$

It is assumed that just before the sawtooth disruption the electron temperature profile reaches a quiescent value $T_0(r)$. This assumption is strictly not correct, as we shall see in the last paragraph of this section and later in the chapter. $\tilde{T}(r,t)$ represents the response of the plasma to the sawtooth crash. By subtracting the equation for T_0 from that for $T_e(r,t)$ and neglecting time changing quantities in the non-diffusive terms, we arrive at an equation for $\widetilde{T_e}$

3.1.3)
$$\frac{3}{2}\frac{\partial}{\partial t}\tilde{T}_e = \frac{1}{r}\frac{\partial}{\partial r} r\chi_e \frac{\partial}{\partial r}\tilde{T}_e$$

which in the limit of $\chi_e(r) = const.$ becomes the same as eq. 3.1.1. They also discuss density profile effects as well as the possibility of measuring $\chi_e(r)$. The diffusion equation depends logarithmically on the denstiy and thus it is not expected to be important. They proposed a method by which one can measure the local diffusivity exactly. If we consider eq. 3.1.3 at the radial location where $\partial\tilde{T}_e/\partial r = 0$, the value of χ_e at this location is

$$\chi(r) = \frac{3}{2}\frac{\partial\tilde{T}/\partial t}{\partial^2\tilde{T}/\partial r^2}$$

This expression is local and thus allows determination of the χ_e profile. The drawback to this method is that very accurate knowledge of $\widetilde{T_e}$ is needed.

Bell [3.4] proposes a more general approach to solving the heatpulse problem. Eq. (3.1.1) is first expressed in flux coordinates. He then solves the diffusion equation numerically for a given initial $\widetilde{T_e}$(taken to be the same as in [3.2]),$n_e(\rho)$, $\chi_e(\rho)$. The resulting $\widetilde{T}$ evolution is then used to generate a line integrated soft X-ray profile. The τ_p profile calculated and measured are then matched by adjusting parameters in $\chi_e(r)$. Three profiles for χ_e are assumed $\chi_e(r) = const.$,$\chi_e(r) \sim 1/n$, $\chi_e(r) = M_\chi \chi_e^{Pb}$, χ_e^{Pb} is determined from power balance calculations. A study is made of the scaling of χ_e with injected beam power for constant background shots. χ_e^{HP} is found to be within a factor of two from χ_e^{Pb}. The error bars in the experiment are such that it is not possible to distinguish between the three different models for $\chi_e(r)$. A sensitivity analysis is done which finds the most important parameter to be ρ_{T_e}(the inversion radius of the temperature) . This can change the estimate of χ_e by as much as 50% . We will find later that this is a simple manifestation of sensitivity to the initial profile.

Fredrickson et. al.[3.5] have performed similar heatpulse measurements on TFTR using an array of soft X-ray diodes and some ECE. In their analysis they use several methods proposed in previous works, as well as expand on a Fourier analysis method proposed by Jahns[3.8]. A phase analysis is developed which is the equivalent of the pulse delay method previously used. An effective flat χ_e can be found from the measured phase of each harmonic at a given radial location.

$$\chi_e \simeq \frac{3p\omega}{4}\left(\frac{d\psi_p}{dr}\right)^{-2}$$

ω:sawtooth frequency

p:harmonic number

$\psi_p(r)$:phase of signal for harmonic p at radius r.

They find that for the case of TFTR all these methods give approximately the same results. The discrepancy between χ_e^{HP} and χ_e^{Pb} seems to increase with sawtooth number. For the case of the first sawtooth the ratio of $\chi_e^{HP}/\chi_e^{Pb} \sim 2$ increasing with subsequent sawteeth to a factor of 4-10 . They perform a sensitivity analysis to try to see if the discrepancy arises from the method of analysis or because

for some physical reason the transient heatpulse actually evolves with a larger χ_e than the bulk. To do this they solved eq.(3.1.3) numerically. To investigate the effects of initial conditions they tried a variety of different profiles, with a mixing radius of $r_M/a = 0.2$(a is the plasma minor radius). They find no significant change with τ_p in the region $0.7a^2 > r^2 > 2r_0^2$. Different profile shapes for the density and χ_e were also used, all arriving at essentially the same conclusion, that is, that the change that can be attributed in the estimate of χ_e^{HP} by inclusion of the above refinements is not sufficient to account for the discrepancy between χ_e^{HP} and χ_e^{Pb}. They conclude that the discrepancy must be attributed to a physical mechanism not observable in the smaller tokamaks where all previous measurements have been done. Three possible mechanisms discussed are 1) a time changing χ_e, $\widetilde{\chi}_e$ which need only be a factor of 2 larger than the χ_e^{Pb} since it comes into the equation for $\widetilde{T}_e$ as

$$\widetilde{\chi}_e \frac{\partial}{\partial r} T_{e0}$$

which can be large because of the zeroth order temperature gradient, 2) use of the so called marginal stability argument, in which any deviation from the canonical electron temperature profile, leads to the generation of a large χ_e to eliminate the perturbation. 3)χ_e is really the χ_e^{HP}, but for some unaccounted inward pinch, the power balance estimates yield a much lower value.

Heatpulse measurements have been done on JET[3.17] using a 12 channel grating polychromator. The heatpulse delay is found to vary linearly with radius. To estimate χ_e they solved eq. 3.1.3 numerically assuming $\chi_e \sim 1/n_e$. Comparisons were made of the simulated temperature traces using their method with those those arrived at using the method discussed in [3.3]. It is found that at various radii their numerical results agree much better with the measured time evolution than the result of [3.3]. A plasma parameter scan was done arriving at a scaling for $\chi_e(0)$ of the form

$$\chi_e(0) \sim \frac{\sqrt{I}}{n_e(0)}$$

The values of χ_e arrived at agreed with those of power balance to within a factor of two, however they were consistently higher.

Experiments have also been carried out on the T-10 tokamak [3.7]. Results of χ_e agree well with the power balance χ_e^{Pb}. They measure an effective mixing radius that is 2-2.5 times larger than that predicted by the Kadomtsev model. The electron thermal diffusivity is found from the formula

$$\chi_e \simeq \frac{(r - r_M)^2}{8\tau_p}$$

The agreement of χ_e^{HP} estimated this way with the χ_e^{Pb} was very good.

Heatpulse propagation measurements have also been done by perturbing the plasma with RF electron heating. Ejima and Okabashi [3.6] first used the method on the spheromak FM-1. Experiments on tokamaks have been done on T-10[3.7] and Doublet III [3.8]. On the T-10 machine the agreement between the power balance estimates and the heatpulse results are in reasonable agreement. In [3.8] the analysis was done by using a Fourier analysis technique, the heating pulse was applied periodically and the heatpulse detection was synchronized to this. The ratio χ_e^{HP}/χ_e^{Pb} varied between 2-4, although the data sample used was limited.

One of the aims of this thesis is to re-examine the assumptions made by previous workers and establish limits for their validity. The first comment to be made has to do with the assumption of the plasma relaxing to a quiescent profile. This requires for $\partial T_{e0}/\partial t = 0$ everywhere just before the sawtooth disruption, while this may be approximately true in the outer region of the plasma, it is rarely seen in the inner regions. For the case of Alcator C, $\partial T_e/\partial t$ at the center can be as large a 100 eV/ms just before the sawtooth crash. This means that the plasma is never in a quiescent equilibrium, but rather a dynamic equilibrium that is probably dependent on the sawtooth mechanism for stability. By using the profiles just before the sawtooth crash as the time independent profiles, we will be underestimating the 'true' quiescent profiles. This will lead to reduced values of $\widetilde{T_e}$ and overestimates of χ_e. In the work done previously, there is an implicit assumption that the heatpulse evolves in the far field where the initial profile effects are not critical. As we shall

show and as Bell[3.4] has pointed out, if the initial profile extends to a radius of order $a/2$, near field effects become important in the measurement. For the case of Alcator C the energy mixing radius extends $1.5-2$ times that predicted by the Kadomtsev model(see chapter II). As we shall see later, accounting for near field effects can reduce the estimated χ_e by a factor of $3-6$.

Firstly we will develop a single sawtooth model to examine the importance of the non-diffusive terms. The assumption that the electron heatpulse evolves in a decoupled manner is essential to this measurement for it allows estimation of χ_e without accurate knowledge of other plasma parameters. Secondly we will propose an analysis technique which does not require the quiescent assumption, but rather relies on measured profiles. We will allow χ_e to have a simple polynomial dependence on r, so as to make a measurement that reflects a local quantity rather than an average.

3.2) Transport equations

We begin development of our model by defining the transport equations. Since one of our objectives is to focus on the important physics under various plasma conditions, we must start from a general set of equations from which to derive the equations describing the electron heat pulse evolution. In solving the problem we shall assume cylindrical symmetry. The electron heat balance equation is from [3.20]

3.2.1)

$$\frac{3}{2}\frac{\partial}{\partial t}\left(n_e T_e\right) = \frac{1}{r}\frac{\partial}{\partial r} r\left(n_e \chi_e \frac{\partial}{\partial r} T_e\right) - \frac{1}{r}\frac{\partial}{\partial r} r\left(\frac{5}{2} T_e \Gamma_e\right) + Q_e$$

where

$$\Gamma_e \equiv n_e V_e - D_e \frac{\partial}{\partial r} n_e$$

$$Q_e = \eta_{\|} j_{\|}^2 - \nu_{ei} n_e (T_e - T_i) - Rad$$

V_e :radial electron convection velocity

D_e : particle diffusivity

$\eta_{\|} j_{\|}^2$:is the Ohmic heating term. In our model it is taken as the only source of input power.

$\nu_{ei} n_e (T_e - T_i)$:is the electron-ion energy exchange term

where $\nu_{ei} = 3m_e/(m_i \tau_e)$ see eq. 3.3.18 for expression.

Rad :is a loss term from radiation damping due to Bremsstrahlung and line radiation.

In our model we will assume a single species of ions. The impurities will be accounted for by the Zeff parameter.

Similarly for the ions the thermal transport equation is:

3.2.2)

$$\frac{3}{2}\frac{\partial}{\partial t}\left(n_i T_i\right) = \frac{1}{r}\frac{\partial}{\partial r} r\left(n_i \chi_i \frac{\partial}{\partial r} T_i\right) - \frac{1}{r}\frac{\partial}{\partial r} r\left(\frac{5}{2} T_i \Gamma_i\right) + Q_i$$

$$\Gamma_i \equiv n_i V_i - D_i \frac{\partial}{\partial r} n_i$$

$Q_i = \nu_{ei} n_e (T_e - T_i)$:energy gained by ions from the electrons. In our model this will be the only source of energy to the ions.

The electron density equation is:

3.2.3)

$$\frac{\partial n_e}{\partial t} + \nabla \cdot \vec{\Gamma}_e = S_e$$

S_e is a density source term generally taken to be significant only in a region near the edge of the plasma.

For the ions

3.2.4)

$$\frac{\partial n_i}{\partial t} + \nabla \cdot \vec{\Gamma}_i = S_i$$

S_i is the ion source term, again taken to be significant near the edge of the plasma.

The sawtooth is usually associated with breaking and rearrangement of magnetic field lines. This gives rise to a magnetic pulse which propagates out of the plasma and through joule heating can couple to the electron heat pulse. To describe this we use Maxwell's equations:

$$a) \nabla \times \vec{B} - \mu_0 \vec{J} = 0$$

$$b) \nabla \times \vec{E} + \frac{\partial \vec{B}}{\partial t} = 0$$

3.2.5)

$$c) \nabla \cdot \vec{B} = 0$$

$$d) \nabla \cdot \vec{E} = \frac{\rho}{\epsilon_0}$$

We can recast eqs 3.2.4 into a more useful current diffusion equation. Take the time derivative of eq. 3.2.5a

$$\mu_0 \frac{\partial \vec{J}}{\partial t} = \nabla \times \frac{\partial \vec{B}}{\partial t}$$

use Faraday's law eq. 3.2.5b to get

$$\mu_0 \frac{\partial \vec{J}}{\partial t} = -\nabla(\nabla \cdot \vec{E}) + \nabla^2 \vec{E}$$

if we assume quasi-neutrality ($\nabla \cdot \vec{E} \simeq 0$) giving

$$\mu_0 \frac{\partial \vec{J}}{\partial t} = \nabla^2 \vec{E}$$

using Ohm's law

$$\bar{\bar{\eta}} \cdot \vec{J} = \vec{E}$$

we get

3.2.6)

$$\frac{\partial \vec{J}}{\partial t} = \nabla \cdot \left(\nabla \frac{\bar{\bar{\eta}} \cdot \vec{J}}{\mu_0} \right)$$

3.3) Single sawtooth model

3.3.1) Outline of model

One of the goals of the electron heatpulse propagation diagnostic is to provide an independent measurement of the electron thermal diffusivity. To do this the evolution of the heatpulse must be dominated by the diffusion term in the electron heat balance equation. All previous workers [3.1-3.8], have taken this condition as a given. For the case of Alcator C under certain operating conditions(i.e. in high density plasmas), it is found that non-diffusive terms may have an important effect in the estimate of χ_e.

Our goal in this section will be to determine whether the diffusive character of eq 3.2.1 is dominant in Alcator. Recognizing the perturbative character of the sawtooth oscillation, we can develop a set of linearized equations from eqs 3.2.1-3.2.6 by expanding in $\delta y/y_0$ where δy is the magnitude of the sawtooth oscillation for a particular parameter and y_0 is its background profile. To simplify the analysis we will use a single sawtooth model, in which the plasma is taken to be quiescent before the sawtooth crash, and relaxes back to the same initial state. One of the assumptions here is that the presence of multiple sawteeth will not affect greatly the relative magnitude of the various terms. The quiescent profiles are taken to satisfy the time independent forms of eq. (3.2.1-3.2.6) in one dimension.

3.3.1)

$$0 = \frac{1}{r}\frac{\partial}{\partial r} r n_{e0} \chi_{e0} \frac{\partial}{\partial r} T_{e0} - \frac{1}{r}\frac{\partial}{\partial r} r \left(\frac{5}{2} T_{e0} \Gamma_{e0}\right) + Q_{e0}$$

3.3.2)

$$0 = \frac{1}{r}\frac{\partial}{\partial r} r n_{i0} \chi_{i0} \frac{\partial}{\partial r} T_{i0} - \frac{1}{r}\frac{\partial}{\partial r} r \left(\frac{5}{2} T_{i0} \Gamma_{i0}\right) + Q_{i0}$$

3.3.3)

$$0 = \frac{1}{r}\frac{\partial}{\partial r} r \Gamma_{e0} - S_{e0}$$

3.3.4)

$$0 = \frac{1}{r}\frac{\partial}{\partial r} r \Gamma_{i0} - S_{i0}$$

3.3.5)

$$0 = \frac{1}{r}\frac{\partial}{\partial r} r \frac{\partial}{\partial r}\left(\frac{\eta_0 j_0}{\mu_0}\right)$$

In the following analysis we will assume χ_e and χ_i have no time dependence. By requiring $n_e = n_i$ and $\Gamma_e = \Gamma_i$ the density evolution can be described by a single diffusion coefficient D and radial convection velocity V, both are also taken to be time independent. We can express all the time dependent quantities in terms of the quiescent profile plus a time dependent incremental piece.

$$T_e(r,t) = T_{e0}(r) + \widetilde{T_e}(r,t)$$

$$T_i(r,t) = T_{i0}(r) + \widetilde{T_i}(r,t)$$

$$n_e(r,t) = n_{e0}(r) + \widetilde{n_e}(r,t)$$

$$n_i(r,t) = n_{i0}(r) + \widetilde{n_i}(r,t)$$

$$\eta(r,t) = \eta_0(r) + \widetilde{\eta}(r,t)$$

$$j(r) = j_0(r) + \widetilde{j}(r,t)$$

$$\nu_{ei}(r) = \nu_{ei0}(r) + \widetilde{\nu_{ei}}(r,t)$$

$$Rad = Rad^0 + \widetilde{Rad}$$

By subtracting eq 3.3.1 from 3.2.1 we get

3.3.6)

$$\frac{3}{2}\left(n_{e0}\frac{\partial}{\partial t}\widetilde{T_e} + T_{e0}\frac{\partial}{\partial t}\widetilde{n}\right) = \frac{1}{r}\frac{\partial}{\partial r} r\left(n_{e0}\chi_{e0}\frac{\partial}{\partial r}\widetilde{T_e}\right) - \frac{1}{r}\frac{\partial}{\partial r} r\left(\frac{5}{2}\widetilde{T}_e\Gamma_{e0}\right)$$

$$+\frac{1}{r}\frac{\partial}{\partial r} r\left(\widetilde{n}_e\chi_{e0}\frac{\partial}{\partial r}T_{e0}\right) - \frac{1}{r}\frac{\partial}{\partial r} r\left(\frac{5}{2}\widetilde{n}V_eT_{e0}\right) + \frac{1}{r}\frac{\partial}{\partial r} r\left(\frac{5}{2}T_{e0}D\frac{\partial}{\partial r}\widetilde{n}_e\right)$$

$$-\nu_{ei0}n_{e0}\left(\widetilde{T_e} - \widetilde{T_i}\right) - \nu_{ei0}\widetilde{n_e}\left(T_{e0} - T_{i0}\right) - \widetilde{\nu}_{ei}n_{e0}\left(T_{e0} - T_{i0}\right)$$

$$+2\eta_0 j_0\widetilde{j} + \widetilde{\eta}j_0^2 - \widetilde{Rad}$$

similarly for the ions we get

3.3.7)

$$\frac{3}{2}\Big(n_{i0}\frac{\partial}{\partial t}\widetilde{T}_i + T_{i0}\frac{\partial}{\partial t}\widetilde{n}\Big) = \frac{1}{r}\frac{\partial}{\partial r}r\Big(n_{i0}\chi_{i0}\frac{\partial}{\partial r}\widetilde{T}_i\Big) - \frac{1}{r}\frac{\partial}{\partial r}r\Big(\frac{5}{2}\widetilde{T}_i\Gamma_{i0}\Big)$$

$$+\frac{1}{r}\frac{\partial}{\partial r}r\Big(\widetilde{n}_i\chi_{i0}\frac{\partial}{\partial r}T_{i0}\Big) - \frac{1}{r}\frac{\partial}{\partial r}r\Big(\frac{5}{2}\widetilde{n}_i V T_{i0}\Big) + \frac{1}{r}\frac{\partial}{\partial r}r\Big(\frac{5}{2}T_{i0}D\frac{\partial}{\partial r}\widetilde{n}_i\Big)$$

$$+\nu_{ei0}n_{e0}\Big(\widetilde{T_e} - \widetilde{T_i}\Big) + \nu_{ei0}\widetilde{n_e}\Big(T_{e0} - T_{i0}\Big) + \widetilde{\nu}_{ei}n_{e0}\Big(T_{e0} - T_{i0}\Big)$$

To get the electron density equation we subtract eq 3.3.3 from 3.2.3

3.3.8)

$$\frac{\partial}{\partial t}\widetilde{n_e} = \frac{1}{r}\frac{\partial}{\partial r}r\Big(D\frac{\partial}{\partial r}\widetilde{n_e} - V\widetilde{n_e}\Big)$$

for the ions

3.3.9)

$$\frac{\partial}{\partial t}\widetilde{n_i} = \frac{1}{r}\frac{\partial}{\partial r}r\Big(D\frac{\partial}{\partial r}\widetilde{n_i} - V\widetilde{n_i}\Big)$$

The equation that describes the evolution of the current pulse (magnetic pulse) becomes from eq 3.2.6 and 3.3.5

3.3.10)

$$\frac{\partial}{\partial t}\widetilde{j} = \frac{1}{r}\frac{\partial}{\partial r}r\frac{\partial}{\partial r}\Big(\frac{\widetilde{\eta}j_0}{\mu_0} + \frac{\eta_0\widetilde{j}}{\mu_0}\Big)$$

The profile shape of χ_e should not affect the relative importance of each term, so we will take the simplest case of $\chi_e = const.$ The background electron temperature and density profiles will be taken as input to the model, all other profiles will be calculated to be consistent with these. The initial incremental profile for the electron temperature has the following form

$$\widetilde{T_e}(y,0) = \begin{cases} T_M cos(\frac{\pi}{2}y^2) & y \le 1 \\ 0.63T_M(y-1)e^{-3(y-1)^2} & y > 1 \end{cases}$$

$y \equiv r/r_i$

r_i :is the inversion radius

This form has been found to fit consistently with the experimental initial profiles(fig 3.4). T_M is chosen so as to flatten the central value of the electron temperature to that at the inversion radius. When the initial perturbation for another parameter is needed it will be taken to be proportional to the electron temperature perturbation unless stated. We can non-dimensionalize the equations in terms of χ_e and (a), the scale length of the problem ,in this case taken to be the limiter radius. Then the distance becomes $x \equiv r/a$ and the time $\tau \equiv (2\chi_e t)/(3a^2)$. Quantities with a hat ($\hat{}$) are normalized to the central electron temperature.

The task of determining the limits in which the diffusive term is dominant in eq. 3.3.6 is complicated by the large number of free parameters present in the problem. The way we will proceed with the anaysis, is to include one non-diffusive effect in eq. 3.3.6 and solve it numerically along with any auxiliary equations. In the next subsections we shall consider the effects of the non-diffusive terms for a parameter range consistent with Alcator. From this study we can focus on the dominant physical effects which limit the validity of the purely diffusive model.

To avoid any boundary effect problems the numerical solution is extended to $r/a = 3.0$. The boundary conditions are $\partial\tilde{T}(0)/\partial x = 0.0$, $\tilde{T}(3) = 0.0$. The inital profiles are set to zero beyond $r/a = 1.0$. Then an effective time compression and amplitude scaling factor will be found for the decoupled solution to give a best fit at a fixed radius. The time compression is equal to the ratio of the thermal diffusivities χ_{eff}/χ_e where χ_e is the 'real' χ and χ_{eff} is the χ we get in trying to fit a decoupled solution to a coupled problem.

3.3.2 Decoupled equation

The equation to which all others in this section will be compared is the decoupled diffusion equation, which from eq. 3.3.6 becomes

$$\frac{3}{2} n_{e0} \frac{\partial \tilde{T}_e}{\partial t} = \frac{\chi_{e0}}{r} \frac{\partial}{\partial r} r \left(n_{e0} \frac{\partial \tilde{T}_e}{\partial r} \right)$$

This equation can then be non-dimensionalized as described above

3.3.11)

$$\frac{\partial \tilde{T}_e}{\partial \tau} = \frac{1}{n}\frac{1}{x}\frac{\partial}{\partial x}(xn(x)\frac{\partial \tilde{T}_e}{\partial x})$$

The effect of changing the thermal conductivity is simply a rescaling of the time coordinate. As a check on the code we have assumed a flat density profile and initial conditions as described above and solved the equation foward in time. With the same initial conditions, the Green's function integral, as found in [3.2], was evaluated and the two solutions match.

3.3.3) Transport coefficients

In this section we will discuss the form of the transport coefficients used in solving the equations. Even though we are solving a dimensionless problem, we must assume models for the plasma parameters so that we can estimate the values of the dimensionless parameters appropriate for Alcator. The global energy confinement time will be consistent with neo-Alcator scaling[3.9]

3.3.12)

$$\tau_E \sim 115 R^{2.3}(m) a^{0.8}(m) \bar{n}(10^{14} cm^{-3}) \qquad \text{ms}$$

In all the cases of interest here $R = 0.64m$, $a = 0.165m$ giving

3.3.13)

$$\tau_E = 9.8\bar{n}(10^{14}) \qquad \text{ms}$$

An effective diffusivity can be found from the simple relation

3.3.14)

$$\chi_e = \frac{3}{8}\frac{a^2}{\tau_E}$$

which assumes a parabolic temperature profile and uniform density and power deposition. Giving

3.3.15)

$$\chi_e \simeq \frac{10}{\bar{n}(10^{14})} \qquad cm^2 ms^{-1}$$

Over the range of interest $1 < \bar{n}(10^{14}) < 5$, the diffusivity can vary from $10 > \chi_e > 2$.

The ion thermal diffusivity will be assumed to have a form similar to the electrons

3.3.16)

$$\chi_i(r) = const.$$

The parameter $\beta \sim \chi_i/\chi_e$ will be a free parameter in our solution. For the purposes of estimating the range of β, we can estimate χ_0 as being the value of 4 times the Chang-Hinton result [3.10] evaluated at the half minor radius. The largest values of χ_0 for Alcator are expected at the highest densities, for $\overline{n} \sim 5 \times 10^{14} cm^{-3}, \chi_0 = 4\chi_{CH}(a/2) \sim 4cm^2/ms, \chi_e \sim 2, so \beta_{max} \sim 2.$

The particle diffusivity will be taken to be consistent that with measured for the impurities. In Alcator impurity transport has been studied by injecting a trace impurity into the plasma and following its evolution[3.18]. There is evidence which suggests that the impurity D is similar to that for the background. The maximum value of D is $D \sim 3cm^2/ms$. The parameter to study particle transport will be $\gamma \equiv D/\chi_e$, which for the range of Alcator parameters is $0 < \gamma < 1.5$.

For the particle convection we will again assume a number that is consistent with impurity convection. The form will be

3.3.17)

$$v(r) = v_0 \frac{r}{a} = v_0 x \qquad x \leq 1$$

$$v(r) = v_0 \qquad x > 1$$

In impurity transport measurements the parameter $S \equiv (av_0)/(2D)$ has been found to be between 0-2[3.18]. With a $D \sim 2\ cm^2/ms$ this gives a convection velocity of $v_0 \sim .5cm/ms$.

In the following analysis we shall neglect particle trapping effects since at the lowest densities the ratio of the collision time/bounce time (ν_*) at the half radius ~ 2. Although this is somewhat close to the transition region for the purpose of this model the effect on the transport parameters can be neglected. For the electron-ion energy equilibration frequency we will assume the classical value.

3.3.18)

$$\nu_{ei} = 7.3 \times 10^3 \frac{Z}{\mu} \frac{n(10^{14})}{(T_e(ev))^{1.5}} \qquad ms^{-1} \quad for \quad x \leq 1$$

$$\nu_{ei} = 0 \qquad x > 1$$

At the higher densities we see that the electron-ion equilibration time $1/\nu_{ei}$ can be faster than the time for the heatpulse to escape $\overline{n} \sim 5 \times 10^{14} cm^{-3}, T_e(a/2) \sim 600eV, \mu = 1, Z = 1 \Rightarrow 1/\nu_{ei} = 0.22ms$. The heatpulse delay at the half radius $\tau_p \sim 0.5 - 0.75ms$. From this simple argument we expect electron-ion coupling effects to play an important role in the evolution of the heatpulse at higher densities. The relevant dimensionless collissionality parameter is

$$\nu \equiv \frac{a^2 \nu_{ei}}{\chi_e}$$

which scales as the ratio of the collision frequency to the confinement time. For typical Alcator parameters this will range between $0 < \nu < 140$.

The model of radiation loss will include two mechanisms. From the background plasma we get bremsstrahlung radiation and from a single impurity(Carbon in our case) bremsstrahlung plus line radiation. For the background

3.3.19)

$$P_B = 1.05 \times 10^{-16} Z_{bd} n_e^2 \sqrt{T_e(ev)} \quad eVms^{-1}cm^{-3} \quad x \leq 1$$

$$P_B = 0 \qquad for x > 1$$

To model the impurity radiation, we use a coronal equilibrium model as outlined by Post[3.11].

3.3.20)

$$P_z = 6.24 \times 10^8 n_e n_c \prod_{i=0}^{i=5} 10^{A_i (log_{10}2)^i (lnT(keV))^i} \quad eVms^{-1}cm^{-3} for x \leq 1$$

$$P_z = 0 \qquad for x > 1$$

n_c:carbon concentration

The coefficients A_i for carbon in the range $200ev < T_e < 2000ev$ are

$$A_0 = -21.2 \qquad A_1 = -.37$$
$$A_2 = 0.73 \qquad A_3 = -.19$$
$$A_4 = -.13 \qquad A_5 = -1.5$$

To find the parameter range for maximum radiation, let us consider a low density case with $\overline{n} \sim 10^{14} cm^{-3}, Z_{eff} \sim 1.5, T_e \sim 1keV$, and a high density case $\overline{n} \sim 5 \times 10^{14}, Z_{eff} \sim 1.2, T_e \sim 0.7keV$. If the only impurity in the plasma is assumed to be carbon, then the impurity density can be found from

$$n_c = \frac{(Z_{eff} - 1)}{Z_c^2 - Z_c} n_e$$

For the low density case $n_c = 1.7 \times 10^{12} cm^{-3}$, the total radiation is $P_T = P_z + P_B = 6.3 \times 10^{14} eV m s^{-1} cm^{-3}$. For the high density case $n_c = 3.3 \times 10^{12} cm^{-3}$, the total radiated power is $P_T = 8.6 \times 10^{15} eV m s^{-1} cm^{-3}$. From the above result we can expect the largest effects of radiation to take place at the higher densities.

From the relation above for P_B and P_z we can arrive at the form for the incremental term of the radiation ($\widetilde{Rad}$ in eq. 3.3.6)

3.3.21)

$$\widetilde{Rad} = \{2P_B + P_z\}\frac{\tilde{n}}{n} + \{\frac{1}{2}P_B + 2.3P_z \sum_i i A_i (log_{10}2)^i (lnT(keV))^{i-1}\}\frac{\tilde{T}}{T}$$

We define two dimensionless parameters for the radiation

$$\rho_1(r) = \frac{a^2}{\chi_e T_e(0) n}\Big(2P_B + P_z\Big)$$

$$\rho_2(r) = \frac{a^2}{\chi_e T_e(0) n}\Big\{\frac{1}{2}P_B + 2.3P_z \sum_{i=0}^{5} i A_i (log_{10}2)^i (lnT_e)^{i-1}\Big\}$$

which for Alcator parameters vary as

$$0 < \rho_1 < 1.0$$

$$-0.6 < \rho_2 < 0$$

Both of these parameters scale as the ratio of the incremental energy loss due to radiation and that lost by diffusion.

The resistivity will be modelled in the following way

3.3.22)

$$\eta_{\|} = [\frac{\eta}{\eta_{cl}}]5.22 \times 10^{-3} ln\Lambda T(eV)^{-\frac{3}{2}} \qquad \Omega cm \quad for x \leq 1$$

$$\eta_{\|} = \eta_{\|}(1) \qquad x > 1$$

where we have neglected trapping effects, for the reasons discussed above. The term η/η_{cl} accounts for the presence of impurities, the relation to Z_{eff} is given by [3.12]

$$[\frac{\eta}{\eta_{cl}}] \equiv \frac{0.914 Z_{eff}}{1.077 + Z_{eff}} + 0.58 Z_{eff}$$

For the range of Z_{eff} of interest $1 < \eta/\eta_{cl} < 2$.

In discussing the effects of Ohmic heating we will define two parameters

$$\lambda \equiv \frac{a^2}{\chi_e} \frac{\eta_0 j_0^2}{n T_e(0)}$$

$$M \equiv \frac{\eta_0}{\mu_0 \chi_e} = \left(\frac{\chi_{mag}}{\chi_e}\right)$$

The first parameter scales as the ratio of the Ohmic heating rate and that lost by diffusion. The second parameter is the ratio of the magnetic and electron thermal diffusivities For Alcator parameters the values of λ, M will vary as

$$1 < \lambda < 4$$

$$0.03 < M < 0.1$$

What is left to be discussed in this section is the form of the background profiles to be used in the analysis. For the density, a profile of the form

$$n_e(r) = n_0\left(1. - \left(\frac{r}{a+\delta}\right)^2\right)^{\alpha} \qquad x \leq 1$$

$$n_e(r) = n_e(a) \qquad x > 1$$

$\delta \Rightarrow 1 - 2cm$ $.2 < \alpha < 2.0$

The reason for the introduction of δ is to avoid a $1/n$ singularity at $r = a$.

The temperature profile will be of the form

$$T_e(r) = T_0 e^{-r^2/a_T^2} \qquad x \leq 1$$

$$T_e(r) = T_e(1) \qquad x > 1$$

where $6.0 < a_T < 9.0$ cm. n_0 and T_0 are taken as free parameters.

The ion density profile is taken to be the same as for the electrons with $n_e = Zn_i$. The ion temperature profile will be solved self consistently using eq. 3.3.2 with $T_e(r)$ as a driving term.

We conclude this section with a summary of the dimensionless parameters that will be used in the subsequent sections.

Parameter table for Alcator

Parameter	Range for Alcator	
$\nu \equiv a^2\nu_{ei}/\chi_e$	$0 < \nu < 100$	electron-ion coupling
$\lambda \equiv a^2\eta_0 j_0^2/(\chi_e n T_e(0))$	$0 < \lambda < 4$	Ohmic heating
$\beta \equiv \chi_i/\chi_e$	$0 < \beta < 2$	ion transport
$S \equiv av_0/2D$	$0 < S < 2$	convection
$\gamma \equiv D/\chi_e$	$0 < \gamma < 1.5$	density transport
ρ_1(see text)	$0 < \rho_1 < 1.0$	radiation damping
ρ_2(see text)	$-0.6 < \rho_2 < 0$	
$M \equiv \chi_{mag}/\chi_e$	$0 < M < 0.1$	magnetic diffusion

From the scaling above we can easily see that the electron-ion coupling effects may play an important role in our analysis. The magnitude of the dimensionless coefficients indicate the relative sensitivity of $\widetilde{T_e}$ to the particular effect that the parameter represents.

3.3.4) Density pulse effects

Previous works assumed the density to be unaffected by the sawtooth crash. However measurements in Alcator indicate a central density fluctuation of $\sim 5\%$. We see from eq. 3.3.6 that terms involving a density fluctuation are multiplied by background quantities which may be large(such as $\tilde{n}\chi_e \partial T_{e0}/\partial r$). To study the density pulse effect in estimating χ_e we will write eq. 3.3.6 keeping only the diffusive term involving $\widetilde{T_e}$ and all terms involving $\tilde{n}$. The equation becomes

3.3.23)

$$\frac{3}{2}n_e\frac{\partial\widetilde{T_e}}{\partial t} = \frac{\chi_e}{r}\frac{\partial}{\partial r}r\Big(n_e\frac{\partial\widetilde{T_e}}{\partial r}\Big)$$

$$-\frac{3}{2}T_{e0}\frac{\partial\tilde{n}_e}{\partial t} + \frac{\chi_e}{r}\frac{\partial}{\partial r}r\tilde{n}_e\Big(\frac{\partial T_{e0}}{\partial r}\Big) - \frac{1}{r}\frac{\partial}{\partial r}r\Big(\frac{5}{2}\tilde{n}_e V_e T_{e0}\Big) + \frac{1}{r}\frac{\partial}{\partial r}r\Big(\frac{5}{2}T_{e0}D\frac{\partial}{\partial r}\tilde{n}_e\Big)$$

$$-\nu_{ei0}\tilde{n}_e\Big(T_{e0}-T_{i0}\Big) - \Big\{2P_B + P_z\Big\}\frac{\tilde{n}_e}{n_e}$$

Together with this equation we must consider the linearized density equation (3.3.8)

3.3.8)

$$\frac{\partial\tilde{n}}{\partial t} = \frac{1}{r}\frac{\partial}{\partial r}rD\Big(\frac{\partial\tilde{n}}{\partial r} - \frac{V}{D}\tilde{n}\Big)$$

We can non-dimensionalize the equation in a similar way as done in sec. 3.3.2 In the equations below we have defined

$$x \equiv \frac{r}{a} \qquad\qquad \tau \equiv \frac{2\chi_e}{3a^2}t$$

$$\widehat{T}_{e1} \equiv \widetilde{T}_e/T_{e0}(0) \qquad \widehat{T}_{e0} \equiv T_{e0}(x)/T_{e0}(0) \qquad \widehat{T}_{i0} \equiv T_{i0}(x)/T_{e0}(0)$$

$$\gamma \equiv \frac{D}{\chi_e} \qquad\qquad s \equiv \frac{av_0}{2D}$$

$$\nu(x) \equiv \frac{a^2\nu_{ei}}{\chi_e} \qquad\qquad \rho_1(x) \equiv \frac{a^2}{n_e T_{e0}(0)\chi_e}\Big\{2P_B + P_z\Big\}$$

The equation for the electron thermal perturbation becomes

3.3.24)

$$\frac{\partial \widehat{T}_{e1}}{\partial \tau} = \frac{1}{n_e}\frac{1}{x}\frac{\partial}{\partial x}x\Big(n_e\frac{\partial \widehat{T}_{e1}}{\partial x}\Big)$$

$$-\widehat{T}_{e0}\frac{\partial}{\partial \tau}\Big(\frac{\widetilde{n}_e}{n_e}\Big) + \frac{1}{n_e}\frac{1}{x}\frac{\partial}{\partial x}x\Big(\widetilde{n}_e\frac{\partial \widehat{T}_{e0}}{\partial x}\Big) - \frac{1}{n_e}\frac{1}{x}\frac{\partial}{\partial x}x^2(5\gamma s\widehat{T}_{e0}\widetilde{n}_e)$$

$$+\frac{1}{n_e}\frac{1}{r}\frac{\partial}{\partial r}r\Big(\frac{5}{2}\widehat{T}_{e0}\gamma\frac{\partial}{\partial r}\widetilde{n}_e\Big)$$

$$-\nu\frac{\widetilde{n}_e}{n_e}\Big(\widehat{T}_{e0} - \widehat{T}_{i0}\Big) - \rho_1\frac{\widetilde{n}_e}{n_e}$$

The density equation becomes

3.3.25)

$$\frac{\partial \widetilde{n_e}}{\partial \tau} = \frac{1}{x}\frac{\partial}{\partial x}x\gamma\Big(\frac{\partial \widetilde{n_e}}{\partial x} - 2sx\widetilde{n_e}\Big)$$

For Alcator $s = 0 - 2.0, \gamma \sim 0 - 1.5$. The parameters ν, ρ_1 are functions of x, for which the central value will be the free parameter. The range of the collisionality term $\nu(0) \sim 0-140$. The radiation parameter is taken to vary between $\rho_1(0) \sim 0 - 1.0$. The temperature profile width will vary $a_T \sim 6 - 10$ cm and the density profile shape factor $\alpha \sim 0.5 - 2.0$. The initial temperature is the same as prescribed before. The density perturbation will have the same shape as that for the electron temperature, with the maximum chosen so as to flatten the density profile(see fig 3.4).

The error in our estimate of χ_e is defined as

$$\frac{d\chi_e}{\chi_{eff}} \equiv \frac{(\chi_e - \chi_{eff})}{\chi_{eff}}$$

The dependence of the error with relevant plasma parameters is shown in fig. 3.5. The strongest variation is found to be with α, the density profile coefficient (fig. 3.5a). For a value of $\alpha = 2$ this effect can introduce an error of $\sim 34\%$. In the case of Alcator for gas puffed discharges $\alpha < 1$, so the expected error in this case is $< 20\%$. The results for fig. 3.5a correspond to a $\gamma = 1.5$, $\nu = 80$, $s = 1$, $\rho_1 = 0.6$ at a radius of $8cm$, to see how the error varies with the other parameters, a scaling was done

for the case of $\alpha = 2$ and changing one other parameter. The range of parameters shown in all cases is larger than that expected for Alcator. A modest variation is found with $\gamma \equiv D/\chi_e$ fig. 3.5b, changing between $0.25 < d\chi_e/\chi_{eff} < 0.45$. The scaling with ν, s are shown in fig. 3.5c,d respectively. We see that in neither case there is a significant variation in the error. The scaling with ρ_1 has not been shown, however the change in the error over a range of $0 < \rho_1 < 1$ is less than 1%.

The dependence on α correlates with the size of the perturbation, rather than with any background profile effect. As we shall see latter, the inferred value of χ_e is weakly dependent on the background density profile. The extra density in the outer regions of the plasma due to the sawtooth tends to slow down the temperature response as compared to the unperturbed density case, thus reducing the apparent χ_e.

3.3.5) Radiation damping

All the remaining terms in eq. 3.3.6 which were not included in the analysis of the previous section involve factors of $\widetilde{T_e}$. We shall proceed by breaking the analysis into physical effects, first considering radiation damping. The governing equation is

3.3.26)

$$\frac{\partial \widehat{T}_{e1}}{\partial \tau} = \frac{1}{n_e}\frac{1}{x}\frac{\partial}{\partial x}x\Big(n_e\frac{\partial \widehat{T}_{e1}}{\partial x}\Big) - \rho_2\frac{\widetilde{T}_{e1}}{\widetilde{T}_{e0}}$$

where

$$\rho_2(x) \equiv \frac{a^2}{\chi_e n_e T_{e0}(0)}\Big\{\frac{1}{2}P_B + 2.3P_z\sum_{i=0}^{5} iA_i(log_{10}2)^i(lnT)^{i-1}\Big\}$$

P_B and P_z are as explained in section 3.3.3 , all other parameters are as defined before. The maximum radiation takes place at the higher densities. For parameters consistent with $\overline{n} = 5\times 10^{14} cm^{-3}$ the central value of $\rho_2 \sim -0.6$. A parameter scan was done with $\rho_2(0) \sim -0.6 - 0$ and $\alpha = 0.5, a_T = 8cm, r_i = 4cm$. In all cases χ_{eff} differed from χ_e by less than 1% .

3.3.6) Thermal convection

A competing transport process to thermal diffusion is convection. This comes about from the motion of the fluid elements in the plasma. This effect is represented in eq. 3.3.6 by the $5\Gamma_{e0}\widetilde{T}_e/2$ term. The convection is driven by two mechanisms, the first is a particle flow due to the density gradient and of the form $-D\nabla n_e$. The second is a center of mass velocity for the particles and is independent of density gradient, it has the form $n_e V$. The total zeroth order flux as discussed before is

$$\Gamma_{e0} = n_{e0}V - D\frac{\partial}{\partial r}n_{e0}$$

In our model V will be taken to represent a radially inward particle pinch and $\nabla n_e < 0$ giving an outward flow. Since the model assumes that the background profiles are in equilibrium, by considering particle transport eq. 3.3.3 and neglecting any sources near the center, thus

3.3.27)

$$\Gamma_{e0} = 0$$

Thus we can expect no contribution from this term. However convection does affect the thermal transport through the $\widetilde{\Gamma}_e$ term which comes about from the fluctuation in the density. This effect has already been taken into account in the density pulse term.

3.3.7) Ohmic heating

Along with the heatpulse there is an associated magnetic pulse caused by the redistribution of the magnetic field at the time of the sawtooth. This pulse, which can also be described by the current evolution, can couple to the electron heatpulse via Ohmic heating. The temperature fluctuation will also cause a change in the resistivity which can change the heating rate. The resistivity will be taken to be Spitzer with corrections for the presence of impurities as discussed in sec. 3.3.3. The change in the resistivity due to a temperature fluctuation can be written as

$$\tilde{\eta} \simeq -\frac{3}{2}\eta_0 \frac{\hat{T}_{e1}}{\hat{T}_{e0}}$$

The form of eq. 3.3.6 which describes the evolution of the current pulse then becomes.

3.3.28)

$$\frac{\partial \hat{T}_{e1}}{\partial \tau} = \frac{1}{n_e}\frac{1}{x}\frac{\partial}{\partial x} x n_e \frac{\partial \hat{T}_{e1}}{\partial x} + \lambda\left(2\frac{\tilde{j}}{j_0} - \frac{3}{2}\frac{\hat{T}_{e1}}{\hat{T}_{e0}}\right)$$

where $\lambda \equiv (a^2/\chi_e)(\eta_0 j_0^2/n_e)$

The equation that describes the evolution of the current is 3.3.10, here recast with the assumption for the resistivity.

3.3.29)

$$\frac{\partial \tilde{j}}{\partial \tau} = \frac{1}{x}\frac{\partial}{\partial x} x \frac{\partial}{\partial x} M j_0 \left(\frac{\tilde{j}}{j_0} - \frac{3}{2}\frac{\hat{T}_{e1}}{\hat{T}_{e0}}\right)$$

where

$$M \equiv \frac{\eta_0}{\mu_0 \chi_e} = \left(\frac{\chi_{mag}}{\chi_e}\right)$$

Since we have made the assumption that the background profiles satisfy the quiescent equations, from eq. 3.3.5 we have

$$\eta_0 j_0 = const.$$

since $\eta_0 \sim T^{-\frac{3}{2}} \Rightarrow j_0 \sim T_e^{\frac{3}{2}}$

In this analysis we will specify the electron temperature profile a_T, the inversion radius r_s, toroidal magnetic field B_t and adjust the total current such that $q(r_s) = 1$, where q is the safety factor.

$$q \equiv \frac{r B_t}{R B_\theta}$$

The above, specify profiles for λ, we will use the central value of $\lambda(0) \equiv \lambda_0$ as a free parameter. The value of $\lambda_0 \sim 1 - 4$ for Alcator. The central value of the ratio χ_{mag}/χ_e is varied between $0.03 - 0.1$. Thus we do not expect much in the way of heating from the current pulse itself, since it hardly evolves during one sawtooth period(fig. 3.6). There can still be an effect from the change in heating due to the resistivity fluctuation. The sawtooth is taken to flatten the current profile about

the value at the inversion radius(fig. 3.6). The extent of the mixing is determined from current conservation, where for this case $r_M^2/r_s^2 = 2.1$. From the simulations we find an effect no larger than 3% on the estimate of χ_{eff}/χ_e, again due mostly to changes in the resistivity.

3.3.8) Electron-ion coupling

Because of collisions with the ions, the evolution of the electron heatpulse is coupled to that of the ion heatpulse. During high density operation this can have a significant effect on the evolution of the electron heatpulse since the electron-ion energy equilibration time can be less than τ_p ($1/\nu_{ei} \sim 0.22ms, \tau_p \sim 1ms$). The equation to describe the electron heatpulse in this case is 3.3.6

3.3.30)

$$\frac{\partial \widehat{T}_{e1}}{\partial \tau} = \frac{1}{n_e}\frac{1}{x}\frac{\partial}{\partial x} x n_e \frac{\partial \widehat{T}_{e1}}{\partial x} - \nu(\widehat{T}_{e1} - \widehat{T}_{i1}) + \frac{3}{2}\nu(\widehat{T}_{e0} - \widehat{T}_{i0})\frac{\widehat{T}_{e1}}{\widehat{T}_{e0}}$$

where $\nu \equiv \nu_{ei}a^2/\chi_e$. From eq. 3.3.7 we get the equation for the ions

3.3.31)

$$\frac{\partial \widehat{T}_{i1}}{\partial \tau} = \frac{1}{n_i}\frac{1}{x}\frac{\partial}{\partial x} n_i \beta \frac{\partial \widehat{T}_{i1}}{\partial x} + Z\nu\left(\widehat{T}_{e1} - \widehat{T}_{i1}\right) - \frac{3}{2}Z\nu\left(\widehat{T}_{e0} - \widehat{T}_{i0}\right)\frac{\widehat{T}_{e1}}{\widehat{T}_{e0}}$$

where $\beta \equiv \chi_i/\chi_e$ and Z is the ion charge. The initial ion temperature perturbation profile was taken to be the same as for the electrons, the peak amplitude fixed to flatten the central temperature to that at the inversion radius. Fig. 3.7a shows the result of a set of simulations for $\nu(1/2) = 90$. The parameter $d\chi_e/\chi_{eff} \equiv (\chi_e - \chi_{eff})/\chi_{eff}$. In fig. 3.7b we can consider the evolution of $d\chi_e/\chi_{eff}$ as a function of $\nu(1/2)$ for two extreme cases of $\beta = 0.1, 3$.

We can understand fig. 3.7a in the following way. When $\beta \ll 1$, the leading edge of the electron heatpulse will store energy in the ions reducing $\widetilde{T_e}$. For the trailing edge of the heatpulse, when $\widetilde{T_e} < \widetilde{T_i}$, the ions will dump their energy back on the electrons thus raising $\widetilde{T_e}$, this action delays the arrival of the apparent peak and reduces χ_{eff}. When $\beta > 1$ the ion heatpulse propagates faster than the electron heatpulse. Since the leading edge of the ion arrives first it heats the electrons, as it goes by the electrons begin dumping their energy back on the colder ions. The net effect is to increase χ_{eff} above the real value. For the case of $\beta \gg 1$. the ions will rapidly dissipate any energy that the electrons give it. In this limit $T_{i0} \ll T_{e0}, \widetilde{T_i} \ll \widetilde{T_e}$ after a finite time and the form of eq. 3.3.30 becomes

$$\frac{\partial \widehat{T_{e1}}}{\partial r} = \frac{1}{n}\frac{1}{x}\frac{\partial}{\partial x} xn \frac{\partial \widehat{T_{e1}}}{\partial x} + \frac{1}{2}\nu \widehat{T_{e1}}$$

We see that the term that dominates the ion coupling in the equation comes from the fluctuation in ν_{ei} due to the electron temperature change $\widetilde{T_e}$. As the electron heatpulse arrives, the increase in $\widetilde{T_e}$ reduces the coupling to the ions; this increases the reheat rate for the electrons. In the trailing edge, the reduced $\widetilde{T_e}$ increases the coupling, thus increasing the cooling rate. These effects cause the $\widetilde{T_e}$ perturbation to peak earlier, thus $\chi_{eff} > \chi_e$. The effects also show a saturation with β. This is an important result, because if in high density operation the ions are the dominant loss channel $\beta > 1$, the saturation with β sets an upper limit for fixed ν on the ion effect in estimating χ_e.

3.3.9) Comments on the single sawtooth model

The single sawtooth model allows us to examine the importance of various terms in the electron thermal transport equation. It has shown that electron-ion coupling is the first important non-diffusive effect in the transport equation. Fig. 3.7b shows that we can underestimate χ_e by as much as 80% for high collissionality and low β. For the expected range of operation for Alcator this corresponds to the highest densities. For high β(i.e. $\beta > 1$) the largest we can overestimate χ_e by about 20%. These results will be of importance latter on when we consider how χ_e scales with plasma parameters.

Another effect which can be of importance is that of coupling to the density pulse. For values of $\alpha \sim 2$ this can have an effect of $\sim 30\%$. However since we will be operating with gas puffing the expected value of $\alpha < 1$, thus the error $< 10 - 20\%$. Given the present accuracy of the measurement for our case, we can neglect this effect.

3.4) Method of analysis

3.4.1) Motivation

The problem at hand is to develop a method of inferring the electron thermal diffusivity from the heatpulse measurements. We will obtain an equation which adequately describes the temperature evolution and find a self consistent χ_e which gives a solution that matches the measured parameters. The model used by previous workers is not greatly different from the single sawtooth model developed in sec. 3.3. Although conceptually simple for understanding the physics of heatpulse propagation it is inadequate for describing the evolution in a real plasma. Hereunder we will elaborate more on some of the shortcomings of previously used models and develop a model which attempts to overcome them.

The first topic to be discussed is the question of a baseline profile. All models which deal with the problem use an incremental temperature to describe the evolution of the heatpulse, the incremental temperature being equal to the difference between the instantaneous electron temperature and some reference profile. In refs.[3.1-3.8] this has been taken to be the quiescent profile i.e. that which satisfies eq. 3.3.1. However this profile never exists in most plasmas and the profiles that are actually measured are strongly determined by the sawtooth mechanism. This leads to considerable uncertainty in determining the initial profile used to solve the diffusion equation. One approach that has been taken is to find the solution in the far field, which is insensitive to the particulars of the initial perturbation. This requires that the measurements be done sufficiently far away from the region directly affected by the sawtooth crash. With the results discussed in chap. II, the mixing region can extend half way out into the plasma(at least for Alcator); thus the far field solution is not appropriate. Ref.[3.2] tried to overcome this problem by including a theoretically determined profile. Since the diffusion equation is linear in $\tilde{T}$, we need only to specify the initial profile to within a multiplicative factor; from the solution we can determine the τ_p profile. The problem with this is that our theoretical understanding of the sawtooth event is poor. As we shall see in the next

section, what we take for the initial profile can have a significant effect on the value of χ_e. Another consequence of the quiescent assumption has to do with multiple sawteeth. By requiring the profile to relax back to the quiescent profile, one makes the implicit assumption that all previous heatpulse effects have dissipated. As was shown in ref.[3.5] multiple sawtooth effects can cause a factor of two increase in the apparent χ_e, which for our case is a large effect. Thus the previously used models do not account for multiple sawteeth in a self-consistent manner. The approach that we will adopt in this work is to develop a model which uses experimentally measured profiles. This avoids the problems with the quiescent assumption and automatically includes multiple sawtooth effects.

A second point to be made has to do with making the χ_e measurement immediately after a sawtooth crash. In making a τ_p measurement we use the sawtooth crash as a time reference and follow the evolution of $\widetilde{T_e}$ for a fixed radius until it peaks. According to the model proposed in ref. [3.2], the magnetic field should be completely reconnected when the temperature profile reaches its minimum value, and its evolution should reflect the bulk properties of the plasma thereafter. However if there are any remnant effects of the sawtooth disruption which reflect themselves in a time changing χ_e, which need only last a short time and does not contribute to global confinement, this can have a large effect on $\widetilde{T_e}$ since

$$\frac{\partial}{\partial t}\widetilde{T_e} \sim \frac{\partial}{\partial r} r \widetilde{\chi_e} \frac{\partial}{\partial r} T_{e0}$$

This can propagate the temperature perturbation out much faster than bulk diffusion. In this case τ_p should reflect strongly the effects of the transient χ_e rather than the bulk. To minimize any transient effects,we will analyze the section of the temperature trace starting several disruption times after a sawtooth crash and end several reconnection times before the next crash.(see chapter II for explanation of reconnection)

3.4.2 Fourier transform method

Given an initial and final electron temperature profile, we must find a χ_e that will propagate the initial profile to the final profile in a manner consistent with

the observed temperature traces. The initial and final profiles are refered to the same sawtooth interval (fig. 3.8), so as to avoid sawtooth boundary effects and allow treatment of non-identical sawteeth. Each sawtooth interval will be treated as independent of the others.

Because of the finite time interval, we can apply a finite Fourier transform technique. This has the advantages that it improves signal to noise and since most of the relevant information is in the lower harmonics, we need to analyze fewer points. Noise in the time signal tends to be at higher frequencies than that associated with the sawtooth evolution, so that the lower harmonics will be less affected by noise. To see why the lower harmonics are more sensitive we consider an exponentially decaying signal

$$\tilde{T}(r,t) = A(r)e^{-t/\tau(r)}$$

Since we generally look after the trace has peaked, this function is a reasonable representation of the signal. If we Fourier decompose the signal over a period Δt and define the quantity $z \equiv \Delta t/\tau$ (which is proportional to χ_e) we get

$$\tilde{T}_p = A\frac{(z+i2\pi p)}{(z^2+(2\pi p)^2)}(1-e^{-z})$$

where p is the Fourier harmonic number. We find that $\partial\tilde{T}_p/\partial z$ decays monotonically with p. Thus we expect the lower harmonics of the signal to be the most sensitive to χ_e.

We begin our development of the formalism by expressing the electron temperature profile in terms of a Fourier series.

3.4.1)

$$T_e(r,t) = \sum_{p=-\infty}^{\infty} T_{ep}(r)e^{-i\omega_p t}$$

where $\omega_p \equiv 2\pi p/\Delta t$

The coefficients can be found by use of the finite Fourier transform

3.4.2)

$$T_{ep}(r) = F_p[T_e] \equiv \frac{1}{\Delta t}\int_0^{\Delta t} dt' T_e(r,t')e^{i\omega_p t'}$$

We immediately see that for $p = 0$, T_{e0} is just the time averaged temperature. The incremental component $\widetilde{T_e}$ corresponds to all the $p \neq 0$ terms. The equation for T_{ep} is found by applying the operator F_p to eq. 3.2.1 . Here we shall write it by condensing all the non-diffusive terms into $L(r,t)$.

3.4.3)

$$\frac{3}{2}\frac{\partial}{\partial t}(n_e T_e) = \frac{1}{r}\frac{\partial}{\partial r} r n_e \chi_e \frac{\partial}{\partial r} T_e + L(r,t)$$

The left hand side(LHS) of eq. 3.4.3 gives

$$F_p[\frac{3}{2}\frac{\partial}{\partial t}(n_e T_e)] = \frac{3}{2}\frac{(n_e T_e)|_{t=\Delta t} - (n_e T_e)|_{t=0}}{\Delta t} - \frac{3}{2} i\omega_p F_p[n_e T_e]$$

If we allowed n_e to have a time dependence we would have $F_p[n_e T_e]$ become a convolution term. However we will assume to operate in the 'flat top' region of the density and with parameters for which the density pulse is unimportant. Then we have

$$F_p[\frac{3}{2}\frac{\partial}{\partial t}(n_e T_e)] = \frac{3}{2}\frac{(n_e T_e)|_{t=\Delta t} - (n_e T_e)|_{t=0}}{\Delta t} - \frac{3}{2} i\omega_p n_e T_{ep}$$

The diffusion term on the RHS of eq. 3.4.3 becomes for time independent $n_e(r), \chi_e(r)$

$$\frac{1}{r}\frac{\partial}{\partial r} r n_e \chi_e \frac{\partial}{\partial r} T_{ep}$$

For brevity we shall define

$$R \equiv \frac{3}{2}\frac{(n_e T_e)|_{t=\Delta t} - (n_e T_e)|_{t=0}}{\Delta t}$$

The Fourier transformed version of eq. 3.4.3 is

3.4.4)

$$R - \frac{3}{2} i\omega_p n_e T_{ep} = \frac{1}{r}\frac{\partial}{\partial r} r n_e \chi_e \frac{\partial}{\partial r} T_{ep} + L_p(r)$$

where L_p is the p^{th} Fourier component of the non-diffusive terms.

For $p = 0$ we get the equation for the time averaged temperature profile.

3.4.5)

$$R = \frac{1}{r}\frac{\partial}{\partial r} r n_e \chi_e \frac{\partial}{\partial r} T_{e0} + L_0(r)$$

Since $R \neq 0$ everywhere, we immediately see that the sawtooth averaged temperature profile,although time independent, does not satisfy the quiescent equation. We shall neglect the non-diffusive terms in our estimate of χ_e (i.e. $L_p \sim 0$). As we saw in sec. 3.3 under certain possible limits these effects may be important. However since we do not have good knowledge of the profiles to account for these, what can be done instead is to recognize the uncertainty introduced by their neglect. The equation for p thus becomes,

3.4.6)

$$R - \frac{3}{2} i\omega_p n_e T_{ep} = \frac{1}{r}\frac{\partial}{\partial r} r n_e \chi_e \frac{\partial}{\partial r} T_{ep}$$

The term R has the dimensions of a reheat term. It's function is to specify the initial and final profiles in the problem. The condition for R to be unimportant in eq. 3.4.6 is

$$\frac{3}{2}\omega_p n T_{ep} \gg R$$

To estimate the terms we again assume $\tilde{T} \sim e^{-t/\tau}$, taking $\tau \sim 1ms$ which is consistent with the parameters specified above and using $\Delta t \sim 3ms$. Then

$$\left|\frac{3}{2}\omega_p T_p\right| \sim \frac{3}{2}\omega_p \frac{(1-e^{-z})}{\sqrt{z^2+(2\pi p)^2}}$$

which for $p = 1$ gives

$$\left|\frac{3}{2}\omega_p T_p\right| \sim 429A$$

We can express $R \sim 1/\Delta t \sim 333$. So we find that the reheat can play a very important role in eq. 3.4.4. The reheat term can be neglected in the far field since $R \to 0$ as $r \to \infty$. In the special case in which we can neglect R, eq. 3.4.3 takes on the form derived in ref.[3.5].

3.4.3) Sawtooth averaging

A technique that can be used to improve the signal to noise is that of sawtooth averaging. We take an ensemble of sawteeth and average the corresponding components to arrive at a composite sawtooth; this reduces the effect of random noise. For the purpose of analysis, we will treat the sawteeth as independent events. We can then represent any time changing quantity as

$$y_l(r,t) = < y(r,t) > + \delta y_l(r,t)$$

where

l:is the sawtooth index

$< >$:is the ensemble average operator

$\delta y_l(r,t)$:is the deviation from the average for sawtooth l

we have $< \delta y_l >= 0$ by definition.

Using the above definitions to express the quantities $R, n_e, T_{ep}, \chi_e, L_p$ eq. 3.4.4 becomes

$$< R > + \delta R_l - \frac{3}{2} i\omega_p (< n > + \delta n_l)(< T_{ep} > + \delta T_{epl})$$

$$= \frac{1}{r}\frac{\partial}{\partial r} r (< n > + \delta n_l)(< \chi_e > + \delta \chi_{el}) \frac{\partial}{\partial r}(< T_{ep} > + \delta T_{epl})$$

$$+ < L_p > + \delta L_{pl}$$

Averaging over the ensemble we get correct to order δ

3.4.6)

$$< R > - \frac{3}{2} i\omega_p < n >< T_{ep} >= \frac{1}{r}\frac{\partial}{\partial r} < n >< \chi_e > \frac{\partial}{\partial r} < T_{ep} > + < L_p >$$

Thus this technique will give us a measurement of the sawtooth averaged χ_e. An implicit assumption in the above equation is that $\delta^2 \ll 1$, that is, the dissimilarity between sawteeth must be sufficiently small. To insure this we shall use the criterion of $(\delta T / < T >) < 0.3$, to determine which sawteeth will be included in

the averaging. The contribution of the neglected terms in determining the ensemble average quantities is $O(\delta^2) < 0.1$.

3.4.4) Measurement procedure

We now want to tie together the various techniques and equations that have been justified in previous sections. Here we describe the sequential procedure that has been followed to make the χ_e meassurements.

1)A $40ms$ window of the data from the ECE grating was digitized at a rate of $200kHz$. The window size allowed sampling of between $10-25$ sawtooth intervals.

2)The ECE channel nearest the center was used to find the times of the sawtooth disruptions. This channel generally has the best signal to noise, which is important for good synchronization.

3)The sawtooth boundaries, that is the sections of the trace not used in fitting for χ_e(fig. 3.8), were set at $\pm 100us$ about each sawtooth crash.

4)The data was then broken up into sawtooth intervals, starting with the first point after a sawtooth boundary and ending with the point just before the next sawtooth boundary. We refer to the points in a single sawtooth as 'bins'. A particular point is referenced by a spatial location, sawtooth interval and a bin number.

5) The sawtooth averaged trace at each radial location was found by averaging the temperature at a particular bin number over all the sawtooth intervals. The number of bins in the sawtooth averaged trace is equal to the minimum number of bins in any of the sawtooth intervals. This keeps the noise amplitude approximately constant from bin to bin. Refer to fig. 3.9 for a graphical explanation. The period Δt was set by the minimum number of bins times the sampling time.

6)We assumed that the density remained constant during the sawtooth evolution, thus the reheat term was determined by the temperature change. The value of the reheat profile at the measured radii was found by subtracting the temperature at the last bin number from that at the first and dividing by Δt. To arrive at a continuous form for $< R >$, the six measured values were fit with an empirical profile of the form

3.4.7)

$$< R >= \begin{cases} Acos(\frac{\pi}{2}x^{\alpha}) & x \leq 1 \\ Be^{-\sigma(x-1)^2} & x > 1 \end{cases}$$

where $x \equiv r/r_i$

The particular form above was arrived at by fitting a number of shots simultaneously.

7)Up to three of the outermost traces which have the best signal to noise, were chosen to be used in estimating χ_e. The innermost traces are dominated by either Ohmic heating or $\chi_e \partial T_{e0}/\partial r$ terms and thus have essentially a linear time dependence. It is the traces with significant curvature which are most sensitive to the heatpulse.

8)The equation that we solved is of the form of eq. 3.4.6. Here we neglect the $< L_p >$ term for the same reason as was done in eq. 3.4.5. We will drop the $< >$ notation with the understanding that all quantities for the remainder of the chapter are sawtooth averaged unless otherwise stated. We divide eq. 3.4.6 by n to get

3.4.8)

$$\frac{R}{n_e} - \frac{3}{2} i\omega_p T_{ep} = \frac{1}{n_e} \frac{1}{r} \frac{\partial}{\partial r} r n_e \chi_e \frac{\partial}{\partial r} T_{ep}$$

The form of χ_e used is

$$\chi_e = c_1 + c_2(\frac{r}{a_l}) + c_3(\frac{r}{a_l})^2$$

The boundary condition at $r = 0$ is $\partial T_{ep}/\partial r = 0.0$ and at $r = a_l$ is $T_{ep} = 0.0$. Forcing $T_{ep} = 0$ at the limiter radius does not seem to affect our result for χ_e in an appriceable way except at the very edge of the plasma.

9)We then found a self consistent χ_e which minimizes the sum of squares between the measured and calculated spectra of the first six harmonics at the given radial locations found in step 7.

3.4.5)Sample result

Let us discuss an example in some detail. We consider a D_2 shot with the following parameters: $B_t = 8.25T$, $\overline{n_e} = 2.1 \times 10^{14} cm^{-3}$, $I_p = 457kA$, $T_{e0} =$

$2000eV$, $a_{T_e} = 9.5cm$. The time evolution of the shot is shown in fig. 3.10. Fig. 3.11 shows the background profiles used in the fitting. The density profile was determined using a five channel interferometer and Abel inversion. The electron temperature profile was measured using the ECE grating as explained in chapter I.

Fig. 3.12 shows the raw traces contained in the sample window, with the fitted sawtooth averaged traces.

By taking the difference between the final temperature and the initial temperature we can arrive at the reheat profile as described in sec. 3.4.4 . Fig. 3.13 shows a graph of R/n . We see that it is significant well past the radius $\sqrt{2}r_i$ and extending to $r/a \sim 0.5$.

The sawtooth averaged signals from the grating were Fourier transformed, fig. 3.14a shows a comparison between the absolute value of the calculated and measured spectrum. Fig. 3.14b shows a time reconstruction of the calculated spectrum for fig. 3.14a with the corresponding sawtooth averaged trace.

Fig. 3.15a shows the estimated χ_e profile. The data can be fit with the central value of χ_e varying between $\sim 0 - 2\ cm^2/ms$. This is not a reliable measure since it is an extrapolation of measurements done in the region near the half radius. However it does show that the value of χ_e near the center is much lower than that at the half radius. As we shall see in the next section, the data can discriminate between a flat χ_e case and one changing with radius.

For comparison, we show two reference profiles for χ_e. The first is a power balance estimate for that shot using the background profiles averaged over sawteeth. The second represents an average model which is consistent with neo-Alcator scaling [3.13] and which has been used to simulate Alcator C discharges.

$$\chi_e = \frac{5 \times 10^3}{n(r)} \frac{r}{R^2}$$

the density is expressed in units of $10^{14}cm^{-3}$ and radii in cm.

We see the neo-Alcator profile agrees well with the heatpulse profile. The discrepancy at either the center or the edge comes from extrapolating the values of χ_e based on a model valid near the half radius region. The power balance model gives

agreement within a factor of two from that estimated by the heatpulse. The flat feature near the center of the plasma in the power balance model is due to sawtooth averaged effects from the simulation. The simulations were done with a modified version of ONETWO [3.19,3.21]. The rapid energy transport due to sawteeth is simulated by introducing a large value of χ_e near the center, at the time of the sawtooth disruption. The time averaged effect this has is to increase the apparent χ_e near the center of the plasma. The heatpulse measurement is not sensitive to the large transient χ_e at the time of the crash, thus it predicts a lower value than power balance at the center. Fig. 3.15b shows the corresponding plots for the electron thermal conductivity. Over the region of the plasma that is measured, we find the heatpulse κ_e to increase linearly with radius. For the case shown agreement with the Alcator model is very good and in general the agreement is within a factor of two. The power balance electron thermal conductivity profile is flatter than that from the heatpulse technique. Part of this flattening may be attributed to sawtooth averaging effects as discussed before. The discrepancy between the heatpulse and power balance values are also larger in this case, still the agreement is within a factor of two.

We have also performed the calculation using a method described in ref.[3.5]. The trace at $r = 7.55cm$ from fig. 3.12 was fit with a function of the form

3.4.9)

$$f(t) = \frac{\widetilde{T}(r,t)}{\widetilde{T}(r,\tau_p)} = \frac{e^{\frac{3}{2}(1-\frac{\tau_p}{t})}}{(t/\tau_p)^{\frac{3}{2}}}$$

giving a time to peak of $\tau_p = .25ms$. The χ_e can then be estimated by

3.4.10)

$$\chi_e = \frac{3}{2}\frac{(r-r_i)^2}{\tau_p}\frac{1}{6+(r-r_i)^2/rr_i}$$

with $r = 7.55cm, r_i = 3.6cm, \tau_p = .15ms$ we find

$$\chi_e \sim 14cm^2/ms$$

or about a factor of four higher than that found by the method proposed here. Fig 3.16 shows the estimated χ_e from the τ_p profile of fig. 3.2. using the same equation

from ref.[3.5]. The agreement with the neo-Alcator estimate improves at larger radii. We believe the discrepancy comes from near field effects being important at the smaller radii. At larger radii near field effects are less important, thus the agreement improves.

3.5) Sensitivity Analysis

In making the χ_e measurement we have assumed that diffusion governs the evolution of the electron heatpulse, and have arrived at a χ_e by solving the transport equation using measured profiles. We have addressed the question of the importance of non-diffusive terms in the transport equation, in discussing the single sawtooth model. In solving the diffusion equation we need to use measured profiles whose uncertainty can affect our estimate for χ_e. We also solve the problem on a finite grid, specifying that all perturbations go to zero at the boundary. The real boundary conditions are unclear, thus we must see how sensitive the value of χ_e is to boundary value effects. It is the purpose of this section to study the sensitivity of χ_e to the various parameters that characterize the measured profiles.

Four effects will be examined. The first is sensitivity to channel calibration. The grating calibration is determined by using an independently measured temperature profile and arriving at a self consistent calibration factor for each of the grating channels. Any error in our calibration will reflect itself as a change in the reheat profile as well as in the measured spectrum, possibly changing χ_e. Second as the gradient of the density plays a role in the transport equations, we would like to see if this has a major effect on the diffusion. Third we consider the sensitivity of χ_e to the model used for the reheat profile. This result has bearing on our measurements as well as those of others, for it determines the importance of near field effects. The parameters for the sample case are $B_t = 8.325T, \overline{n_e} = 2.9 \times 10^{14}, I_p = 556kA$

As was discussed in chapter I, the ECE grating was calibrated using a self-consistent scheme. The way this was accomplished was by using the measured temperature profile from some other diagnostic (i.e. Thomson scattering or using the ECE fast scanning Fabry-Perot). The electron temperature profile measured by these instruments was parametrized by a function of the form $T_e(r) \sim T_0 e^{-r^2/a_{T_e}^2}$. The calibration for each of the grating channels is then

$$K_j \equiv \frac{T_0 e^{-r_j^2/a_{T_e}^2}}{Sig(j)}$$

where $Sig(j)$ is the signal from the detector for channel (j) consistent with the Thomson or Fabry-Perot. Any error in our channel calibration comes from an error in estimating the reference profile. An error made in estimating T_0 will not affect the resulting χ_e, since the diffusion equation is linear in T_e. The parameter that does matter is a_{T_e}, changing this is equivalent to changing the channel calibrations. Fig. 3.17 shows the dependence of χ_e for a range of a_{T_e} wider than expected. We see that the variation is no more than 20% over this range.

The density comes into the diffusion equation as the ratio of the density profile gradient to the total density

$$\chi_e\Big(\frac{1}{r}+\frac{\partial}{\partial r}ln(n)\Big)\frac{\partial}{\partial r}\widetilde{T_e}$$

so that the important parameter is the profile shape and not its magnitude. If we take

$$n \sim (1-(\frac{r}{a})^2)^\alpha$$

then

$$\frac{\partial}{\partial r}ln(n) = \frac{2\alpha}{(1-(\frac{r}{a})^2)}\frac{r}{a^2}$$

For measurements at a fixed radius the density term varies liniarly with α. A reasonable condition for neglecting density profile effects is then

$$\frac{1}{r} \gg |\frac{\partial}{\partial r}ln(n)|$$

for the case we have measured $\alpha \sim 0.5$,$r \sim 8cm$,$a = 16.5cm$ which gives $\partial ln(n)/\partial r \sim 0.04cm^{-1}$ and $1/r \sim 0.125cm^{-1}$. From this result we expect density profile effects to play a weak role in the region of interest. Fig. 3.18 shows the scaling of χ_e with α holding all other parameters constant. We see very little variation as expected from the above argument.

In our analysis the reheat profile is the driving term in eq 3.4.8. We would like to find out how sensitive our results are to the form of the reheat profile, in

particular we are interested in varying the spatial extent (or mixing radius) of the perturbation. We will compare two forms for the reheat profile. The first is the one we have already calculated using the measured profiles. The second will be consistent, with a post disruption profile which is flat out to a radius of $\sim \sqrt{2}r_i$. The central reheat rate and the inversion radius are kept the same in each model. Fig. 3.19 shows the profiles. We find that the diffusivity goes up by a factor of $\sim 3-5$ at $r = 8cm$ becoming larger with radius (fig. 3.20). Thus the extent of the initial profile is very critical in the estimate of χ_e. This may have some consequence to the results arrived at in ref. [3.5], in which the authors find values of χ_e that are about an order of magnitude larger than those found from power balance. As mentioned earlier in this chapter, their conclusion was that some physical mechanism may allow the heatpulse to diffuse faster than the bulk. The above analysis suggests that near field effects may increase the apparent χ_e sufficiently to account for the discrepancy. Thus the problem may lie in the analysis technique rather than any new physical effects.

By forcing the perturbations to zero at the boundary, we effectively introduce a reflective layer to the problem. In the real case the boundary conditions at the edge of the plasma are unclear. We have performed a sensitivity study to see how much of an effect forced boundary conditions have on our estimate of χ_e. To check this, a case was run in which the reflection layer was moved to twice the limiter radius. The estimated χ_e using this model varied by less than 3% from that found by putting the boundary at the edge of the plasma. The reason for this is that we make the χ_e measurement near the half radius of the plasma, so that any boundary effects take longer than a sawtooth period to propagate to this region.

Fig. 3.21 shows the variation in χ_e, by varying the measured parameters used in the diffusion equation. For the case discussed the average parameters are $a_{T_e} = 10.4cm$, $\alpha = 0.5$, $r_i = 3.7cm$. To estimate the change in χ_e due to an error in any of these parameters, a number of cases were run with the input parameters varied over the expected range of error fig. 3.21. We immediately see that the most sensitive parameter is the form of the reheat profile or equivalently, the initial perturbation.

In this study r_i was varied while keeping the shape of the reheat profile constant and conserving energy. The results from the analysis show a variation of up to 30% in the estimate of $\chi_e(a/2)$ due to uncertainties in the initial profile.

One of the main objectives in this work has been to make a local measurement of χ_e, rather than an average value. To do this we must ascertain wether our experiment can differentiate between different fit profiles. The three profiles considered will be,$\chi_e = const.$,$\chi_e = c_1 + c_2(r/a)$ and $\chi_e = c_1 + c_2(r/a) + c_3(r/a)^2$. To see if the goodness of fit changes as a function of the χ_e profile assumed, we use the reduced χ^2 test, since this is insensitive to the number of fit parameters. We have used the value of χ^2_ν for the parabolic model as a reference ($\chi^2_{\nu par} \sim 0.9$. For the case we have considered $\chi^2_{\nu lin}/\chi^2_{\nu par} = 1.1$ and $\chi^2_{\nu const}/\chi^2_{\nu par} = 1.6$ We see a clear preference for a spatially varying χ_e profile. The difference between the parabolic and linear profile shapes is small, but there is an increase in χ^2_ν when the data is fitted with a constant profile. In fig. 3.22 we compare the estimates for the three profiles. We see that the linear and parabolic models agree well over the region where the measurements are done $r \rightarrow 6 - 10cm$.

3.6) Scaling of χ_e

In this section we discuss the scaling of the heatpulse χ_e with line averaged density and with the χ_e inferred from power balance calculations. In order to reduce electron-ion coupling effects we have used D_2 plasmas which have a lower Z/μ than H_2 plasmas. Scalings with plasma current and toroidal fields were not possible because the range of parameters and the experimental error were such that no definite scaling was discerned.

3.6.1) General observations on χ_e scaling

Comparisons have been made of χ_e determined by heatpulse propagation and that determined by power balance. A modified version of the ONETWO[3.19,3.21] code has been used to arrive at the power balance χ_e. Fig. 3.23 shows a scatter plot of χ_{ehp}(heatpulse) vs. χ_{epb}(power balance) at three radial locations $r/a = 0.3, 0.5, 0.7$. The data seems to be bounded by $1 < \chi_{ehp}/\chi_{epb} < 3$ with an average slope of $\chi_{ehp}/\chi_{epb} = 1.7$. The scatter in the data is due to two things. The first is experimental error made in the heatpulse measurement. For similar plasma conditions the value of χ_{ehp} can change by as much $\pm 30\%$. The largest scatter takes place at the largest radii, this may be attributed to the fact this radius ($r = 11.5cm$) lies at the edge of our region of measurement with the lowest signal to noise. Thus this region is not constrained as well as those at the two inner radii. Another source of error comes from the power balance estimates. In moderate to high density operation the transport equation becomes very sensitive to the electron-ion coupling. To take proper account of this term, we need a good knowledge of the electron and ion temperature profiles, since a small error in these will be 'amplified' by the large value of ν_{ei}. One source of error in this case is the ion temperature profile, since it is not measured. The ion temperature profile is found self-consistently from the transport equation assuming a form for χ_i and requiring the central value of T_i to match that measured. Error in estimating the electron-ion coupling term can also lead to a large discrepancy between the value of χ_{ehp} and χ_{epb}. In this case we

would expect the scatter in the χ_{epb} estimates to increase with $\overline{n}_e$. Fig. 3.24 shows a scaling of $1/\chi_{ehp}$ and $1/\chi_{epb}$ vs. $\overline{n}_e$ for values at the half radius. As we shall argue below $\tau_{Ee} \sim 1/\chi_e$, the electron energy confinement time. We see that the discrepancy increases at high densities.

The estimates for χ_{ehp}, although scattered, are consistently higher than the power balance estimates. This may be an effect of electron-ion coupling, when $\beta > 1$ it can lead to an overestimate of the apparent χ_e. In considering the single sawtooth model we considered only single effect terms. In a real plasma multiple effects act simultaniously, possibly combining to reduce the threshold at which non-diffusive effects become important and increasing the magnitude of the total shift. Another possibility may be a systematic underestimation of the initial profile width, which as we saw earlier can increase the apparent χ_e. This explanation is unlikely, since the measured profile would tend to be slightly broader than the real profile due to finite instrumental resolution. Another possibility as was mentioned before, might be the existence of a time changing χ_e, which when multiplied by the gradient of the background profiles may lead to a rapid evolution of the apparent heat pulse. As was discussed in the introduction, TFTR[3.5] measures a discrepancy of $\chi_{ehp}/\chi_{epb} \sim 10-20$. They attribute it to a mechanism which causes the heatpulse to evolve with a χ_e which is larger than that which controls bulk energy transport. Although our discrepancy is smaller such a mechanism may not be discounted.

A scaling has been done of χ_e as a function of line averaged density. This is another test which we can apply to see if the χ_{ehp} has a similar scaling as that which governs bulk transport. The electron energy confinement time can be related to the electron thermal diffusivity at a given radius by the relation

$$\tau_{Ee} = \frac{f}{\chi_e}$$

where f is a proportionality constant that depends on the profile shape of χ_e, thus for constant χ_e profile, τ_{Ee} should scale with $1/\chi_e$. The parameters for the scan were $(1.5 < \overline{n} < 4.7) \times 10^{14} cm^{-3}$, $(500 < I_p < 560) kA$ and $B_t = 8T$. The range of the toroidal field is limited by instrumental constraints. We want a reasonably high

field to increase the available signal, while at the same time higher fields increase the channel spacing in the plasma, reducing the number of channels in the region of interest.

Fig. 3.25 shows the scaling of $1/\chi_{ehp}$ with line averaged density at three radial locations ($r/a = 0.3, 0.5, 0.7$). The points shown represent the average trend of a much larger data set. Each data point represents the average value of $1/\chi_e$ for that region of density with the error bars representing the scatter in the data. For comparison we have included the scaling of $1/\chi_e$ based on a model for χ_e which has been used to simulate Alcator discharges and is cosistent with neo-Alcator scaling[3.13]. The reduced form for this model is

$$\chi_e(r) = \frac{1.22r}{n_e(r)} \qquad cm^2/ms$$

$n_e(r)$ is in units of $10^{14}cm^{-3}$, the profile assumed for the density is

$$n(r) = n_p\left(1 - \left(\frac{r}{a}\right)^2\right)^{1/2}$$

for this case

$$n_p \sim 1.27\overline{n}_e$$

Fig. 3.25 shows good agreement between the standard model discussed above and the measured values of $1/\chi_{ehp}$. Again the data suggests that χ_{ehp} is greater than the value derived using the model above, but the data is consistent with $1/\chi_e \sim \overline{n}_e$ at all three radii. The ratio of the average values of χ_e at the various radii is fairly constant, suggesting that the average profile shape is only weakly dependent on the line averaged density. This is consistent with $1/n$ scaling since for gas puffed discharges the shape of the density profile does not change much in the central region of the plasma (i.e. it is fairly flat). There is however some scatter in the profiles when considered shot-shot as evidenced in fig. 3.26. Here we plot the inverse scale length of the χ_e profile at $r/a = 0.5$.

3.6.2) Scaling of χ_e at high densities

In this section we consider the heatpulse inferred χ_e as a method for studying the mechanism of confinement saturation observed in Alcator C[3.14].

Power balance calcualtions, have shown the electrons to be the dominant loss mechanism at low densities[3.14], with the total energy confinement time scaling with the density. This is contrary to that predicted by neo-classical theory, which predicts the ions to be the loss channel at these densities. In fact the empirical χ_e is found to be several orders of magnitude higher than that predicted by theory. At higher densities $\overline{n} > 3 \times 10^{14} cm^{-3}$ we find a saturation in the confinement fig. 3.27. The saturation density is too low to be explained by neo-classical ions, in ref. [3.15] it has been suggested that the ion conduction is anomalous with $\chi_i \sim 4\chi_{iNC}$ and the electrons $\chi_e \sim 1/n$ This picture has been supported by experiments done at low densities ref.[3.16]. It is found that $\chi_i/\chi_{iNC} \sim 3-5$ for $\overline{n} < 3 \times 10^{14}$ with the electron thermal diffusivity scaling as $\chi_e \sim 1/n$. In fig. 3.28 we show the scaling of $1/\chi_e$ with line averaged density for $(r/a) = 0.5$. In this case the complete data set is shown. Confinement saturation according to fig. 3.27 takes place between $(2 < \overline{n}_e < 2.5) \times 10^{14} cm^{-3}$, but as we see from fig. 3.28, $1/\chi_e$ continues increasing with density. At first this would tend to support the idea of $\chi_e \sim 1/n$ and the ions becoming the loss channel. However since we are in the high density region we must consider the effects of the non-diffusive terms. We expect from the results of sec. 3.3 for electron-ion coupling effects to be most dominant since the density profiles in all cases considered had $\alpha < 1.0$. In order to calculate the collissionality parameter we must use the measured χ_e. For the point of $\overline{n}_e = 4.6 \times 10^{14} cm^{-3}$, $1/\chi_e = 0.44$ we arrive at an effective $\nu_{eff} = 115$ (see sec. 3.3.8). Based on the results of the single sawtooth model fig. 3.7b $d\chi_e/\chi_{eff} = 0.82$ for $\beta = 0.1$ and $d\chi_e/\chi_{eff} = -0.25$ for $\beta = 3$. Since we have no knowledge of β the range

$$-0.25 < d\chi_e/\chi_{eff} < 0.82$$

represents the maximum possible variation for the 'real' χ_e. If $\beta > 1$ then χ_{eff} would overestimate the real χ_e, this case is consistent with the ions being the energy

loss channel. If $\beta < 1$, then χ_{eff} underestimates the real χ_e. This is consistent with the case for which the electron energy confinement time saturates with density, making the electrons the energy loss channel. In fig. 3.28 the error bar at the point at $\overline{n} = 4.6 \times 10^{14} cm^{-3}$ shows the maximum possible variation as predicted by the single sawtooth model. This comparison is strictly not valid, since the single sawtooth model makes assumptions which are not true in the real case, however it can give a rough estimate for the range of possible values for χ_e. The above discussion indicates that the heatpulse propagation technique for measuring χ_e at moderate to high densities may be strongly influenced by the evolution of the ion heatpulse. In order to differentiate between the electrons and ions, measurements of the ion heatpulse are necessary.

3.7)Conclusions

In this section we shall recapitulate the main results for this chapter and make suggestions for future work.

Except for the JET [3.17] and TFTR[3.15] results, all previous measurements of the heatpulse evolution have involved use of soft-Xray signals. Although this technique provides a large number of spatial channels and good signal to noise, it has the drawback that it does not measure the electron temperature alone, but rather it is a strong function of the electron density and the impurity concentration. The measured signal is also the line averaged value of the local emissivity, so that deconvolution of the electron temperature profile requires an accurate knowledge of the density and impurity profiles. For this reason workers using this technique, have been limited to parametrizing the signal in terms of a simple parameter felt to be representative of the electron temperature evolution. This parameter has been the delay for the signal to peak after a sawtooth crash (τ_p) at a given radial location. The electron thermal diffusivity was inferred by simulating the τ_p profile with the solution of the electron thermal energy transport equation assuming the diffusive term dominates and $\chi_e = const.$ The use of τ_p only, limits the amount of information available and the parameter may be strongly influenced by any transient transport effects due to the sawtooth itself.

In this thesis we have used a six channel FIR grating polychromator to study the evolution of the temperature at six radial locations. The advantage this technique has is that it is a single parameter measurement which is spatially resolved. This allows use of the complete temperature trace in inferring the electron thermal diffusivity. In performing the measurements we have weighted the fitting to the decaying portion of the trace.

A single sawtooth model was developed to study the parameter range over which the diffusion term dominates the electron thermal transport equation. This model represents the lowest order attempt at assessing the effects of non-diffusive terms on the evolution of the heatpulse. It assumes the idealized model of a single

sawtooth perturbation, with the background profiles satisfying the quiescent diffusion equation. The electron diffusivity profile is assumed constant. A dimensionless linearized set of equations was developed to describe the evolution of the heatpulse. The model considers only one non-diffusive term at a time, thus excluding the possibility of multiple terms combining to reduce the effective threshold for which non-diffusive effects become important. The effect of the non-diffusive term was determined by fitting the decoupled diffusion equation (eq. 3.3.11), to the temperature trace determined by solving the coupled diffusion equation with χ_e (the real χ). In this way eq. 3.3.11 gave a χ_{eff}, the apparent χ which includes the non-diffusive effects. The ratio χ_{eff}/χ_e is then a measure of the importance of the non-diffusive term. Five non-diffusive effects were considered, density pulse, radiation damping, thermal convection, Ohmic heating and electron-ion coupling. Of these, electron-ion coupling is the most significant effect, defining the lowest threshold for non-diffusive constributions. This effect couples the evolution of the electron and ion heatpulse. In this case the measured χ_{eff} should reflect in some complicated way both the electron and ion thermal transport. The dominant parameters for this effect were found to be β and ν (defined in sec. 3.3.3). Fig. 3.7a shows how $d\chi_e/\chi_{eff}$ varies as a function of β for $\nu = 90$. The largest values of $d\chi_e/\chi_{eff}$ are found for $\beta < 1$, with more moderate values found for $\beta > 1$. Taking extreme values for β (i.e. $\beta = 0.1, 3$) fig. 3.7b shows how $d\chi_e/\chi_{eff}$ scales with the collisionality parameter. We found that for even moderate values of ν ($\nu \sim 50$), electron-ion coupling could still have a significant effect ($d\chi_e/\chi_{eff} \sim 0.7$ for $\beta = 0.1$). It is for $\nu < 20$ that the predicted deviations are less than the experimental error.

The second dominant effect was found to be that of the density pulse. The parameter for which the strongest dependence was found is α, the density profile parameter. It was found that for $\alpha \sim 2$ the χ_e would be underestimated by 30%. We can interpret the dependence on α more as a dependence on the size of the initial density perturbation than on any basic transport effect. According to the initial models used, the peak density perturbation can be related to α by

$$\frac{\delta n(0)}{n(0)} \sim \alpha \frac{r_i^2}{a^2}$$

the peak temperature perturbation is

$$\frac{\delta T(0)}{T(0)} \sim \frac{r_i^2}{a_{T_e}^2}$$

for $\alpha = 2$, $r_i = 4cm$, $a = 16cm$, $a_{T_e} = 10cm$ then

$$\frac{\delta n(0)}{n(0)} \sim 0.12 \qquad \frac{\delta T(0)}{T(0)} \sim 0.16$$

This leads to the intuitive condition that the density pulse effects become important when

$$\frac{\delta n(0)}{n(0)} \sim \frac{\delta T(0)}{T(0)}$$

For Alcator $\alpha \sim 0.5$ for the case of gas puffed discharges, so that we can expect density pulse effects not to be important.

Starting from the general transport equations and neglecting the non-diffusive terms, a Fourier transform hierarchy was developed to describe the evolution of the heatpulse. The signal is Fourier decomposed over a time interval shorter than a sawtooth period. This method gives rise to a natural ordering of the various terms, with $p = 0$ representing the background sawtooth averaged profile. All terms with $p > 0$ represent the incremental profiles. The method of analysis proposed in [3.12], assumes that the background profile satisfies the quiescent transport equation (i.e. $\partial T_e/\partial t = 0$). In general the equilibrium achieved by the plasma is dynamic, determined by the sawtooth mechanism. The method proposed here takes this into account automatically, manifesting itself in a non-zero reheat term (R), which appears in the equation for every order p. It is through this reheat term that the initial and final profiles are specified. The lowest orders in p are the ones most sensitive to χ_e, in our case we only used the first six harmonics beyond $p = 0$. Each equation was solved numerically using an empirically determined reheat profile.

A sensitivity analysis was done to determine how each of the input parameters affects the estimated χ_e. The parameters studied were channel calibration,density profile,reheat profile and boundary effects. It was found that the most sensitive parameter is the spatial extent of the reheat profile. Fig. 3.20 shows the estimated χ_e profile from the same shot using the experimentally measured reheat profile (trace A) and a reheat profile consistent with a mixing radius of $r_M \sim \sqrt{2}r_i$. Variation with the other parameters is not as severe as shown in fig. 3.21.

We used the expression for χ_e derived in ref. [3.5] and compared it to the result arrived at by using our method. The estimated χ_e using the model of ref. [3.5]($\chi_e \sim 14cm^2/ms$) was a factor of three larger than that found using our method ($\chi_e \sim 5cm^2/ms$). This shows the importance of having a good estimate of the reheat profile, for the evolution of the heatpulse in the plasma is clearly very sensitive to near field effects.

We also checked to see whether the data showed any preference for a spatially varying χ_e profile. Comparisons were made between three models, a constant χ_e profile, a linearly varying χ_e and a parabolic χ_e profile. The reduced χ^2 test showed a preference for the spatially varying models over the constant model. The difference between χ^2 for the linear and parabolic models is too small to be able to differentaite between them.

The estimates for χ_e (heatpulse) were compared to those arrived at by two other models, power balance and a model which has been used to simulate Alcator discharges and which is consistent with neo-Alcator scaling. One problem of making these comparisons is that both of the 'reference' models have uncertainties which are comparable to that of the heatpulse propagation. Because of high density operation there is considerable uncertainty in estimating the electron-ion energy coupling term in the power balance formulation. This leads to large variations in the estimates for χ_{epb}. The second or standard model as it has been refered to in this work was developed to simulate the transport over a wide range of parameters and as such there can be large variations in the value this model predicts and that are actually present in the plasma.

In comparing the profiles we found the power balance estimates to be flatter than the heatpulse estimate and the overall magnitudes to be within a factor of two from each other in the measurement region. Part of the reason for the flatness of the power balance profiles is due to sawtooth effects incorporated in the analysis. The standard model gives χ_e profiles which give better agreement with the heatpulse estimates. The overall agreement is also within a factor of two. The heatpulse estimates for κ_e give a profile which increases roughly linearly with radius over the measurement region fig. 3.15b.

Fig. 3.23 shows the scaling for χ_{ehp} vs. χ_{epb}. Although there is scatter, the trend is for χ_{ehp} to increase with χ_{epb}. The ratio χ_{ehp}/χ_{epb} is bounded between $1-3$, with a mean value of 1.7 . As we can see from the figure all the data points lie above $\chi_{ehp} = \chi_{epb}$ line, suggesting a systematic over estimation of the thermal diffusivity especially at the higher densities. The reason for this remains unclear, although several possible effects were proposed. Multiple non-diffusive effects could be acting together to increase the estimated χ_e. A systematic under estimation of the reheat profile could account for the discrepancy, however this seems unlikely for if anything, instrumental width effects will tend to overestimate r_M. In chapter II we found that the effective χ_e during a sawtooth disruption can be two orders of magnitude larger than the bulk. There could be a time changing remnant of this anomalous value affecting the evolution near the center of the plasma. This can have large effects on the evolution of the incremental profiles and not on the time averaged profiles. A similar trend is found in TFTR[3.5], however they find a discrepancy which is a factor of $\chi_{ehp}/\chi_{epb} \sim 10-20$. They attribute this discrepancy to the possibility that the heatpulse may evolve with a χ_e which is higher than that effective for the bulk.

We argued that the quantity $1/\chi_e$ is proportional to the energy confinement time. In fig. 3.25 we showed the scaling of $1/\chi_e$ at three different radii. At all three radii the data is consistent with $1/\chi_e \sim \overline{n}$. This also implies that the average profile shape for χ_e must be weakly dependent on $\overline{n}_e$.

The scaling of $1/\chi_e$ shows no saturation with density as does the global energy confinement. While this picture is consistent with the ions being the loss channel, it is not definitive because as we have shown electron-ion coupling effects are important in this region. If $\beta < 1$, which is the case for the electrons being the loss channel (i.e. $\chi_e > \chi_i$), electron-ion coupling effects indicate that $\chi_{real} > \chi_{eff}$. This picture is consistent with the 'real' electron energy confinement time saturating with density. If $\beta > 1$, which is the case for the ions being the loss channel(i.e. $\chi_i > \chi_e$), electron-ion coupling gives $\chi_{real} < \chi_{eff}$. In this case the 'real' electron energy confinement time continues rising with density. The final interpretation thus depends sensitively on the value of β, without knowledge of χ_i this introduces large variations in the possible values for the real χ_e. In order to make the measurement in this region, a simultanious measurement of the ion heatpulse will have to be done.

We believe future work in this area, should center on improving the model which describes the evolution of the heatpulse. With emphasis in trying to understand why χ_{ehp} seems to be always higher than χ_{epb}. If this technique is to be used to measure the energy transport at high densities, ways must be found to include the effects of the ion heatpulse. We only considered simple non-diffusive effects in our single sawtooth model, however multiple effects may combine to reduce, the effective threshold below that defined by electron-ion coupling.

References for chapter III

[3.1] Callen J.D.,Jahns G.L.,Phys. Rev. Lett. 39(1977)491

[3.2] Jahns G.L.,et. al., Nucl. Fus. 18,5(1978)

[3.3] Soler M.,Callen J.D.,Nucl. Fus. 19,6(1979)

[3.4] Bell J.D.,ORNL report ORNL/TM-8851 (1984)

[3.5] Fredrickson E.D., et. al. to be published

[3.6] Ejima S.,Okabashi M.,Phys. Fluids 18,7(1975)904

[3.7] T-10 Group, EPS Conf. Proc. (1985)

[3.8] Jahns G.L.,et. al., GA report GA-A17858 (1985)

[3.9] Alcator Group, MIT-PFC report PFC/IR-82-3 (1982)

[3.10] Chang C.S., Hinton F.L., Phys. Fluids 25,9(1982)1493

[3.11] Post D.E.,Jensen R.V., Atomic Data and Nucl. Tables 20,5(1977)

[3.12] Stacey W.M., Fusion Power Analysis, Wiley and Sons, N.Y. (1981)264

[3.13] Wolfe S.M.,private communication

[3.14] Parker R.R.,et. al.,MIT-PFC report PFC/JA-85-14

[3.15] Blackwell B.,et. al., MIT-PFC report PFC/CP-82-7

[3.16] Wolfe S.M.,MIT-PFC report PFC/JA-85-31

[3.17] Piekaar H.W.,et. al., Bull. Am. Phys. Soc. 30,9(1985)

[3.18] Terry J., private communication

[3.19] Pfeiffer W.W.,et. al., GA report GA-A16178 (1980)

[3.20] Braginskii S.I.,Rev. of Mod. Phys. vol. I Consultants Bureau,N.Y. (1965)

[3.21] Wolfe S.M.,private communication

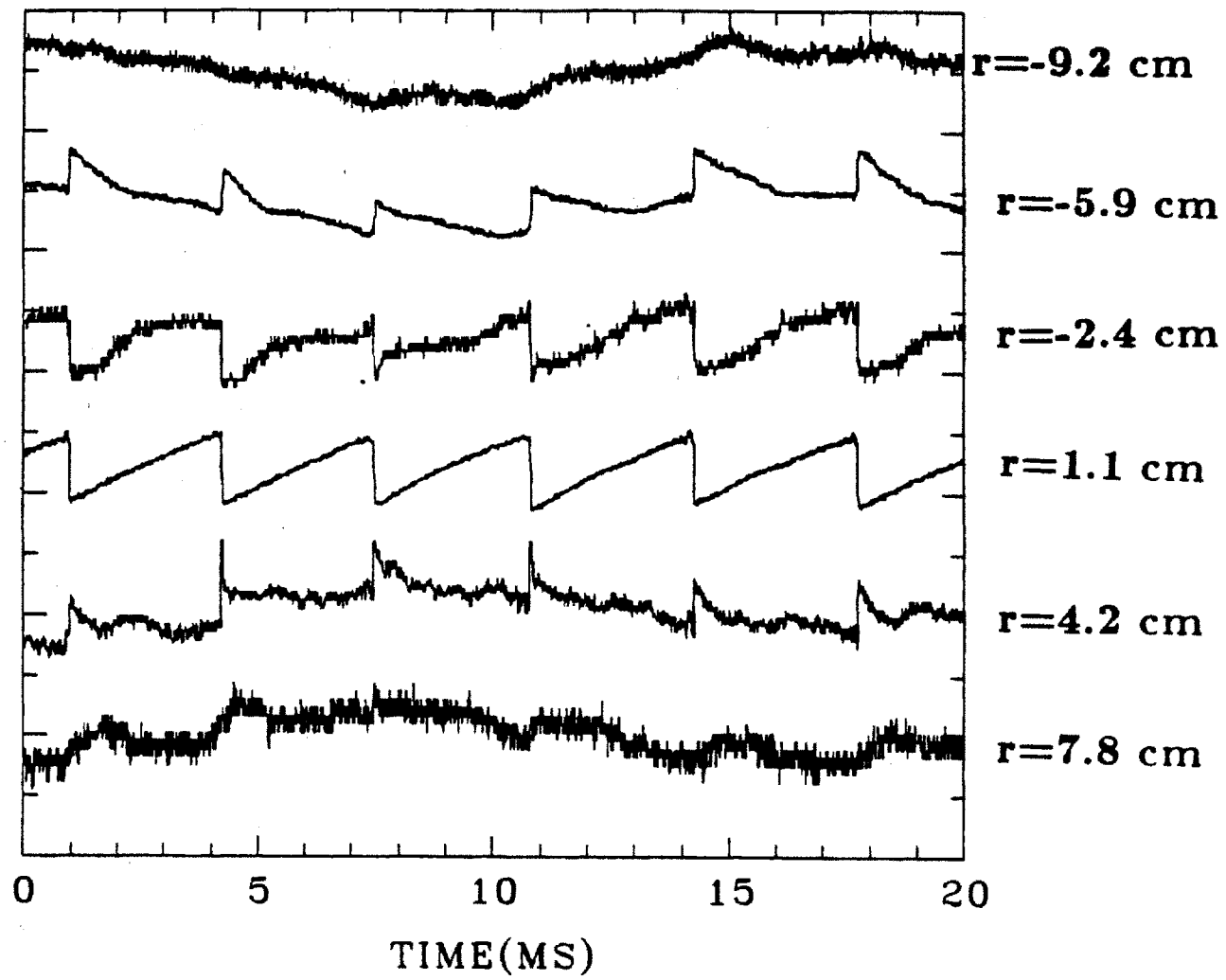

Figure 3.1 — Example of output of six channel grating showing evolution of electron temperature at six radial locations during sawtoothing.

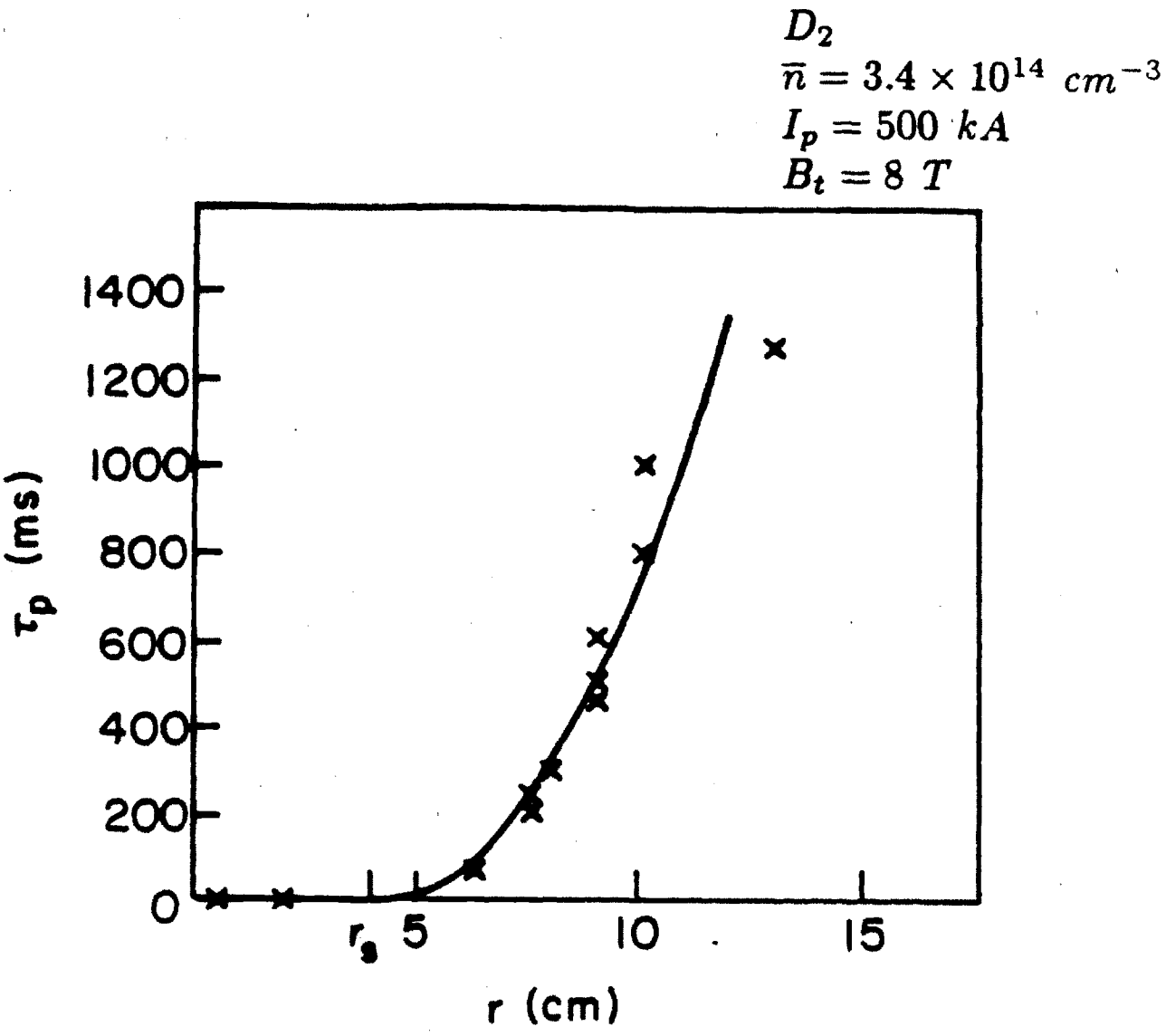

Figure 3.2 — Radial dependence of τ_p (the delay for the signal to peak at a given radial location).

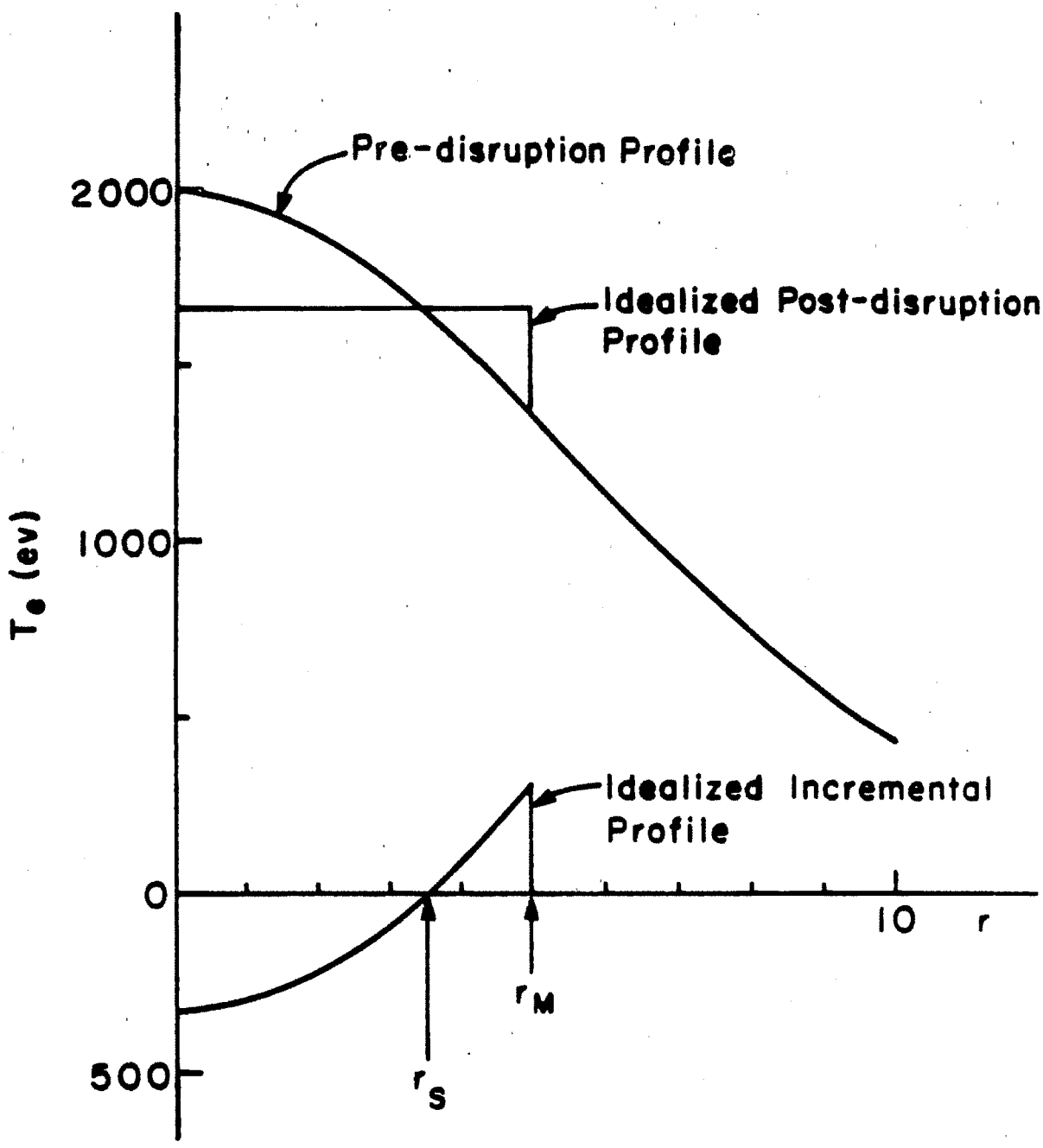

Figure 3.3 — Parametrization of initial perturbation used in ref. [3.2].

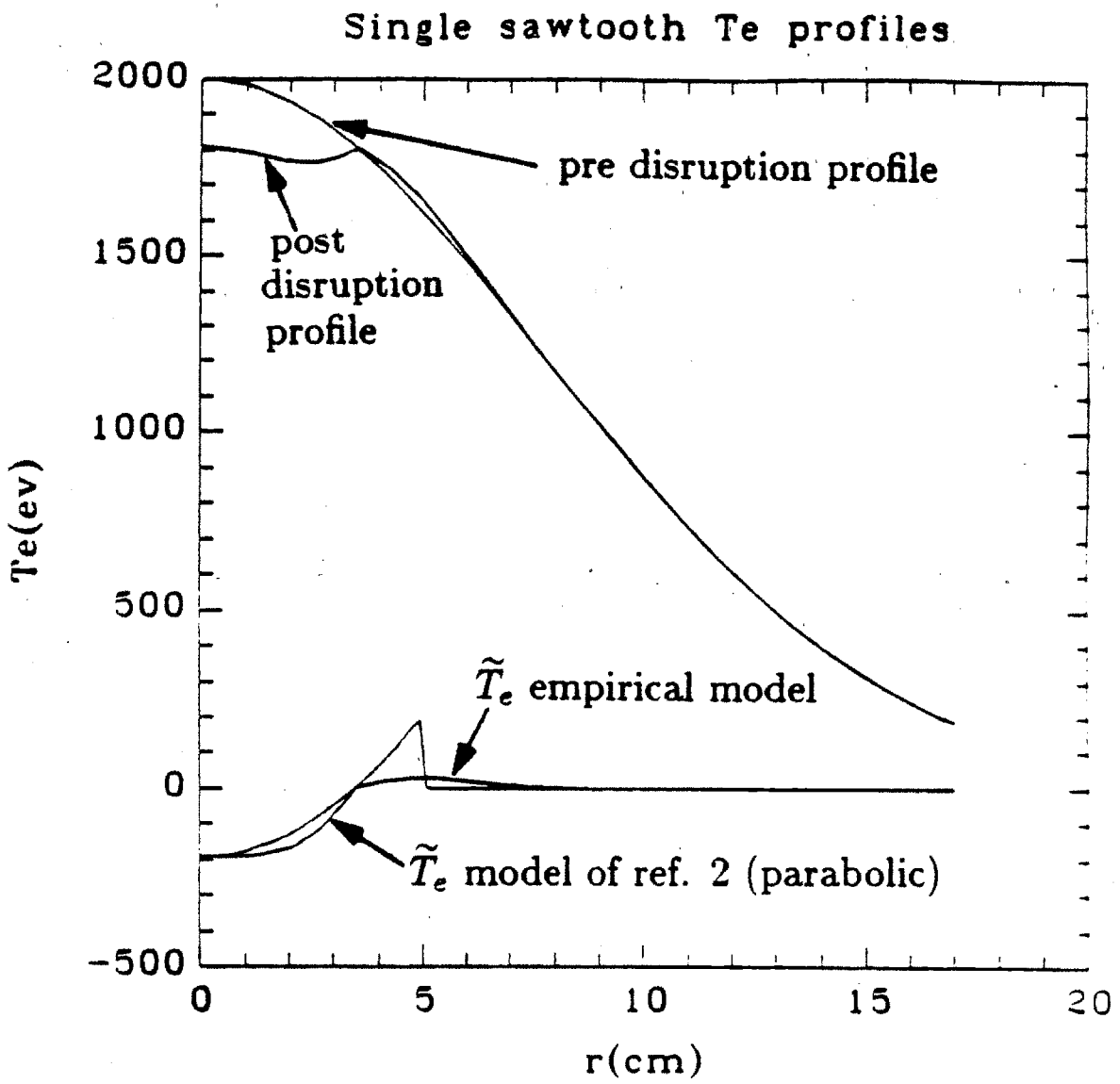

Figure 3.4 — Electron temperature profiles used in single sawtooth model.

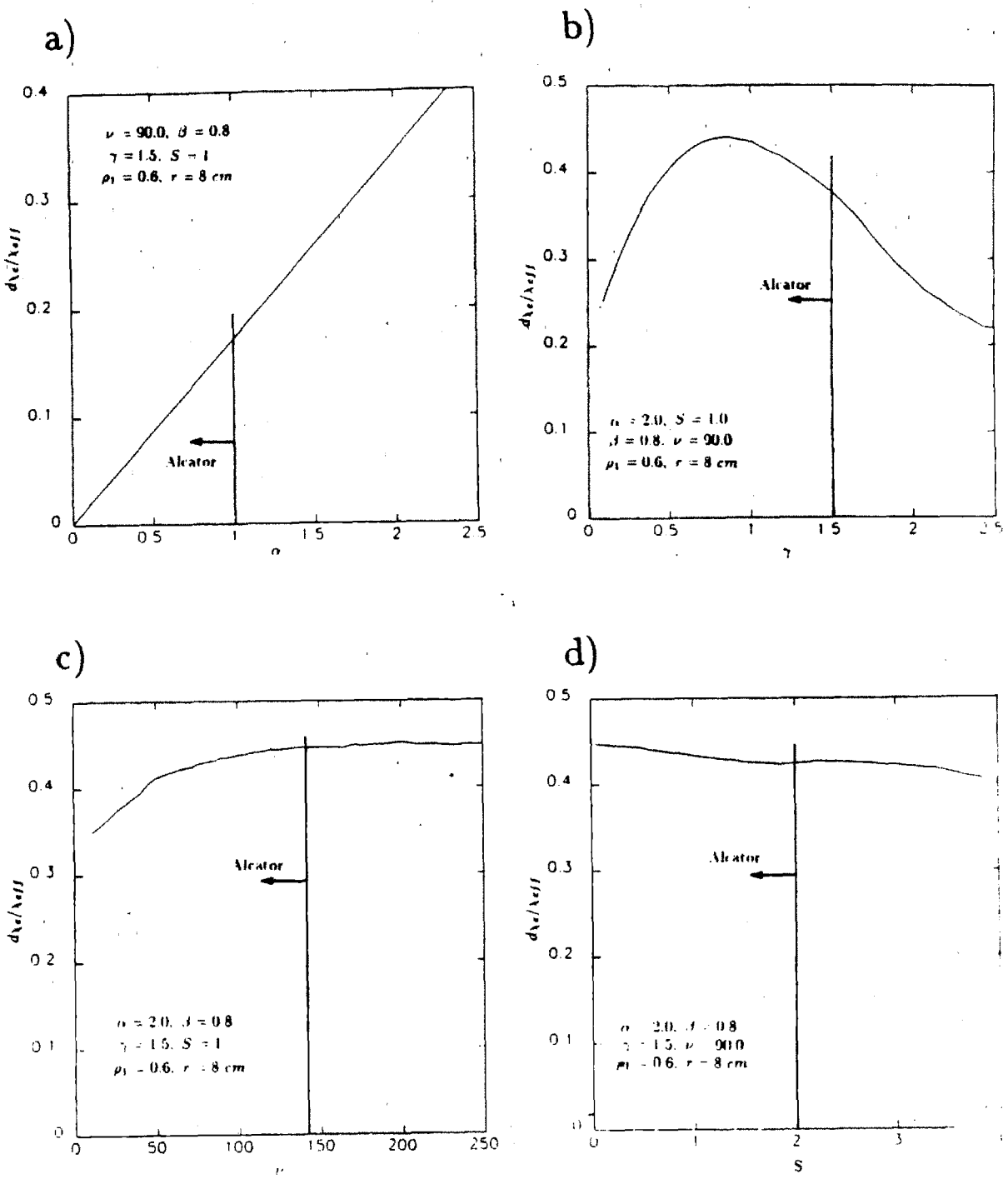

Figure 3.5 — Variation of error in estimate of χ_e with various plasma parameters.

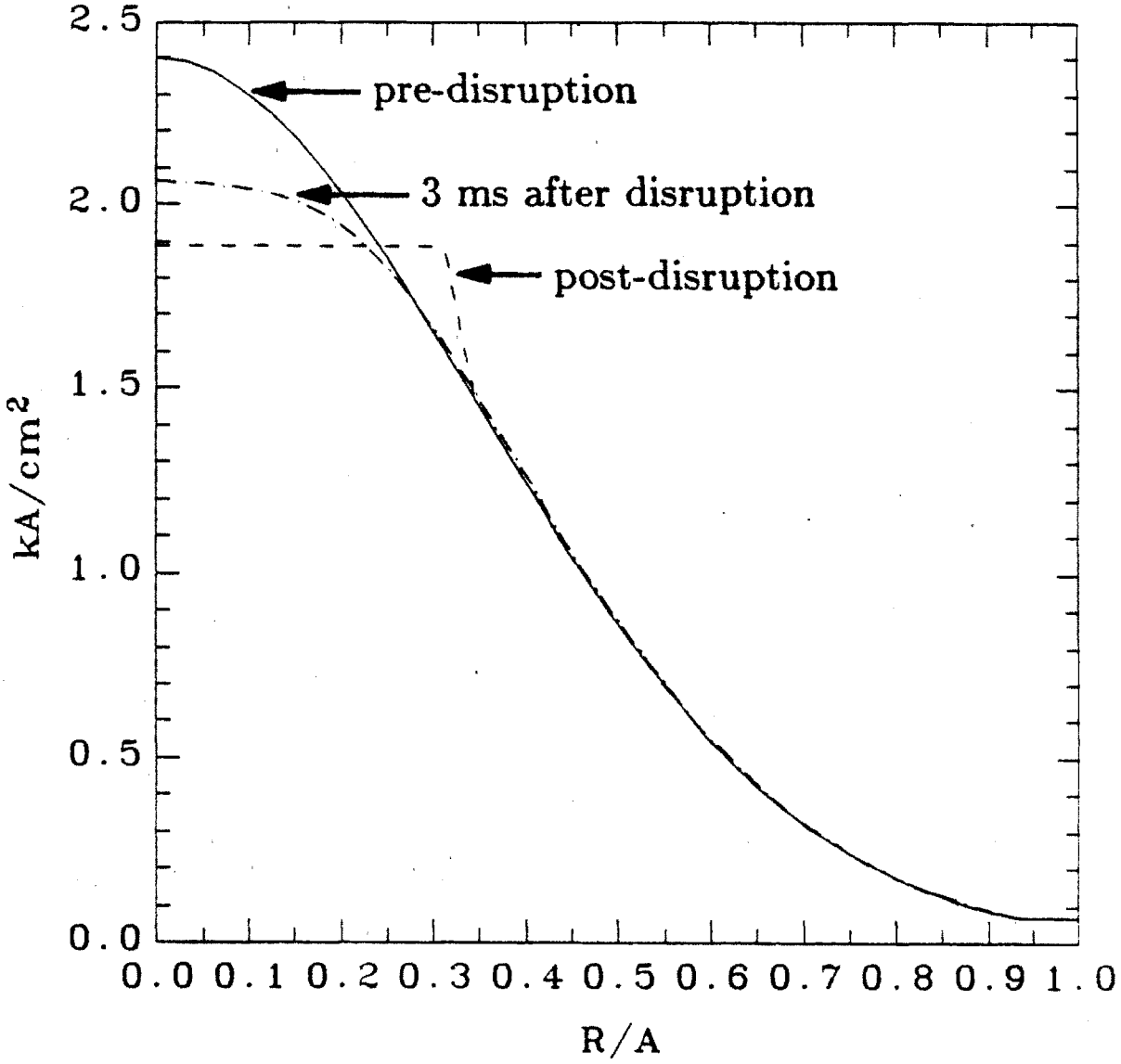

Figure 3.6 — Evolution of current profile after sawtooth disruption.

a)

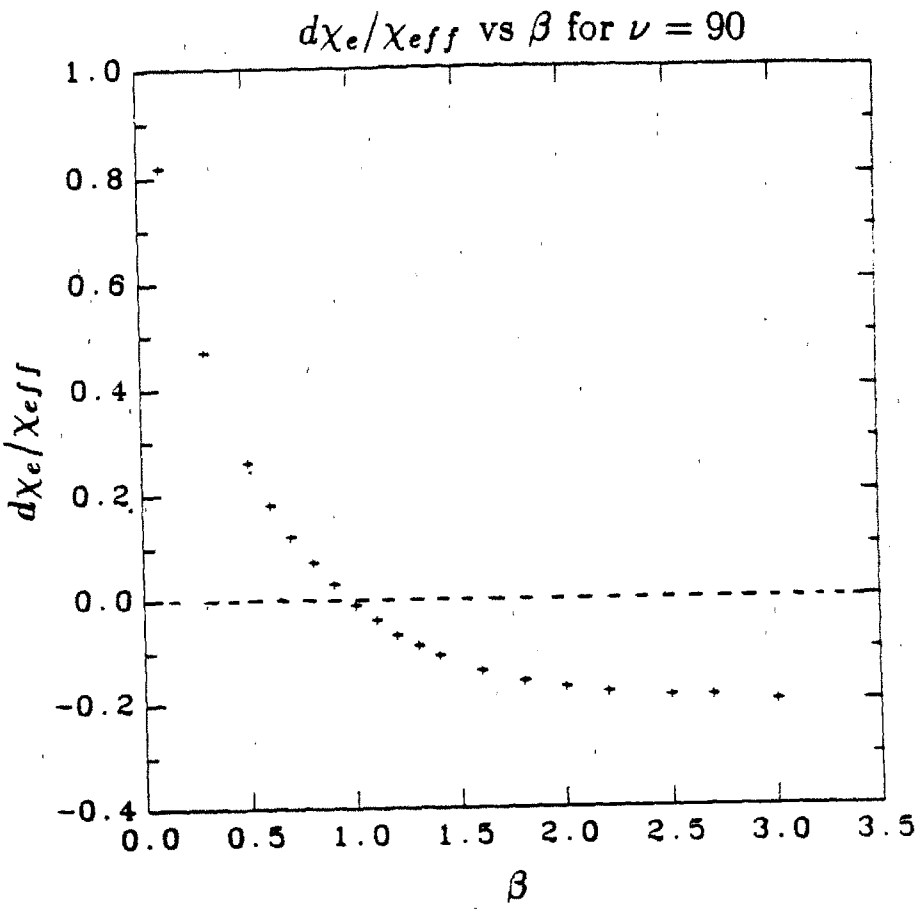

b)

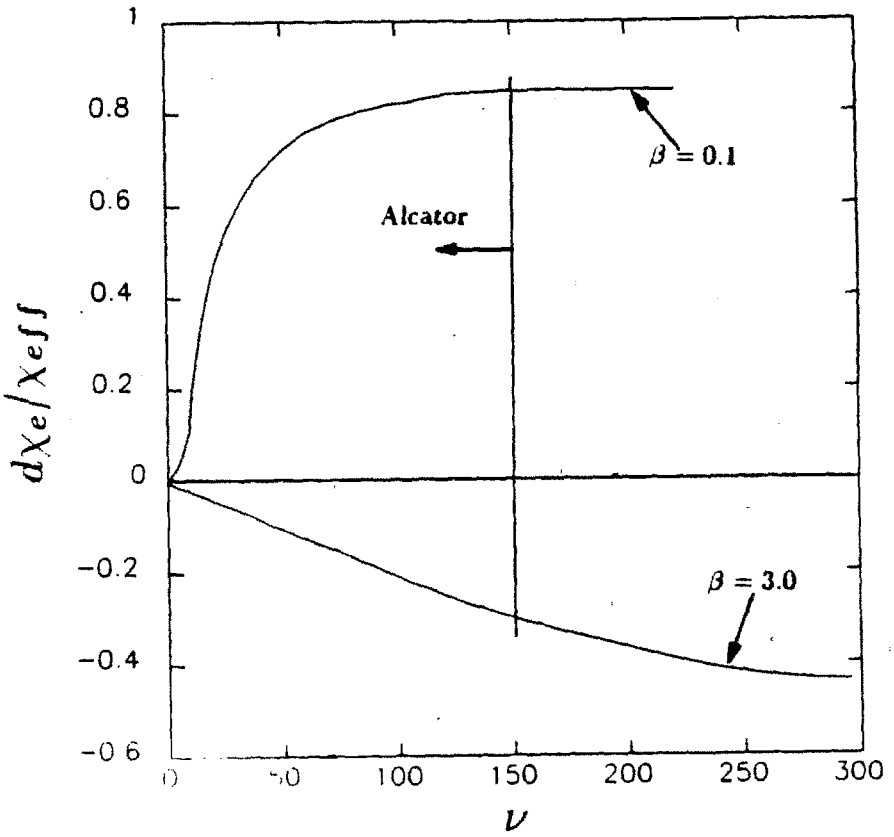

Figure 3.7 — Effects on χ_{eff} due to electron-ion coupling a)shows dependence on β for fixed ν, b)shows dependence on ν for extreme values of $\beta = 0.1, 3$.

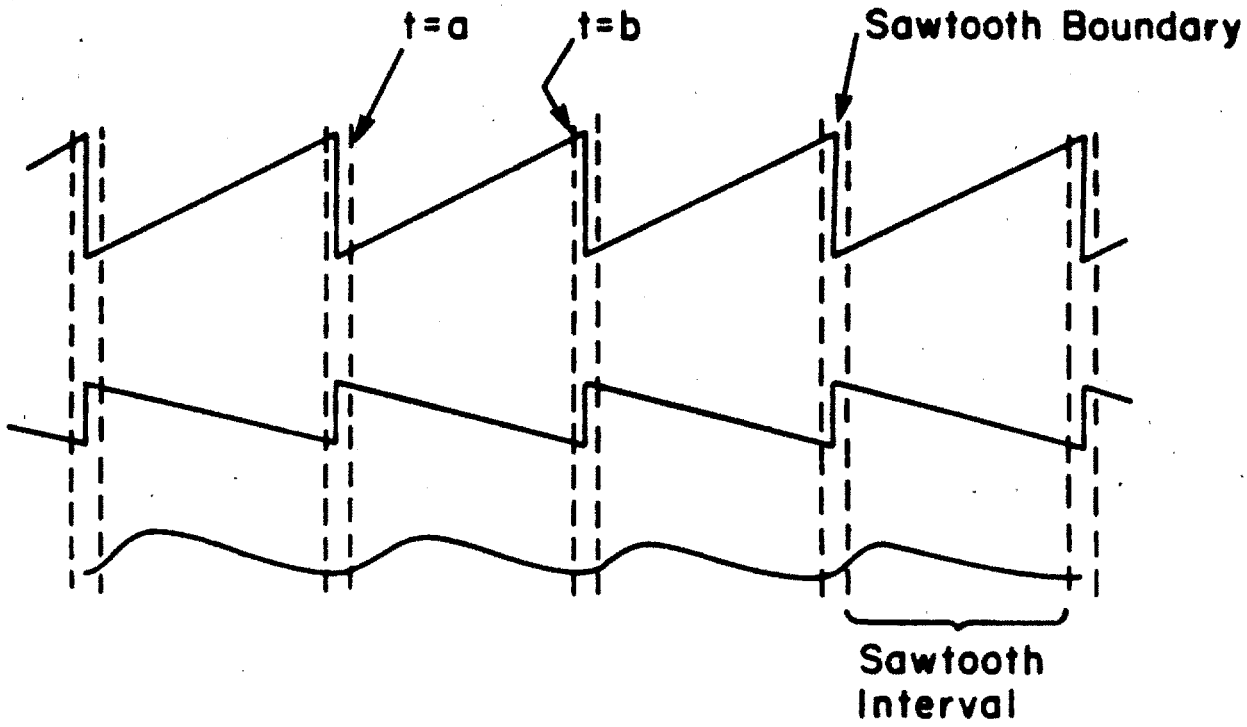

Figure 3.8 — Decomposition of sawtooth sequence for analysis.

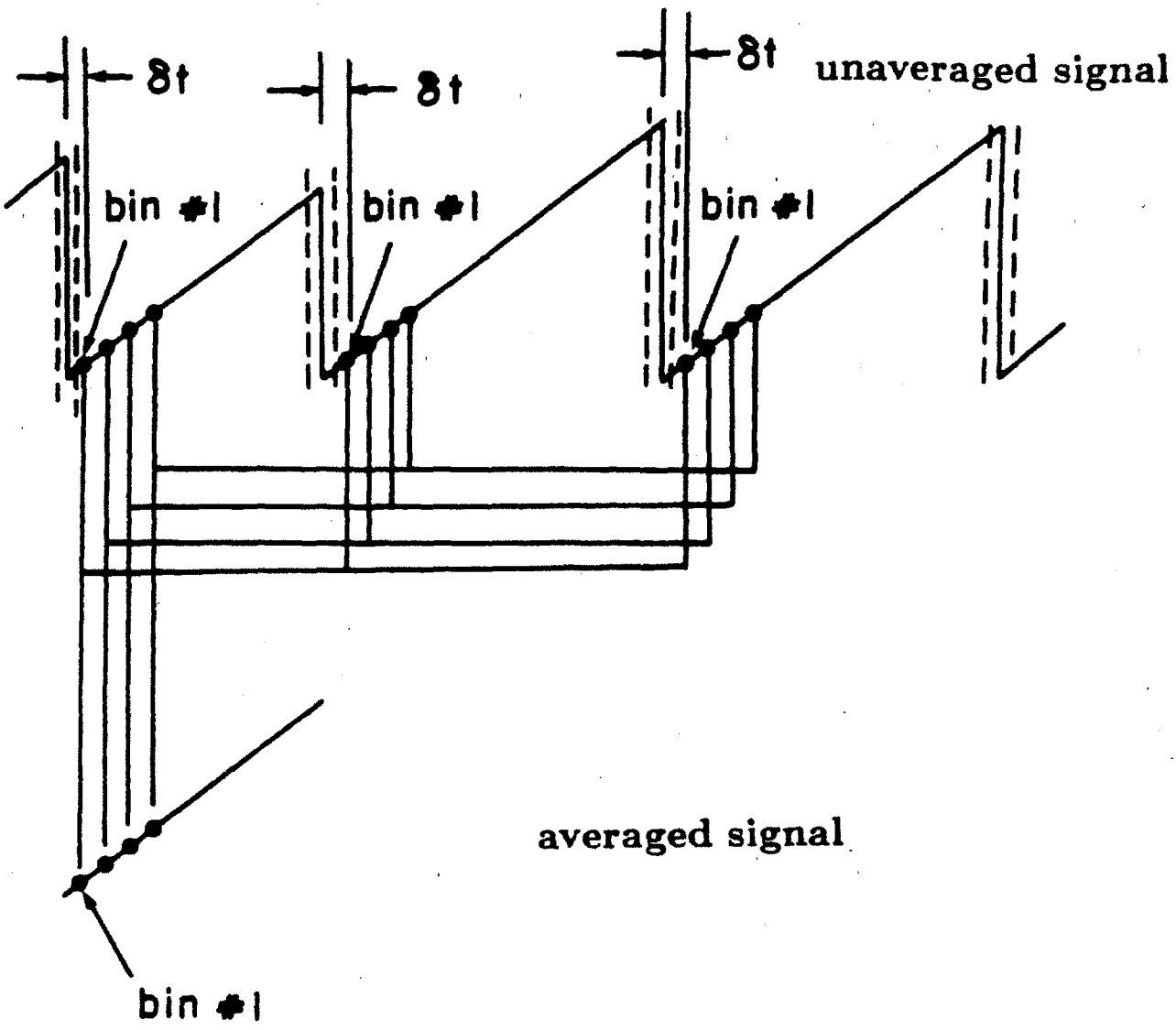

Figure 3.9 — Scheme for sawtooth averaging.

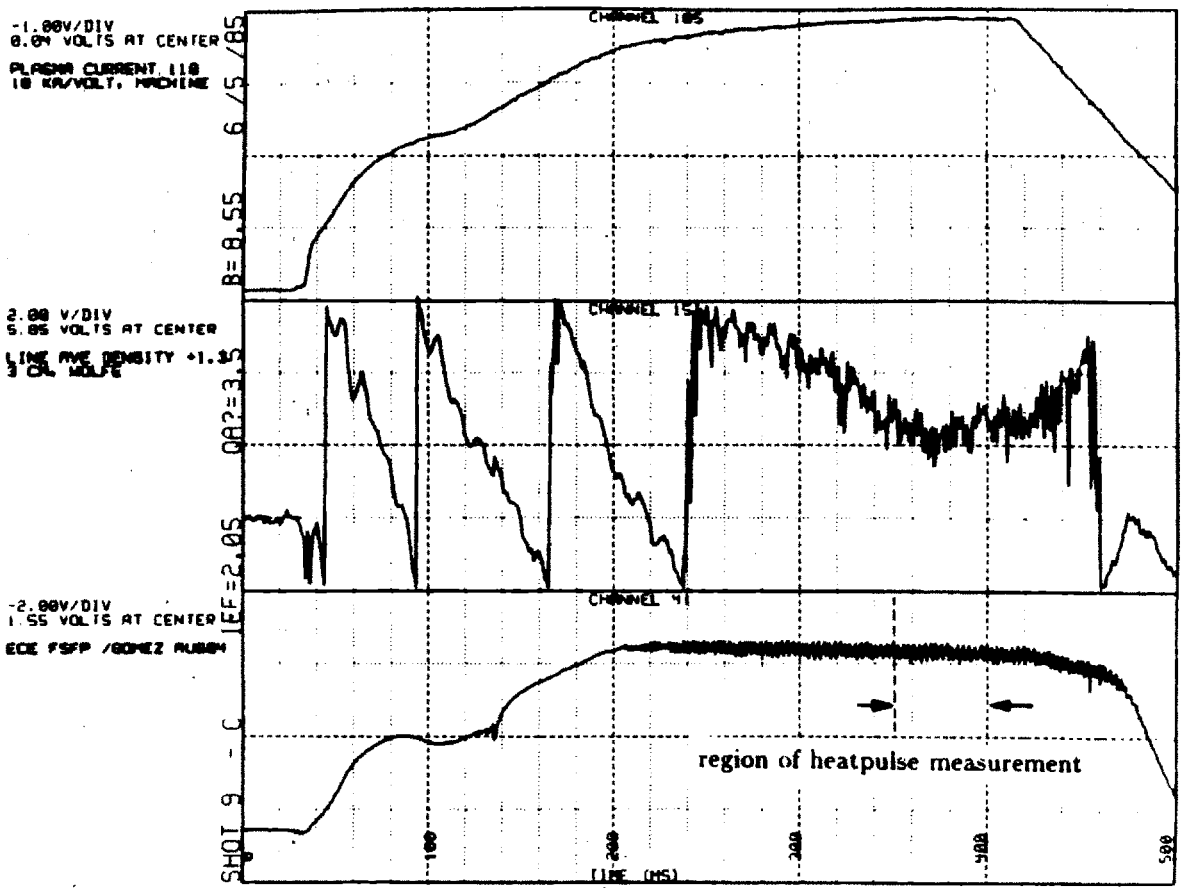

Figure 3.10 — Plasma parameter evolution for sample case discussed in sec. 3.4.6.

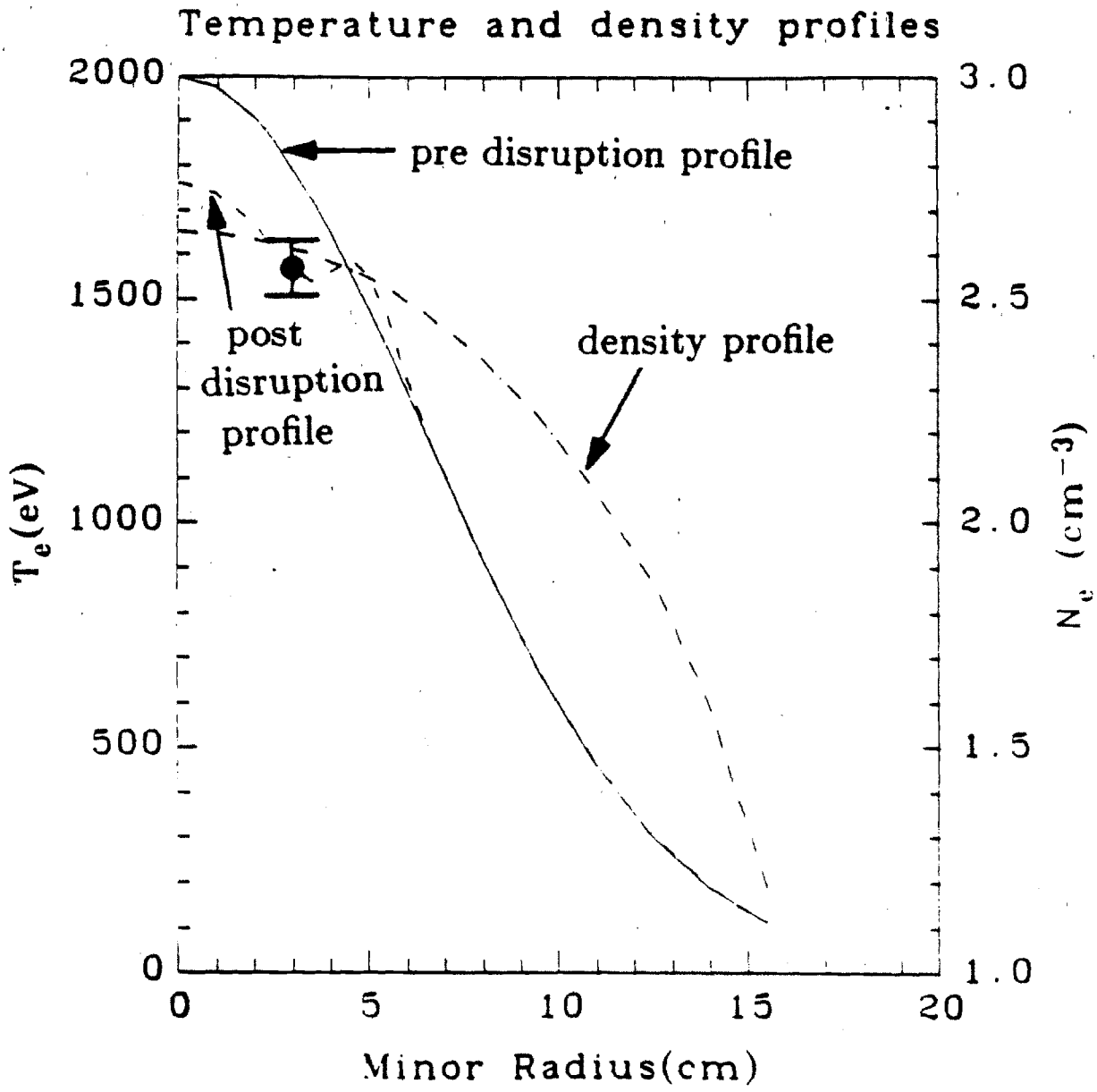

Figure 3.11 — Background profiles used in sample case of sec. 3.4.6.

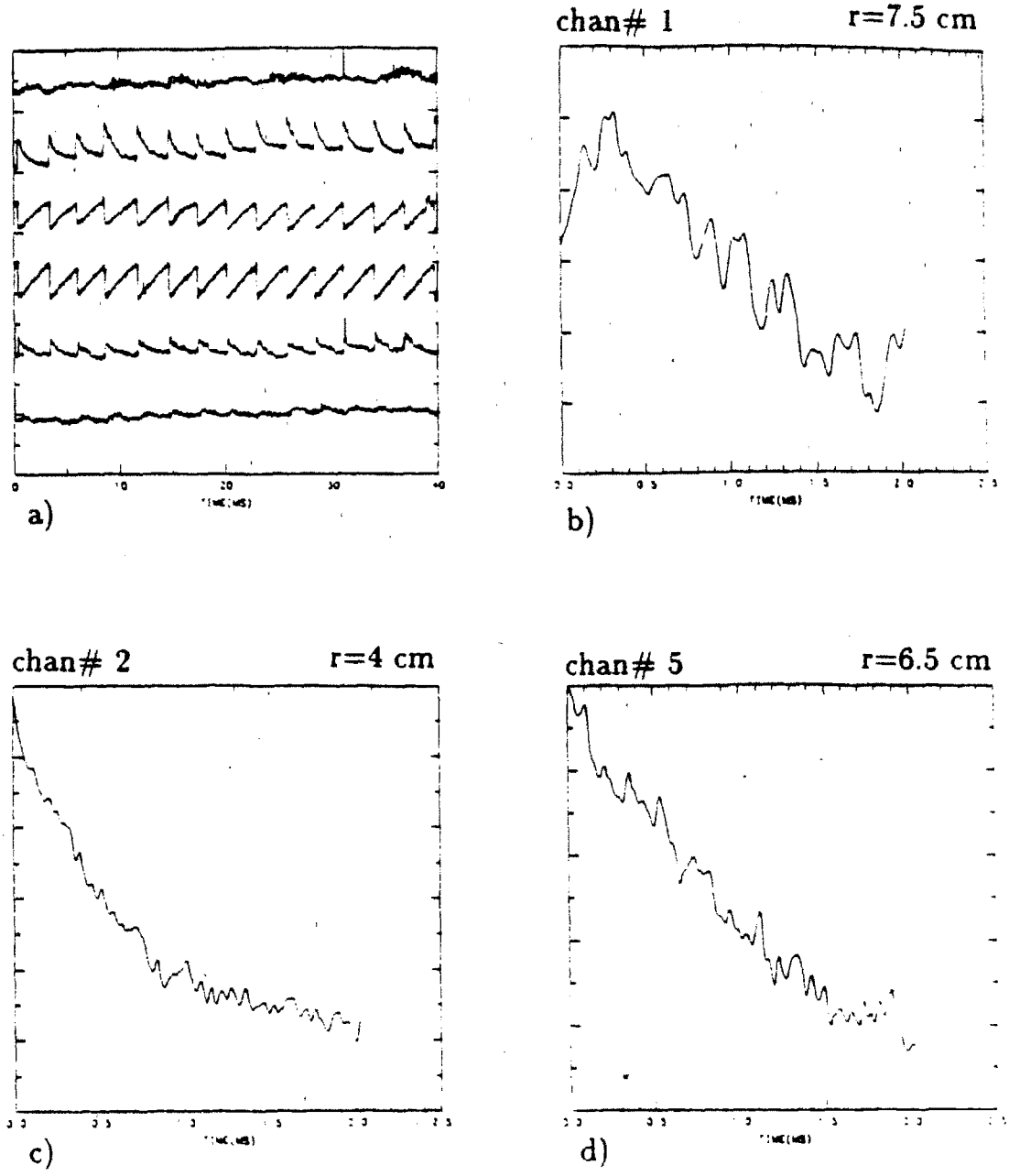

Figure 3.12 — ECE traces for sample case of sec. 3.4.6. Fig. a shows the trace data for the six grating channels, the other three figures show the sawtooth averaged traces used in the fitting.

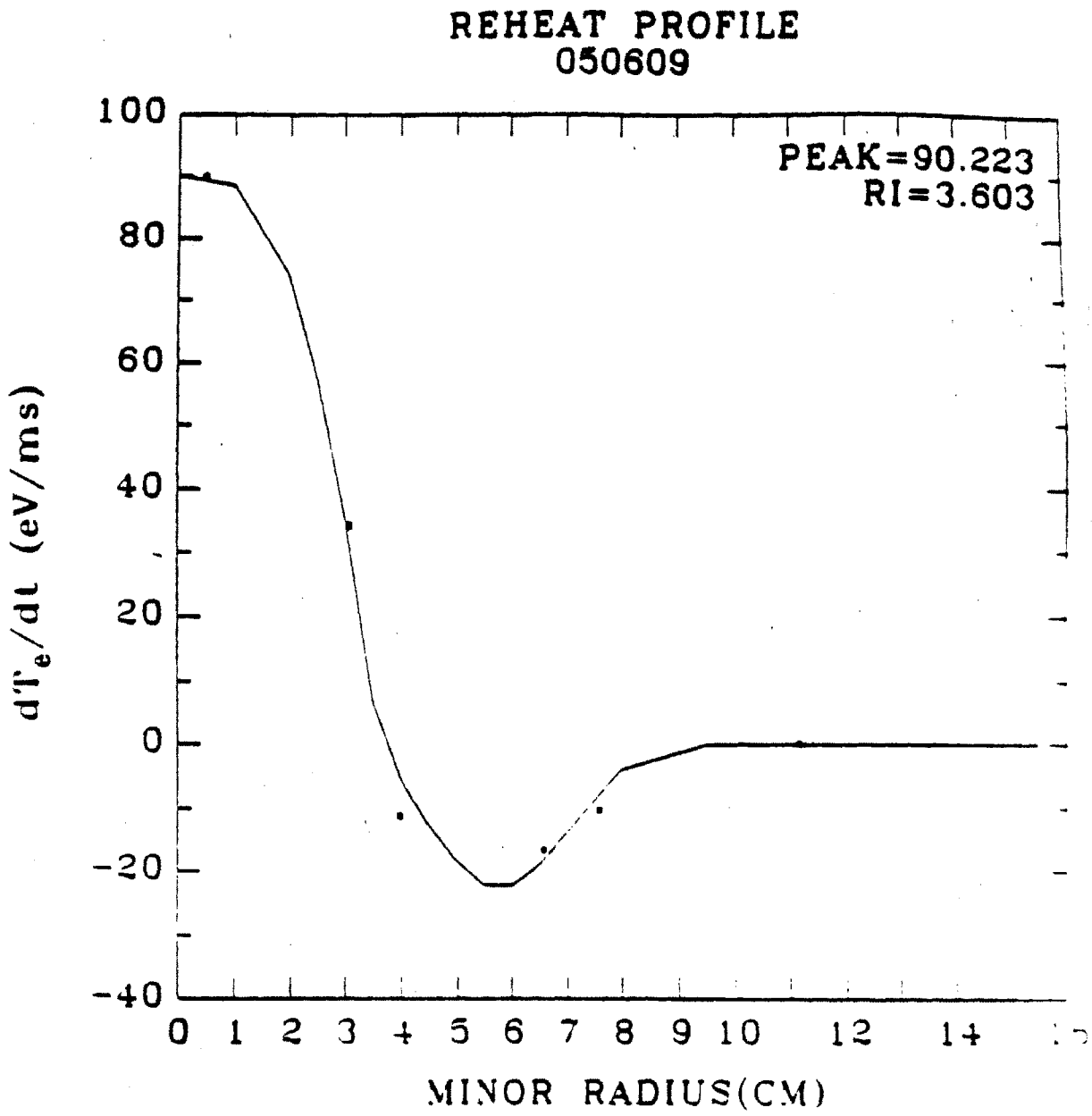

Figure 3.13 — Reheat profile for sample case of sec. 3.4.6.

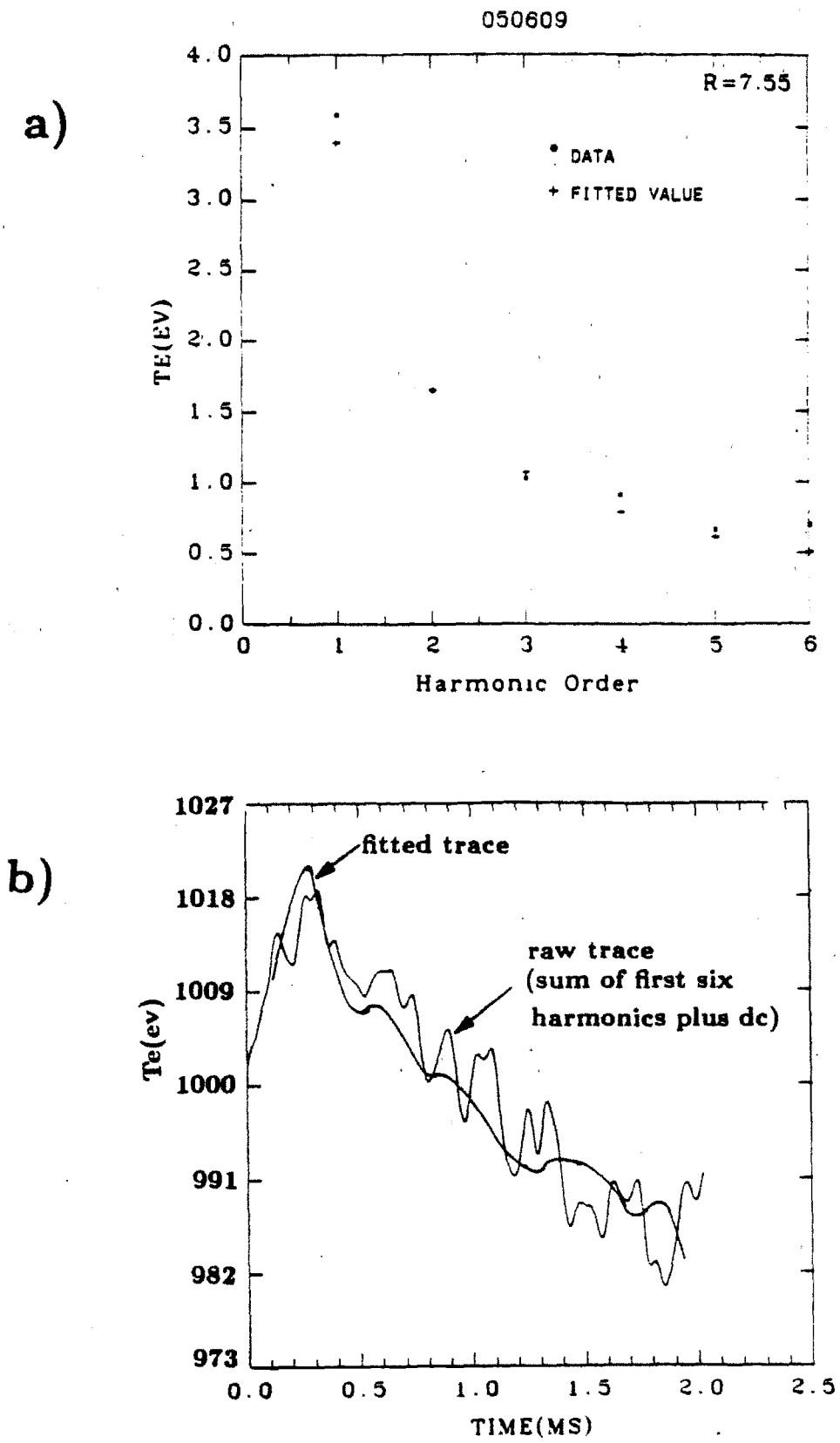

Figure 3.14 — a)Comparison of absolute value of calculated and measured spectrum for sample case of sec. 3.4.6. b)Time reconstruction of spectra shown in (a).

a)

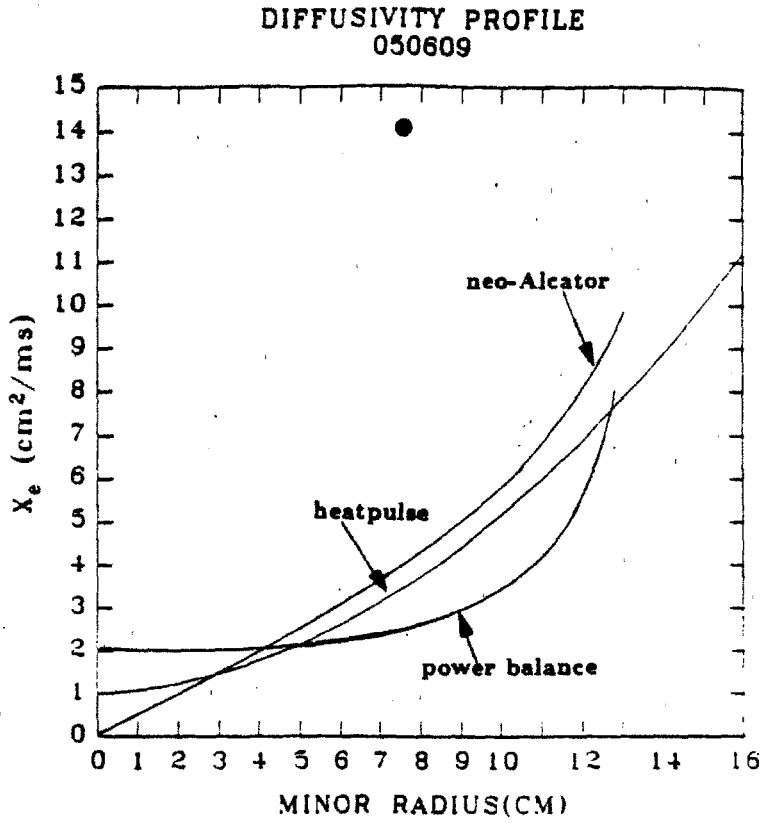

b)

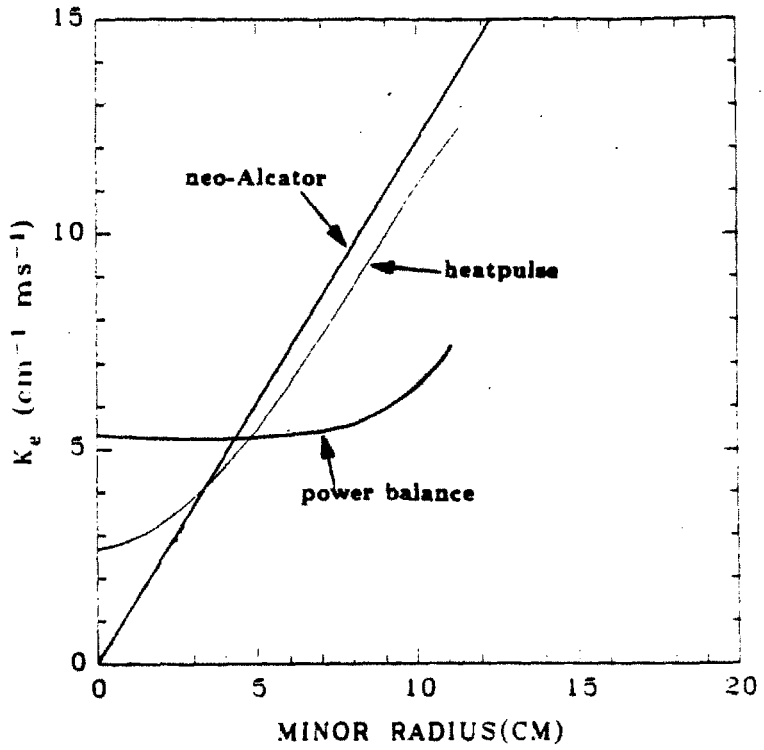

Figure 3.15 — a)Comparison of χ_e profile as estimated using heatpulse propagation,'neo-Alcator' model (discussed in text) and power balance model. We also show (bullet) the χ_e estimated by using the form of ref. [3.5]. b)Thermal conductivity profiles for traces shown in (a).

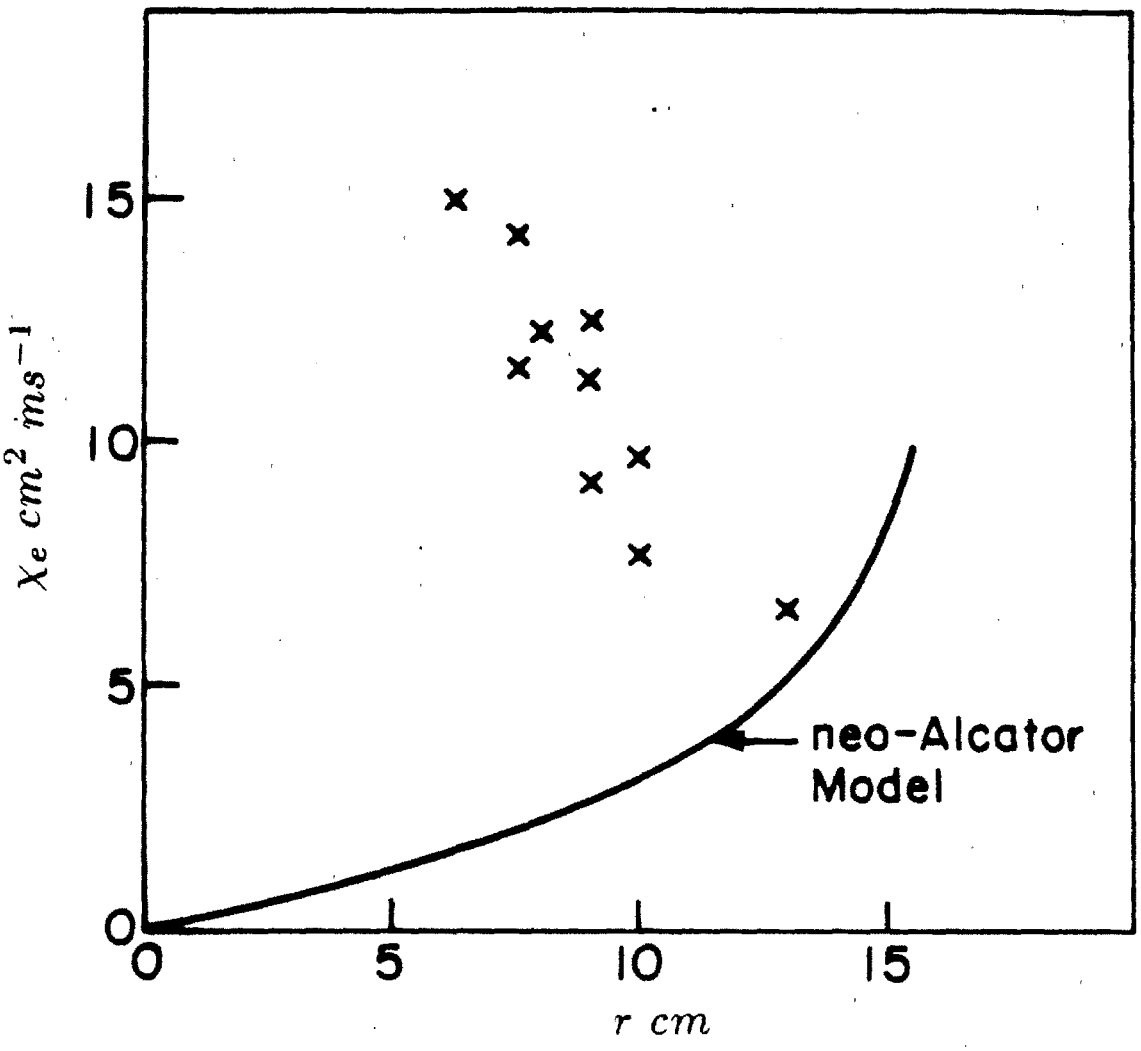

Figure 3.16 — Estimated values of χ_e using the τ_p data from fig. 3.2 and the model from ref. [3.5]. The solid line represents the 'neo-Alcator' model.

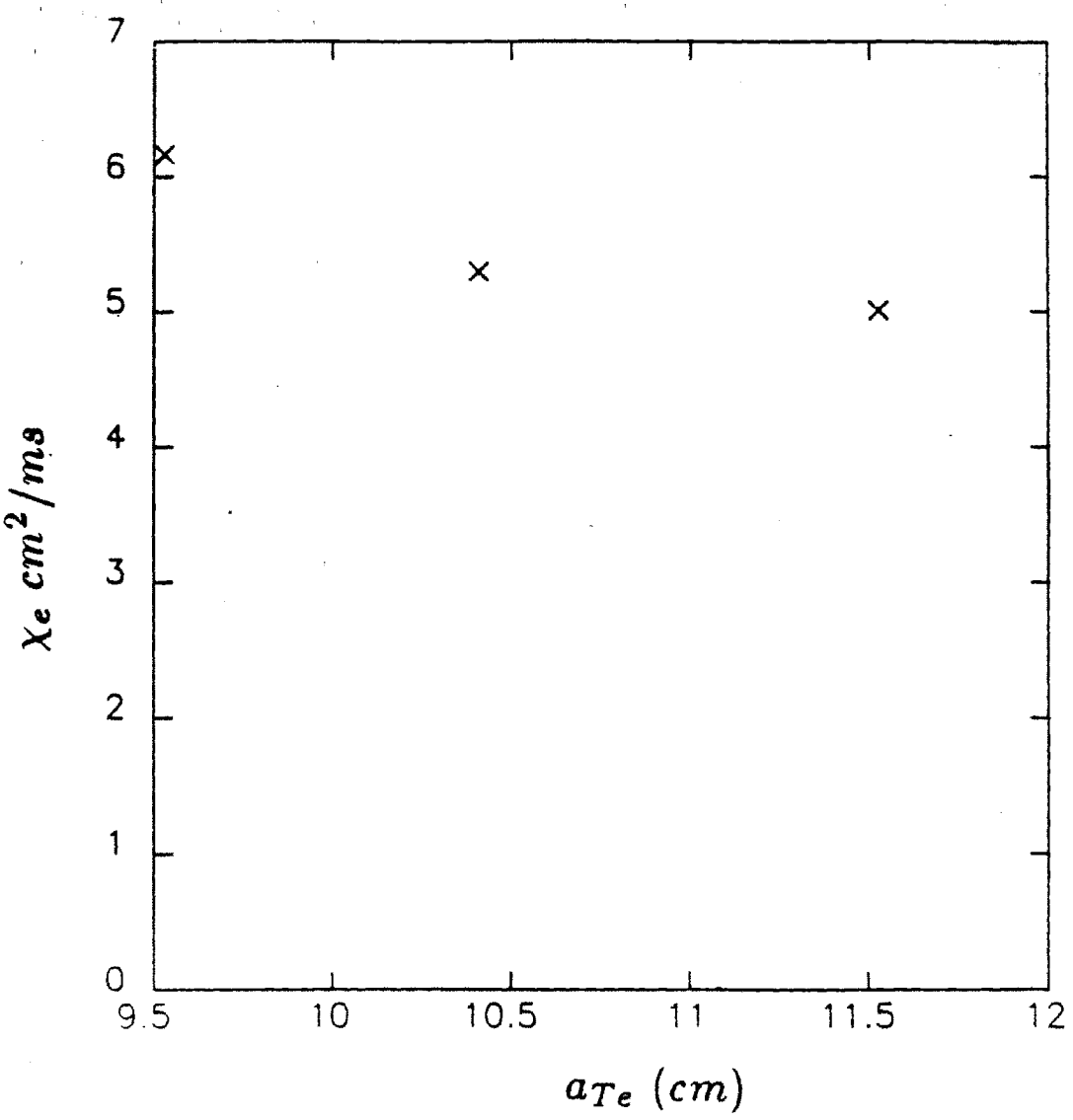

Figure 3.17 — Sensitivity of χ_e on background profile width.

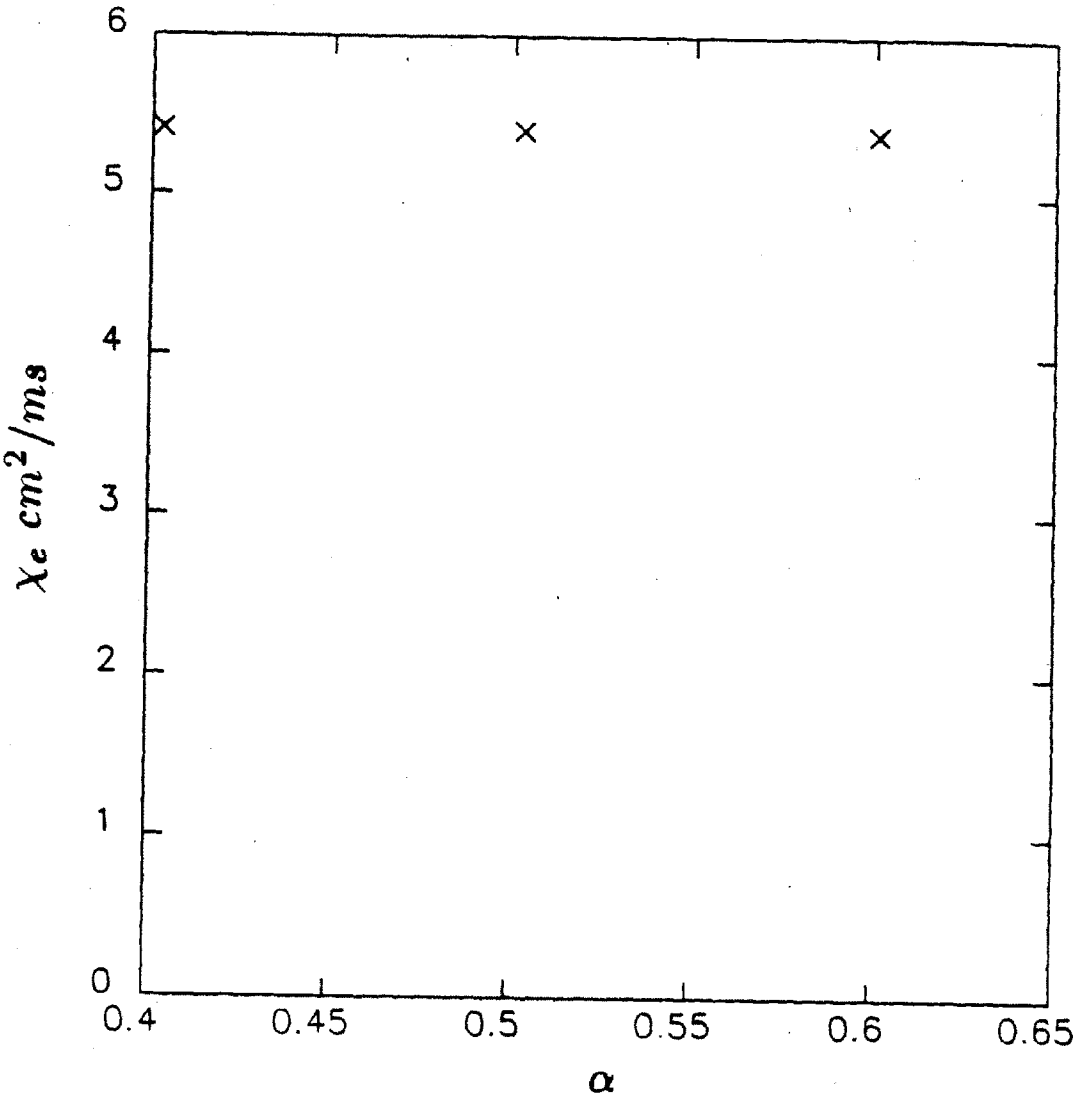

Figure 3.18 — Scaling of χ_e with density profile shape coefficient α.

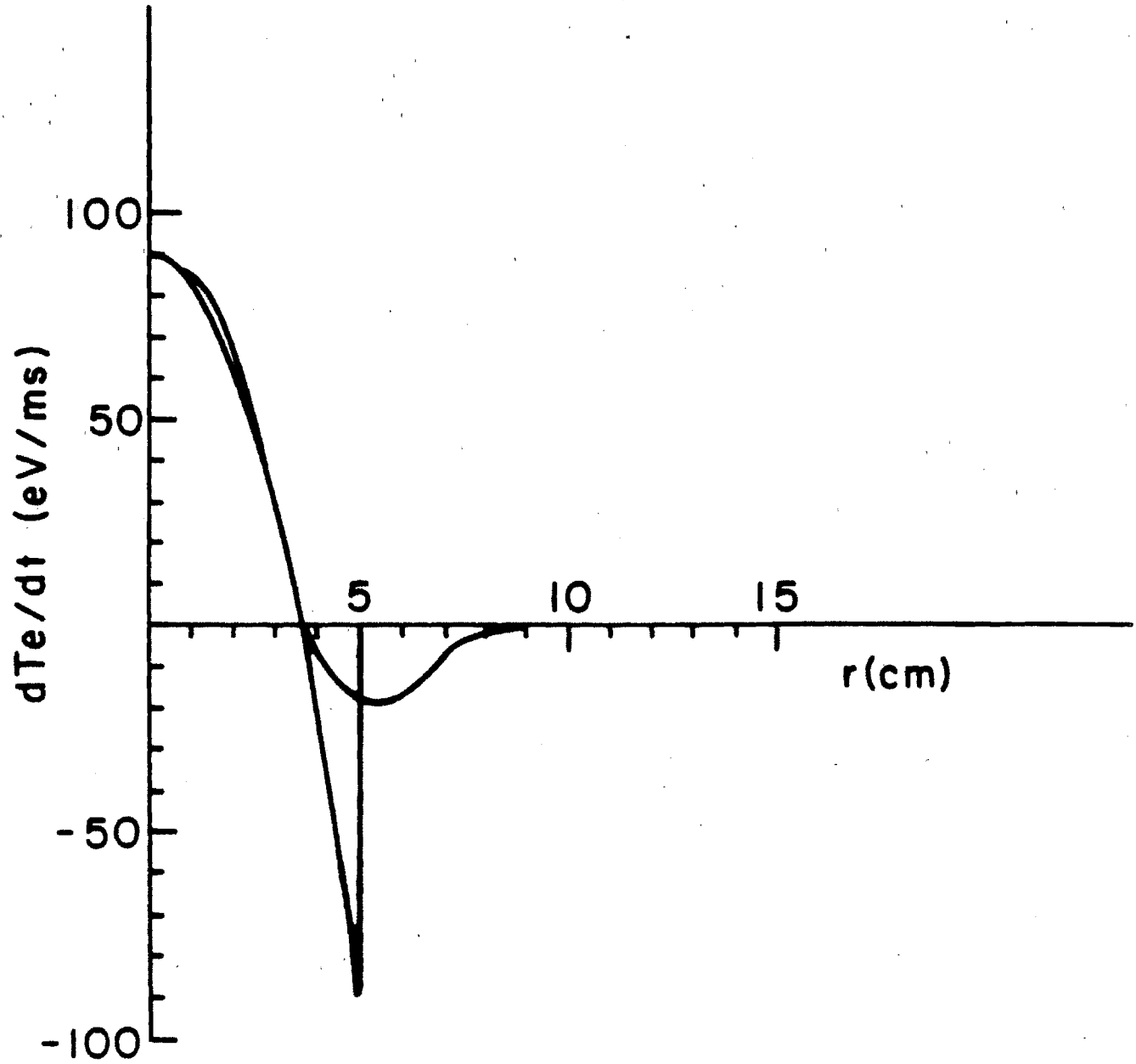

Figure 3.19 — Reheat profiles used in sensitivity analysis of sec. 3.5

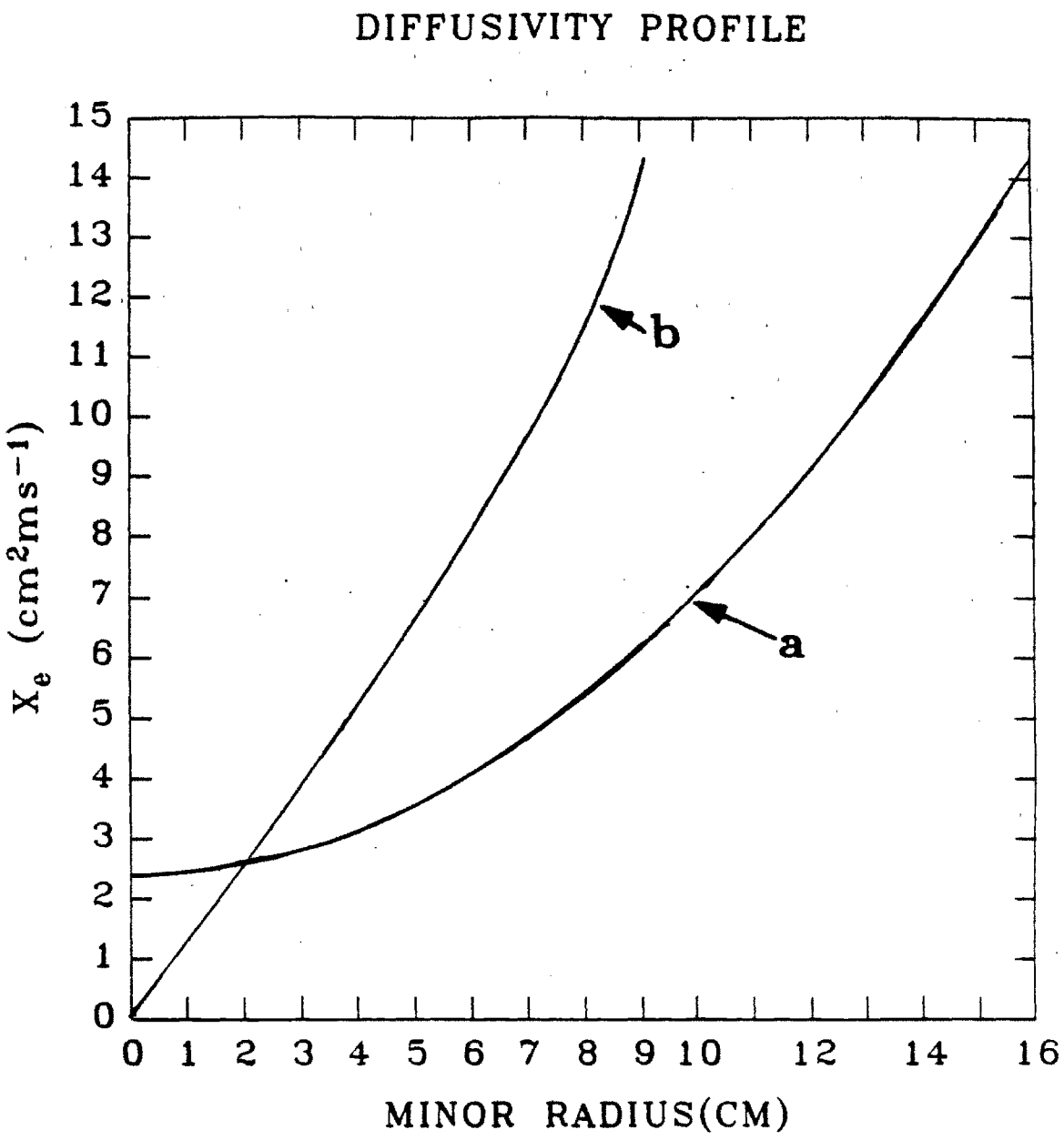

Figure 3.20 — Sensitivity of χ_e to initial reheat profile. Trace A uses the measured reheat profile while trace B uses a parabolic profile.

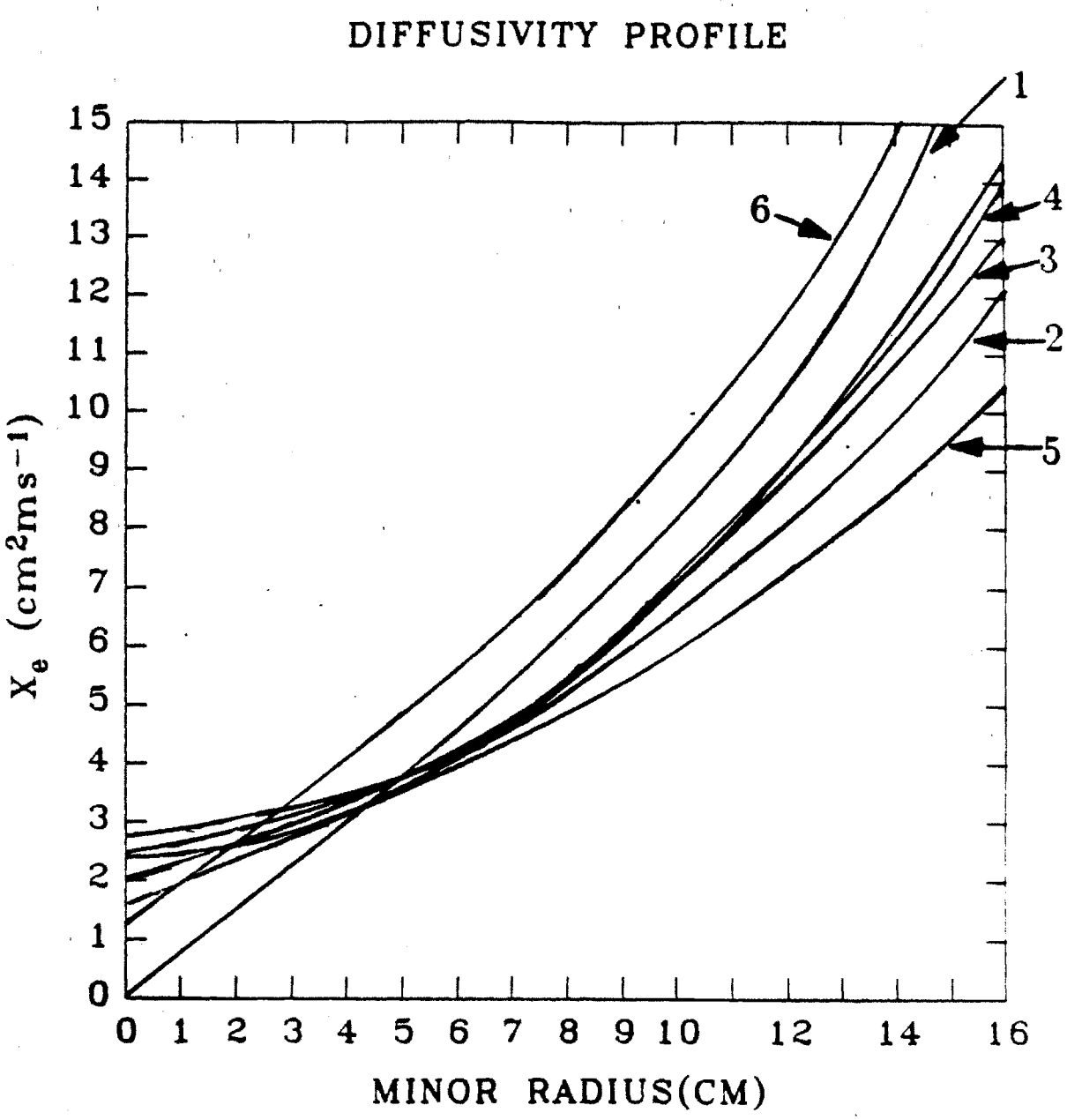

Figure 3.21 — Variation of χ_e with background profile parameters. The standard parameters for this case were $a_{T_e} = 10.4$, $\alpha = 0.5$, $r_i = 3.7$. Each parameter was varied within the expected error. Trace 1- $a_{T_e} = 9.5cm$,trace 2- $a_{T_e} = 11.5cm$, trace 3- $\alpha = 0.4$, trace 4- $\alpha = 0.6$, trace 5- $r_i = 4.4cm$, trace 6- $r_i = 3.2cm$.

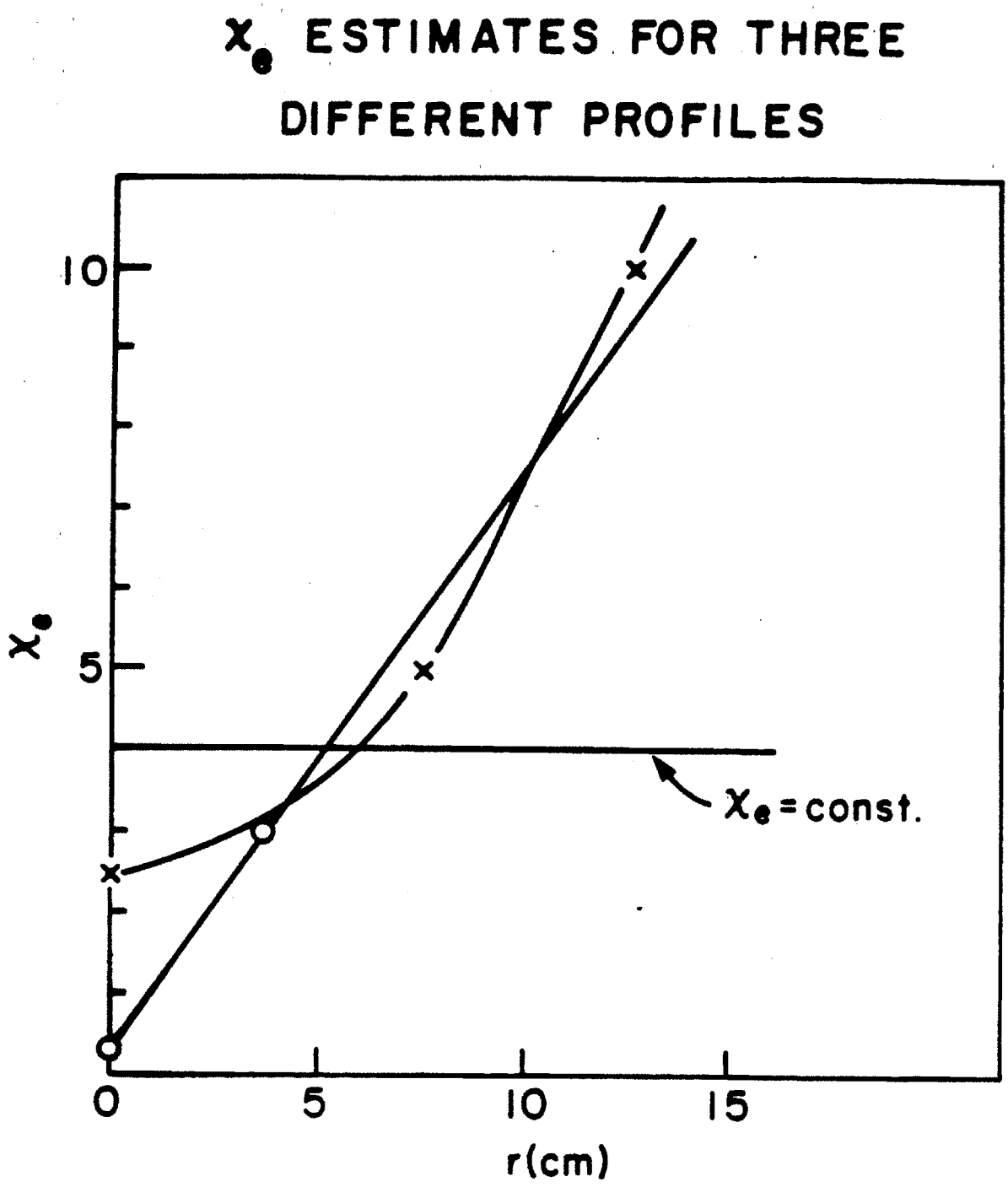

Figure 3.22 — Comparison of χ_e estimates for three different profiles. $\chi_e = const.$, $\chi_e = c_1 + c_2(r/a)$ and $\chi_e = c_1 + c_2(r/a) + c_3(r/a)^2$.

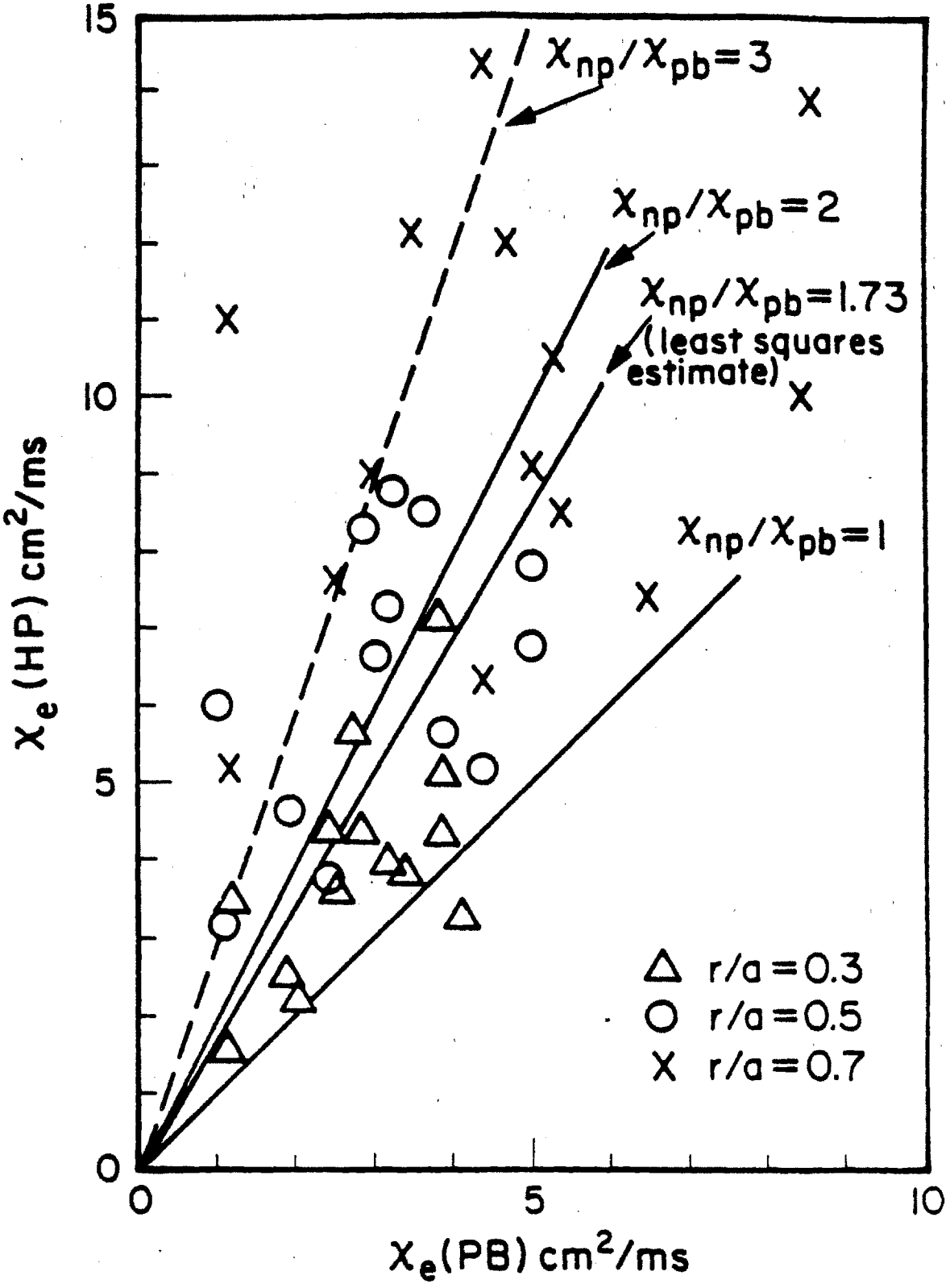

Figure 3.23 — Comparison of χ_e(heatpulse) with χ_e(power balance) at various radii.

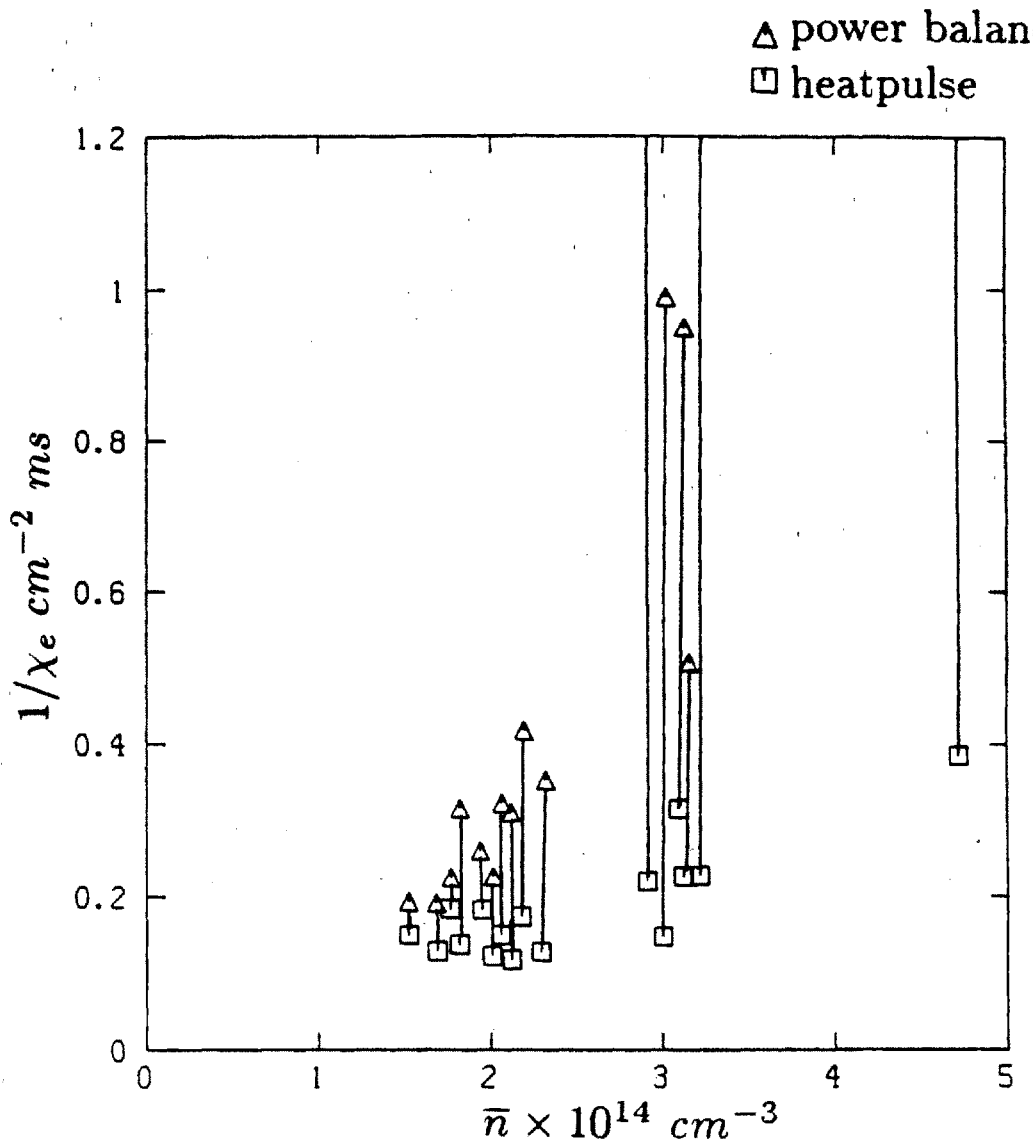

Figure 3.24 — Difference between $1/\chi_e$(heatpulse) and $1/\chi_e$(power balance) as a function of density. The open circles indicate the heatpulse value while the triangles represent the power balance values.

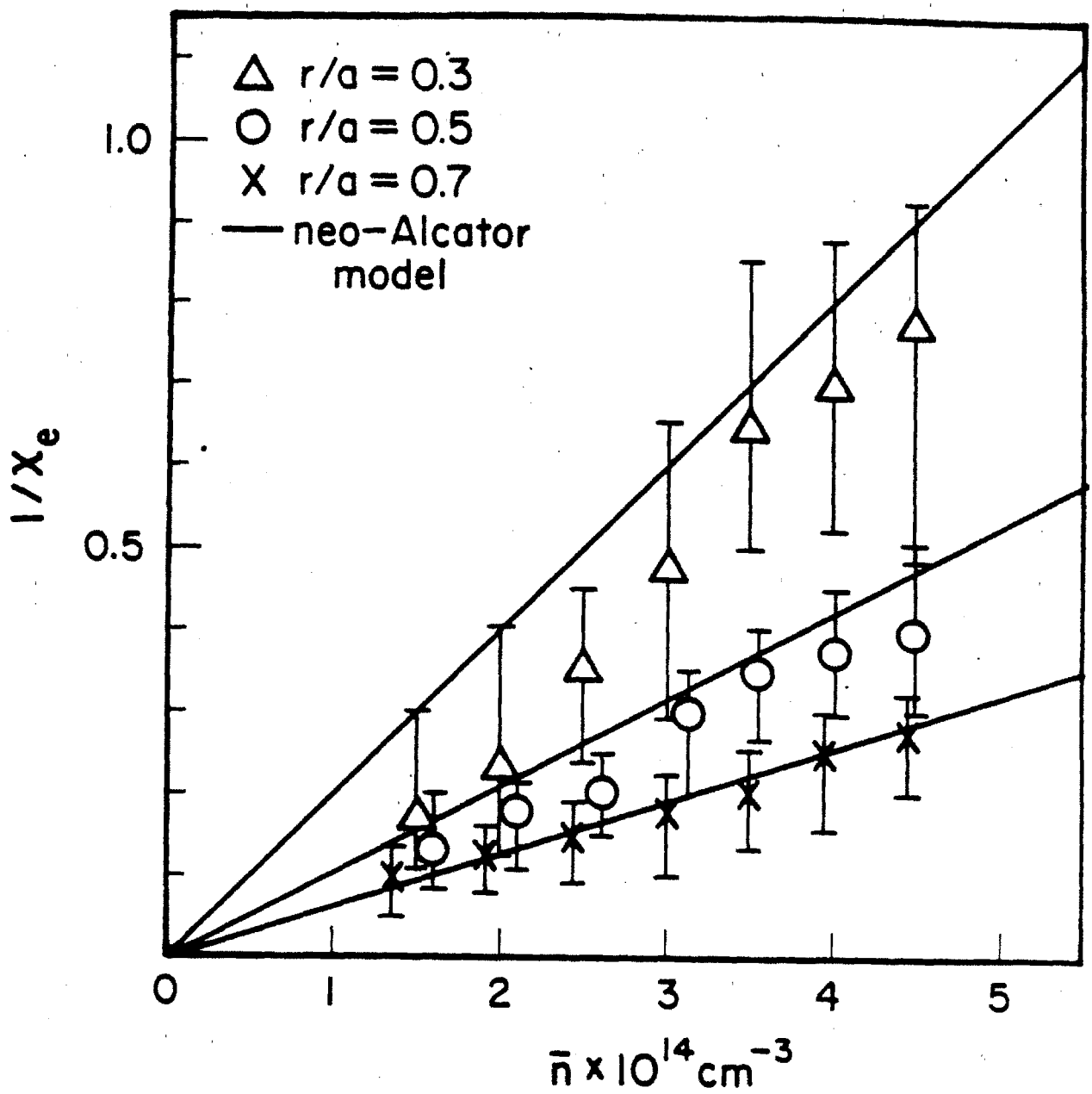

Figure 3.25 — Scaling of $1/\chi_e$ with line averaged density at three different radial locations. Each data point with error bar represents the average and scatter of a larger data set.

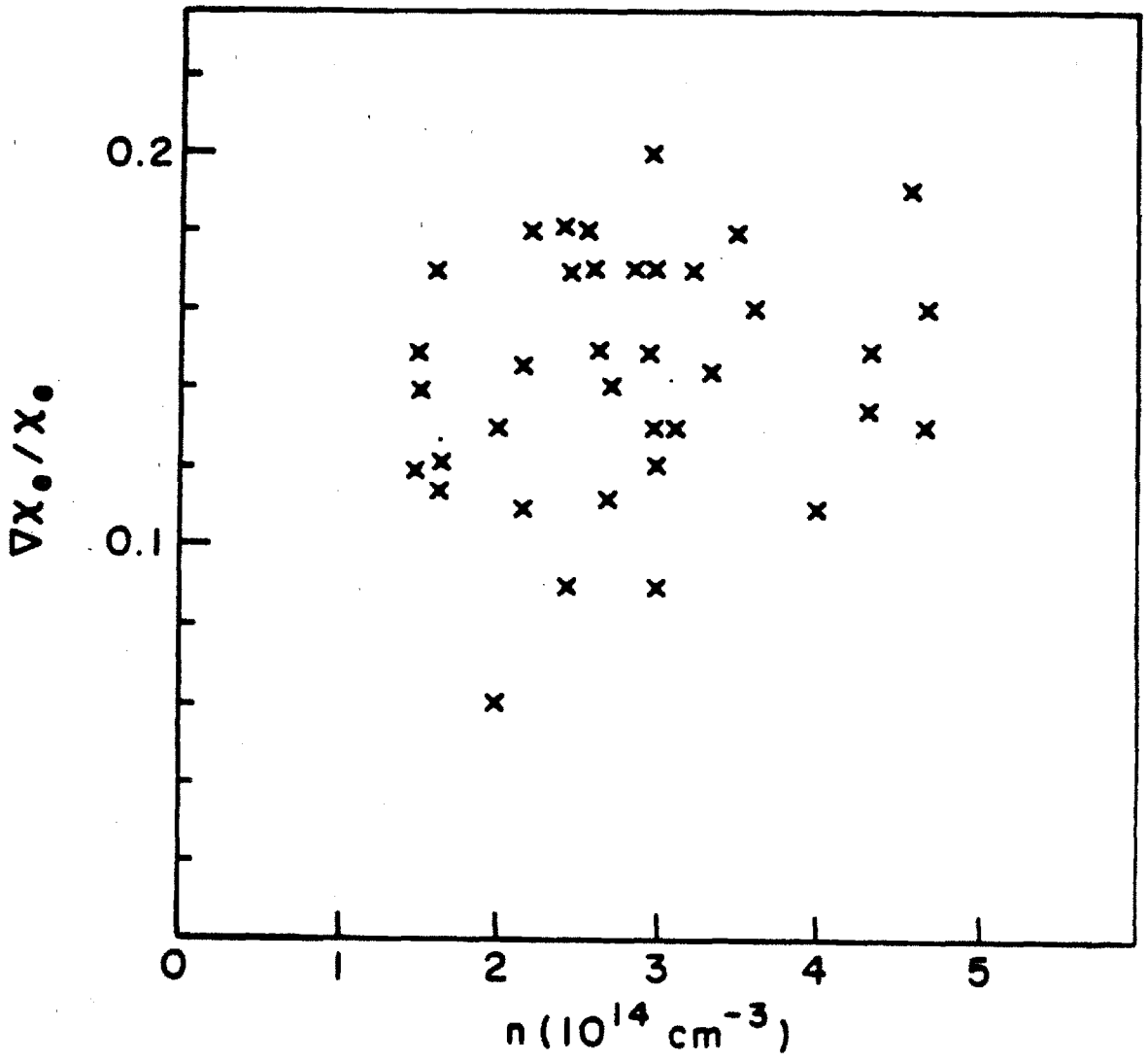

Figure 3.26 — Inverse scale length of χ_e with $\overline{n}_e$ at the half radius.

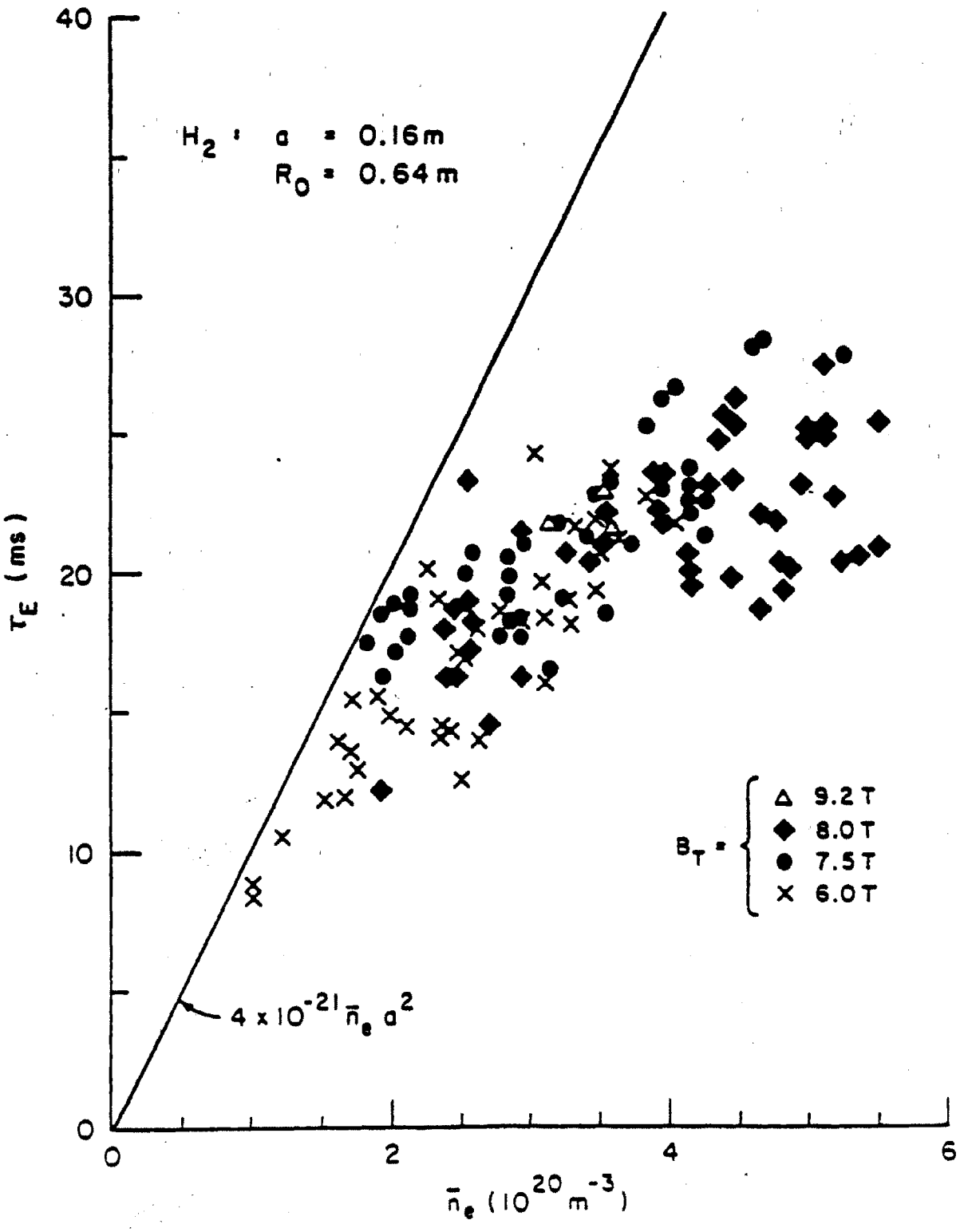

Figure 3.27 — Scaling of global energy confinement time vs. central line averaged density.

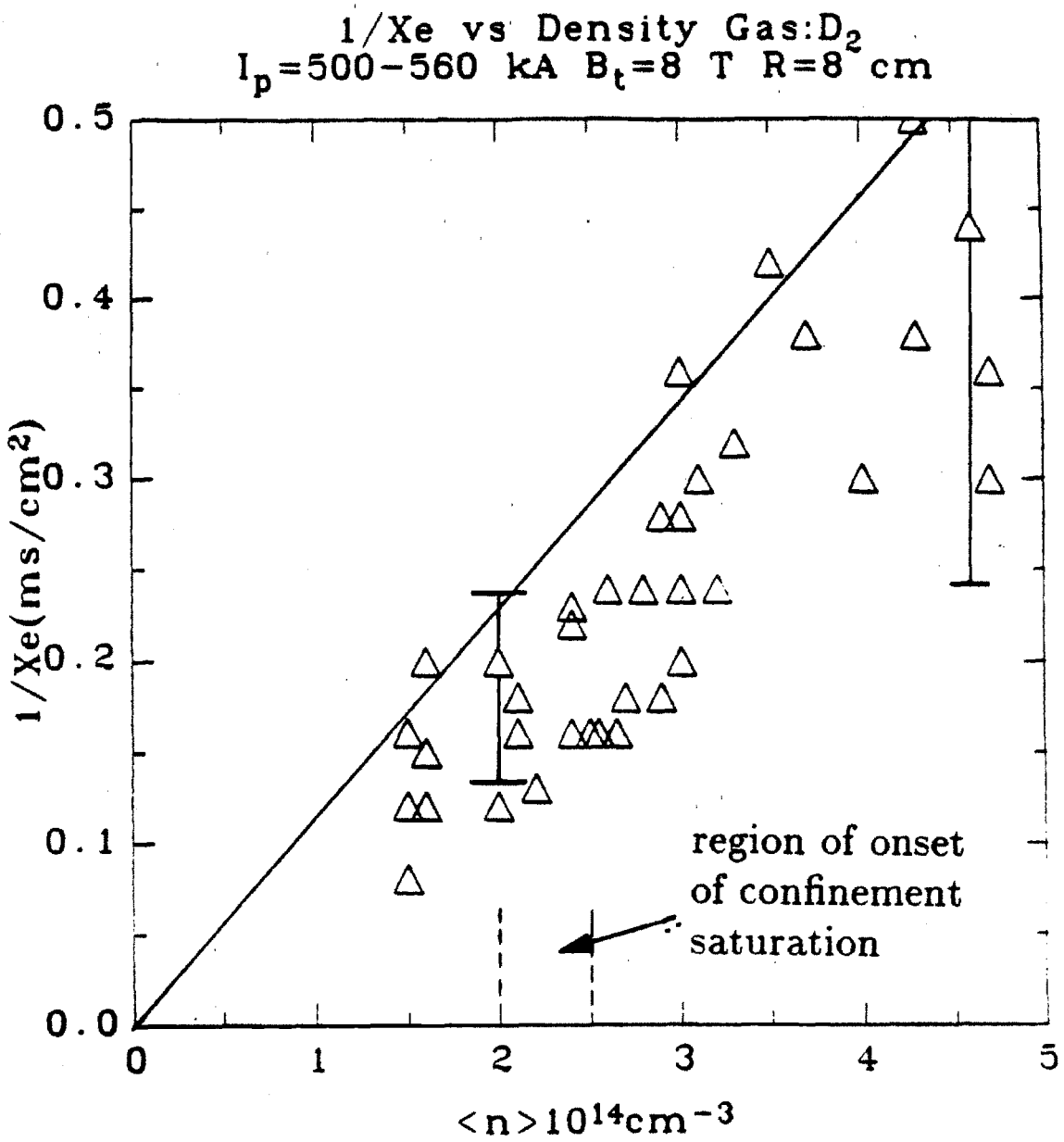

Figure 3.28 — Scaling of $1/\chi_e$ vs. $\bar{n}_e$ at the half radius.

IV) Electron temperature response to pellet injection

4.1)Introduction

In order to develop a thermonuclear reactor, an efficient way of delivering fuel to the burning plasma must be found. There are a variety of methods under current investigation. The most common of these is gas puffing, in which neutral gas(the fuel) is puffed in at the edge and then transported into the core of the plasma by some mechanism. Two possible models of the inward transport which have been proposed are an inward particle pinch (either Ware pinch[4.1]or of anomalous form) or multiple charge exchange. Another technique of fuelling which has increased in popularity in recent years is pellet injection. In this method the fuel is frozen into a solid pellet and then injected at high speed into the hot plasma. This enables fresh fuel to be deposited deep inside the plasma.

Although gas puffing is a much simpler method, its efficiency for fuelling has been shown to have limitations which may make it unfavorable for a reactor. It has been found that at high densities, the energy confinement time of gas puffed discharges saturates [4.2], while pellet fuelled discharges exhibit improved confinement[4.3]. The high recycling rates needed for high density operation can also lead to detrimental effects which have been found to reduce the efficiency of bundle divertors[4.4]. For these as well as other reasons, activity in understanding the pellet fuelling method has increased.

Spitzer [4.5] suggested pellet injection while considering fuelling for the stellarator concept. The general requirements arrived at, were that the pellet should be large and fast so as to deposit fuel directly into the core of the plasma. The first pellet injection experiment carried out on tokamaks was on the ORMAK device [4.6]. In this experiment, small H_2 pellets($72\mu m$ and $210\mu m$ dia.) were injected into the plasma at velocities of $\sim 100m/s$. Because of their small size and low speed, they penetrated a maximum of 6 cm from the edge of the plasma or $r/a \sim 0.74$ before being consumed. This experiment created no discernable difference in the central line averaged density($< 1\%$), however it did show that a pellet could be injected

into a plasma without detrimental effects to the stability. It also allowed study of the pellet ablation process, but because of poor diagnostics and the size of the pellet perturbation, a study of the plasma response was not possible.

The next set of experiments were done on ISX-A[4.7] with pellets that contained 30 times the mass of those in the ORMAK experiment and an injection velocity of $300m/s$. A penetration depth of $\sim 12cm$ or an $(r/a \sim 0.5)$ was achieved with a density increase of $\sim$ 30%. Subsequent experiments on other machines [4.3,4.8,4.9,4.10,4.11,4.12] have been carried out in which pellets have been able to more than triple the background density. In the case of Alcator C, experiments have shown an improved confinement time over gas puffed discharges and have exceeded the Lawson $n\tau$ criterion (at a lower temperature than required for breakeven[4.5]).

The injector used in the Alcator C experiments is based on a prototype used on ISX-A[4.15]; a much more complete description of the MIT injector can be found in[4.16]. Here we will only present an outline of the injector characteristics. A schematic of the injector is shown in fig. 4.1. Pellets are injected along the toroidal midplane, perpendicular to the magnetic axis. Up to 4 pellets of H_2 or D_2 can be injected simultaneously or delayed. The H_2 pellets contain an average of $N_H \sim 5.4 \times 10^{19}$ atoms and D_2 pellets $N_D \sim 6 \times 10^{19}$ atoms. The shape of the pellets are approximately a right circular cylinder with a base diameter of $\sim 1.4mm$ and a height of $\sim 1mm$. The propellant normally used is He at $300psi$, giving a terminal velocity of $v_H \sim 850m/s$ for H_2 pellets and $v_D \sim 625m/s$ for D_2 pellets. The penetration depth achieved is anywhere from a few centimeters to $> 10cm$ from the plasma edge or an $r/a \sim 0.76 - 0.39$ depending on plasma and pellet conditions.

Fig. 4.2 shows a set of traces for a pellet fuelled plasma shot in Alcator C. Although this shot is particular to Alcator, the same general behaviour has been observed in other machines. Immediately after pellet injection we see a rapid rise in the line averaged density as the pellet atoms are ablated and ionized. Simultaneous with this, there is a fall of the electron temperature as the cold pellet fuel dilutes the background plasma. This process in Alcator C and elsewhere has been found to be adiabatic[4.3,4.9,4.13]. The temperature recovery is on a time scale of $15 - 20ms$.

The total current is found not to change appreciably during injection. Because the readjustment time is much shorter than the skin time and the fact that the electron temperature profile remains constant, leads us to expect the current density profile to be relatively unaffected. The increased resistivity due to the colder temperatures raises the loop voltage at the edge. Magnetic transport codes indicate the voltage at the center to be much higher. This causes the increased heating rate, which leads to the fast recovery of the temperature. The higher value of β_p indicates a higher plasma energy content. The case shown is for injection of a D_2 pellet into a D plasma; the rapid rise in the neutron rate represents the increasing concentration of deuterons near the plasma center and/or an increase in the central ion temperature.

During injection, in many cases the electron temperature profile has been seen to relax on a very fast time scale across the whole plasma, even though the pellets usually do not reach the central region. The time scale of pellet penetration in Alcator is $100 - 150\mu s$ while the central temperature is observed to fall in some cases as fast as $200\mu s$. The fast evolution is also observed for the density, which seems to relax on a time scale $\sim 500\mu s$. This is surprising since we would expect the evolution of the central values to be much slower if the transport coefficients are consistent with the pre-injection values. Similar results have been found on PDX[4.9],ASDEX[4.13], TFR[4.12], DIII[4.11]. Early measurements on Alcator-C[4.14] showed two different kinds of behaviour for the relaxation. In one, the electron temperature profile readjusts in a time scale of $200\mu s$ (type A fig. 4.3). In the other (type B), the edge channels where the pellet penetrates, behave in a similar fashion as type A, but the channels near the center evolve much slower. At the time, a qualitative correlation was found with pellet size or increase in density. Similar evolution of the temperature was found on DIII[4.11]; there however it was found that the fast relaxation took place when the pellet crossed the $q = 1$ surface.

Understanding of the initial plasma response to the pellet will be important in determining injector requirements for fuelling a hot plasma. The fast relaxation of the electron temperature can reduce the ablation rate of the pellet over one arrived at by assuming a slower response of the plasma. There is also evidence that the

pellet generates large inward flows of particles. This may reduce the requirement of the pellet having to directly fuel the center of the plasma.

In this chapter we shall study the scaling of the fast electron thermal relaxation with plasma parameters. Based on these results we shall try to develop a qualitative picture of how the eletron thermal transport must behave in order to simulate the experiment.

Pellet injection provides a unique way in which to study 'profile consistency'. Profile consistency states that the electron temperature will always tend to relax to a canonical profile; the shape of this profile depends only on q_l. Pellet injetion can generate electron temperature profiles which differ from the canonical shape, we will then be able to see whether the electron temperature recovers its canonical form.

A wide variety of sawteeth have been observed after pellet injection. We shall discuss some of these as well as the possible interpretations that have been suggested. Recent experiments of impurity injection in post pellet plasmas, show improved impurity confinement with the same scaling on plasma parameters as the fast electron temperature relaxation that takes place during pellet injection. This is interesting because the improved impurity confinement takes place a long time after injection, while the fast relaxation takes place during injection. This implies that events taking place during injection are linked to the long time behaviour of the plasma.

4.2)Initial response of temperature

4.2.1)General observations

As was mentioned above we observe two types of temperature relaxation rates in pellet fuelled plasmas. Fig. 4.4a,b show the time evolution of the temperature at six radial locations as measured by the FIR grating polychromator described in chapter I of this work. The parameters for the fast case shown here are, $B_t = 10T$, $I_p = 443kA$, $\overline{n}_p = 2.6 \times 10^{14} cm^{-3}$ (target line averaged density), $\Delta\overline{n} = 2.3 \times 10^{14} cm^{-3}$ (maximum change in central line averaged density); for the slow case, $B_t = 10, I_p = 458kA$, $\overline{n}_i = 2.15 \times 10^{14} cm^{-3}$, $\Delta\overline{n} = 1.16 \times 10^{14} cm^{-3}$. The fast or slow labeling at the moment is somewhat arbitrary but the distinction will become more meaningful later. The depth of penetration in these shots was determined from the delay between the end of the $H\alpha$ signal and the estimated time that the pellet crosses the limiter radius, assuming a linear constant velocity trajectory. The depth of penetration for the fast case is $l = 9cm$ or $r = 7.5cm$(ablation minor radius) and for the slow case $l = 7.7cm(r = 8.8cm)$. From fig. 4.4a,b we see that the evolution of the temperature in the channels which the pellet crosses is similar in both cases. The difference in the two types of evolution comes from the channels inside of the ablation radius. A reconstruction of the profiles has been done and is shown in fig. 4.4c,d. For the fast case the reconstruction has been done over a $300\mu s$ period and for the slow case the period is $5ms$. We see that in both cases the profiles decay nearly continuously to a final profile, the discontinuity in the evolution of the slow decay case in this example is associated with a sawtooth crash that takes place at $t = 9ms$. The increased amplitude of the crash during this period may be due to the more peaked electron temperature profile. Both profiles seem to decay to the same final profile shape with nearly the same amplitude. For the fast case $\Delta\overline{n}/\overline{n} = 0.88$, for the slow case $\Delta\overline{n}/\overline{n} = 0.54$, since the initial parameters in both shots are similar we would expect the final temperature in the fast case to be lower than that in the slow case. One possible resolution for the discrepancy is that the change in line averaged density is only a rough indicator of the actual pellet size, the pellets in

these two cases may actually be closer in size than the line averaged density change indicates.

4.2.2)Propagation of leading and trailing edges

As an indicator to the dynamics of the evolution we will study the difference in the propagation of the leading and trailing edges for both cases. Fig. 4.5 shows the temperature evolution for the location $r = 10cm$ and the evolution of the $H\alpha$ signal. We define the leading edge of the pellet 'heat pulse' to have reached a given radius if the temperature changes by an amount larger than the pre-injection noise level. A similar definition holds for the trailing edge. For the case shown, we see that the leading edge has reached the $r = 10cm$ radius while the pellet is crossing the $r = 13cm$ radius. Fig. 4.6 shows a propagation study done for the two cases of fig. 4.4. The leading edge behaviour is found to be similar in both cases and propagates with a velocity $\sim 1500m/s$ or about twice the pellet velocity. The trailing edge seems to track the pellet trajectory outside the ablation radius(the minor radius location at which the pellet is completely consumed). However inside the ablation radius, the fast case evolution seems to propagate into the center at a rate similar to the pellet velocity, while the slow case shows a much slower propagation of the effect into the center. The pellet affects the edge similarly in both cases fig. 4.4a,b suggesting that the mechanism that generates the leading edge effect, originates at the edge of the plasma and then propagates into the plasma independent of the pellet. The mechanism that transports the bulk of the energy as evidenced by the propagation of the tail seems to be strongly coupled to the subsequent pellet evolution. The almost linear propagation of the leading and trailing edges does not rule out a diffusive process since it is a complicated problem with a moving source, time changing density and diffusivity.

Since the key difference between the two cases seems to lie in the temperature evolution near the central region, we shall use the central decay rate as an indicator of the profile evolution. To try and shed some light on the mechanisms that drive the bulk evolution, we have done a series of scaling studies of the central electron

temperature relaxation time (Δt_0). The central decay time is determined by fitting the decay of the central trace with a three step linear function. The time difference between the two intersects of the three lines defines Δt_0.

4.2.3)Correlation of Δt_0 vs central line averaged density and change in central temperature

In ref. [4.14] we made the suggestion that pellet size was correlated to the rate of decay of the electron temperature. Fig. 4.7 is a plot from [4.14] showing this difference in behaviour. The discrepancy is seen most clearly near the center of the plasma, while the edge decay rate in the two cases is similar. The trace marked by the triangles represents a case of a fragmented pellet, thus the cascade effect in the outer trace. The difference between the two is the overall change in central $\Delta\overline{n}$ caused by the pellet and the penetration depths for the two cases. For the fast case $\Delta\overline{n} = 2.4 \times 10^{14} cm^{-3}$ and $l = 11cm$, while for the slow case $\Delta\overline{n} = 10^{14} cm^{-3}$ and $l = 8cm$. The pre-injection background density is $\overline{n} = 2 \times 10^{14} cm^{-3}$. The interpretation given in [4.14] was that the larger pellet could generate larger inverted density profiles and that this somehow could drive the fast relaxation in response to the pellet.

To expand on the scaling suggested in [4.14] we show in fig. 4.8 how Δt_0 scales with the change in central line averaged density normalized to the pre-injection density ($\Delta\overline{n}/\overline{n}$). There appears to be a threshold in the value of Δt_0 for

$$0.8 < \frac{\Delta\overline{n}}{\overline{n}} < 1.1$$

in this region Δt_0 changes by over an order of magnitude. The width of the transition region can be attributed to several things. As we have mentioned before the change in line averaged density is somewhat insensitive to profile effects, which if accounted for may remove some of the scatter.

The central electron temperature may be a better indicator of events taking place near the center, for this reason we have done a scaling of Δt_0 vs the fractional

change in the central temperature ($\Delta T/T$) fig. 4.9. The threshold can be seen much better in this case, with the transition region being

$$0.4 < \frac{\Delta T}{T} < 0.6$$

and a residual slope to either side. This is consistent with the pellet size scaling since as shown in fig. 4.10 larger pellets tend to make larger changes in the central temperature.

4.2.4)Scaling of Δt_0 with penetration depth and q(safety factor)

In trying to make a connection with the results of ref.[4.11], which suggest that the two types of decays depend on whether the pellet crosses the $q = 1$ surface or not, we have done a study to see if there is a correlation between penetration depth and Δt_0. Fig. 4.11 shows such a scaling. We again see a transition in the region $8 < l < 9$ or $8.5 < r < 7.5$.

To see if this transition is associated with a critical q, we have plotted Δt_0 vs the pre-injection q profile. As we have argued before, the current profile should not change much during injection thus not changing the safety factor profile. If we assume the temperature to scale as $T \sim T_0 e^{-r^2/a_T^2}$ and that the current roughly follows the temperature as $J \sim T^{3/2}$ in the outer region of the plasma. This form of the current profile gives a safety factor profile of the form,

$$q(r) = q_l(\frac{r}{a})^2 \frac{(1 - e^{3a^2/2a_T^2})}{(1 - e^{-\frac{3}{2}r^2/a_T^2})}$$

where q_l: safety factor at limiter, a:limiter radius, a_T: temperature profile width.

Fig. 4.12 shows the scaling of Δt_0 vs q estimated at the ablation radius. We see that none of the pellets penetrate the $q = 1$ surface. Between $q \sim 1.3 - 2.5$ the cases seem to be evenly distributed with respect to the relaxation time. The splitting for $q > 2.5$ is an artifact of the data. The fast relaxation cases correspond to a penetration depth $l > 8$ and low current in fig.4.11, while the slow relaxation cases, having similar $q_{ablation}$, correspond to shallow penetration in high current shots. As a further check to see if the central relaxation time is somehow related to

the sawtooth mechanism, we have compared the central relaxation time Δt_0 with the sawtooth phase of the central decay(p). The parameter (p) is defined by

$$p \equiv \frac{d}{\delta t}$$

d:is the time delay between the start of fall of the central temperature due to the pellet, and the previous sawtooth crash.

δt: is the sawtooth period immediately preceding injection.

For shots which are outside of the transition region in fig. 4.11, no correlation is found with sawtooth phase. However some correlation is found for the shots which lie inside of the transition region. Fig.4.13 shows two types of shots. The ones for which $l > l_c = 8.5cm$ tend to have a fast decay, and are uncorrelated with the sawtooth phase. However the ones for which $l < l_c$ show a rather clear correlation with pellet phase. For low (p) the decay tends to be slow, while for $p \sim 1$ it is fast. A possible interpretation is that immediately after a sawtooth crash the current profile is at its most stable point with respect to the sawtooth instability, as the current peaks it becomes progressively more unstable to the sawtooth instability. If a pellet is injected with a phase such that $p \sim 1$ it encounters a more unstable current profile, the pellet may then drive the magnetic fields into reconnection and help drive the fast relaxation. If the pellet is injected with $p \sim 0$, it will encounter the most stable current profile and thus the temperature relaxation is much slower.

4.2.5)Scaling of relaxation with density gradient

Although some correlation was found in the previous section between the temperature relaxation and the sawtooth mechanism, it is clear that it does not play a role as the primary driver of the fast relaxation. One likely candidate is the large inverted density gradients expected to be set up by the pellet, which can then drive an instability which generates the rapid transport. One of the problems was estimating the inverted density profile since no direct measurement was available for the set of shots analyzed. It can be argued that the $H\alpha$ signal is proportional to the ablation rate profile[4.8]. If we assume there is no radial particle diffusion on

a time scale of $\sim r_p/v$ (r_p is the ablation cloud radius,v pellet velocity), then the initial density profile has a shape determined by the ablation profile. We find that the $H\alpha$ signal can be parametrized by a function of the form (see fig. 4.14)

$$x^2 sin(\pi \frac{x}{L})$$

where L:is the $H\alpha$ length.

The penetration depth as used in the previous section is not necessarily the same as the $H\alpha$ length. The $H\alpha$ length is usually found to be slightly less than the penetration depth; this is probably because very little of the pellet is deposited at the edge of the plasma.

The initial density profile is assumed to be of the form

$$\delta n = C \frac{1}{r} \left(\frac{x}{L}\right)^2 sin(\pi \frac{x}{L})$$

The coefficient C is found by requiring this profile to match the incremental change in the central line averaged density immediately after injection. We can show that the maximum slope set up by the profile is proportional to $a\Delta\overline{n}/(L\overline{n})$. Fig. 4.15 shows the scaling of Δt_0 with $a\Delta\overline{n}/(L\overline{n})$. The data does not show a transition as in the previous cases, but it does show a clear dependence on the density gradient. The central decay rate grows exponentially with the ratio of the density gradient set up by the pellet to that of the background plasma.

To see if there was a similar correlation with the temperature gradient , we modelled the transient temperature profile with a function of the form $T_0 e^{-r^2/a_T^2}$ at each point in time. It can be shown that the quantity T_0/a_T scales with the maximum gradient(the dimensionless parameter in this case is a/a_T). No clear scaling was found with the temperature gradient as was found with the density. A reason for this can be attributed to the fact that the transition profiles do not differ greatly for the fast and slow relaxation cases.

4.3)Model of fast relaxation

Several questions have been raised by the measurement of the evolution of the electron temperature during pellet injection. One of these is whether the relaxation has a diffusive or convective character. If it is diffusive, is the transport coefficient consistent with bulk diffusion? To try and answer this question, we have used a simple one dimensional model to simulate the injection. We expect the diffusion of temperature and density to be much faster along the magnetic field lines than across it, so we assume poloidal and toroidal symmetry in the source term and in the subsequent evolution. Because the density and temperature change on similar time scales, we must solve the density and temperature equation simultaneously.

4.3.1)

$$\frac{3}{2}\frac{\partial}{\partial t}nT_e = \frac{1}{r}\frac{\partial}{\partial r}rn\chi_e\frac{\partial}{\partial r}T_e$$

4.3.2)

$$\frac{\partial}{\partial t}n = \frac{1}{r}\frac{\partial}{\partial r}rD\frac{\partial}{\partial r}n + S_n$$

where S_n is the particle source term. In the above equations we have neglected the possibility of convection, and, because of the short time scales involved, we may neglect contributions from Ohmic heating. Other contributions such as electron-ion coupling are not as clearly negligible, but for the qualitative picture we will ignore them as well.

The particle source term is related to the ablation rate and has been taken to be of the form

$$\frac{1}{\sqrt{\pi}\sigma}e^{-(r-x(t))^2/\sigma^2}\frac{\partial}{\partial t}N$$

where $x(t)$ is the radial trajectory of the pellet. The exponential is the radial deposition shape function of the pellet, and we assume that in the other two directions the deposition is uniform. The factor $\partial N/\partial t$ is the total ablation rate; as was mentioned in the previous section, this is related to the $H\alpha$ intensity. We will take a function consistent with the shape of fig. 4.14

4.3.3)

$$\frac{\partial}{\partial t}N = K\left(\frac{l}{L}\right)^2 sin\left(\pi\frac{l}{L}\right)$$

Here l is the penetration depth from the edge of the plasma and L is the maximum penetration depth. The constant K is set by the total number of particles in the pellet,which works out to be

$$K = 5.26\frac{v}{L}N_T$$

v:pellet velocity

N_T:total number of particles

Because of the tenuous nature of the plasma and the large momentum carried by the pellet we have assumed a trajectory of constant velocity. We can then arrive at an effective density source

4.3.4)

$$S_n = \frac{\delta n}{\delta t} = \frac{1}{4\pi^2\sqrt{\pi}R_0 r\sigma}e^{-(r-z(t))^2/\sigma^2}\frac{\partial}{\partial t}N$$

where R_0 is the machine major radius.

A useful quantity to use for comparison is the line averaged density of the static distribution, that is, the profile we would get in the absence of any radial particle transport. This is related to the total number of particles by

4.3.5)

$$\Delta\overline{n}_e = \frac{5.26}{4\pi^2 R_0 aL}W(\frac{L}{a})N_T$$

where

4.3.6)

$$W(\rho) \equiv \int_0^1 dy\frac{y^2}{(1-\rho y)}sin\pi y$$

where $\rho = L/a$. If we assume the pellet does not go through the center then ρ can only vary between $0 \rightarrow 1$; the value of $W(\rho)$ over this range is shown in fig. 4.16.

We shall analyze a case with the following pellet and plasma properties $L = 12cm$, $v = 850m/s$, $N_T = 5\times10^{19}atoms$, $\overline{n} = 2\times10^{14}cm^{-3}$, $\Delta\overline{n}_e = 1.9\times10^{14}cm^{-3}$, $T_{e0} = 2000eV$, $a_{T_e} = 10cm$.

To address the question of whether the fast decay could be accounted for by bulk diffusion, a case was run in which the diffusivity value used is consistent with the pre-injection value. The model used is that of a flat χ_e whose value is determined by eq. 3.3.14, which for the above specified parameters gives $\chi_e \sim 5cm^2/ms$. We have very little information on the transient density profile, for this series of shots. We do know from previous cases that the inverted density washes out on a time scale of $500\mu s$. This is not a very stringent condition for determining the consistent value of D, but from the point of view of the temperature it is not a very sensitive number. For the bulk density diffusivity we shall take $D \sim 3cm^2/ms$ consistent with eq. 3.3.16. The result of the simulation is shown in fig. 4.17. We see from fig. 4.17a that steep profiles are set up with the central channels decaying on a time scale much longer than $200\mu s$ (fig. 4.17d). However in the channels which the pellet crosses, the decay is much faster and as we shall see, do not differ significantly from the fast diffusion case. The small pressure inversion that develops around $r \sim 5cm$, can be attributed to the large temperature density gradients set up by the pellet (fig. 4.17a) in this region. Fig. 4.18 shows a case for which $\chi_e = 300cm^2/ms$, $D = 90cm^2/ms$. The value of the thermal and particle diffusivity was calculated to be consistent with the evolution of the lowest eigenmode of the diffusion equation using as electron temperature relaxation time of $\sim 250\mu s$ and a particle relaxation time of $\sim 500\mu s$. While this model does maintain flat profiles, the evolution as seen from fig.4.17d is clearly not consistent with observed plasma behaviour. The instantenious response of the temperature everywhere in the plasma comes from the immediate change in the transport coefficients.

What the above two cases tell us is that the pellet must generate a very high χ_e in order to drive the fast decay diffusively, and the anomaly must propagate into the center with the pellet. One idea that has been suggested is that the large inverted density and pressure gradients can drive an instability which generates the fast diffusion. One possible scenario is for the large density gradients, set up by the pellet, to generate drift waves which can then cause the magnetic fields to become stochastic. The magnetic field turbulance can then give rise to large perpendicular transport.

To study how this kind of transport coefficients would affect the temperature evolution, a case was run in which, if the local density gradient is negative, the local thermal diffusivity is consistent with the bulk value, however if the density gradient is positive the local diffusivity is equal to the bulk plus an anomalous value. For the case shown in fig. 4.19, $\chi_e \sim 5cm^2/ms$(bulk), $\chi_1 \sim 250cm^2/ms$(anomalous), for the density $D_0 = 3cm^2/ms$, $D_1 = 90cm^2/ms$. We see that there is qualitative agreement between this case and a fast case as shown in fig. 4.20. We see that the edge behaviour in this case and that shown in fig. 4.17 are very similar, the main difference comes in the evolution of the central channels, something that is reminiscent of the difference between the slow and fast decay cases shown in fig. 4.4.

We have done a propagation study (fig.4.21) of the simulation cases in (fig. 4.17,4.19). The leading edge in both cases propagates at about the same rate and about a factor of two faster than the pellet. Since case in (fig. 4.17) does not contain any anomalous diffusion, this would suggest that the leading edge in both cases propagates with a diffusion coefficient consistent with the bulk. This same kind of behaviour is seen experimentally (fig. 4.6), with the leading edge of the slow and fast decay propagating at roughly the same rate.

The initial behaviour of the trailing edge is not as well simulated by the model. However the evolution of the two cases is similar until the ablation radius is approximately reached. From this point on the two models differ significantly. The implications this has is that the fast decay case seems to be able to generate an anomalous χ_e which is roughly two orders of magnitude higher than the bulk, while the cases which exhibit the slow decay are somehow not able to drive as large an anomaly. The anomaly need only be driven near the center of the plasma, thus not leading to a net loss of energy from the plasma.

Another question that may be addressed with this model is whether the driving mechanism is the density gradient or the pressure gradient. As we see from fig. 4.18b, for the case of the fast decay no large pressure gradients are generated, while a much larger density gradient is possible. Although there are large uncertainties in our modelling of the density evolution, we believe the qualitative behaviour to be correct. Thus the mechanism may be density driven or be very sensitive to inverted pressure profiles.

4.4)Profile consistency during pellet injection

It is a general observation in many machines, that under certain operating conditions the gross profile shape of the electron temperature is primarily determined by R_0, a_l, q_l (major radius, limiter radius, limiter safety factor). This phenomenon is usually called profile consistency, that is, given enough time the electron temperature profile will relax to a canonical shape dependent only on the above parameters.

For the case of Alcator-C, the sawtooth averaged temperature profile can generally be well fit by a function of the form

4.4.1)

$$T_e(r) = T_e(0)e^{-r^2/a_T^2}$$

In the steady state limit the temperature profile and the current profile are tied together through the resistivity. We assume Spitzer resistivity and neglecting neo-classical effects as discussed in sec. 3.3.3, the current profile has the form

4.4.2)

$$J(r) = J_0 e^{-\frac{3}{2}r^2/a_T^2}$$

We can then relate a_T to the poloidal magnetic field profile. In tokamaks a usefull parametrization for a_T is q, the cylindrical safety factor defined as

$$q(r) = \frac{rB_t}{R_0 B_\theta(r)}$$

where R_0:is the major radius of the magnetic axis, B_t: the toroidal field at the magnetic axis, $B_\theta(r)$:poloidal field at minor radius r. In a sawtoothing plasma, the current profile of eq. 4.4.2 is not expected to hold since the sawteeth will tend to flatten the current near the center. However for the purposes of estimating the gross profile width of the temperature, the above model has proved an excellent approximation.

We can then relate the parameter a_T to the safety factor at the limiter q_l, an effective central safety factor q_0 and assuming the current to be of the form 4.4.2 giving

4.4.4)

$$a_T = a_l \sqrt{\frac{3}{2}\frac{q_0}{q_l}}$$

a_l:is the limiter minor radius.

A sawtoothing plasma is never really in static equilibrium, thus q_0, as defined above, should not be strictly identified with the real central safety factor. In a sawtoothing discharge we can expect $q_0 \sim 1$, from stability considerations. Studies have previously been done on Alcator C, with gas puffing discharges, under a variety of plasma parameters[4.17]. It is found that for sawtoothing discharges q_0 is bounded by

$$0.8 < q_0 < 1.0$$

and $q_0 > 1$ increasing with q_l for non-sawtoothing discharges.

Pellet injection provides a powerful way by which to study profile consistency by comparing the pre and post injection profiles. Early indications that the profile consistency mechanism was active during pellet injection came from data measured with the Fast Scanning Fabry-Perot[4.18]. The FSFP scans the plasma in frequency of the second harmonic spectrum X-mode, or, equivalently, in major radius position, with a plasma scan period of $2ms$. Fig. 4.22 shows a case in which the pellet was 'caught' near the center of an FSFP scan,(trace 2). We see that even before the scan is finished the temperature profile has relaxed to the canonical shape, as evidenced by the right side of trace 2. Fig. 4.23 shows the peak electron temperature and width on a much longer time scale. We see no apparent change in the profile width even though the peak electron temperature undergoes a drastic fall and a slower recovery. Results from the grating, fig. 4.4, show that the profile width recovers on a time scale consistent with the central relaxation time, or in $200 - 300\mu s$ for the fast decay and somewhat longer (1-3 ms) for the slow decay.

The plot of fig. 4.24 shows the change in the electron temperature profile width as a function of q_l, for pellet injection shots. The data represents the value of a_T immediately before injection, and $5ms$ after injection. The reason for the $5ms$ delay

is to allow comparison between the fast and slow decaying cases. The location of the data point represents the width just before injection, while the tip of the arrow extending from the data point represents the width $5ms$ after injection. Points which have no arrow represent cases which had the same profile width, within the accuracy of the measurement. For comparison we have plotted several traces of eq. 4.4.4 for different values of q_0 and $a_l = 16.5cm$. We shall define profiles widths for which $q_0 \sim 0.8 - 1.0$ as the self consistent profile width.

For $q_l < 6$ all cases are well within $0.8 < q_0 < 1.0$ before as well as after injection; the profile width change is $< 10\%$. The behaviour is consistent with the change in temperature as described in ref.[4.17], with the pre-injection (high temperature) cases close to $q_0 \sim 0.8$ and after injection (low temperature) either having no change in the small pellet case or increasing towards $q_0 \sim 1.0$ in the large pellet case. For $q_l > 6$, the pre-injection profile width begins to go above the self consistent value. The discrepancy between the pre and post injection values also tends to increase with q_l. What this suggests is that the self consistent mechanism has turned itself off somewhere around $q_l \sim 6-8$ the value of q_l at which sawtoothing ceases. The general trend seems to be for a_T to increase after injection, although there are a few cases for which a_T decreases after injection. For these latter cases the final value of a_T seems to fall within the self-consistent limits, even in the case of $q_l \sim 10.5 - 11.0$.

Profile consistency seems to hold even in cases for which the plasma was sawtoothing before injection and stopped afterwards. These cases are associated with a large influx of impurities into the plasma, which can stabilize the sawtooth instability.

A possible explanation that has been suggested is that at high current (low q_l) the electron temperature profile is primarily determined by the current profile, which is determined by stability considerations, such as the sawtooth condition. At lower currents (high q_l) the stability condition is not the limiting criterion and the profiles become dominated by transport.

We believe that the similarity in the value of q_l at which the profile consistency seems to turn off and the sawteeth cease, is no accident. We propose the following interpretation which is consitent with the results of fig. 4.24. Suppose that eq. 4.4.4 with $q_0 \sim 0.8 - 1.0$ represents the narrowest possible T_e profile width that can be achieved, if the width becomes narrower than this, the sawtooth instability will broaden it back to the width as defined by eq. 4.4.4. Whether this width is accessible or not depends on plasma transport. If the plasma transport is sufficiently good, such that the transport determined a_{T_e} (that is the one we would get if we ignored the sawtooth instability) is less than that from eq. 4.4.4, then the current profile can peak sufficiently to turn on the sawtooth instability and 'clamp' the value of a_{T_e} to that determined by eq. 4.4.4. If the plasma transport is sufficiently bad such that the final transport determined a_{T_e} is wider than that determined by eq. 4.4.4, then the current profile never peaks sufficiently to turn on the sawtoothing; in this case the stable profile width is determined by the transport. Thus we can express whether profile consistency is active or not by an accessibility condition of the form

4.4.5) If $a_{T_e}(trans) < a_{T_e}(q_l)$ then we have sawtooth limited profiles

4.4.6) If $a_{T_e}(trans) > a_{T_e}(q_l)$ then the sawtooth limited profile is not accessible with the final profile determined by the transport.

In the above $a_{T_e}(q_l)$ is the sawtooth limited width determined from eq. 4.4.4 and $a_{T_e}(trans)$ is the final width of the electron temperature profile that would be achieved through the transport equations without considering MHD stability.

Armed with this model we can understand the results of fig. 4.24. For low q_l operation even in a non-pellet plasma the confinement may be sufiiciently good that $a_{T_e}(trans) < a_{T_e}(q_l)$ and thus the observed profile width is limited by the sawtooth instability. For this range of q_l, pellet injection is normally associated with improved confinement thus it would be natural to expect $a_{T_e}(trans)$ in this case to be even narrower than in the pre-injection case. Since the post-pellet $a_{T_e}(trans)$ satisfies the accesibility condition for eq. 4.4.5 we expect then the profile to be sawtooth limited. Since current is conserved, q_l is the same before and after the pellet

and since q_0 is determined by the sawtooth instability, we would not expect it to change. With this picture then it is not surprising that the post pellet temperature profile width is not very different is not very different from that before the pellet. As was mentioned before, in some of the low q_l cases, either sawtooth oscillations were not observed after the pellet or their start was delayed. All of these cases are associated with large impurity concentration in the center. An interpretation that has been suggested by Petrasso et. al. [4.22] is that the build up of impurities, hollows the condictivity profile which can then flatten the current profile in such a way as to stabilize the sawteeth. One perplexing question is that for the same q_l in the low q_l regime, the measured a_{T_e} in the non-sawtoothing case does not differ significantly from that observed in the sawtothing case. A possible explanation for this may be that, long before the impurity concentration has reached a sufficiently high level so as to broaden the current profile width significantly, a disruption limit is reached. Thus in low q_l operation we can never see a plasma with significantly broader a_{T_e} than that defined by the sawteeth.

For high q_l the transport may have degraded sufficiently so that

$$a_{T_e}(trans) > a_{T_e}(q_l)$$

In this case the profile width is no longer limited by sawteeth, but rather by the transport properties of the plasma. In fig. 4.24, we see that the profile width tends to broaden after injection suggesting a degradation of confinement. However there seem to be a few notable exceptions around $q_l \sim 10 - 11$, in these cases as was mentioned before, the final profile width was narrowed by the pellet and consistent with the sawtooth limited values. In none of these cases were sawteeth observed, although at these high q_l's the sawtooth amplitude can be expected to be very small thus they might be present but not observable.

The transition between the two regions is then $a_{T_e}(trans) \sim a_{T_e}(q_l)$. For the case of Ohmic heated Alcator plasmas this takes place around $q_l \sim 6 - 8$. The transition layer then in general is determined by the particular of the transport independent of MHD, and the MHD limitations. The reason why the electron

temperature seems to be the only measureable plasma parameter which obeys profile consistency, may be because it is the one parameter that is the strongest coupled to the current profile(i.e. through the resitivity and Ohmic heating). Thus we can expect any limitation placed on the current profile to reflect itself most strongly on the electron temperature.

4.5)Sawtoothing and impurity confinement in post-pellet plasmas

Sawtooth oscillations in post-pellet plasmas can evolve in four different ways. Fig. 4.25

a) for small pellets no significant change in the sawtooth characteristics take place, except for a brief increase in frequency immediately after injection.

b) for medium to large pellets, the initial recovery is accompanied by an increase in the sawtooth frequency and a decrease in amplitude. During recovery the sawtooth frequency drops below the pre-injection value and undergoes a slow recovery back to the pre-injection value. During this time the sawtooth amplitude increases and ultimately becomes as large as that at pre-injection.

c) there are cases for which the initial recovery is the same as in case (b), but undergoes a suppression for a long period of time (20-50ms) and then ressumes sawtoothing with the frequency increasing asymptotically to the pre-injection value. Again the amplitude does not increase appreciably above the pre-injection value. The long suppression of sawteeth and the subsequent crash are always associated with the giant sawtooth event as seen by the soft-Xrays.

d) this is one in which the plasma never sawtooths, this seems to be a radical extension of case (c) above.

The time evolution of the sawtooth period for the first three cases discussed is shown in fig. 4.26.

The case of the giant sawtooth is seen much more dramatically by the soft X-rays fig. 4.27. However as was mentioned above, the corresponding change in the central electron temperature is too small to account for the large change in the soft X-rays. It has been found, that just before the large X-ray crash the impurity profile is very peaked and subsequently flattens after the disruption[4.19]. This is consistent with the finding that the impurity confinement increases dramatically just before a giant sawtooth and immediately relaxes to a much lower value[4.20]. Case (d) discussed above is one in which the improved impurity confinement never degrades.

Impurity conifinement measurements have been carried out in pellet plasmas. By using a laser blow off tehnique a highly localized source of tracer impurities can be injeted into the plasma. The evolution of these impurities can be followed by spectroscopic method. From this, the effective particle transport can be deduced[4.21]. Fig.4.28 shows the result of scaling τ_I[4.20](the impurity confinement time) with peak $\overline{n}_{epost}/\overline{n}_{epre}$ for $q_l < 6.5$, where $\overline{n}_{epost}$ is the post-pellet density and $\overline{n}_{epre}$ is the pre-injection density. We see a transition at around $\overline{n}_{epost}/\overline{n}_{epre} \sim 1.8$ between the long and short confinement regimes. We see that it has the same scaling as for the transient T_e evolution during pellet injection although the two events are wide apart in time. The impurity confinement time is measured $5 - 20ms$ after pellet injection. For $\overline{n}_{epost}/\overline{n}_{epre} > 1.8$ we find a significantly improved confinement compared to that at pre-injection confinement. For $\overline{n}_{epost}/\overline{n}_{epre} < 1.8$ the post pellet impurity confinement is similar to that in the pre-pellet plasma. Fig. 4.29 shows the scaling of τ_I with Δt_0 (the central T_e relaxation time). For the case of $q_l < 6.5$ we see a clear correlation between the two. For the case of $q_l > 6.5$ we find that the impurity confinement time does not improve after the pellet. The apparent degradation in this case may be due to a current dependence of particle transport as is suggested by fig. 4.30. Here we show the fringe added interferometer trace for the central line averaged density. Fig. 4.30a has $q_l \sim 8.5$, while fig. 4.30b has $q_l \sim 4.5$. We see that the particle decay time for case (a) is much shorter than that for case (b).

These results suggest a link between the events happening during injection and the subsequent evolution of the plasma. One possible interpretation is that the profile set up during injection sets the initial conditions for the physics that governs the subsequent evolution of the plasma and through this the two are linked. Another possibility may be that both the profile evolution during injection and the long time evolution of the profiles are governed by the same physical mechanism and thus each may be a reflection of the same thing.

4.6) Conclusion

Most workers have focused on the long time behaviour of the plasma after pellet injection. We have focused on the transient behaviour of the electron temperature during the injection process. The initial behaviour has been found to be much more complicated than initially expected. Evidence indicates that the events taking place at this early stage may play a role in the subsequent evolution of the plasma.

The studies done in this chapter were performed primarily using an FIR grating polychromator (see chapter I). This allowed us to monitor the evolution of the electron temperature at several radial locations with very good time resolution. Soft Xrays have been the primary diagnostic used by other workers to make any transient measurements, the problem with these is that the signal depends on a number of plasma parameters. The ECE in the regime used in this thesis is sensitive only to the local electron temperature at the location of the emission.

During injection we observe two types of relaxations of the electron temperature in the central region of the plasma. A fast relaxation case which takes place on a time scale much faster than bulk diffusion and a slow relaxation case in which the central region of the plasma evolves on a time scale consistent with bulk diffusion. The fast relaxation is associated with large $\Delta\overline{n}/\overline{n}$ and the slow relaxation with low $\Delta\overline{n}/\overline{n}$. This seems to imply that the pellet size relative to the number of plasma particles is what determines the fast or slow relaxation. The evolution of the channels which the pellet reaches, seem to evolve in a similar manner in both cases.

Energy transport during injection can be described by the evolution of a heat(cold) pulse in the plasma. This pulse can be characterized by the propagation of its leading and trailing edges. In fig. 4.6 we show the propagation of the leading and trailing edges, for the fast and slow central decay cases. We see that the leading edge in both cases propagates at the same rate, with roughly twice the pellet velocity. The difference in behaviour is noticed most clearly in the evolution of the trailing edge. Outside the ablation radius the evolution of both cases is similar,

with a propagation velocity that is less than or on the order of the pellet velocity. However inside the ablation radius, the relaxation of the tail is very different. The tail for the fast decay case continues propagating into the center at roughly the same rate as outside the ablation radius, while the slow decaying case slows its evolution dramatically. Since the difference in the two cases lies in the central temperature evolution, we used the decay of the center to characterize the slow and fast decay case.

A scaling was done of Δt_0 with $\Delta\overline{n}/\overline{n}$ fig. 4.8. We found a transition in the region of $0.8 < \Delta\overline{n}/\overline{n} < 1.1$ in which Δt_0 changes by an order of magnitude. For $\Delta\overline{n}/\overline{n} < 0.8$ the central decay time is $\Delta t_0 > 1ms$ increasing with lower $\Delta\overline{n}/\overline{n}$. For $\Delta\overline{n}/\overline{n} > 1.1$ the decay times are $\Delta t_0 < 200\mu s$. A scaling has been done with $\Delta T_e/T_e$ fig. 4.9 which is a parameter much more sensitive to events taking place at the center, than the line averaged density. In this case we see the transition more clearly and taking place at $0.4 < \Delta T_e/T_e < 0.6$.

In ref. [4.11] it was suggested that the two types of decay depend on whether the pellet crossed the $q = 1$ surface or not. We have done a scaling of the relaxation time with the penetration depth from the edge of the plasma fig. 4.11. We found the fast decay turned on for $l > 8cm$. To see how this radius relates to the $q = 1$ surface, we compare the relaxation Δt_0 with $q_{ablation}$ fig. 4.12. We see that none of the pellets penetrate the $q = 1$ surface and yet are able to drive the fast relaxation. A dependence was found between Δt_0 and the sawtooth phase of the pellet fig. 4.13 for pellets in the transition region, suggesting that the sawtooth mechanism may still play a role in the fast relaxation eventhough the pellets do not penetrate $q = 1$.

To see if the fast relaxation could be driven by density gradients a study of Δt_0 and a parametrized value of the density gradient was done. By assuming a constant deposition profile shape, we showed the appropriate parameter to be $a\Delta\overline{n}/(L\overline{n})$. Fig. 4.15 shows that the central decay rates tends to grow exponentially with the density gradient parameter.

To try and understand the evolution of the anomalous transport involved in the fast relaxation, a simple diffusive model was used to simulate the temperature

evolution during injection. The deposition was assumed adiabatic with the profile being consistent with the $H\alpha$ signal. Three cases for the transport coefficients were studied. The first consisted of both χ_e and D being consistent with the bulk transport active before the pellet. In this case it was found that the leading edge of the temperature perturbation propagates into the plasma at roughly twice the pellet velocity. The propagation of the trailing edge tracks the pellet up to the ablation radius, at this time the evolution becomes much slower. This behaviour is qualitatively consistent with the slow decay case of fig. 4.4b. The second case had the transport coefficients become anomalously high as soon as the pellet penetrates the plasma. While this case could make the central temperature response be on a time scale consistent with the fast case, the start of the decay was immediate. This model then is clearly not correct, for it can not reproduce the observed propagation delay. A third model was studied, in which the transport coefficients were composed of two parts. The first component was consistent with bulk transport and the second had an anomalous value roughly two orders of magnitude larger than the bulk, which was turned on for positive density gradient. These results were qualitatively consistent with the observed behaviour of the fast $T_e(0)$ relaxation case. What these simmulations imply is that the anomalous transport necessary for the fast relaxation must propagate into the plasma with the pellet. The leading edge propagation for the first case (consistent with the slow decay case) and the third case (consistent with the fast decay case) are similar. This implies that the leading edge in both cases propagates with a thermal diffusivity consistent with bulk transport.

By considering this model we can draw some conclusions as to what may be the driving mechanism. We found that the inverted pressure profiles are much less than the inverted density profiles. If the deposition process is adiabatic, the pressure profiles should remain constant. It is only through the fast transport of the background plasma that a significantly inverted pressure profile can be generated. However this requires the anomalous transport to exist before the inverted pressure profiles. Both of these observations support the model in which the inverted density profiles drive the anomalous transport.

Pellet injection has been used to perturb the plasma in order to study the evolution of the electron temperature. In this way we were able to study the so called profile consistency principle. In all cases for $q_l < 8$ the final electron temperature profile always re-adjusted back to its pre-injection shape consistent with the canonical form whose width is given by eq. 4.4.4. This was found to be true even for cases in which the plasma was sawtoothing before, but not after injection. When $q_l > 8$ the pre-injection T_e width is found to be wider than the self-consistent width, in this region it is transport which determines the profile widths. The effects of the pellet were generally to broaden the T_e width, however there were a few cases in which the post-pellet T_e width was narrower, all these never went below the self-consistent limit.

A possible interpretation is that the self-consistent width as defined by eq. 4.4.4 is a limit which represents the narrowest stable width that can be achieved by the plasma. Whether this limit is achieved depends on the plasma transport. This reflects itself in the conditions of eq. 4.4.5 and 4.4.6. The transition between the two regimes according to this model is when $a_{T_e}(trans) \sim a_{T_e}(q_l)$, which for the case of Alcator may be when $q_l \sim 6-8$. In this respect the term 'profile consistency' is somewhat of a misnomer, for in this case the current and electron temperature profiles are sawtooth limited and in the time averaged sense independent of the transport. In this case transport only plays the role of taking the plasma to the sawtooth limit.

In sec. 4.5 we discussed the variety of sawtooth behaviour found in a post pellet plasma fig. 4.25. The evolution of the sawtooth is probably dependent on a number of plasma parameters, one parameter which may play a role in the evolution of the sawteeth is the behaviour of the impurities, whose confinement generally improves after injection. The factor by which τ_I improves seems to be dependent on pellet size, in a similar manner as the fast temperature relaxation. This suggests a link between the events taking place during the injection process, and the subsequent evolution of the plasma. Thus in order to understand the long term behaviour of the plasma, we must also understand the fast time scale physics taking place during

injection. It was also found that the improved confinement could only take place when $q_l < 6 - 8$, which is the same condition for plasma to be in the self-consistent regime.

Future work should include efforts to understand how the density evolves during pellet penetration, this will provide important information about the pressure profile and about the transport. Theoretical efforts towards understanding the mechanism by which the pellet can effect rapid transport in the plasma are essential. The model discussed here to explain profile consistency can explain the data shown. Further support for the model must await numerical simulations. Impurities may play an important role in sawtooth stabilization in low q_l discharges. We must understand what kind of electron temperature profiles can be set up by the impurities and how the electron temperature profile may differ from the canonical shape.

References for chapter IV

[4.1] Ware A.A.,Phys. Rev. Lett. 25(1970)916

[4.2] Blackwell B.,et. al. MIT-PFC report PFC/CP-82-7

[4.3] Greenwald M., et. al. Phys. Rev. Lett. 53,4(1984)352

[4.4] Fielding S.J.,et. al. Proc. 8^{th} Eur. Conf. on Cont. Fus. and Plas. Phys. (1977)

[4.5] Spitzer L.,et. al. NYO-6047, USAEC(1954)

[4.6] Foster C.A., et. al. Nucl. Fus. 17,5(1977)1067

[4.7] Milora S.L.,et. al. Phys. Rev. Lett. 42,2(1979)97

[4.8] Milora S.L.,et. al. ORNL/TM-7422 (1980)

[4.9] Milora S.L.,et. al. NUcl. Fus. 22,10(1982)

[4.10] Buchl K.,Bull. Am. Phys. Soc. 28(1984)

[4.11] Sengoku S.,et. al. Nucl. Fus. 25,10(1985)

[4.12] Lazare O., TFR report

[4.13] Vlases G.,ECA Cont. Fus. and PLas. Phys. 7d(1983)

[4.14] Gomez C.C.,et. al. Bull. Am. Phys. Soc. 28(1984)

[4.15] Milora S.L.,Foster C.A. Rev. Sci. Inst. 50(1979)482

[4.16] Parker J.K.,MIT-PFC report PFC/RR-85-8

[4.17] Kissel S.E.,MIT-PFC report PFC/RR-82-15

[4.18] Gomez C.C.,et. al. Bull. Am. Phys. Soc. 28(1983)1249

[4.19] Petrasso R.D.,et. al. to be published

[4.20] Terry J.L.,private communication.

[4.21] Marmar E.S.,et. al. Nucl. Fus. 22,12(1982)

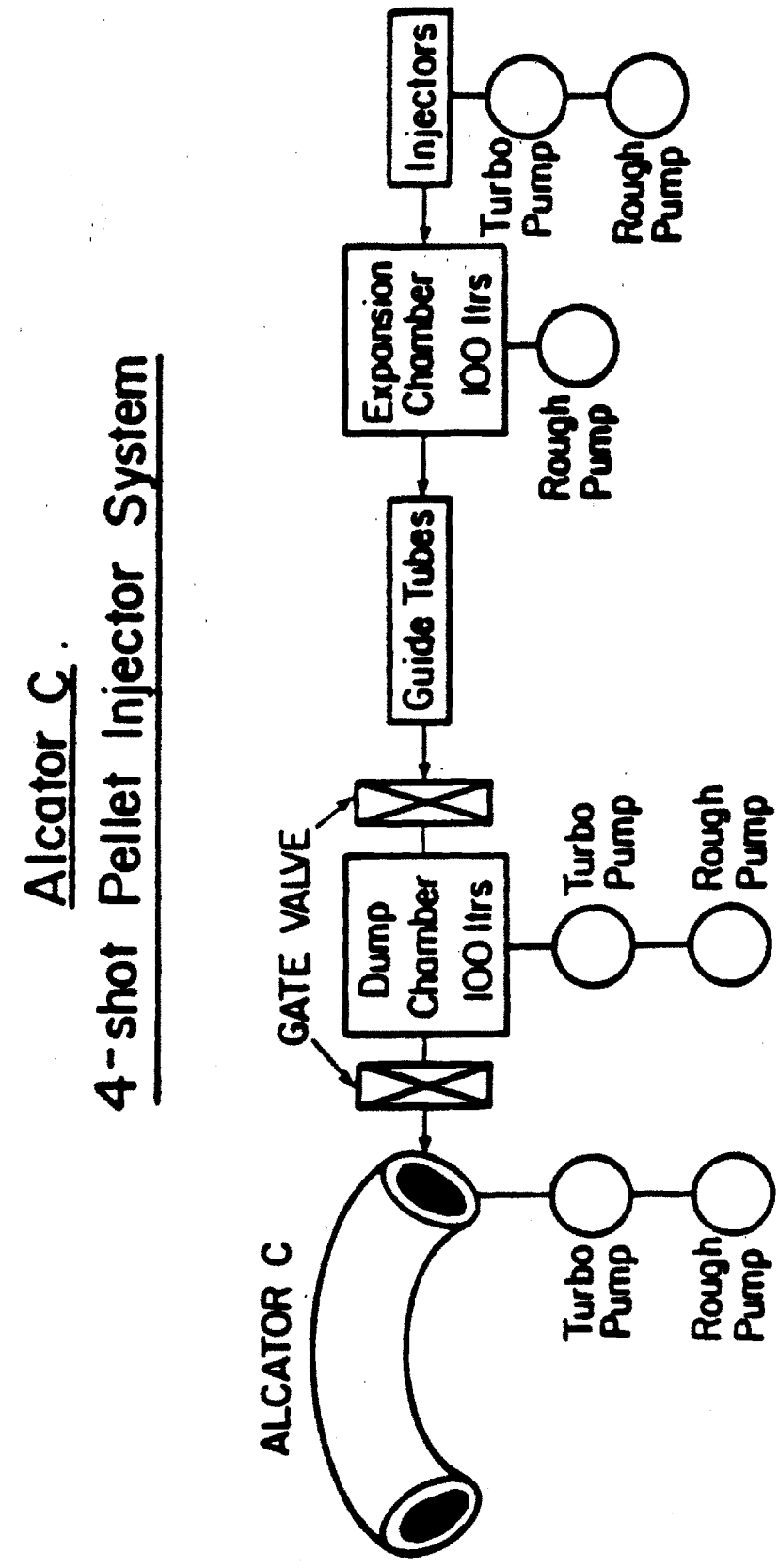
Alcator C
4-shot Pellet Injector System
Injectors
Turbo Pump
Rough Pump
Expansion Chamber 100 litrs
Turbo Pump
Rough Pump
Guide Tubes
GATE VALVE
Dump Chamber 100 litrs
Turbo Pump
Rough Pump
ALCATOR C
Turbo Pump
Rough Pump

Figure 4.1

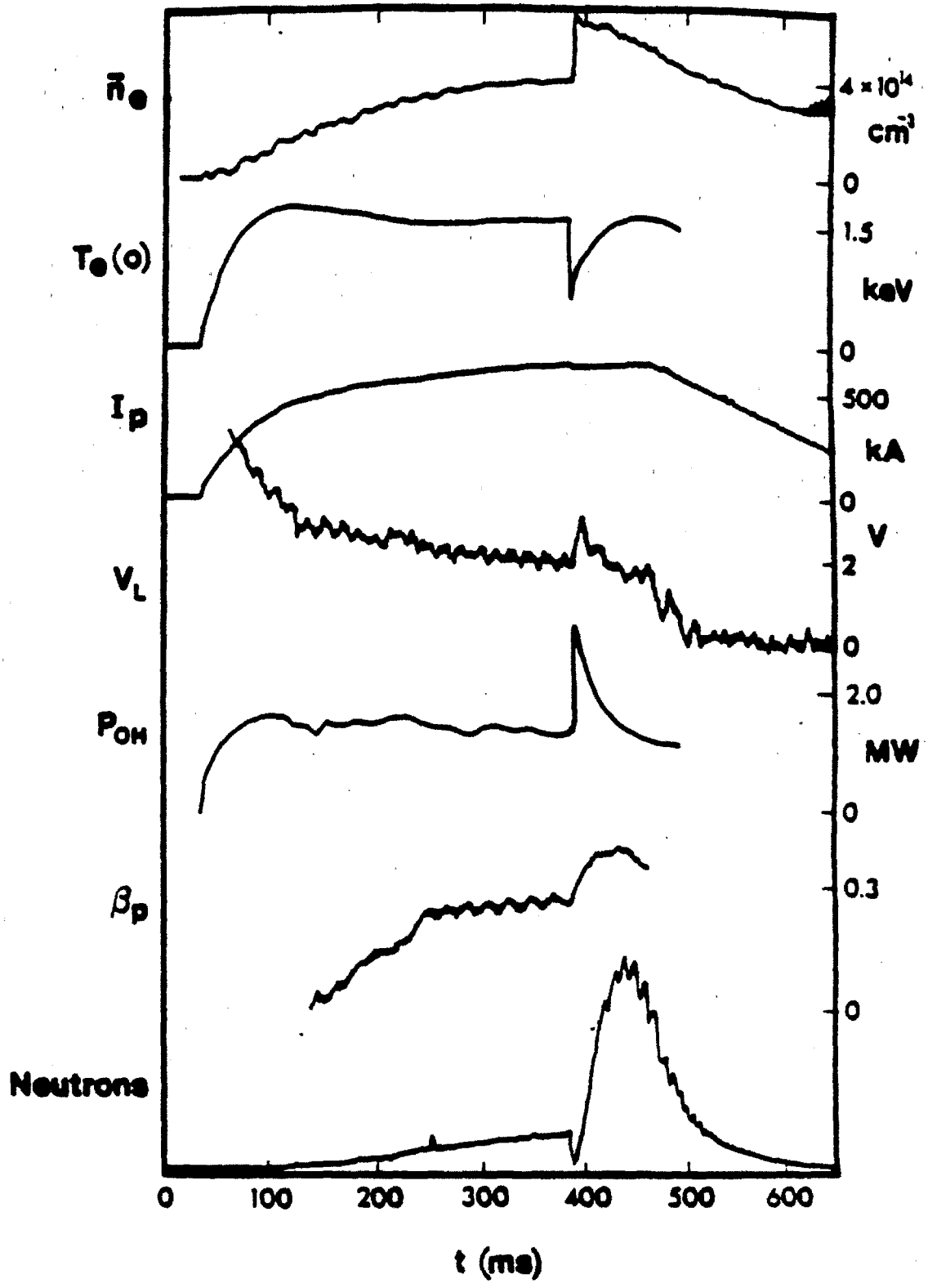

Figure 4.2 — Typical response of various plasma parameters to pellet injection.

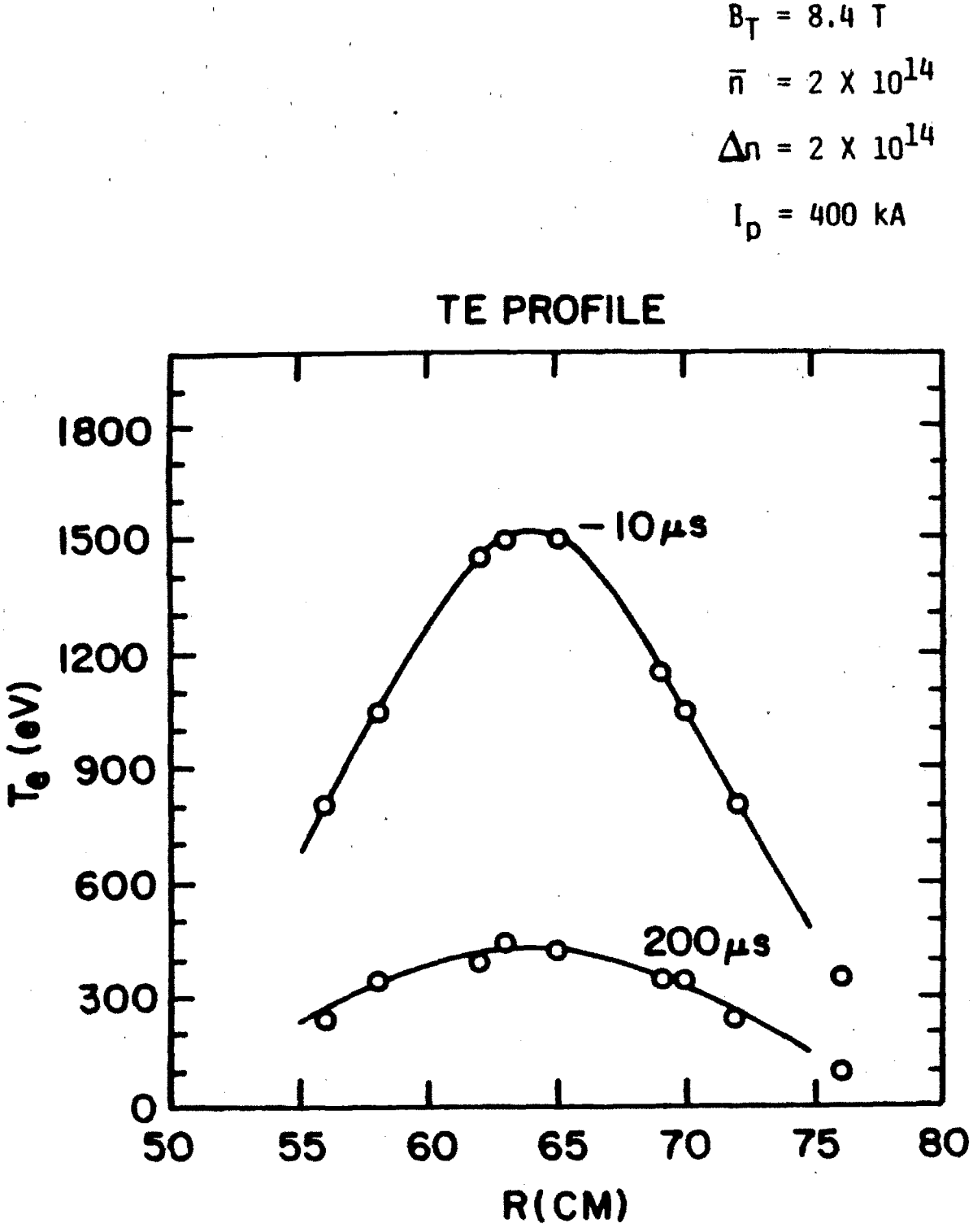

Figure 4.3 — Electron temperature profiles before and after pellet injection showing fast recovery of profile shape.

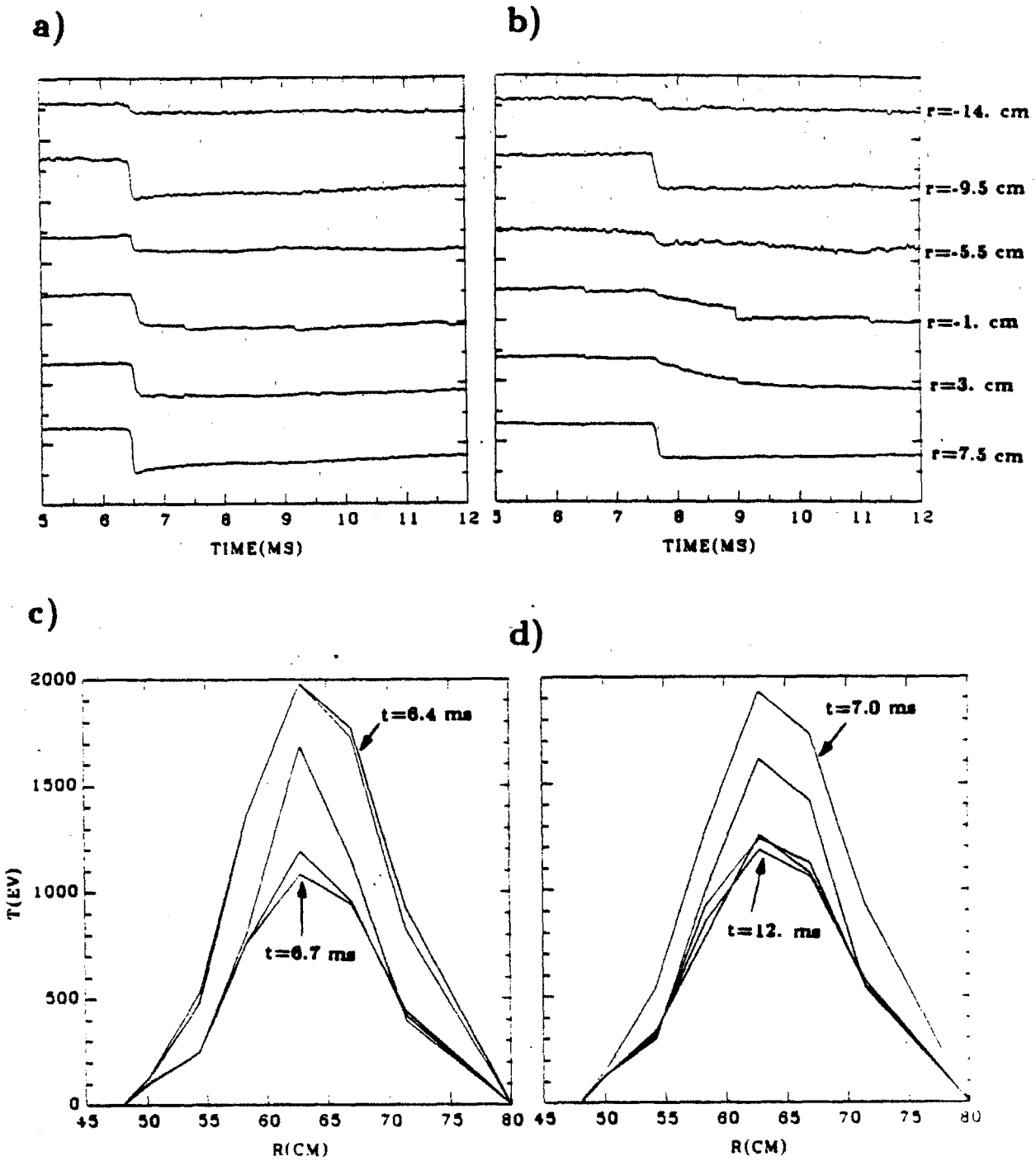

Figure 4.4 — The top figures show the temperature traces for a)fast, b)slow relaxation. The bottom two figures show the profile evolution for c) fast, d) slow case.

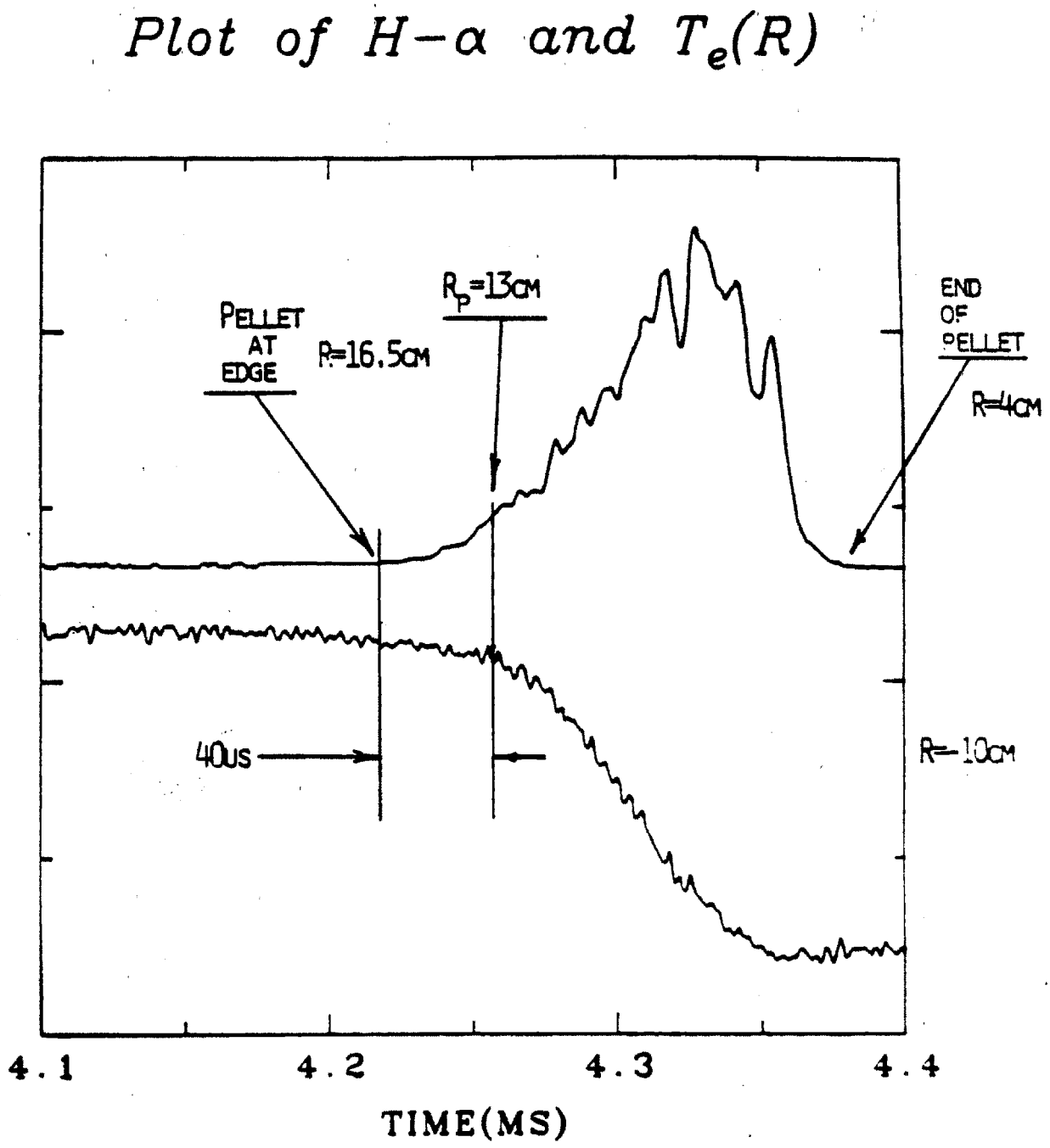

Figure 4.5 — The top trace is the evolution of the $H\alpha$ signal and the bottom trace is that for the electron temperature at $r = 10cm$.

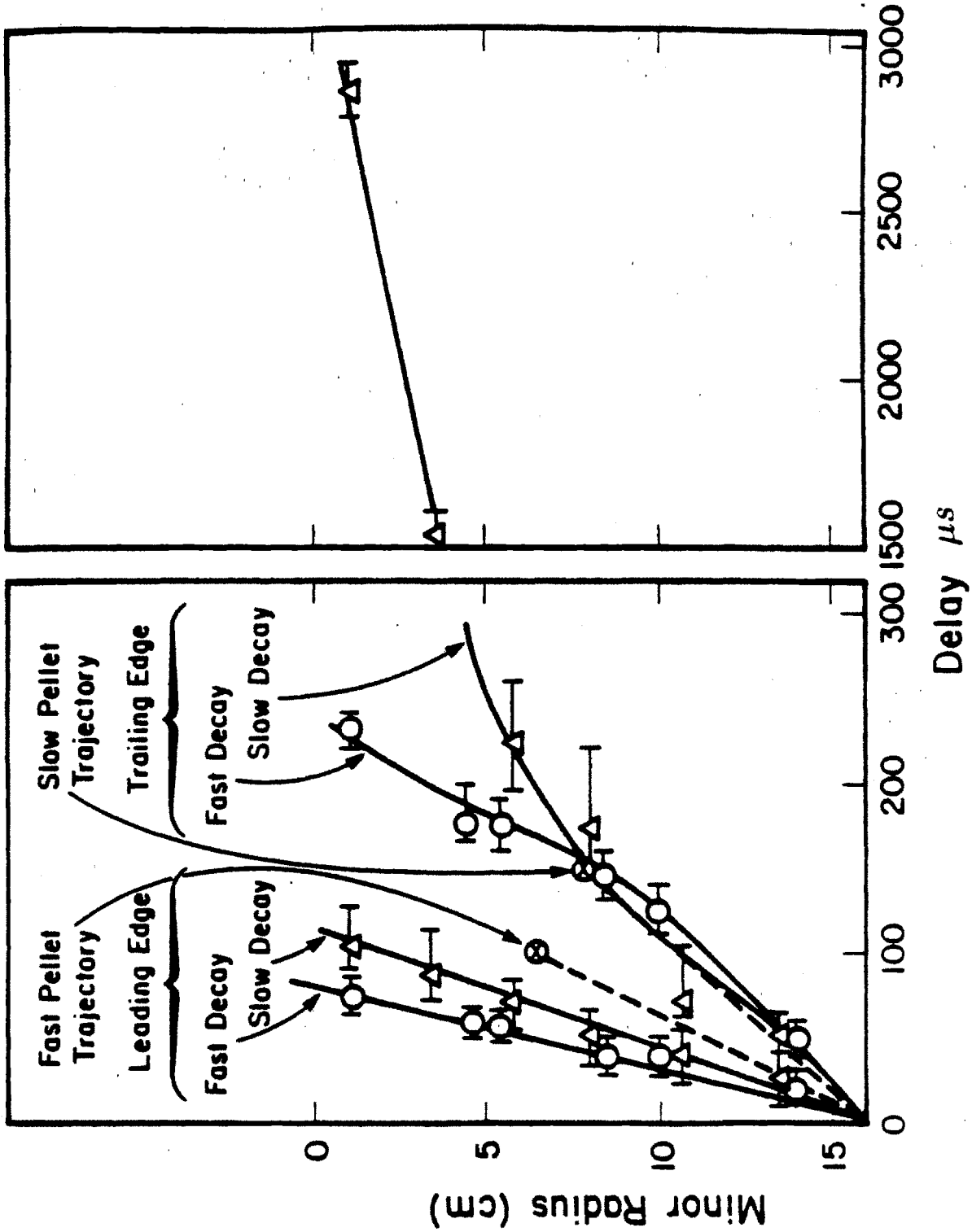

Figure 4.6 — Propagation study of leading and trailing edges for the fast and slow decaying cases.

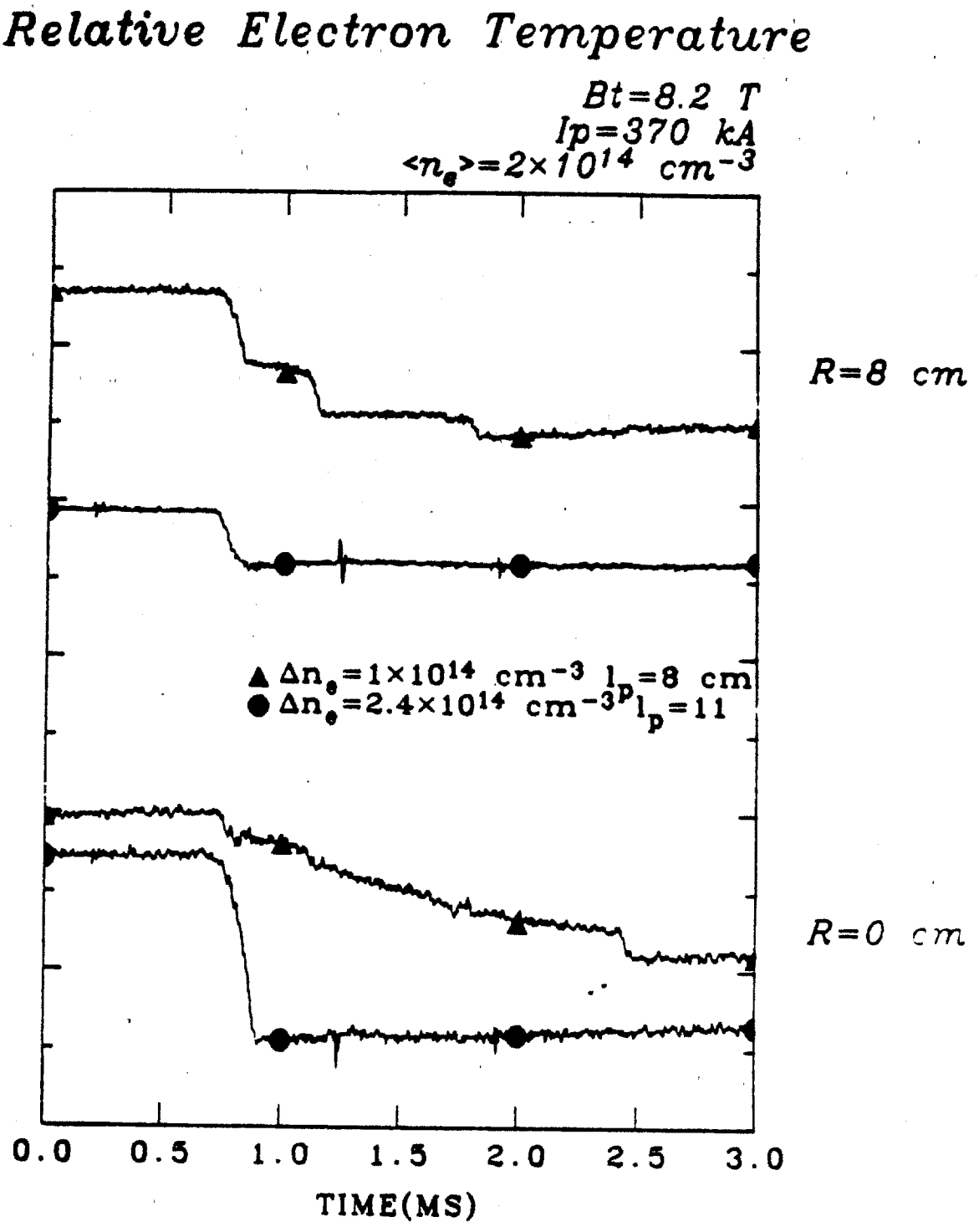

Figure 4.7 — Comparison of evolution of fast and slow decaying cases as discussed in ref.[4.14]. The main difference found between the two cases is the size of the density change due to the pellet.

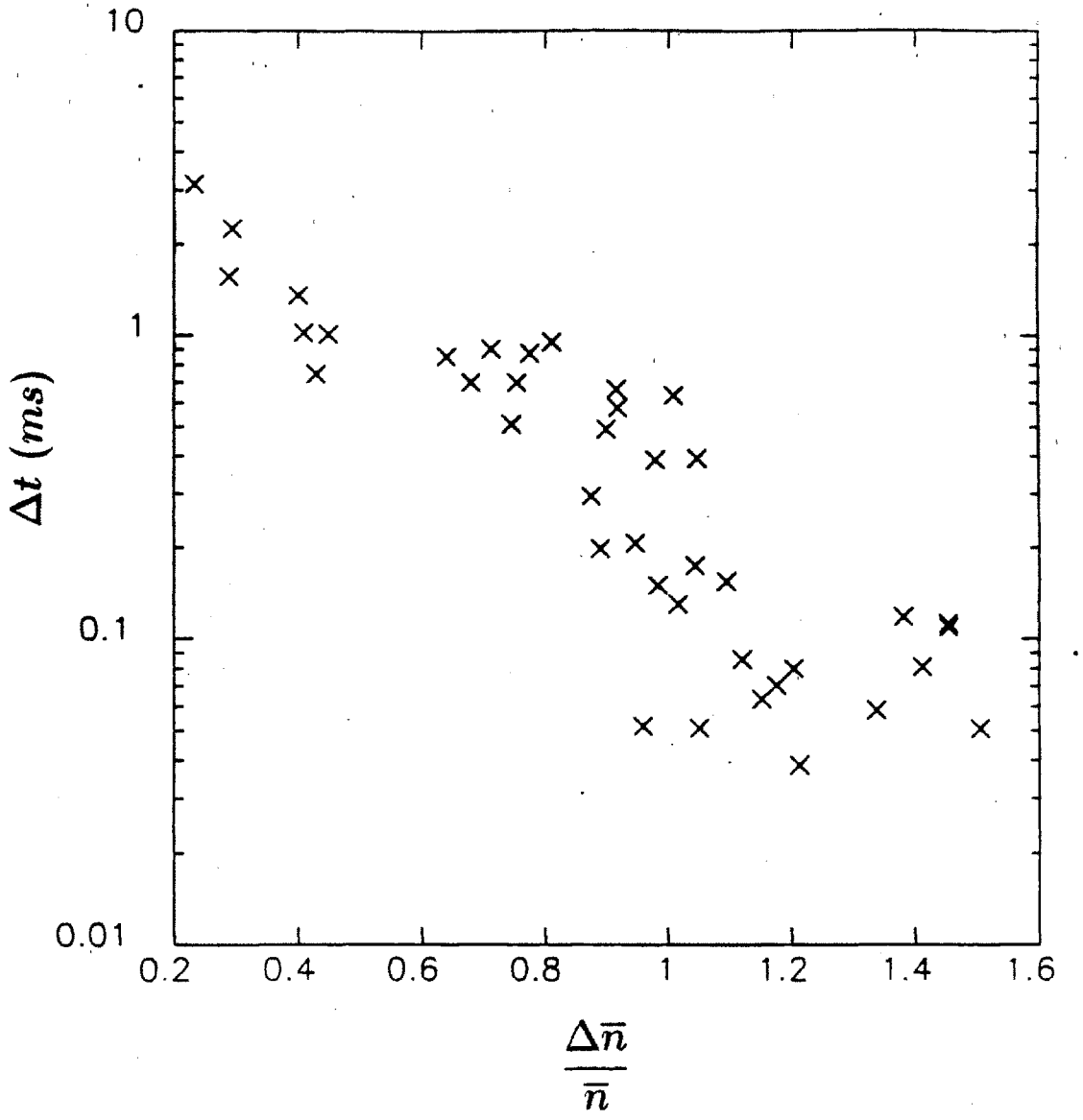

Figure 4.8 — Scaling of central T_e relaxation time with normalized change in the central line averaged density.

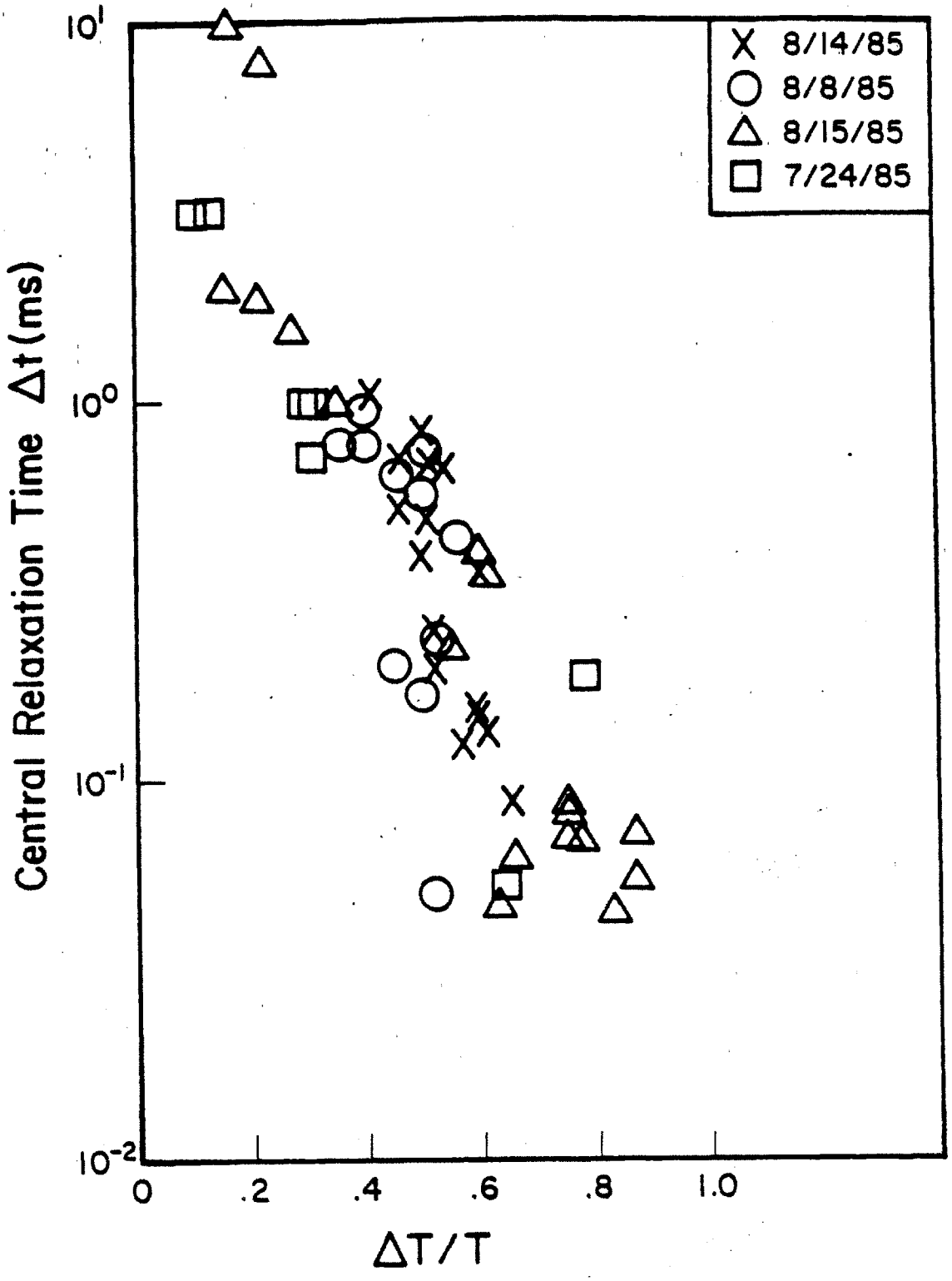

Figure 4.9 — Scaling of central T_e relaxation time with normalized change in central T_e.

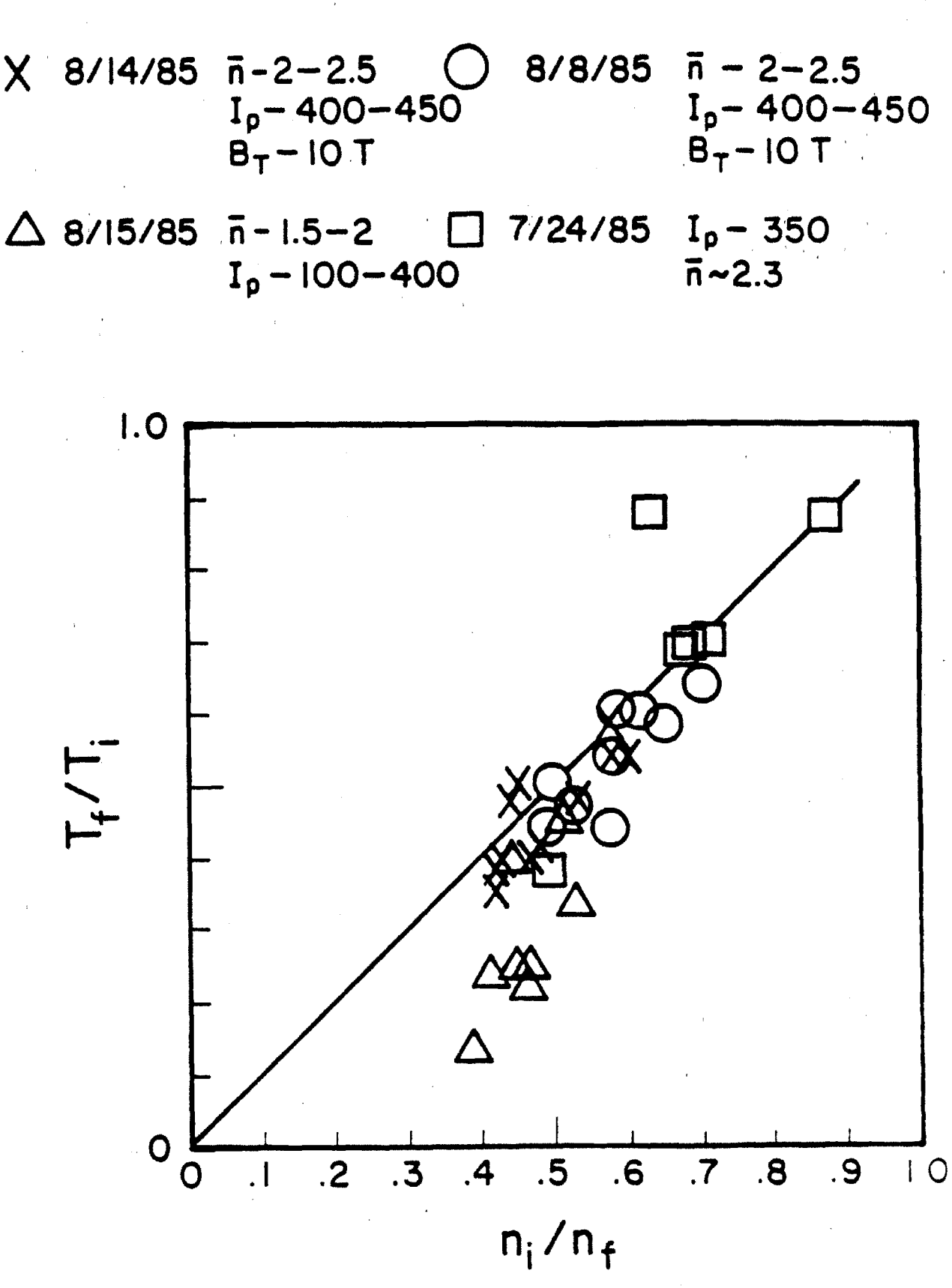

Figure 4.10 — Correlation of change in central T_e and line averaged density.

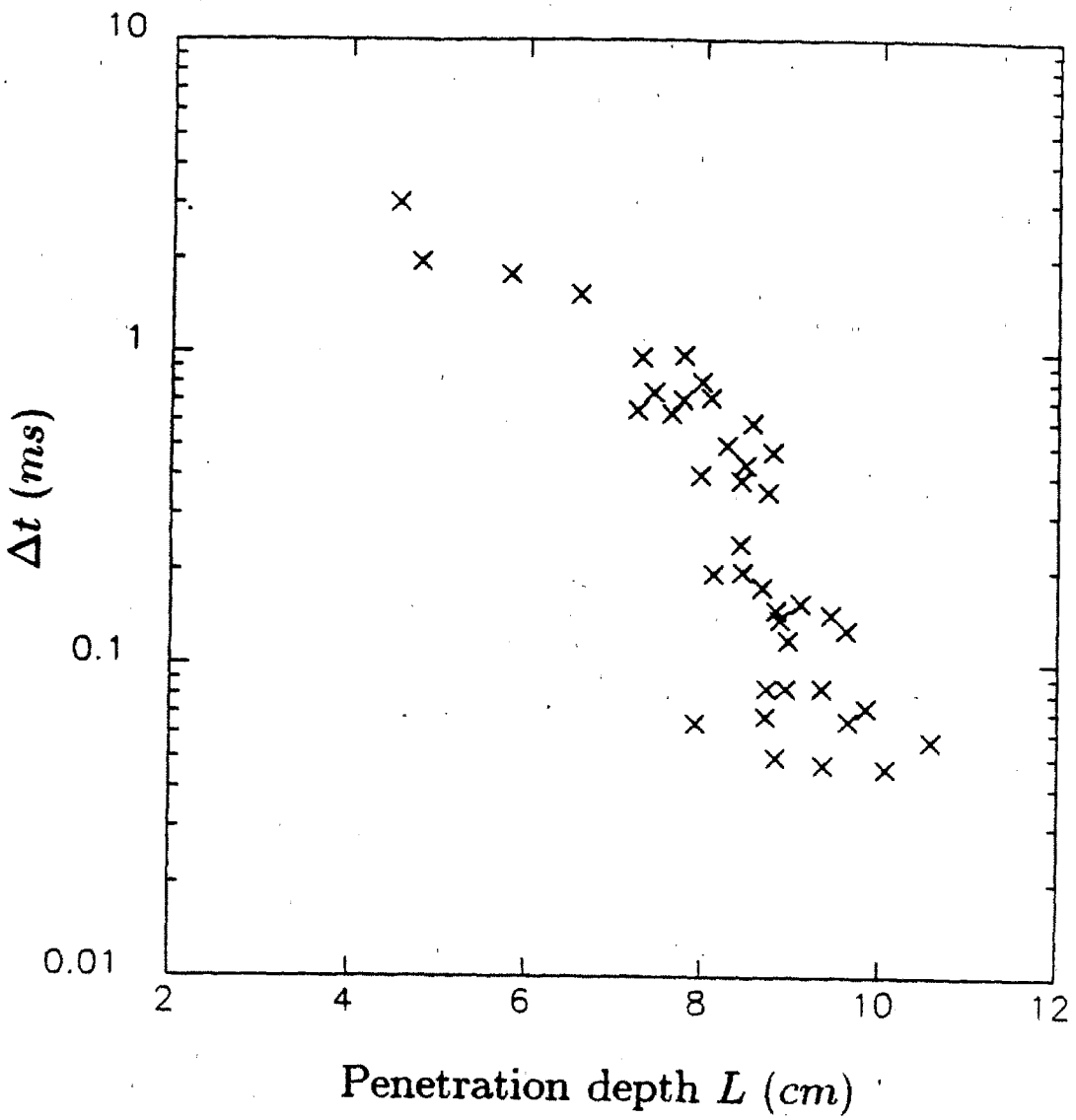

Figure 4.11 — Dependence of central T_e relaxation time on penetration depth of pellet measured from the plasma edge.

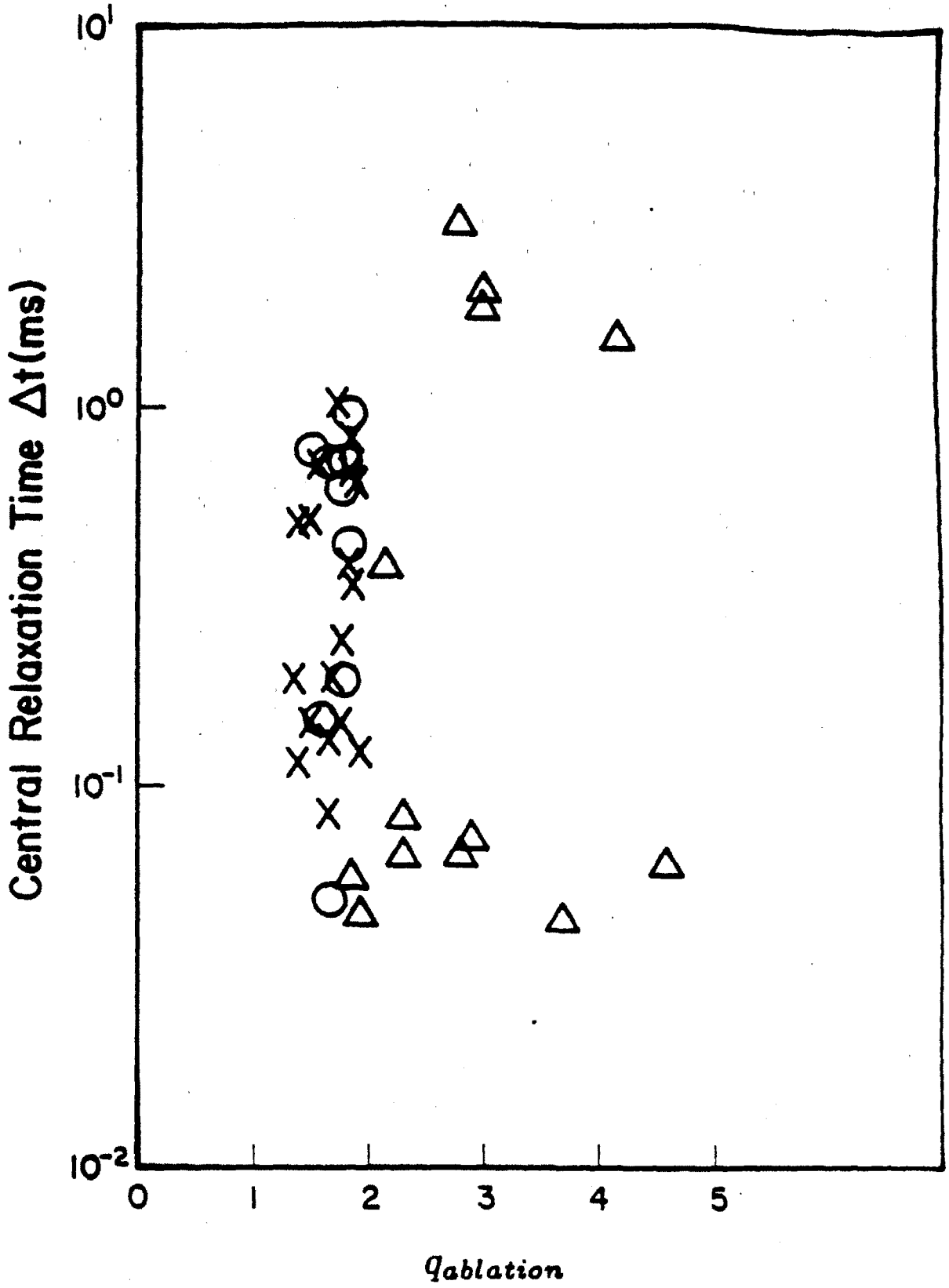

Figure 4.12 — Scaling of central relaxation time with safety factor value at the ablation radius.

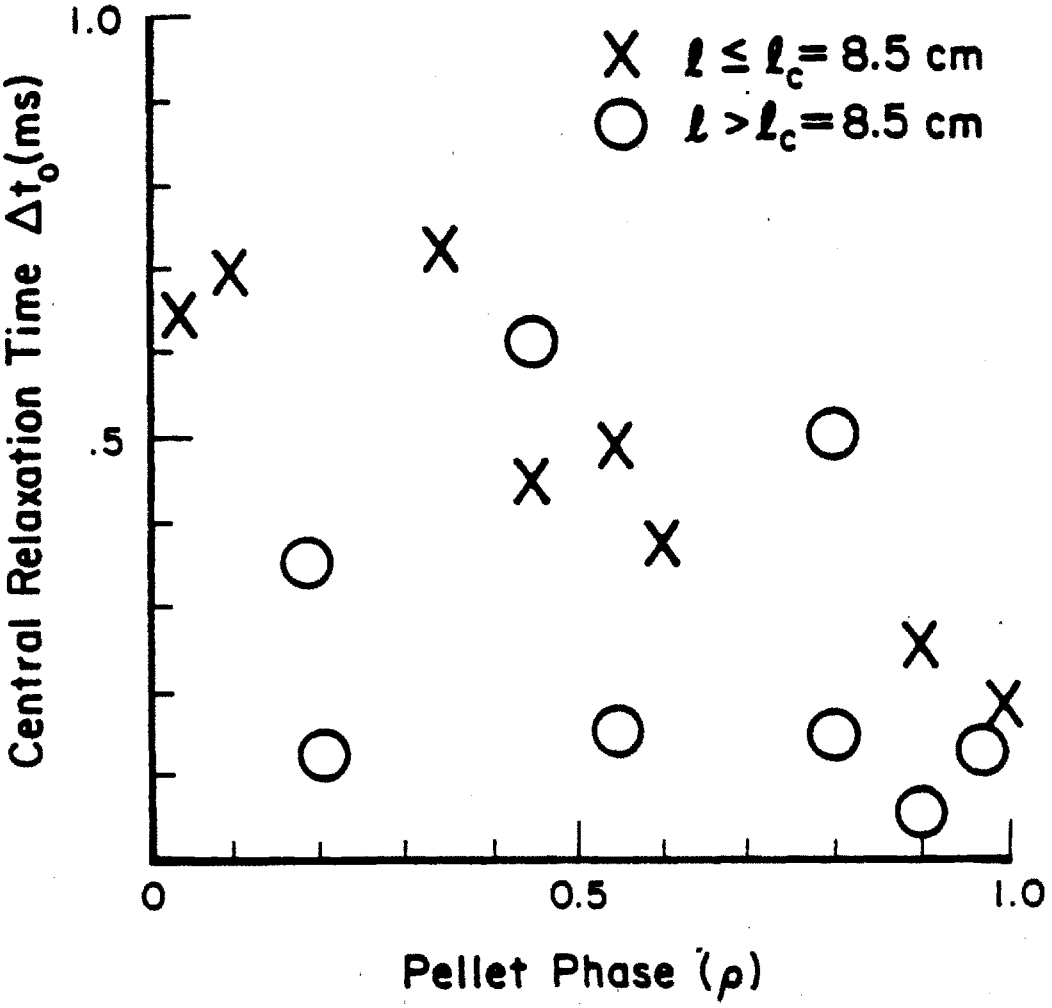

Figure 4.13 — Correlation of central T_e relaxation time with pellet phase for shots within the transition region ($8 < l < 9$) in fig. 4.11

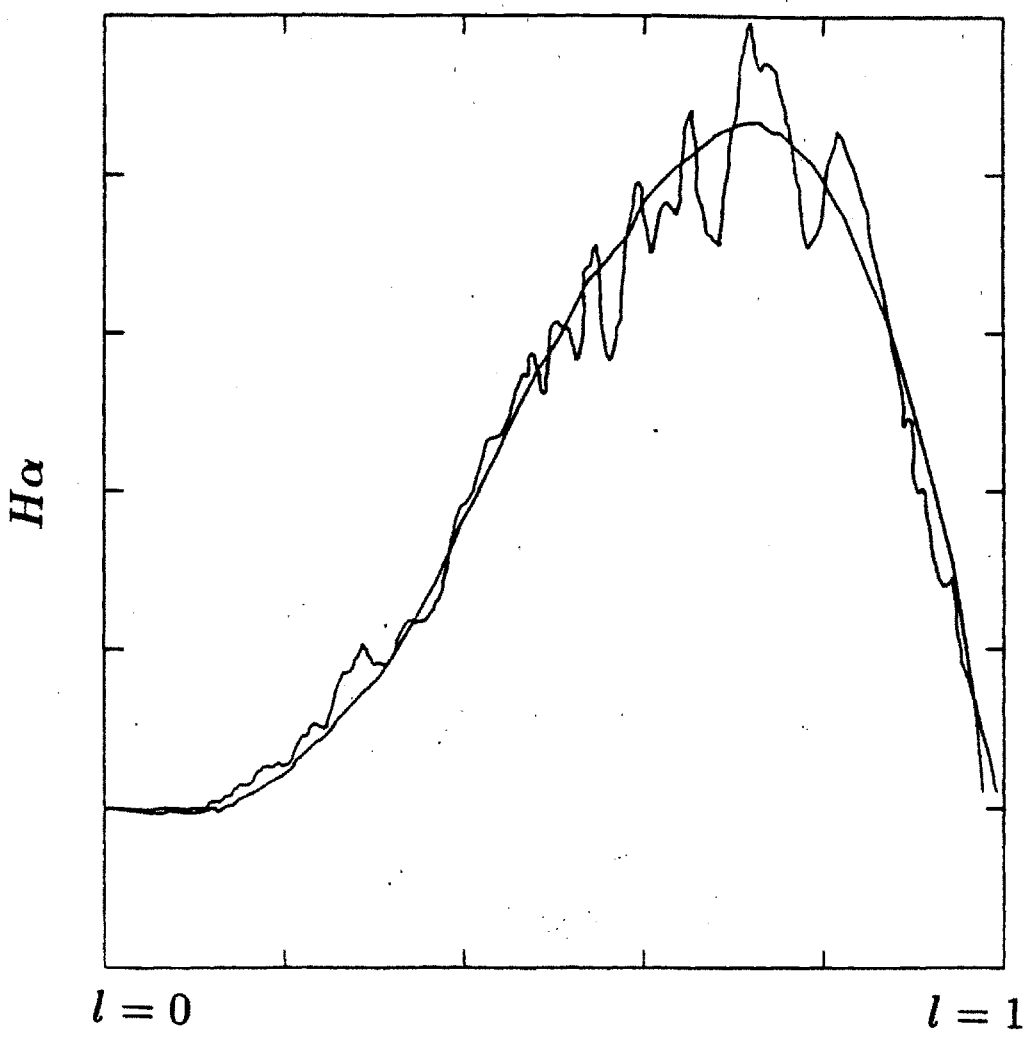

Figure 4.14 — $H\alpha$ signal with parametrization function as discussed in sec. 4.2.5

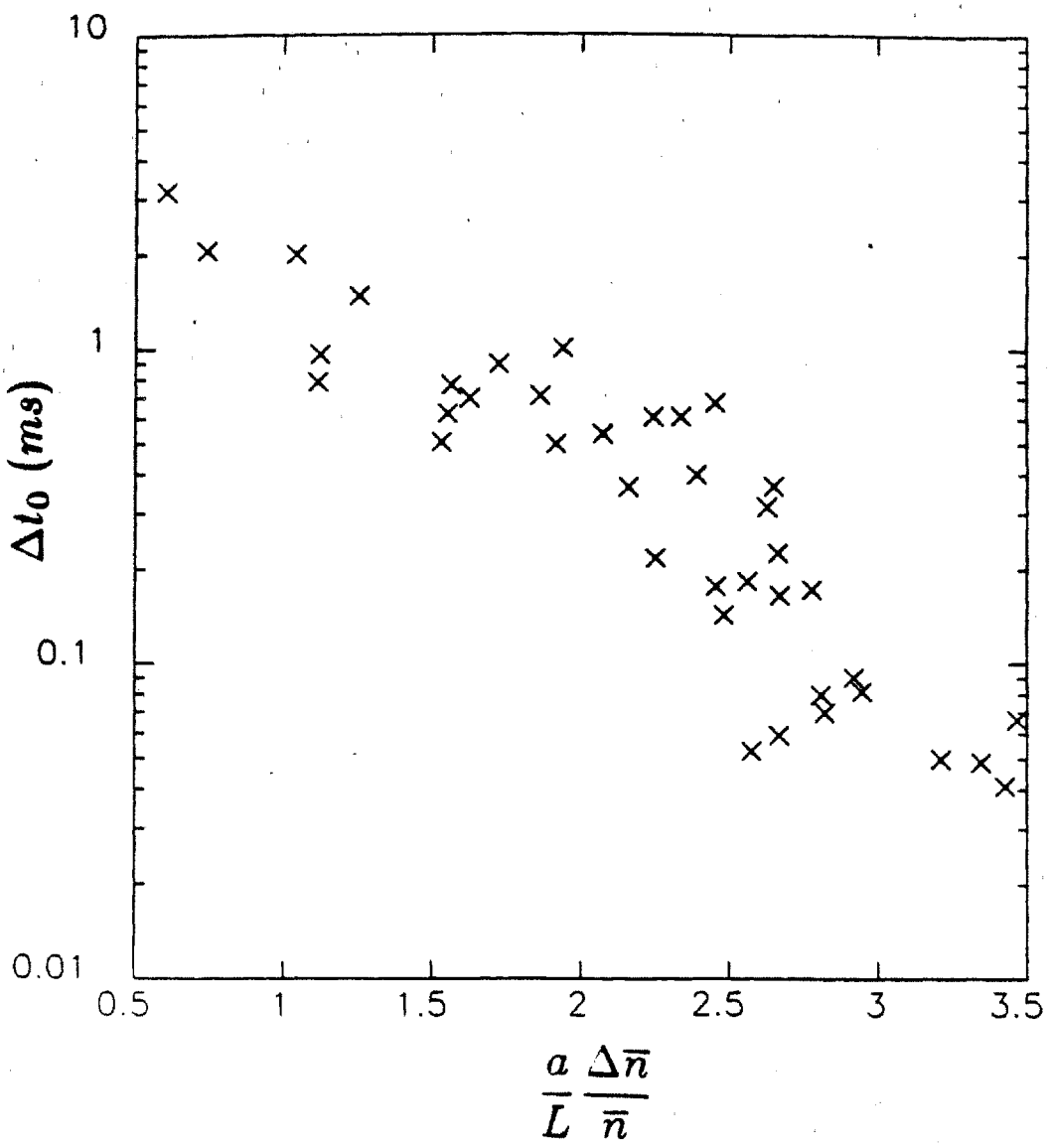

Figure 4.15 — Scaling of central T_e relaxation with normalized density parameter.

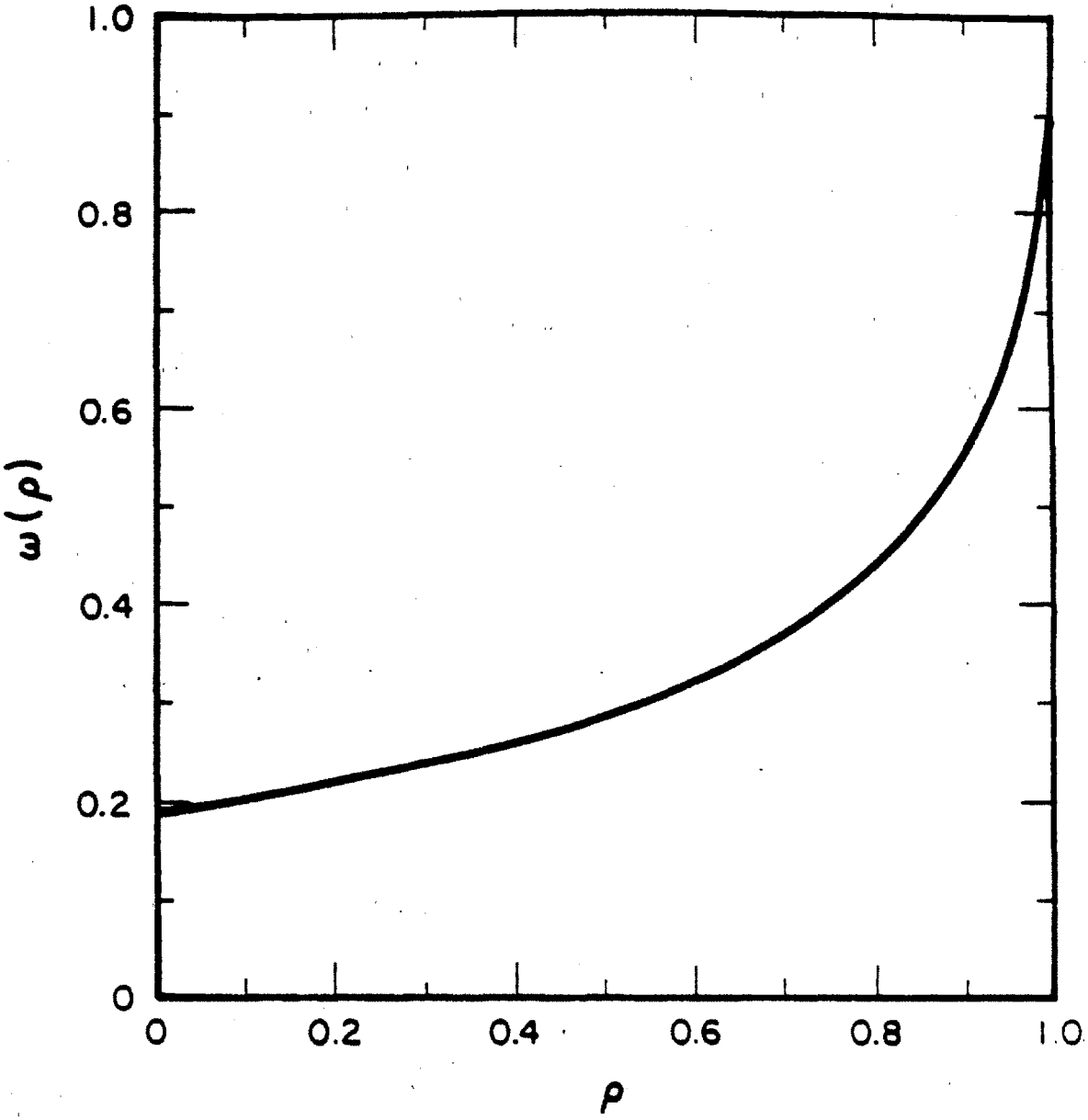

Figure 4.16 — Evaluation of integral shown in eq. 4.3.6.

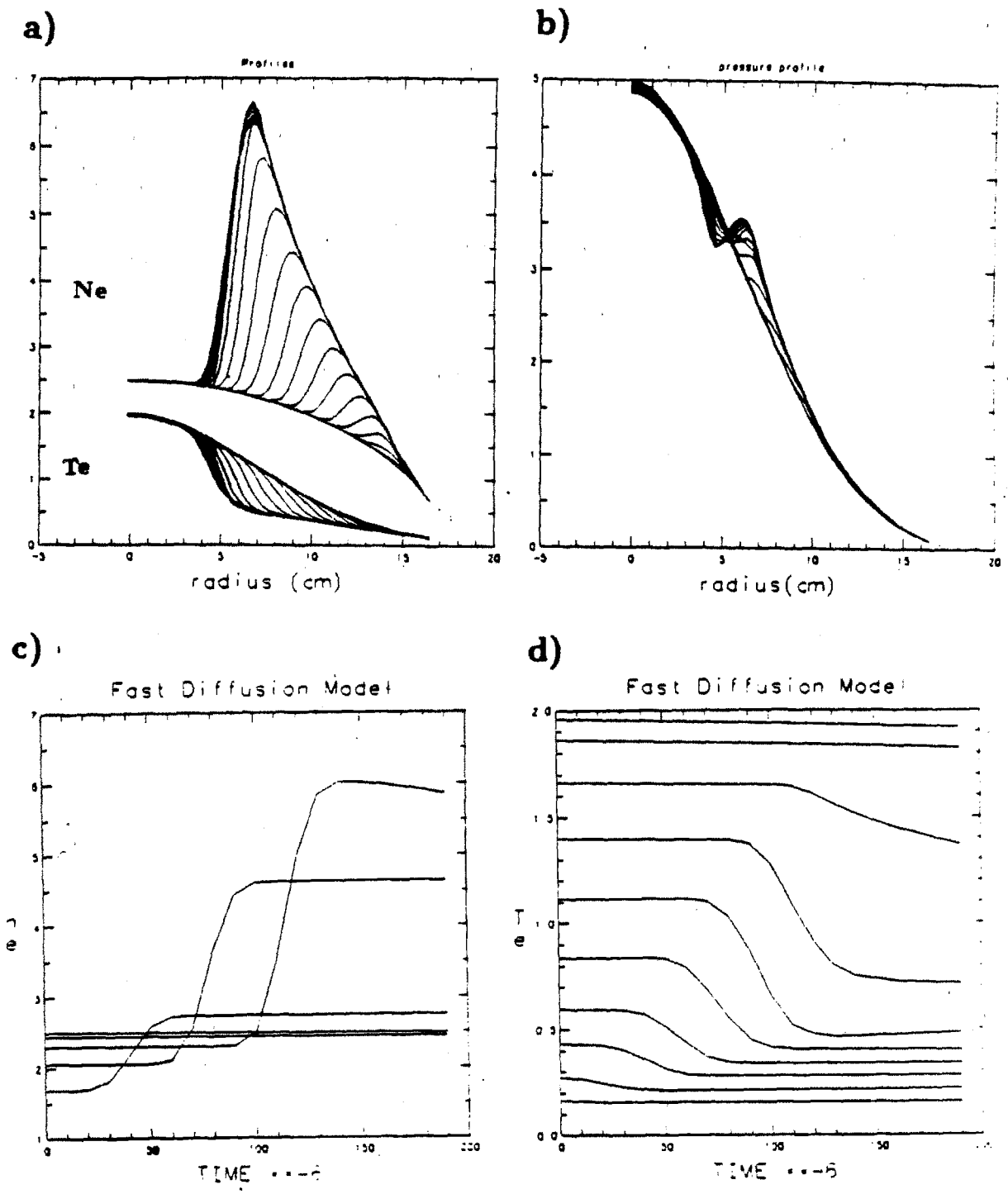

Figure 4.17 — Time evolution of a)top trace density,bottom T_e and b)pressure profiles, c,d)show time evolution at various radii of T_e and n_e. The case shown has $\chi_{e0} = 5cm^2/ms$ and $D_0 = 3cm^2/ms$.

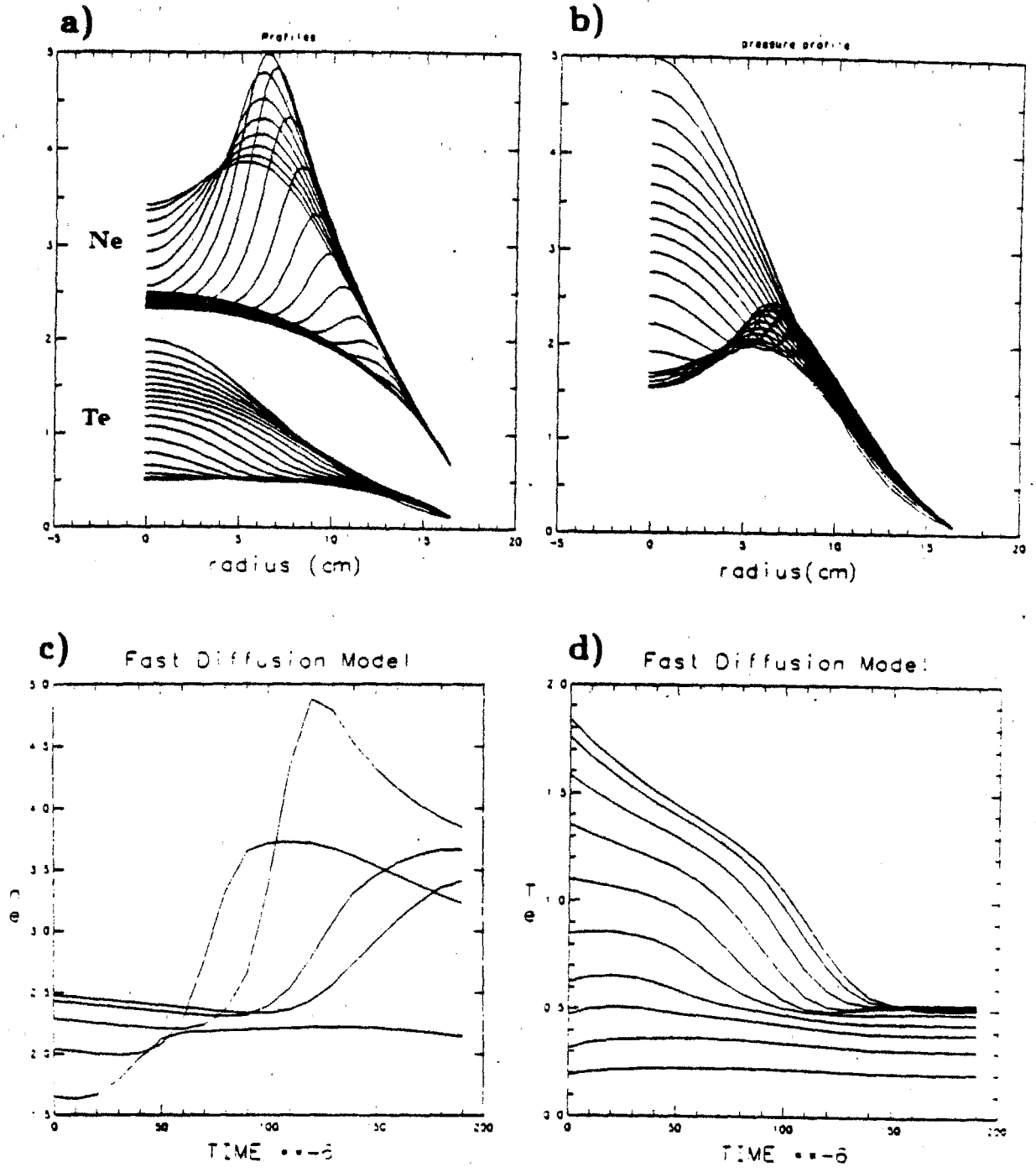

Figure 4.18 — Time evolution of a)top trace density,bottom T_e and b)pressure profiles, c,d)show time evolution at various radii of T_e and n_e. The case shown is for $\chi_{e0} = 300cm^2/ms$ and $D_0 = 90cm^2/ms$.

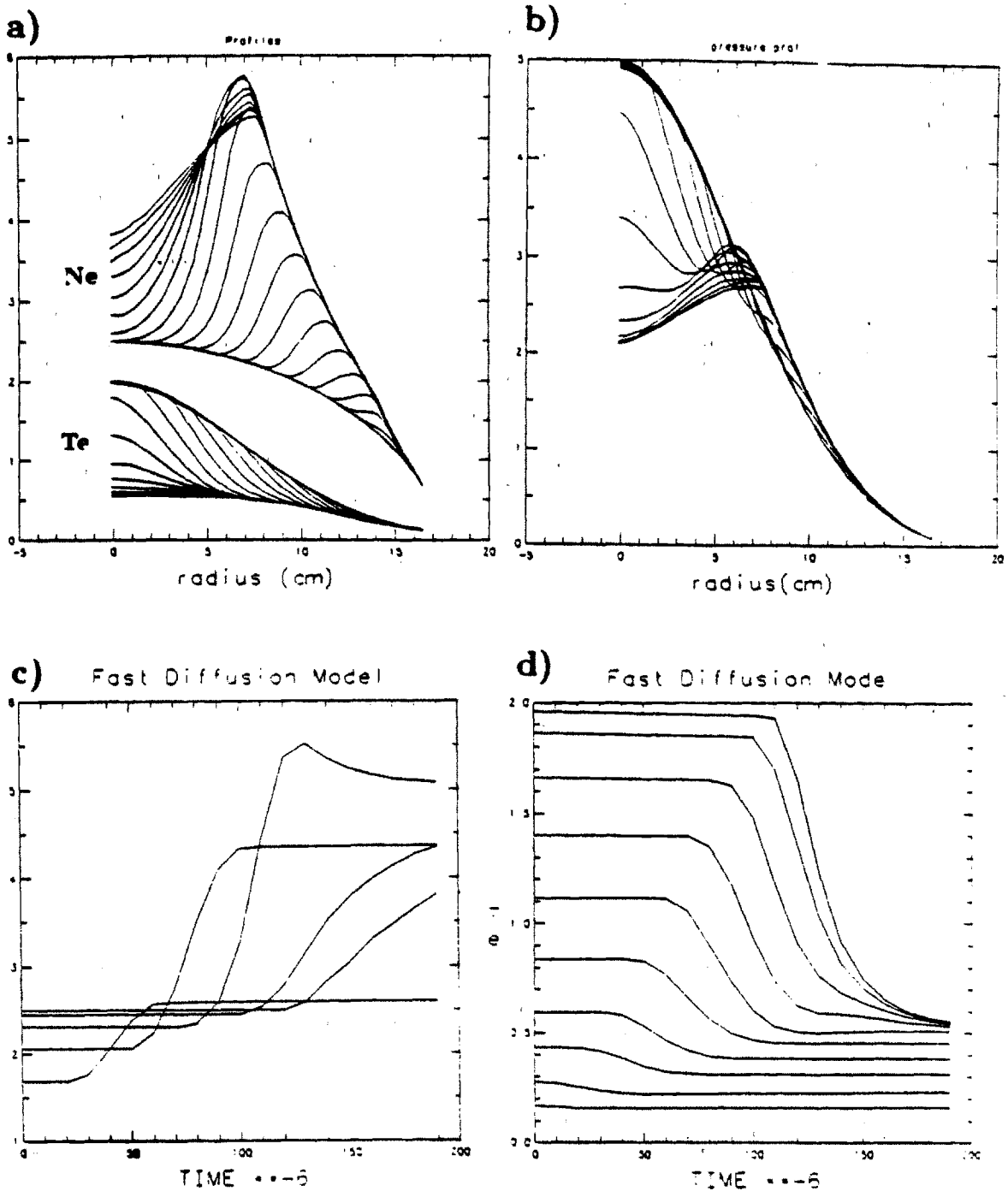

Figure 4.19 — Time evolution of a)top trace density,bottom T_e and b)pressure profiles, c,d)show time evolution at various radii of T_e and n_e. This case has $\chi_{e0} = 5cm^2/ms$, $\chi_{e1} = 250cm^2/ms$, and $D_0 = 3cm^2/ms$, $D_1 = 90cm^2/ms$ (see text for details).

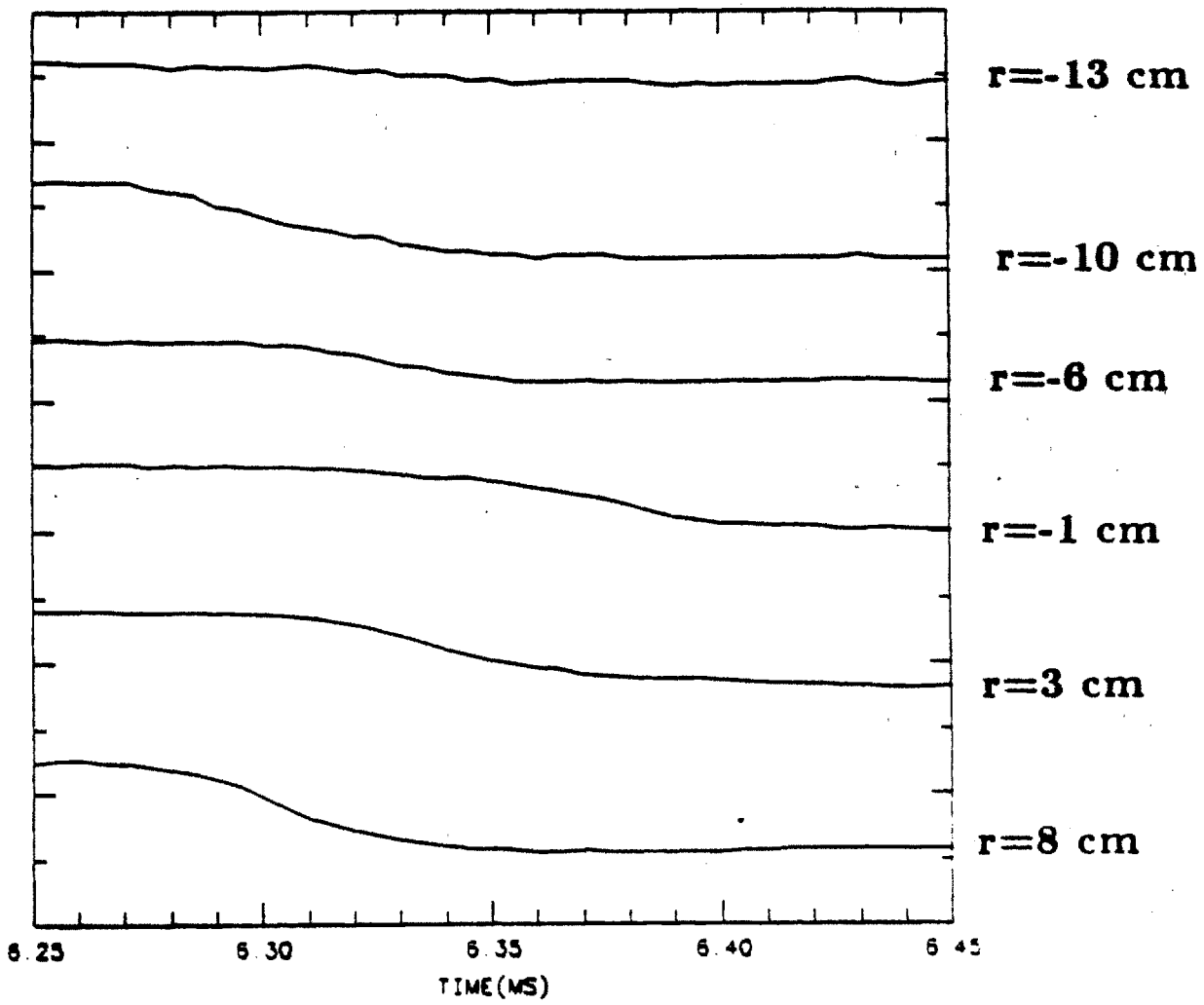

Figure 4.20 — Detail of evolution of fast decay case.

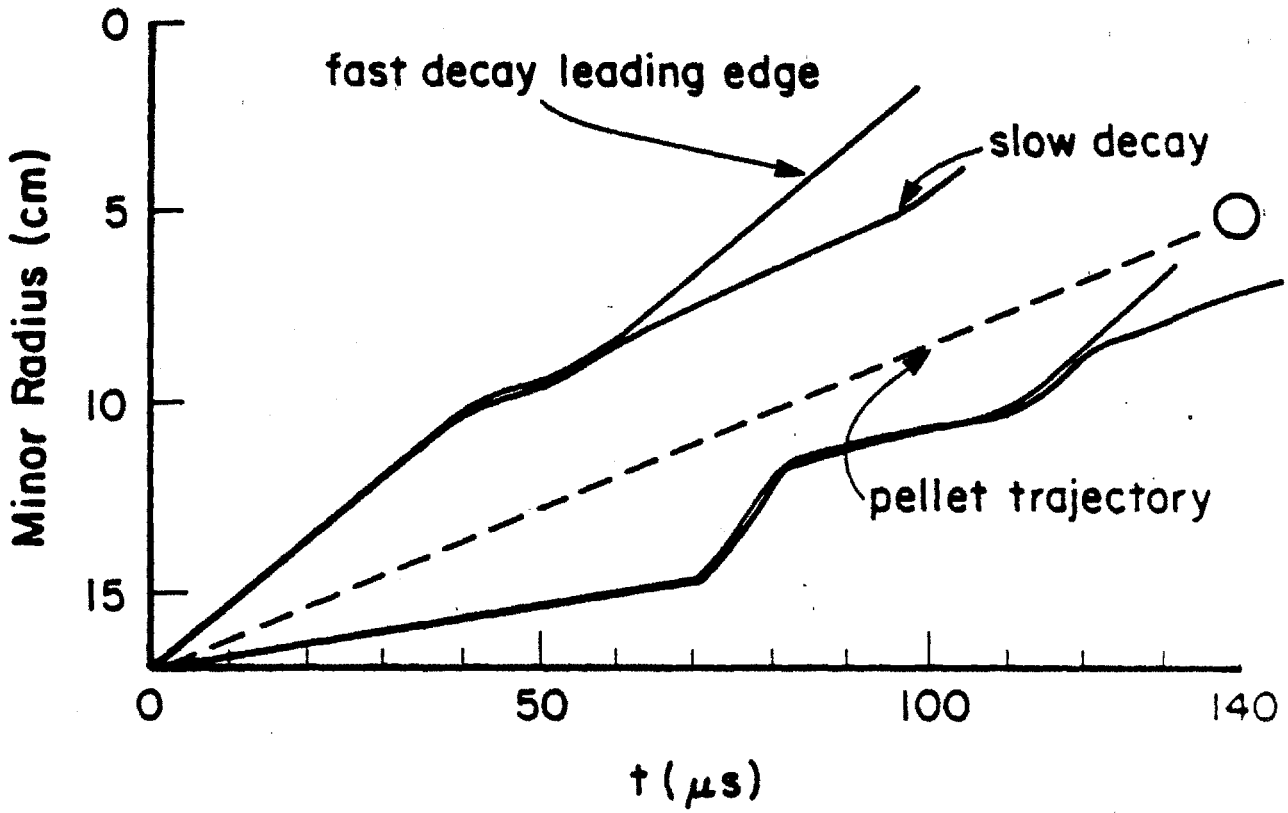

Figure 4.21 — Propagation study of simulated leading and trailing edges of pellet heatpulse for the cases shown in fig. 4.17 and 4.19.

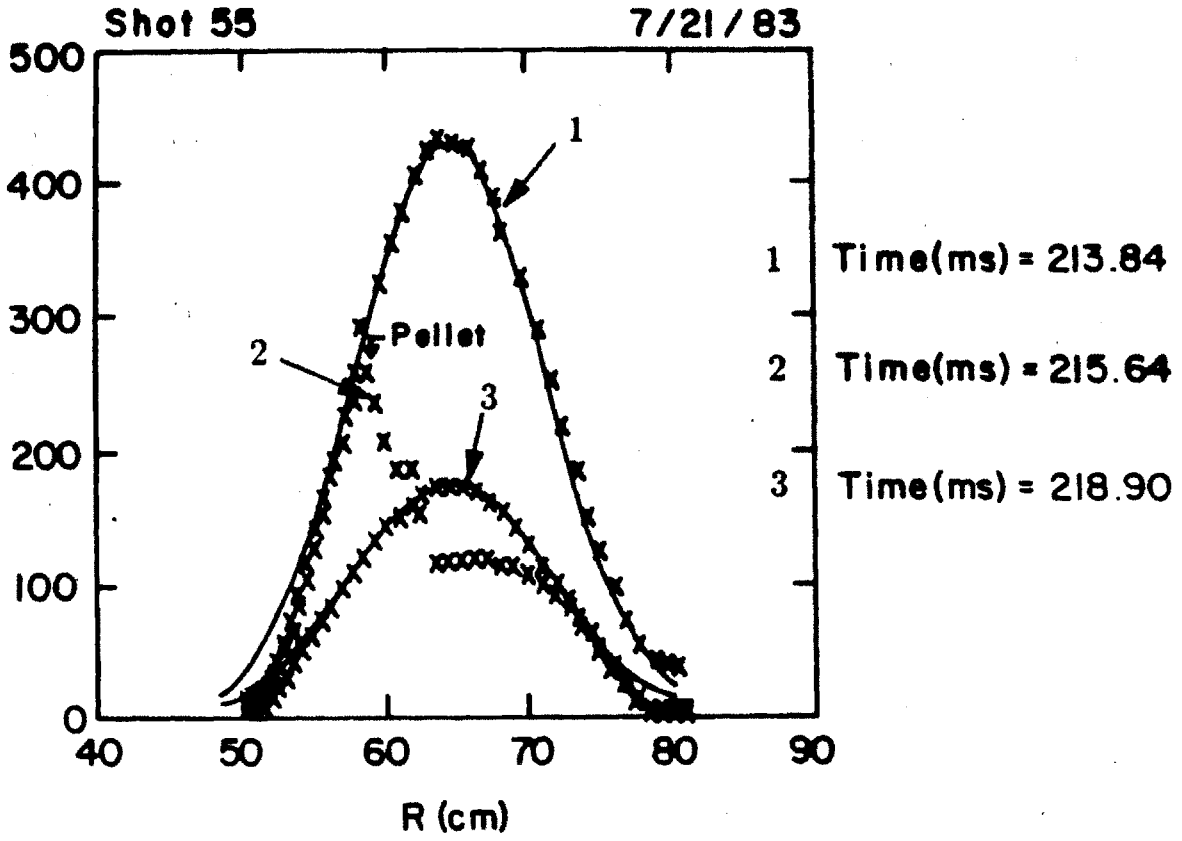

Figure 4.22 — The Fabry-Perot scans the plasma every $2ms$. In the middle trace it 'caught' the pellet during a scan, the discontinuity around $R = 60cm$ is due to the fast temperature relaxation. By the time the scan is finished the profile shape has recovered.

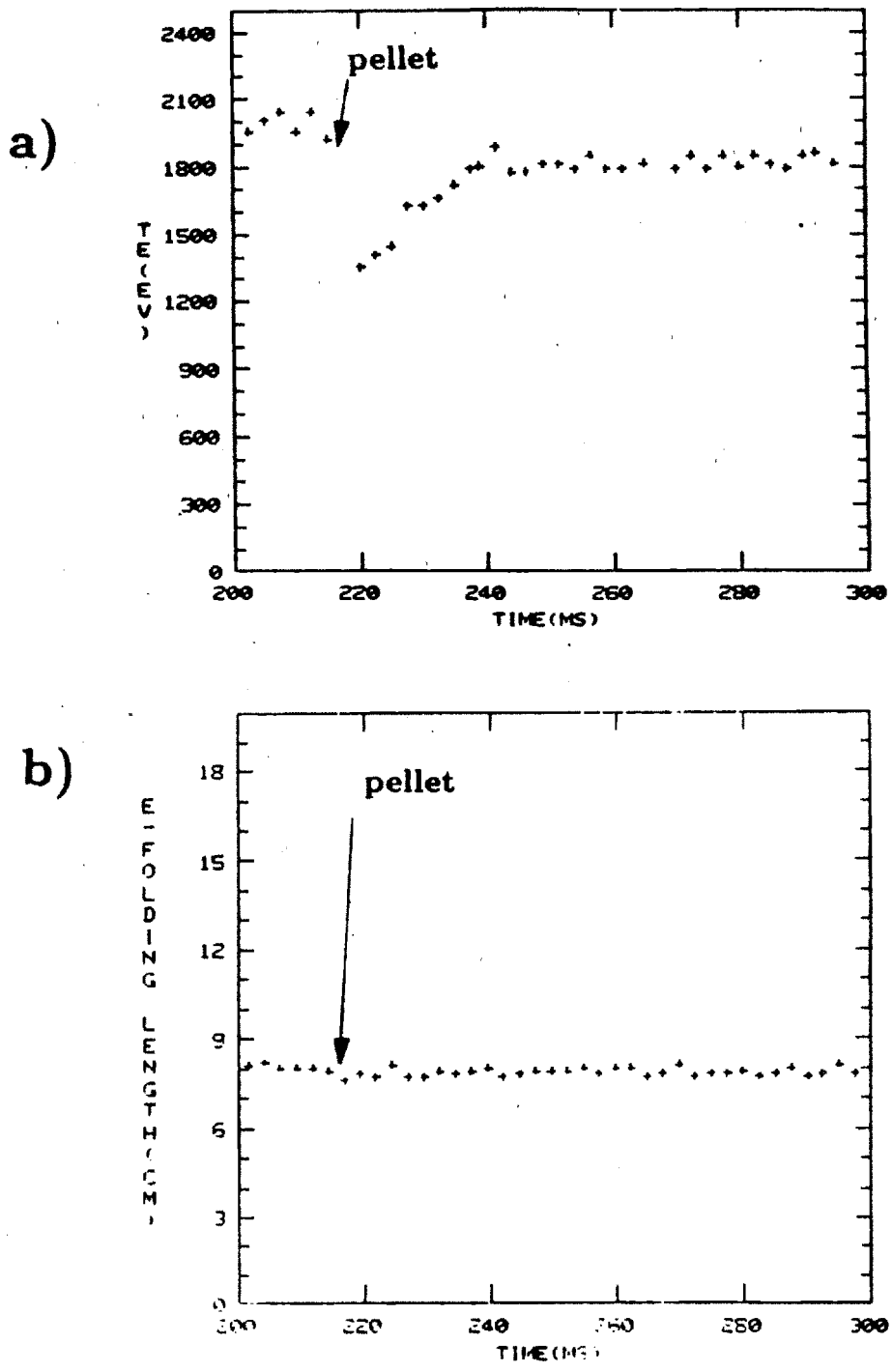

Figure 4.23 — Long time scale evolution of the temperature as measured by the scanning Fabry-Perot.a)central temperature,b)e-folding width of temperature profile.

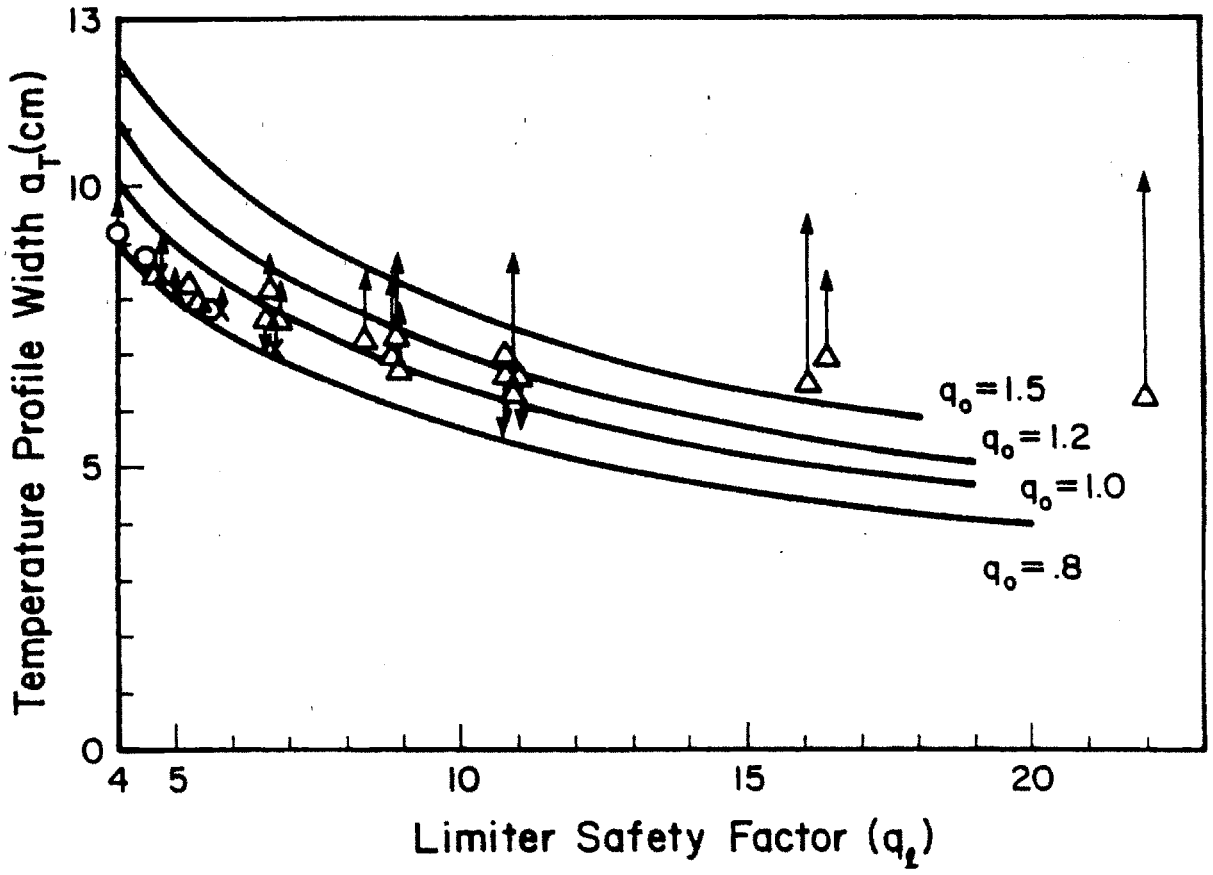

Figure 4.24 — Scaling of T_e profile width with q_l(limiter safety factor). The data markers represent the value of a_{T_e} before injection and the tips of the arrows eminating from the markers show a_{T_e} at $5ms$ after injection. If no arrow is shown, then there was no discernable change in a_{T_e}. The solid lines represent the self-consistent a_{T_e}(eq. 4.4.4) for constant q_0.

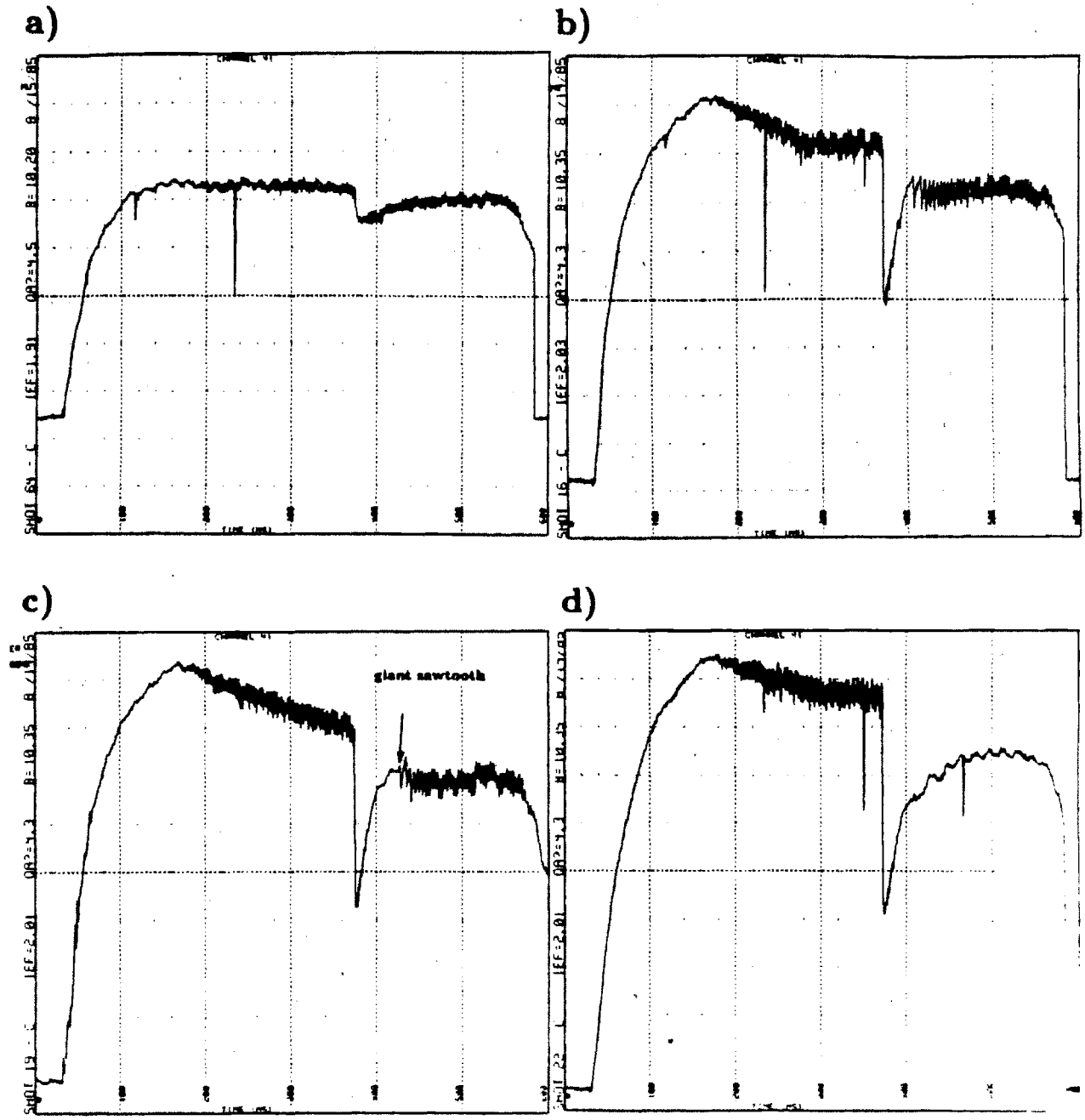

Figure 4.25 — Evolution of central T_e showing four different cases of sawtoothing after pellet.

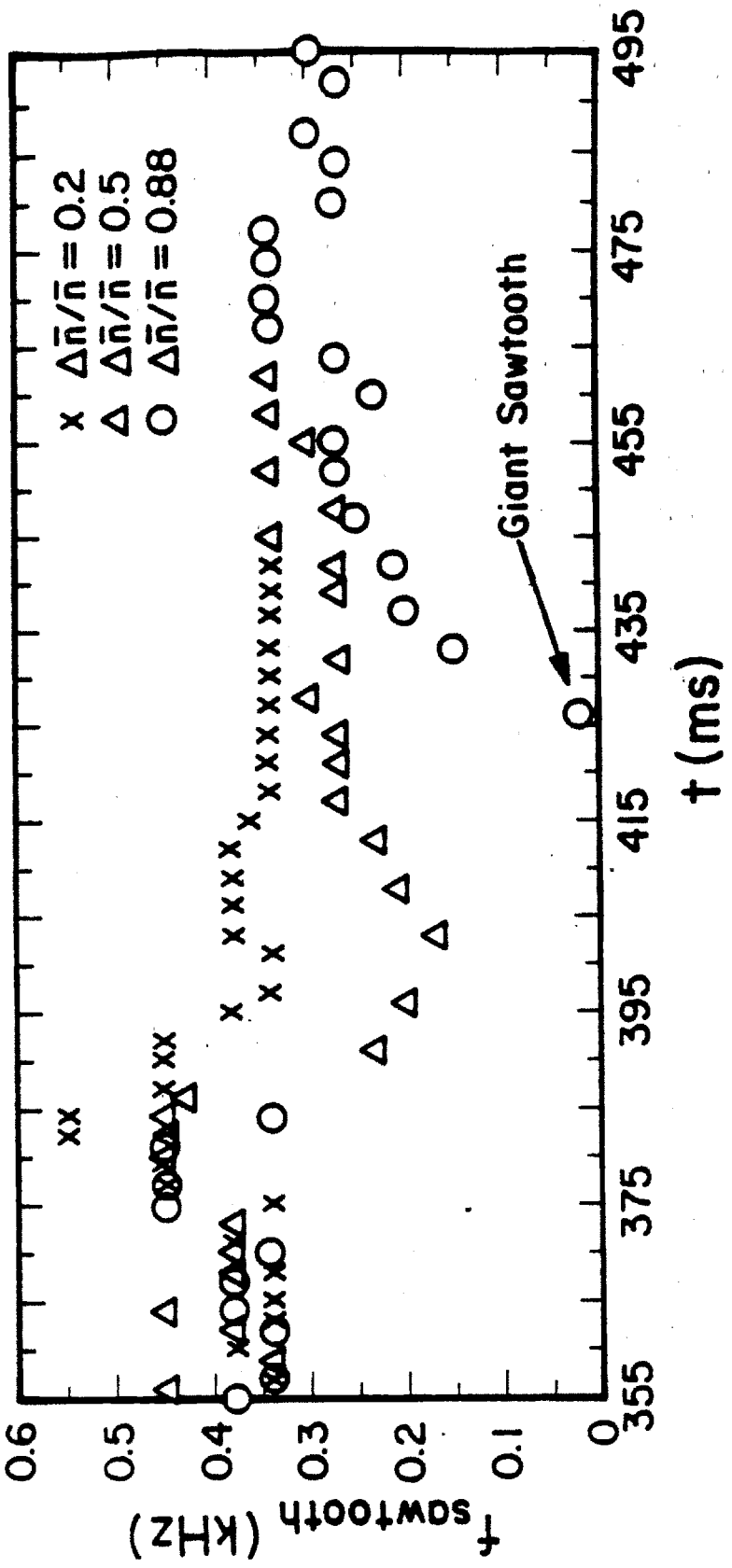

Figure 4.26 — Time evolution of sawtooth period for first three cases shown in fig. 4.25

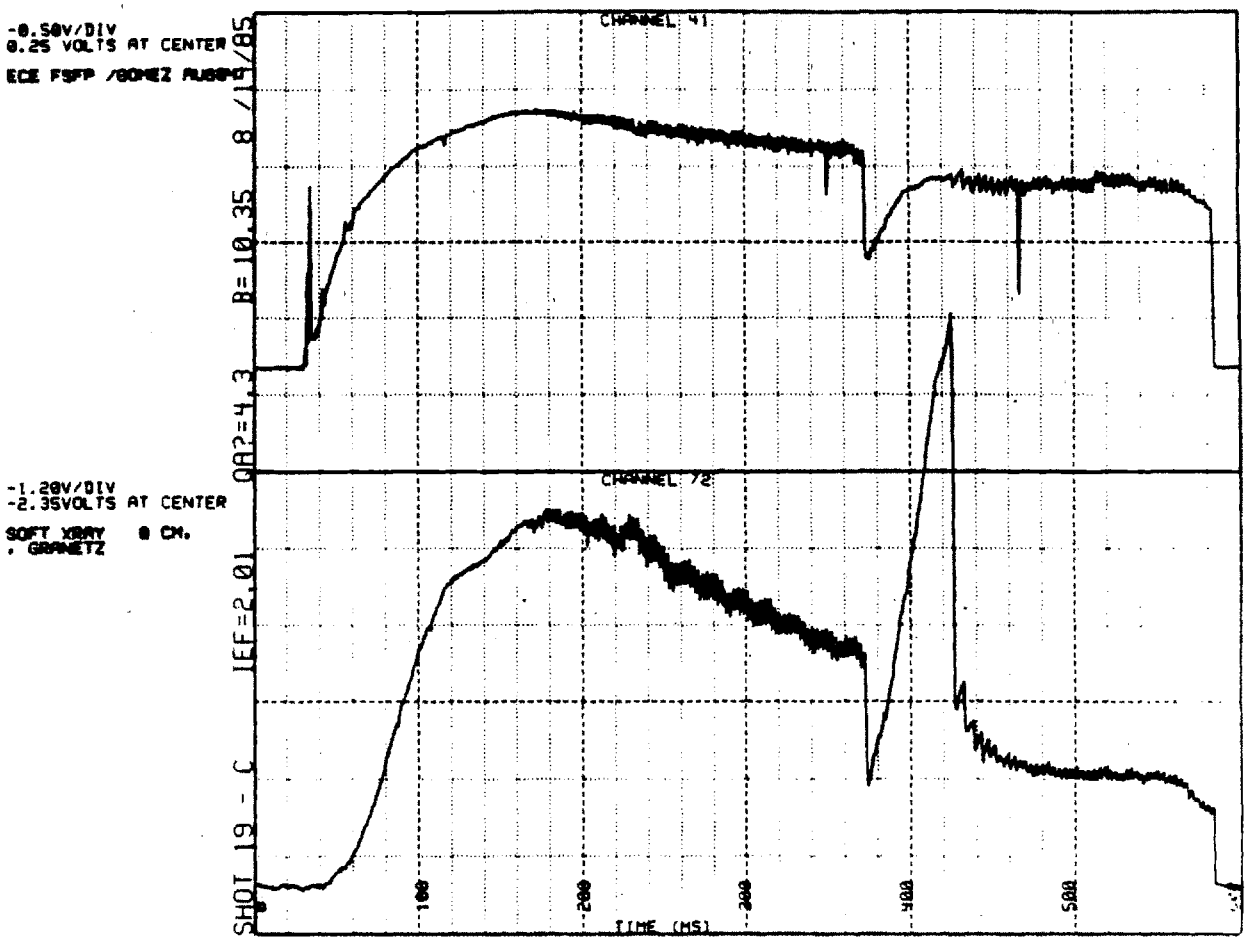

Figure 4.27 — Time evolution of central T_e and soft-Xrays. At $t \sim 425ms$ we see a giant sawtooth crash on the Xrays but no abnormal change in $T_e(0)$.

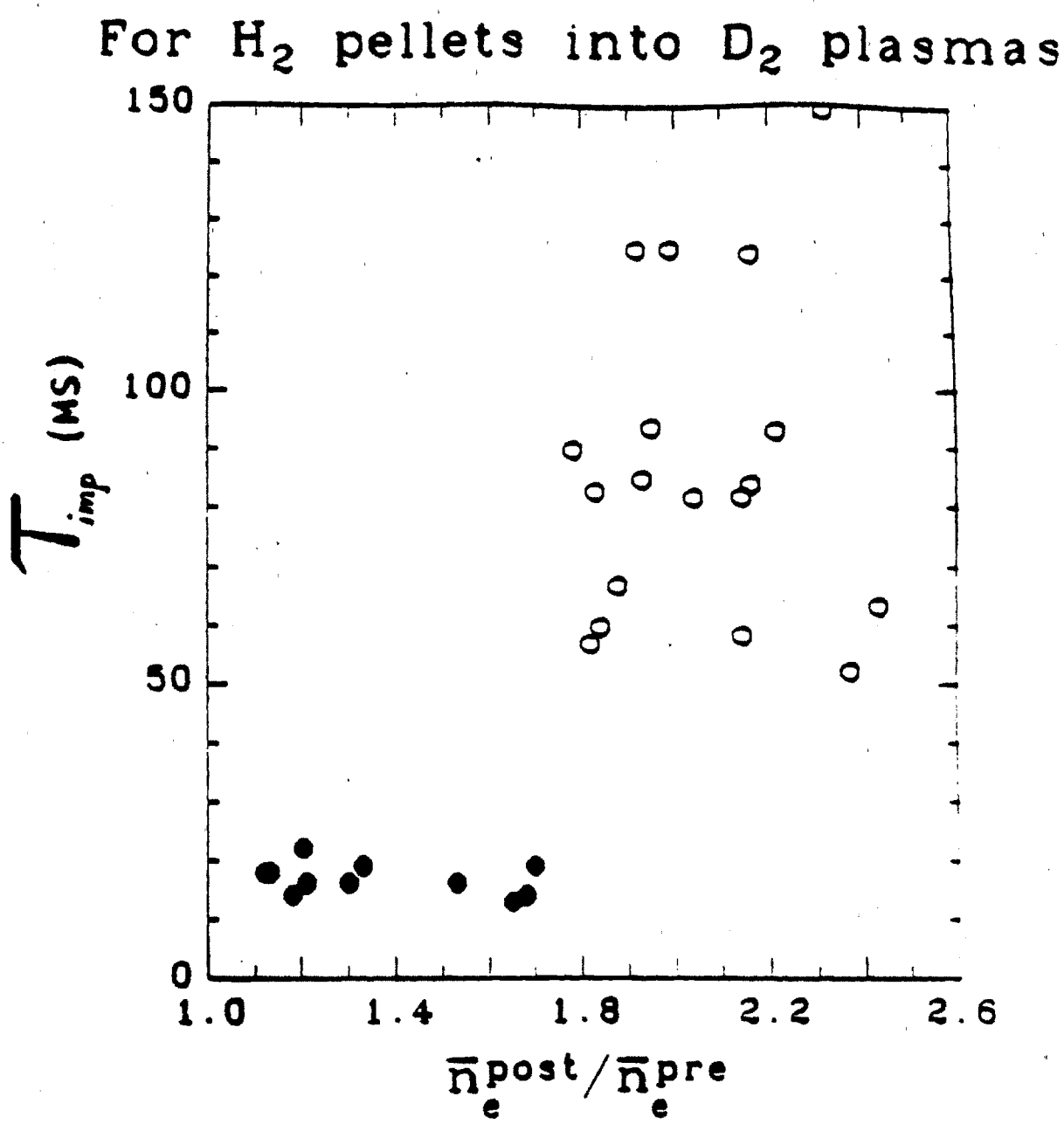

Figure 4.28 — Dependence of post pellet τ_I on pellet size (from ref. [4.20]).

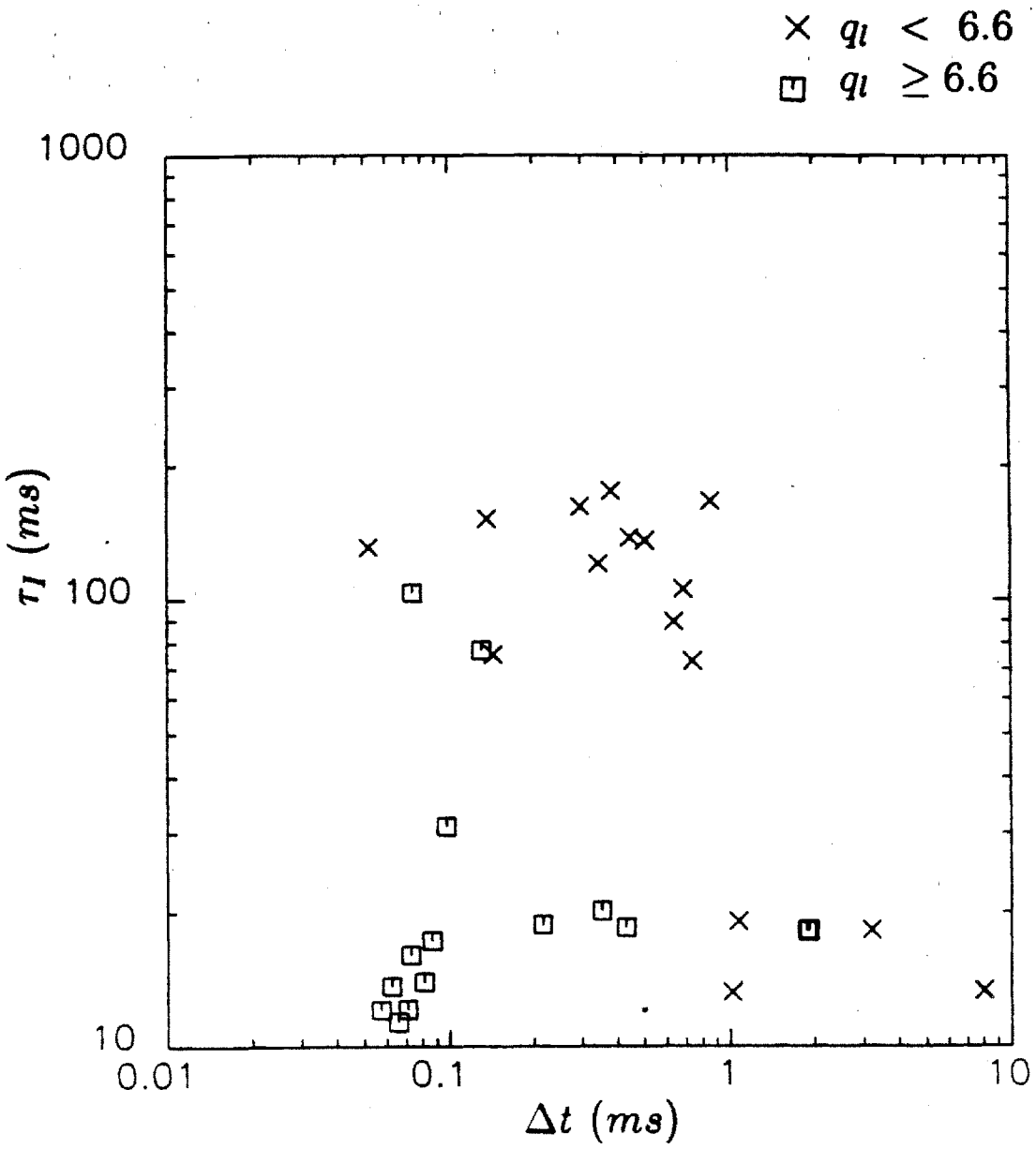

Figure 4.29 — Scaling of τ_I (impurity confinement time) and central T_e relaxation time.

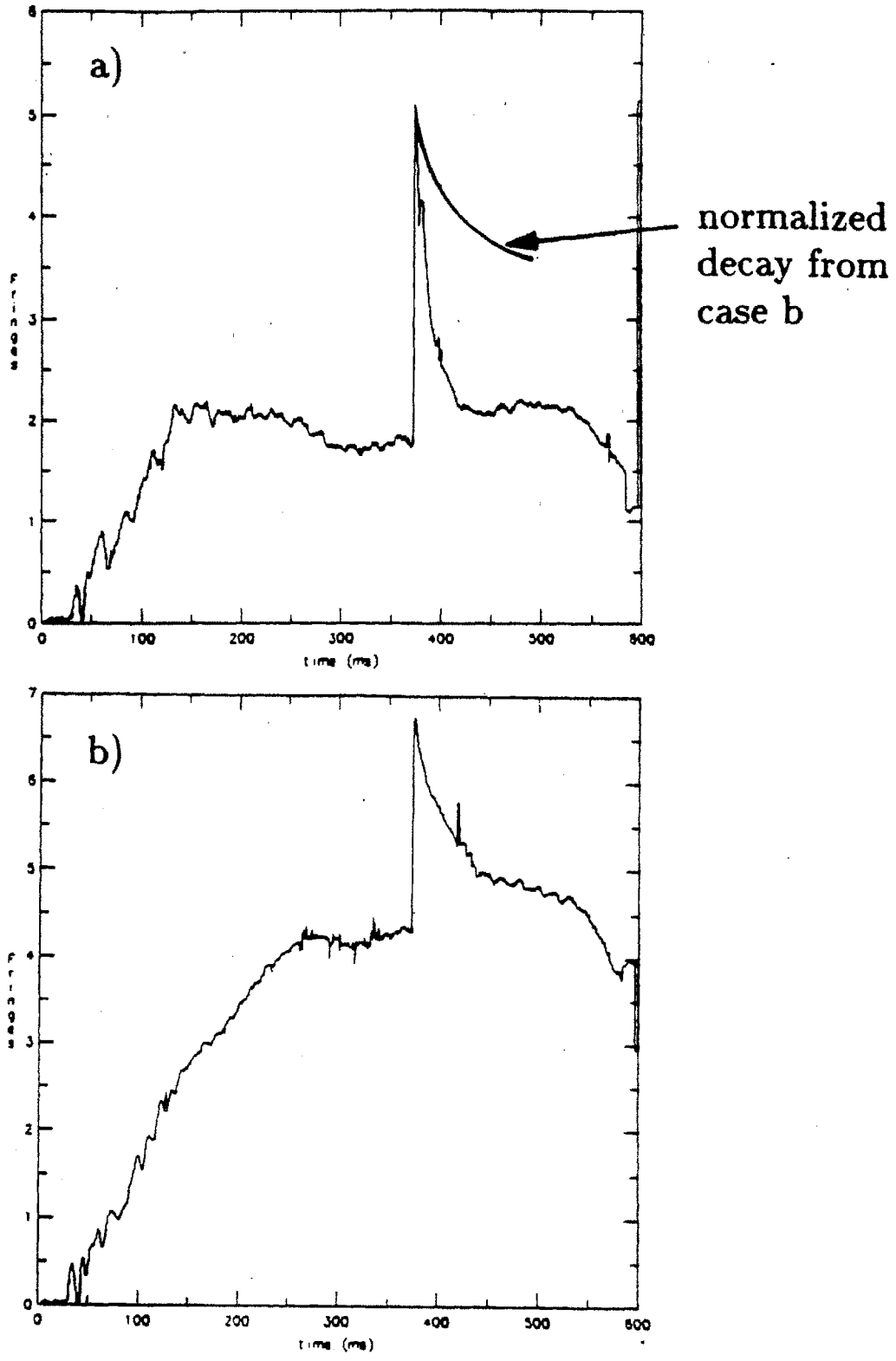

Figure 4.30 — Time evolution of central line averaged density for pellet fuelled plasmas. a)high q_l case($q_l = 10.8$), b)low q_l case ($q_l = 4.8$).

V) Conclusions

In the previous chapters we have discussed the study of sawteeth and the plasma response to pellet injection from the point of view of the electron temperature. The diagnostic technique used has been electron cyclotron emission(ECE). This is a rather unique diagnostic for it is capable of making essentially a point measurement of the electron temperature without directly sampling the plasma and with a single view. Most other diagnostics involve the measurement of line integrated quantities which have to be deconvolved to arrive at a profile. Because of instrumental and space limitations the deconvolution ususally must employ assumptions about the plasma, which of course limits the kinds of profiles one is sensitive to. What gives ECE its ability to make spatially resolved measurements is the monotonically varying toroidal magnetic field in a tokamak.

Cyclotron radiation takes place at the harmonics of the local cyclotron frequency at the radiator. If we know the spatial distribution of the magnetic field then under certain conditions a frequency can be identified as originating at a specific spatial location in the plasma. The frequencies of interest to ECE in Alcator are $60 - 600GHz$, which lie in the far-infrared range.

In order to make a temperature measurement we need to look at regions of the spectrum which are optically thick. In this case the radiation intensity is proportional to the local electron temperature at the emitter. For the case of Alcator, two harmonics are optically thick, the O mode fundamental and the X mode second harmonic. For this thesis all measurements have been done using the second harmonic, because of its higher frequency and thus intensity. This allows measurement of the electron temperature profile to at least $\pm 13cm$ in the minor radius.

The instrument used in making the measurements has been a six channel FIR grating polychromator(fig. 1.8). This allows the simultanious monitoring of the electron temperature at six radial locations. The effective spatial resolution of this instrument for typical Alcator toroidal fields ($B_T = 8T$) is about $2.5cm$ along the major radius. The vertical and horizontal resolution is fixed by the imaging

system to match the radial resolution. Signal detection was done through six InSb detectors. The time resolution of the instrument is detector limited. The detectors have a maximum time resolution of $\sim 1\mu s$, the actual time resolution was bandwidth limited by the preamp in order to reduce noise, giving an effective resolution of $\sim 3\mu s$.

In this thesis we have focused on the study of some cases of transient phenomena. By studying the transient behaviour of a system we can have access to physics which is normally shielded from us on a longer time scale, but which can have an important effect on the long time behaviour of the system. The study involved the temperature evolution in a sawtoothing plasma and in a pellet fuelled plasma.

In all these cases previous workers have used the soft-Xray emission to study the dynamics of the plasma. While this has the advantage of very good signal to noise and many spatial channels, it has the disadvantage that the signal depends in a complicated way on a number of plasma parameters. This has limited the usefulness of the technique in determining the behaviour of the plasma. Use of ECE to study these effects constitutes a novel approach in many of these areas.

The first subject we considered was that of the sawtooth disruption. This is important to have done first because in the third chapter we use some of these results to drive the development of the model used to study the problem of the electron heatpulse propagation.

The magnetic reconnection model was used to describe how the current profile rearranged itself during the disruption. We showed that for the case of Alcator the skin current which would be generated according to Kadomtsev, dissipates within $300\mu s$. The reconnection time as predicted by Kadomtsev[2.4] can be as much as an order of magnitude larger than the measured disruption time. The discrepancy is such that it may reflect the roughness of the model used in the estimation. For the case of Alcator a more detailed calculation may reduce the discrepancy. Results from TFTR[2.19] indicate however that the discrepancy is even larger. They measure disruption times which can be as low as $40\mu s$ a number which is not consistent with their predicted Kadomtsev reconnection value.

By considering the incremental profiles set up during normal sawteeth we found the ratio of the energy mixing radius to the profile inversion radius (r_M/r_i) to be > 2. By considering single resonant surface reconnection we showed that the maximum possible value this ratio could have is $e^{1/2}$ which is well below that measured. The implication is that even the case of normal sawteeth is incompatible with single resonant surface reconnection. To account for the large values of r_M/r_i the disruption must either involve multiple resonace surface reconnection as discussed by Parail[2.7] or some other mechanism such as the turbulent model proposed by TFR[2.13].

The $m = 1$ precursors found on Alcator have a frequency of oscillation consistent with the electron diamagnetic drift. The amplitude however is incompatible with a single resonant surface model. This was one observation used by TFR to propose that the $m = 1$ precursors could not lead to the sawtooth disruption. Another interpretation which we have suggested is that if two resonant surfaces develop they evolve in such a way as to reduce their net $m = 1$ signature, in this way rather large islands may develop without large precursors.

Empirical studies of the sawtooth period, amplitude and inversion radius were done to compare the behaviour of these parameters with scalings developed for other machines. The sawtooth period compares well with the scaling of McGuire and Robinson [2.12] and Jahns et. al. [2.11]. It was found that the inversion radius agreed well with the TFR scaling[2.13]. The sawtooth amplitude showed reasonable agreement with the TFR scaling and a scaling based on the McGuire-Robinson form. These scalings are empirical in nature, the fact that they agree with Alcator results gives more confidence to their use, since in general Alcator operates in a different regime than the ones for which the scalings were developed(except the McGuire-Robinson case). Any theory developed to explain the sawtooth mechanism should compare favorably with these scalings.

We have studied the case of exotic sawteeth which seem to come in three varieties, partial(fig. 2.21), giant (fig. 2.22) and compound giant (fig. 2.24). The frequency of ocurence for these is a strong function of impurity content (fig. 2.25).

All three cases are characterized by two consecutive disruptions separated by a time less than or equal to one sawtooth period. Between the disruptions large $m = 1$ oscillations are seen inside of the profile inversion radius. Their frequency is consistent with the electron diamagnetic drift frequency. In these cases there is little if any precursors before the first disruption or successors after the second disruption. The delay between the previous sawtooth disruption and the first disruption of the exotic sawtooth is the same as a normal sawtooth period. This implies that the trigger condition in the case of a normal sawtooth and that of an exotic sawtooth must be the same.

Based on the results arrived at from the study of both normal and exotic sawteeth a model was suggested which may explain their respective behaviour in a unified manner. We assume that the trigger condition for the normal sawtooth and an exotic sawtooth is the same. Normal sawteeth reconnect to the center, while exotic sawteeth have their initial disruption arrested before reconnection to the center can occur. In the latter case the system is left in a highly asymmetric state(thus the $m = 1$) until the second disruption takes place, which completes reconnection to the center. A possible mechanism to arrest the disruption may be the creation of a magnetic barrier. The delay between the first and second disruption is the time the plasma takes to overcome the magnetic barrier. The creation of this barrier may be associated with the presence of impurities. The absence of $m = 1$ precursors may be due to the development of multiple resonant surfaces as suggested. This model is suggested by the data although it is not the only possible interpretation. The self consistency of the model must be checked. Work must be done studying how magentic barriers may arise in a tokamak and whether impurities may play a role in their creation.

The heatpulse generated by the sawtooth disruption has been used to estimate the transport coefficients. Previous workers in the area have used the soft-Xray signal to make these measurements[3.1]. Because of the uncertainty in making a temperature measurement using soft-Xrays, workers have been limited to using τ_p(the delay for the signal to peak at a given radial location after the previous

sawtooth crash) to parametrize the diffusion process. Using ECE to measure the electron temperature, has allowed us to make use of the complete temperature trace in inferring the electron thermal diffusivity.

In order to infer the electron thermal diffusivity, the diffusive term of the electron thermal transport equation must dominate. Previous workers have assumed this to be the case, however in Alcator the situation is not as clear. During high density operation the ions may have a significant effect on the electron energy transport. A single sawtooth model was developed to study the parameter range over which the diffusion term dominates the electron thermal transport equation. Five non-diffusive effects were considered, density pulse, radiation damping,thermal convection, Ohmic heating and electron-ion coupling. Of these electron-ion coupling was found to be the most significant. This effect couples the evolution of the electron and ion heatpulse, thus the measured χ_{eff} reflects a complicated function of the two. The degree of coupling is a sensitive function of the dimensionless collisional coupling coefficient ν and $\beta \equiv \chi_i/\chi_e$. Electron-ion coupling effects may play a significant role even at moderate collisionalities ($\nu \sim 50$) depending on the value of β. For the case of Alcator these correspond to densities $> 2.5 \times 10^{14} cm^3$. Density pulse effects were found to be important when the size of the density pulse perturbation is roughly the same as the temperature perturbation.

A method of analysis was developed which automatically accounts for the plasma not being in a quiescent state. Starting from the general transport equations and neglecting the non-diffusive terms, a Fourier transform hierarchy was developed to describe the evolution of the heatpulse. This method gives rise to a natural ordering of the various terms, with $p = 0$ representing the time averaged profiles and $p > 0$ the incremental profiles. The reheat term R which appears in the equation for every order p, specifies the initial and final profiles over the interval of the solution. Based on results of chapter II, we found the initial perturbation to extend far out into the plasma, this may make near field effects important. For this reason we have used measured profiles for R. The form for χ_e was allowed to have a simple parabolic dependence on radius. It is found that the lowest orders of p are the ones

most sensitive to χ_e. Thus only the six lowest harmonics in p beyond $p = 0$ were used to find a self-consistent χ_e.

Analysis has shown that the most sensitive parameter in estimating χ_e is the reheat profile R. A comparison was done of the estimated χ_e as found by the method proposed in ref. [2.5] and the method used here. We find that our method predicts a value for χ_e roughly three times lower than that of [2.5]. These results show that at least for the case of Alcator near-field effects play an important role in the χ_e estimate.

The data showed a preference for a radially increasing χ_e over a flat χ_e. The κ_e(thermal conductivity) profiles were also found to increase with radius. Comparison with power balance estimates show $\chi_{ehp}/\chi_{epb} \sim 1 - 3$ with a mean about 1.7. With the data showing a systematic overestimation of χ_e over that of power balance. The reason for this remains unclear although several were proposed. One possibility might be a time changing χ_e(a remnant from the sawtooth) which affects the central region of the plasma, power balance estimates may be much less sensitive to this than the heatpulse estimate. Another possibility proposed by TFTR[2.5] is that the heatpulse evolves with a χ_e different than that for bulk transport.Multiple non-diffusive effects may also play a role in the enhancement of χ_e.

A scaling of $1/\chi_e$ with density showed no saturation as does the global energy confinement time. While this result is consistent with the ions being the loss channel, it is not definitive because of the possible importance of non-diffusive effects. In the high density regime the final interpretation is very sensitive to the value of β, which has large uncertainties.

Because of the importance of non-diffusive effects in regimes like Alcator's, explicit accounting of non-diffusive effects must be done in our estimates for χ_e. Multiple non-diffusive effects may lower the threshold at which χ_{eff} becomes significantly influenced by them.

In studying the evolution of the electron temperature during pellet injection we focused on the transient behaviour during the early stages of injection. The physics taking place at this early stage not only plays an important role in the ablation and

deposition process, but evidence shows that the events taking place at this stage may play a role in determining the subsequent evolution of the plasma.

With reguards to the evolution of the electron temperature we have observed two types of relaxations. A fast relaxation which takes place on a time scale much faster than would be predicted by bulk diffusion and a slow relaxation which is more consistent with bulk diffusion. Which of these two cases takes place seems to be a function of the pellet size relative to the plasma.

A propagation study of the pellet generated heat(cold) pulse was done. We found the leading edge in both the slow and fast decay case to propagate into the plasma with a velocity roughly twice that of the pellet. The difference between the two cases is found with the behaviour of the trailing edges. This is not surprising since it is the trailing edge which reflects the main energy transport of the pulse. Outside the ablation radius the evolution of both cases is similar and consistent with the pellet velocity. Inside the ablation radius the evolution is very different for the two cases. The tail for the fast decay case propagates into the center at the same rate as outside the ablation radius. The slow decaying case undergoes a drastic reduction in the rate of propagation (fig. 4.6).

A scaling has been done of the central relaxation time Δt_0 with $\Delta\overline{n}/\overline{n}$. A transition is found between the slow and fast decay around $\Delta\overline{n}/\overline{n} \sim 1$. A similar correlation was found with the change in central temperature. Larger temperature variations tend to have fast decays.

In ref.[2.11] it was suggested that the fast relaxation is triggered by the pellet crossing the $q = 1$ surface. In Alcator we find that none of the pellets studied penetrated to $q = 1$, yet were able to drive the fast relaxation. The fast decay was found for pellets that are able to penetrate past the half radius with a transition at $l \sim 8cm$, in this region a correlation of the decay time with sawtooth phase was found, suggesting that at least in this region the sawtooth mechanism may play a role in the relaxation. No correlation with sawtooth phase was found for the cases which lie outside this region. If $l < 8cm$ the relaxation was always slow and if $l > 8$ the relaxation was fast.

During injection we expect the density profile to develop large positive gradients toward the center of the plasma. A scaling was done which showed that the fast relaxation scaled with the parametrized maximum density gradient. This is consistent with the picture that it is the density gradients which may drive the instability which leads to the fast relaxation.

A model was developed to simulate the electron temperature relaxation during injection assuming it is diffusive. It was found that the fast propagation of the leading edge in both cases is consistent with bulk diffusion. The evolution of the tail for the slow decay case was also consistent with bulk diffusion. The fast decay case could only be simulated if we assume an anomalous χ_e about two orders of magnitude larger than the bulk, which operates whenever the density gradient becomes positive.

The pressure profile is not as strongly affected by the injection process as is the density profile, large changes in the pressure profile can only come about if preceeded by anomalous transport. These results coupled with the measured correlation of relaxation time and density gradient suggest that it is the density gradient which drives the fast relaxation.

Pellet injection has been used to study the effect of profile consistency in the plasma. When $q_l < 8$, the initial and final electron temperature profiles are found to be similar. This was found to be true even for the cases in which the plasma was sawtoothing before but not after injection. When $q_l > 8$ profile consistency seems to turn itself off.

The results suggest that profile consistency is a limit which represents the narrowest stable width that can be achieved by the plasma. Whether this limit is accessible or not depends on the plasma transport. Low q_l discharges exhibit better confinement than high q_l discharges. According to this picture accesiibilty to profile consistency is expressed by conditions of eq. 4.4.5 and 4.4.6. The transition takes place when $a_{T_e}(trans) \sim a_{T_e}(q_l)$ which for Alctor is when $q_l \sim 6 - 8$.

A wide variety of sawtooth behaviour was found in post-pellet plasmas. Impurities seem to play an important role in controlling the sawteeth just as in the case of

exotic sawteeth. The impurities exhibit improved confinement for the case of larger pellets. A transition in confinement is seen with $\Delta\overline{n}/\overline{n}$ which is similar to that for the central electron temperature relaxation. This suggests a link between events taking place early during injection and the long time behaviour of the plasma.

Future work in this area should improve our understanding of how the density may generate such fast transport in the early stages of injection. A better measurements of how the density profile evolves, are needed in order to assess the evolution of the pressure profile and provide more information about the transport in the plasma. Based on results of the temperature profiles for different values of q_l, it is found that the pellet seems to improve confinement for low q_l discharges and in some cases degrade confinement for high q_l discharges. The dependence of transport on current is not well understood. The impurities again have come to center stage in determining sawtooth behaviour as in the case of exotic sawteeth. We must understand how the impurities affect the sawteeth. For the case of non-sawtoothing plasmas in which the electron temperature profile seems to have the self-consistent profile width, we must understand how the impurities can affect the temperature profile and how different can it be from the canonical shape.